

<https://doi.org/10.15388/vu.thesis.673>

<https://orcid.org/0000-0003-1781-4660>

VILNIUS UNIVERSITY
CENTER FOR PHYSICAL SCIENCES AND TECHNOLOGY

Vladislovas Čižas

Coexistence of High-Frequency Parametric and Bloch Gain in Doped GaAs/AlGaAs Superlattices

DOCTORAL DISSERTATION

Natural Sciences
Physics (N 002)

VILNIUS 2024

This dissertation was prepared between 2019 and 2023 at the Center for Physical Sciences and Technology. The research was supported by:
TPP-03-049 – Technological development project
01.2.2-CPVA-K-703-03-0019 – Research and experimental development project
S-MIP-22-76 – National scientific group project

Academic supervisor:

Prof. Habil. Dr. Gintaras Valušis (Center for Physical Sciences and Technology, Natural sciences, Physics – N 002).

Dissertation Defense Panel:

Chairman – Prof. Habil. Dr. Gintautas Tamulaitis (Vilnius University, Natural Sciences, Physics – N 002).

Members:

Prof. Dr. Ramūnas Aleksiejūnas (Vilnius University, Natural Sciences, Physics – N 002),

Dr. Vytautas Karpus (Center for Physical Sciences and Technology, Natural Sciences, Physics – N 002),

Prof. Dr. Saulius Marcinkevičius (KTH Royal Institute of Technology, Natural Sciences, Physics – N 002),

Dr. Vaidas Pačebutas (Center for Physical Sciences and Technology, Technological Sciences, Material Sciences – T 008).

The dissertation shall be defended at a public meeting of the Dissertation Defence Panel at 14:00 on October 7th in Room D401 of the Center for Physical Sciences and Technology.

Address: Saulėtekio av. 3, NFTMC, Room D401, Vilnius, Lithuania.

Tel. +370 5 264 9211; email: office@ftmc.lt.

The text of this dissertation can be accessed at the libraries of Center for Physical Sciences and Technology and Vilnius University Library, as well as on the website of Vilnius University: www.vu.lt/naujienos/ivykiu-kalendorius.

<https://doi.org/10.15388/vu.thesis.673>

<https://orcid.org/0000-0003-1781-4660>

VILNIAUS UNIVERSITETAS
FIZINIŲ IR TECHNOLOGIJOS MOKSLŲ CENTRAS

Vladislovas Čižas

Aukšto dažnio signalo Blocho ir
parametrinio stiprinimo sambūvis
legiruotose GaAs/AlGaAs
supergardelėse

DAKTARO DISERTACIJA

Gamtos mokslai
Fizika (N 002)

VILNIUS 2024

Disertacija rengta 2019–2023 metais Fizinių ir technologijos mokslų centre.
Mokslinius tyrimus rėmė:
TPP-03-049 – Technologinės plėtros projektas
01.2.2-CPVA-K-703-03-0019 – Mokslinių tyrimų ir plėtros projektas
S-MIP-22-76 – Mokslinių grupių projektas

Mokslinis vadovas:

Prof. habil. dr. Gintaras Valušis (Fizinių ir technologijos mokslų centras, gamtos mokslai, fizika – N 002).

Gynimo taryba:

Pirmininkas – Prof. Habil. Dr. Gintautas Tamulaitis (Vilniaus universitetas, gamtos mokslai, fizika – N 002).

Nariai:

Prof. Dr. Ramūnas Aleksiejūnas (Vilniaus Universitetas, gamtos mokslai, fizika – N 002),

Dr. Vytautas Karpus (Fizinių ir technologijos mokslų centras, gamtos mokslai, fizika – N 002),

Prof. Dr. Saulius Marcinkevičius (KTH Royal Institute of Technology, gamtos mokslai, fizika – N 002),

Dr. Vaidas Pačebutas (Fizinių ir technologijos mokslų centras, technologijos mokslai, medžiagų mokslas – T 008).

Disertacija ginama viešame Gynimo tarybos posėdyje Spalio 7-ą dieną Nacionalinio fizinių ir technologijos mokslų centro D401 auditorijoje.

Adresas: Saulėtekio al. 3, NFTMC, D401 aud., Vilnius, Lietuva.

Tel. +370 5 264 9211; el. paštas: office@ftmc.lt.

Disertaciją galima peržiūrėti Fizinių ir technologijos mokslų centro bei Vilniaus universiteto bibliotekose ir VU interneto svetainėje adresu: www.vu.lt/naujienos/ivykiu-kalendorius.

LIST OF ABBREVIATIONS

NDC	Negative Differential Conductivity
SL	SuperLattice
NDV	Negative Differential Velocity
NDr	Negative Differential resistivity
NDR	Negative Differential Resistance
IV	Current-Voltage
THz	TeraHertz
GHz	GigaHertz
DFWM	Degenerate Four-Wave Mixing
WSL	Wannier-Stark Localization
LSA	Limited Space-charge Accumulation
VACH	Volt Ampere Characteristics
TEOS	Transmittive Electro-Optic Sampling
HIPS	High Impact PolySterene
3D	3 Dimensional
QCL	Quantum Cascade Laser
DC	Direct Current
AC	Alternating Current

LIST OF VARIABLES

v_d	m/s	drift velocity
e	C	electron charge
d	nm	superlattice period
Δ	eV	miniband width
Δ_s	eV	height of the Wannier-Stark step
E_{tot}	V/m	total electric field strength
τ	s	characteristic relaxation time
E_{cr}	V/m	Critical electric field strength
v_p	m/s	peak drift velocity
E_{pump}	V/m	pump electric field strength
E_{probe}	V/m	probe electric field strength
E_{dc}	V/m	pump DC electric field strength
E_{ac}	V/m	amplitude of pump AC electric field
$E_{1,2}$	V/m	amplitude of probe 1,2 AC electric field
ω_0	rad/s	angular frequency of the exciting radiation
$E_{1,2}$	V/m	amplitude of probe AC electric field
$\omega_{1,2}$	rad/s	angular frequency of probe AC electric fields
$\varphi_{1,2}$	rad	relative phase of probe AC electric fields
φ_{opt}	rad	optimal relative phase of probe AC electric field
μ	$\text{m}^2/(\text{V} \cdot \text{s})$	complex mobility
μ_r	$\text{m}^2/(\text{V} \cdot \text{s})$	real part of complex mobility
μ_i	$\text{m}^2/(\text{V} \cdot \text{s})$	imaginary part of complex mobility
μ_0	$\text{m}^2/(\text{V} \cdot \text{s})$	Drude mobility
μ_{inc}	$\text{m}^2/(\text{V} \cdot \text{s})$	incoherent mobility component
μ_{coh}	$\text{m}^2/(\text{V} \cdot \text{s})$	coherent mobility component
μ^{opt}	$\text{m}^2/(\text{V} \cdot \text{s})$	optimal mobility
m^*	kg	effective mass at the bottom of the miniband
N	m^{-3}	electron volume density
L	m	superlattice length
NL	m^{-2}	Kroemer coefficient
NL_{cr}	m^{-2}	critical Kroemer coefficient
$A_h, A_{\text{inc}}, A_{\text{coh}}$	V/s^2	real relative mobility components
P_0	W	peak power

n_i	amount of photons participating in the process
P	power density
\overline{P}	unitless power density
x	unitless frequency
$F_{1,2}$	unitless probe 1,2 electric field strength
F_{pump}	unitless pump electric field strength
F_{tot}	unitless total electric field strength
F_{dc}	unitless DC pump electric field strength
F_{ac}	unitless AC pump electric field strength
$\overline{P}_{1,2}$	relative power at $\omega_{1,2}$ frequency
p, q	integer numbers of fractional subharmonics

CONTENTS

INTRODUCTION	10
1 LITERATURE OVERVIEW	22
1.1 High-frequency generation and amplification effects in bulk semiconductors	22
1.2 High-frequency generation and amplification effects in quantum semiconductor superlattices	25
1.2.1 On the nature of negative differential velocity in superlattices . .	25
1.2.2 On the matter of Bloch oscillations in superlattices.	28
1.2.3 Parametric gain in superlattices	33
2 SAMPLES AND EXPERIMENTAL TECHNIQUES	35
2.1 Architecture of the superlattice	35
2.2 Experimental technique and the setup	37
2.3 Theoretical Models	40
3 EXPERIMENTAL OBSERVATION OF DISSIPATIVE PARAMETRIC GAIN IN DOPED GAAS/ALGAAS SUPERLATTICES AND SMALL SIGNAL APPROACH	42
4 DEGENERATE AND NON-DEGENERATE LARGE SIGNAL GAIN IN GAAS SUPERLATTICES	57
4.1 Influence of the Large Signal Gain Model on the degenerate gain processes	57
4.2 Influence of the Large Signal Gain Model on the non-degenerate gain processes	68
5 SIGNATURES OF STABLE BLOCH GAIN OBSERVED VIA HYBRID BLOCH PLASMON MODES IN INJECTOR-CONTROLLED STRONGLY-COUPLED GAAS/ALGAAS SUPERLATTICE DIODE	74
APPENDICES	85
6.1 Appendix A. Additions to the literature review section . .	85
6.1.1 Addition to the matter of negative differential velocity effects in bulk materials	85
6.1.2 On the matter of proper contact selection	92
6.1.3 Comment on the Manley-Rowe relations	97
6.1.4 Evolution and negative differential velocity effect of the quantum semiconductor superlattices	99
6.1.5 On the matter of Bloch oscillations in semiconductor superlattices	101
6.1.6 Esaki-Tsu drift velocity/electric field dependency derivation . . .	105
6.2 Appendix B. Additions to the methods section	107

6.2.1	Derivation of the critical electric field equation	107
6.2.2	Derivation of the high-frequency mobility equations for the de- generate case	108
	REFERENCES	117
	SANTRAUKA	138
7.1	Įvadas	138
7.2	Metodai	142
7.2.1	Supergardelės architektūra ir eksperimentinis stendas	142
7.2.2	Teoriniai modeliai	143
7.3	Rezultatai	145
7.3.1	Disipatyvaus parametrinio stiprinimo stebėjimas legiruotose Ga- As/AlGaAs supergardelėse ir mažo signalo stiprinimo metodas	145
7.3.2	Didelio signalo stiprinimas GaAs/AlGaAs supergardelėje išsigi- musių ir neišsigimusių procesų metu	151
7.3.3	Stabilus Blocho stiprinimas registruotas per hibridinę Bloch- plazmoninę modą GaAs/AlGaAs supergardelėje	156
7.4	Paveikslų ir lentelių sąrašas	159
	CURRICULUM VITAE	168

INTRODUCTION

Semiconductor superlattices - quantum structures comprising at least two different materials in a way resulting in formation of electronic minibands is the main object of the research for the particular thesis [A1–A4, 5]. The formation of the minibands features possibility of superior charge transport control making the superlattices an attractive media for the exploration of different physical effects. During the decades of extensive research a variety of effects has been observed including, but not limited to Bloch oscillations [5–7], coherent Hall effect [8], Zener tunnelling [9], and high-order fractal quantum oscillations in graphene/n-BN superlattices [10]. Semiconductor superlattices have been shown to take an essential part as a terahertz (THz) or sub-terahertz (sub-THz) generator. Superlattices are vastly employed in modern electronic and optoelectronic devices like quantum cascade lasers [11]. Furthermore, superlattices are predicted to perform as generators employing parametric generation [12,13] or scattering-assisted inversionless Bloch [14–16] gain mechanisms. The employment of the latter two effects for the applications in the THz frequency range were of particular interest for this research.

THz radiation – frequency range spanning between 0.1 THz and 10 THz, are currently experiencing a peak of scientific interest resulting in constant increase of experimental and theoretical investigation, leading to the enlarging of applicational possibilities including communications, sensing, and imaging [17–22]. The latter is worth of additional mention due to the vast application including security [23, 24], packaging inspection [25, 26], pharmaceutical [27], cosmetics [28], and food control [29]. Being low energy radiation (0.4 meV to 40 meV), THz radiation is basically harmless to live creatures making this frequency range appealing for the medical imaging applications [30], providing a huge amount of novel medical capabilities such as live scanning or water content analysis in different tissues [31,32]. In any of the cases, small size, efficient and cost effective system is required for successful widespread. Most simplified imaging system comprises THz source, detector and some beam-shaping optics. A successful example of system size reduction is displayed by the change of bulky optical components with modern metasurface or diffractive optic-based beam-shaping elements [33–35]. The works with novel materials like 3D printed high impact polystyrene (HIPS) allowing to achieve extremely cheap beam-shaping solutions within comparably simple fabrication process are also worth to be mentioned [36]. Significant contribution has already been done to the research of sensitive, high-speed THz detectors. These include high-electron mobility transistor [37,38], photoconductive THz antenna [39,40], superconductor [41], quantum structure-based solutions [42,43], Golay cells [44], pyroelectric detectors [45], and bolometers [46] each technology comprising its advantages

and disadvantages. Moreover, huge amount of emitter selection variety exists, including quantum vacuum electronic sources (klystrons [47], free electron lasers [48, 49]), solid-state sources (Gunn diode [50, 51], high-frequency transistors [52, 53]), laser sources (quantum cascade lasers (QCL) [54, 55], elemental semiconductor lasers [56]), difference frequency generators [57, 58], crystal parametric oscillators [59–61] and more. Despite the provided variety of choice, cost- and power-efficient broadband THz frequency range generator, capable of operating in room temperature conditions is still missing [62]. Employment of the semiconductor superlattice structures as small, tunable and efficient THz frequency source has been discussed for a very long time [63]. Such structures are predicted to fulfil all of the above-discussed requirements, still, despite fruitful long-lasting theoretical research, up to now no experimental evidence of the stable gain has been recorded.

Thus, the major goal of the research covered within this thesis was **to investigate both experimentally and theoretically high-frequency gain mechanisms in GaAs/AlGaAs superlattices under room temperature conditions in order to reveal their features, parameters and to determine optimal experimental conditions for the observation of stable gain.**

Appearance of both Bloch and parametric gain mechanisms has been predicted due to the superlattice featuring negative differential mobility regime under appropriate biasing conditions. It is shown by Esaki and Tsu [63] that in the DC-biased superlattice drift velocity experiences a peak before the decrease which is attributed to the Bragg reflections of electrons in periodic k-space. For the case of dissipative parametric gain, appearing in the AC and DC biased superlattice, the latter is expected to visit the negative differential velocity (NDV) state during part of the AC bias period, resulting in the appearance of degenerate and non-degenerate generation processes [64]. Moreover, due to the application of bias field, formation of Wannier-Stark ladders, being the key ingredient for the observation of Bloch gain in semiconductor superlattices, is revealed [5]. By controlling the applied bias one may gain the control as on the spectral characteristics of the broadband dissipative parametric gain processes, as on the Bloch frequency. However, despite the long-lasting theoretical research, experimental evidence is considered to stand behind. No experimental evidence on the dissipative parametric gain have been previously provided. Furthermore, the experimental evidence on the inversionless Bloch gain has been only provided employing optical experiments, wherein Wannier-Stark ladders have been coupled using the optical broadening of the excitation laser source [65]. Finally, no comprehensive theoretical analysis have been performed neither on the possible coexistence of both gain mechanisms, nor on the large signal gain effects which are essential to be included as the experiments, performed during this research, revealed generation levels far exceeding the classically employed

limits of the small signal gain models.

Scientific Novelty

- It was shown that DC biased superlattice structure in the microwave electric field can not be treated as pure optical system, but nonlinear optoelectronic system operating in negative differential velocity regime with predominating multiphoton generation/amplification process.
- Stable coherent parametric gain at various harmonics and sub-harmonics of the pump frequency was observed from the DC biased GaAs/AlGaAs superlattice, stimulated by the intensive microwave pump in the waveguide-based experiment under room temperature conditions.
- The observed effect is explained via formation of slow longitudinal waves, travelling with the drift velocity, thus, ensuring gain coefficients exceeding 10^4 cm^{-1} due to the differences of speed of light and drift velocity in the superlattice.
- Multiplicity of simultaneously occurring multiphoton processes was revealed. The frequencies of the analysed spectra were found to be connected via up- or down-conversion equations ($\omega_1 \pm \omega_2 = n_{\pm}\omega_0$). The existence of both types of the processes was found to be a remarkable property of the dissipative mechanism for the superlattices operating in the Esaki-Tsu NDV regime.
- Processes involving up to 8 excitation photons participating in the reaction were recorded.
- Under dissipative parametric gain conditions ($\omega_0\tau \ll 1$), Manley-Rowe relations, describing the power transfer in the nonlinear elements, are shown to be broken for the superlattices operating in the Esaki-Tsu NDV regime.
- Importance of proper probe electric field phase selection was addressed, revealing the existence of optimal relative phase, supplementing significantly larger gain in comparison to the non-optimal relative phase, which under several biasing conditions may result in the total absence of gain.
- Formation of the amplification islands have been shown, wherein amplification from the threshold probe electric field strength is allowed for specific selection of biasing conditions and frequencies.
- Coexistence of phase-independent Bloch gain and phase-dependent parametric gain may be observed under DC bias exceeding critical Esaki-Tsu electric field conditions. The dominance between the two processes changes with the change of AC pump electric field strength.

- For the case of $\omega_0/2$ sub-harmonic frequency, which is generated by degenerate process, pure parametric mode can be achieved at considerably high DC and AC pump electric field strengths (effect unavailable for any other frequency).
- Possibility to achieve pure parametric gain for any other frequency was suggested by placing the superlattice into "amplification island" mode via DC switching, allowing to achieve pure parametric generation without applying the external AC source of particular frequency to overcome the threshold electric field strength.
- For the case of non-degenerate process, generation possibility (from negligibly small probe signal) of fractional sub-harmonics in the area of $F_{ac} > F_{dc}$ was shown to be available.
- The coupled Bloch-plasmon (Epshtein) modes were experimentally demonstrated in quantum semiconductor superlattice for the first time.
- The gain mechanism from the coupled plasmon mode to the stable Bloch gain displays the sharp transition with the applied DC voltage.
- Stable inversionless Bloch gain can be observed in GaAs/AlGaAs superlattice in microwaves at room temperature. The gain mechanism is preserved in both miniband transport and non-resonant interminiband (Zener) tunnelling regimes.
- Carrier transport mechanisms in quantum semiconductor superlattices from Ohmic mode, via Bloch gain/oscillations up to interminiband transport domination can be tuned by variation of the applied voltage.

Statements to be defended

- **Statement 1:**

Dissipative parametric gain under intense microwave pumping in biased sub-critically doped quantum GaAs/AlGaAs superlattices at room temperature manifests itself as a coherent emission at various fractional sub-harmonics of the pump frequency via multiplicity of simultaneously occurring up-conversion and down-conversion processes.

- **Statement 2:**

Manley-Rowe relations are not valid for description of dissipative parametric gain in biased and subcritically doped GaAs/AlGaAs superlattices.

- **Statement 3:**

High-frequency gain in sub-critically doped semiconductor quantum superlattices is coexistence of Bloch and parametric mechanisms; the interplay and contribution of these gain mechanisms can be adjusted by the sweeping the pump strength and leveraging a proper phase between the pump and strong probe electric fields.

- **Statement 4:**

Transition of the dominating gain mechanism from the Bloch to the parametric one in sub-critically doped semiconductor superlattices with an increase of probe electric field is conserved in both degenerate and non-degenerate gain processes; in case of strong signal and two probe frequencies in the parametric gain, the energy can be transferred not only from the bias, but also between the probes.

- **Statement 5:**

Inversionless Bloch gain can be observed in biased GaAs/AlGaAs superlattice in microwaves at room temperature via manifestation of coupled Bloch-plasmon (Epshtein) modes; the gain features a sharp transition from plasmonic absorption to the Bloch gain which is preserved in both miniband transport and non-resonant interminiband (Zener) tunnelling regimes.

List of publications

On the dissertation topic

- [A1] **Vladislovas Čižas**, Liudvikas Subačius, Natalia V. Alexeeva, Dalius Seliuta, Timo Hyart, Klaus Köhler, Kirill N. Alekseev, and Gintaras Valušis, Dissipative Parametric Gain in a GaAs/AlGaAs Superlattice, *Physical Review Letters*, **128**, 236802 (2022). **Editor choice.**
- [A2] Gintaras Valušis, Kirill Alekseev, **Vladislovas Čižas**, Linas Minkevičius, Natalia Alexeeva, Dalius Seliuta, Liudvikas Subačius, Broad-band High-Frequency Radiation Generating/Amplifying Device Based on Quantum Semiconductor Superlattice, *Lithuanian Patent*, **7000**, 1-13 (2023).
- [A3] **Vladislovas Čižas**, Natalia Alexeeva, Kirill N. Alekseev, and Gintaras Valušis, Coexistence of Bloch and Parametric Mechanisms of High-Frequency Gain in Doped Superlattices, *MDPI Nanomaterials*, **13**, 1993 (2023).
- [A4] **Vladislovas Čižas**, Natalia Alexeeva, Kirill N. Alekseev, and Gintaras Valušis, Sum-Frequency Generation and Amplification Processes in Semiconductor Superlattices, *Lithuanian Journal of Physics*, **63-3**, 148-154 (2023).
-
- [A5] **Vladislovas Čižas**, Liudvikas Subačius, Natalia V. Alexeeva, Dalius Seliuta, Timo Hyart, Klaus Köhler, Kirill N. Alekseev, and Gintaras Valušis, Dissipative Parametric Gain and Multiphoton Effects in Quantum GaAs/AlGaAs Superlattice, *Conference Proceedings of the 47th International Conference on Infrared, Millimeter and Terahertz Waves (IR-MMW-THz)*, 1-3 (2022).

Conference presentations

- [B1] **Vladislovas Čižas**, Liudvikas Subačius, Natalia V. Alexeeva, Dalius Seliuta, Kirill N. Alekseev, and Gintaras Valušis, Fractional Frequencies in Microwave Response of GaAs/AlGaAs Superlattices, *Advanced Properties and Processes in Optoelectronic Materials and Systems, Apropos 17*, **O21**, 44 (2020). Vilnius, Lithuania. **Oral presentation.**
- [B2] **Vladislovas Čižas**, Liudvikas Subačius, Kirill N. Alekseev, and Gintaras Valušis, Netiesinis Mikrobangų Atsakas GaAs/AlGaAs Super-gardelėse, *10-oji doktorantų ir jaunųjų mokslininkų konferencija, FizTech 2020*, **24**, 27 (2020). Vilnius, Lithuania. **Oral presentation.**

- [B3] Vladislovas Čižas, Kirill Alekseev, and Gintaras Valušis, Experimental Evidence of the Nondegenerate Parametric Gain in Quantum Superlattices, *66th international conference for students of physical and natural sciences, Open Readings 2023*, **O1-1**, 30 (2022). Vilnius, Lithuania. **Oral presentation.**
- [B4] Vladislovas Čižas, Liudvikas Subačius, Natalia V. Alexeeva, Dalius Seliuta, Timo Hyart, Klaus Köhler, Kirill N. Alekseev, and Gintaras Valušis, Analysis of the microwave dissipative parametric gain in biased GaAs/AlGaAs Superlattice, *International Conference on the Physics of Semiconductors, ICPS2022*, **800**, 30 (2022). Sydney, Australia. **Oral presentation.**
- [B5] Vladislovas Čižas, Liudvikas Subačius, Natalia V. Alexeeva, Dalius Seliuta, Timo Hyart, Klaus Köhler, Kirill N. Alekseev, and Gintaras Valušis, GaAs/AlGaAs Superlattices as Dissipative Room Temperature High-Frequency Amplifiers, *50th International School & Conference on the Physics of Semiconductors, Jaszowiec 2022*, **ThO8**, 177 (2022). Szczyrk, Poland. **Oral presentation.**
- [B6] Vladislovas Čižas, Liudvikas Subačius, Natalia V. Alexeeva, Dalius Seliuta, Timo Hyart, Klaus Köhler, Kirill N. Alekseev, and Gintaras Valušis, Quantum GaAs/AlGaAs Superlattice: Multiphoton and High-Frequency Gain Effects at Room Temperature, *International Conference on Free Electrons Laser Applications in Infrared and THz Studies of New States of Matter*, (2022). Warsaw, Poland. **Oral presentation. Invited talk.**
- [B7] Vladislovas Čižas, Liudvikas Subačius, Natalia V. Alexeeva, Dalius Seliuta, Kirill N. Alekseev, and Gintaras Valušis, Biased GaAs/AlGaAs Superlattice as Dissipative Parametric Amplifier in Microwaves, *24th International Conference-School Advanced Materials and Technologies 2022, AMT2022*, **B-P72**, 109 (2022). Palanga, Lithuania. **Poster presentation. Best poster award.**
- [B8] Vladislovas Čižas, Liudvikas Subačius, Natalia V. Alexeeva, Dalius Seliuta, Timo Hyart, Klaus Köhler, Kirill N. Alekseev, and Gintaras Valušis, Dissipative Parametric Gain and Multiphoton Effects in Quantum GaAs/AlGaAs Superlattice, *47th International Conference on Infrared, Millimeter and Terahertz Waves, IRMMW-THz 2022*, 1-3 (2022). Delft, Netherlands. **Oral presentation. Key-Note presentation.**
- [B9] Vladislovas Čižas, Liudvikas Subačius, Natalia V. Alexeeva, Dalius Seliuta, Timo Hyart, Klaus Köhler, Kirill N. Alekseev, and Gintaras Valušis, Dissipative Parametric Generation in a Biased Superlattice: the

Case of Small Signal Gain, *Advanced Properties and Processes in Optoelectronic Materials and Systems, APROPOS 18*, **S5-O5**, 37 (2022). Vilnius, Lithuania. **Oral presentation.**

- [B10] **Vladislovas Čižas**, Dalius Seliuta, Liudvikas Subačius, Kirill N. Alekseev, Natalia Alekseeva and Gintaras Valušis, Disipacinis Parametrinis Stiprinimas Supergardelėse: Silpno Signalo Stiprinimo Ypatumai, *12-oji doktorantų ir jaunųjų mokslininkų konferencija, FizTech 2022*, **O31**, 36 (2022). Vilnius, Lithuania. **Oral presentation.**
- [B11] **Vladislovas Čižas**, Liudvikas Subačius, Natalia V. Alexeeva, Dalius Seliuta, Kirill N. Alekseev, and Gintaras Valušis, Parametrinės Aukštadažnės Spinduliuotės Stiprinimas ir Harmonikų Generacija GaAs/AlGaAs Supergardelėse, *45-oji Lietuvos nacionalinė fizikos konferencija; LNFK-45* (2023). Vilnius, Lithuania. **Oral presentation. Invited talk.**
- [B12] **Vladislovas Čižas**, Natalia Alexeeva, Kirill N. Alekseev, and Gintaras Valušis, High-Frequency Gain Effects in Doped Semiconductor Superlattices, *TeraTech 2023 International Symposium, TeraTech 2023*, **Th3-2**, 66-67 (2023). Aizu-Wakamatsu, Japan. **Oral presentation.**

Other publications

- [C1] Ignas Grigelionis, **Vladislovas Čižas**, Mindaugas Karaliūnas, Vytautas Jakštas, Kęstutis Ikamas, Andrzej Urbanowicz, Marius Treideris, Andrius Bičiūnas, Domas Jokubauskis, Renata Butkutė, and Linas Minkevičius, Narrowband Thermal Terahertz Emission from Homoepitaxial GaAs Structures Coupled with Ti/Au Metasurface, *MDPI Sensors*, **23**, 4600 (2023).
- [C2] Rusnė Ivaškevičiūtė-Povilauskienė, **Vladislovas Čižas**, Ernestas Nacius, Ignas Grigelionis, Karolis Redeckas, Matas Bernatonis, Sergej Orlov, Gintaras Valušis, and Linas Minkevičius, Flexible terahertz optics: light beam profile engineering via C-shaped metallic metasurface, *Frontiers in Physics*, **11**, 4600 (2023).
- [C3] Kasparas Stanaitis, Karolis Redeckas, Augustė Bielevičiūtė, Matas Bernatonis, Domas Jokubauskis, **Vladislovas Čižas**, and Linas Minkevičius, Study of the low-cost HIPS and paraffin-based terahertz optical components, *Lithuanian Journal of Physics*, **63-4**, 233-240 (2023).
-
- [C4] **Vladislovas Čižas**, Ignas Grigelionis, Kęstutis Ikamas, Vytautas Jakštas, Domas Jokubauskis, Andrius Bičiūnas, Andrzej Urbanowicz, Marius Treideris, Renata Butkutė, and Linas Minkevičius, Resonant Thermal Terahertz Metasurface-Based Emitters on n-GaAs/GaAs, *Conference Proceeding of the 47th International Conference on Infrared, Millimeter and Terahertz Waves, IRMMW-THz 2022*, (2022).
- [C5] Rusnė Ivaškevičiūtė-Povilauskienė, **Vladislovas Čižas**, Ernestas Nacius, Ignas Grigelionis, Karolis Redeckas, Matas Bernatonis, Sergej Orlov, Gintaras Valušis, and Linas Minkevičius, Flexible C-shaped Metallic Metasurface Based Optics for Terahertz Beam Shaping, *Conference Proceeding of the 48th International Conference on Infrared, Millimeter and Terahertz Waves, IRMMW-THz 2023*, (2023).
- [C6] **Vladislovas Čižas**, Ignas Grigelionis, Kęstutis Ikamas, Vytautas Jakštas, Barbora Škėlaitė, Domas Jokubauskis, Andrius Bičiūnas, Andrzej Urbanowicz, Marius Treideris, Renata Butkutė, and Linas Minkevičius, Polarization Selective Dual Frequency Metasurface-Based Resonant Thermal Terahertz Emitters on n-GaAs/GaAs, *Conference Proceeding of the 48th International Conference on Infrared, Millimeter and Terahertz Waves, IRMMW-THz 2023*, (2023).

Other conferences

- [D1] Vladislovas Čižas, Ignas Grigelionis, Kęstutis Ikamas, Vytautas Jakštas, Domas Jokubauskis, Andrius Bičiūnas, Marius Treideris, Renata Butkutė, and Linas Minkevičius, THz/sub-THz Frequency range Thermal Metamaterial Emitters, *11-oji doktorantų ir jaunųjų mokslininkų konferencija, FizTech 2021*, **16**, 16 (2021). Vilnius, Lithuania. **Oral presentation.**
- [D2] Karolis Redeckas, Ignas Grigelionis, Vladislovas Čižas, Vytautas Jakštas, Renata Butkutė, Andrius Bičiūnas, and Linas Minkevičius, Kvantinių Duobių Infraraudonosios Srities Fotodetektorius, Veikiantis Kambario Temperatūroje, *11-oji doktorantų ir jaunųjų mokslininkų konferencija, FizTech 2021*, **64**, 64 (2021). Vilnius, Lithuania. **Poster presentation.**
- [D3] Vladislovas Čižas, Ignas Grigelionis, Kęstutis Ikamas, Vytautas Jakštas, Domas Jokubauskis, Andrius Bičiūnas, Marius Treideris, Renata Butkutė, and Linas Minkevičius, Thermal metamaterial emitters for THz/sub-THz frequency range, *44-oji Lietuvos nacionalinė fizikos konferencija, LNFK-44*, **O44**, 84 (2021). Vilnius, Lithuania. **Oral presentation. Best presentation award.**
- [D4] Karolis Redeckas, Ignas Grigelionis, Vladislovas Čižas, Vytautas Jakštas, Renata Butkutė, Andrius Bičiūnas, and Linas Minkevičius, Quantum Well Infrared Photodetector Operating at Room Temperature, *66th international conference for students of physical and natural sciences, Open Readings 2023*, **P3-43**, 253 (2022). Vilnius, Lithuania. **Poster presentation. Best poster award.**
- [D5] Vladislovas Čižas, Ignas Grigelionis, Kęstutis Ikamas, Vytautas Jakštas, Domas Jokubauskis, Andrius Bičiūnas, Andrzej Urbanowicz, Marius Treideris, Renata Butkutė, and Linas Minkevičius, Resonant Thermal Terahertz Metasurface-Based Emitters on n-GaAs/GaAs, *47th International Conference on Infrared, Millimeter and Terahertz Waves, IRMMW-THz 2022*, 1-2 (2022). Delt, Netherlands. **Oral presentation.**
- [D6] Ignas Grigelionis, Vladislovas Čižas, Kęstutis Ikamas, Vytautas Jakštas, Domas Jokubauskis, Andrzej Urbanowicz, Marius Treideris, Renata Butkutė, and Linas Minkevičius, Excitation of Magnetic Polaritons in n-GaAs/GaAs/metal Structure in the Terahertz Range, *Advanced Properties and Processes in Optoelectronic Materials and Systems, APROPOS 18*, **S6-O1**, 44 (2022). Vilnius, Lithuania. **Oral presentation.**
- [D7] Karolis Redeckas, Ignas Grigelionis, Vladislovas Čižas, Vytautas Jakštas, Renata Butkutė, Andrius Bičiūnas, and Linas Minkevičius, Quan-

tum Well Infrared Photodetector Operating at Room Temperature, *Advanced Properties and Processes in Optoelectronic Materials and Systems, APROPOS 18, S2-P4*, 84 (2022). Vilnius, Lithuania. **Poster presentation.**

- [D8] Karolis Redeckas, Ignas Grigelionis, **Vladislovas Čižas**, Vytautas Jakštas, Renata Butkutė, Andrius Bičiūnas, and Linas Minkevičius, Quantum Well Infrared Photodetector Operating at Room Temperature, *12-oji doktorantų ir jaunųjų mokslininkų konferencija, FizTech 2022, P24*, 87 (2022). Vilnius, Lithuania. **Poster presentation.**
- [D9] Ignas Grigelionis, **Vladislovas Čižas**, Kęstutis Ikamas, Vytautas Jakštas, Barbora Škėlaitė, Domas Jokubauskis, Andrius Bičiūnas, Andrzej Urbanowicz, Marius Treideris, Renata Butkutė, and Linas Minkevičius, Polarization Selective Dual Frequency Metasurface-Based Resonant Thermal Terahertz Emitters on n-GaAs/GaAs, *48th International Conference on Infrared, Millimeter and Terahertz Waves, IRMMW-THz 2023, We-PM2-3-5*, 160 (2023). Montreal, Canada. **Oral presentation.**
- [D10] Linas Minkevičius, Rusnė Ivaškevičiūtė-Povilauskienė, **Vladislovas Čižas**, Ernestas Nacius, Ignas Grigelionis, Karolis Redeckas, Matas Bernatonis, Sergej Orlov, and Gintaras Valušis, Passive and Flexible Metasurface-Based Elements for THz Imaging Applications, *48th International Conference on Infrared, Millimeter and Terahertz Waves, IRMMW-THz 2023, Mo-P2-39*, 88 (2023). Montreal, Canada. **Poster presentation.**
- [D11] Rusnė Ivaškevičiūtė-Povilauskienė, **Vladislovas Čižas**, Ernestas Nacius, Ignas Grigelionis, Karolis Redeckas, Matas Bernatonis, Sergej Orlov, Gintaras Valušis, and Linas Minkevičius, Flexible C-shaped metallic metasurface based optics for terahertz beam shaping, " *2023 48th International Conference on Infrared, Millimeter, and Terahertz Waves, IRMMW-THz 2023*. Montreal, Canada. **Oral presentation**
- [D12] **Vladislovas Čižas**, Rusnė Ivaškevičiūtė-Povilauskienė, Ernestas Nacius, Karolis Redeckas, Matas Bernatonis, Sergej Orlov, Ignas Grigelionis, Gintaras Valušis, and Linas Minkevičius, Terahertz Imaging Employing Flexible Metasurface-Based Optics, *TeraTech 2023 International Symposium, TeraTech 2023, WeP-08*, 12 (2023). Aizu-Wakamatsu, Japan. **Poster presentation.**
- [D13] Augustė Bielevičiūtė, Karolis Redeckas, Kasparas Stanaitis, Ernestas Nacius, **Vladislovas Čižas**, and Linas Minkevičius. Comparative Analysis of Beam Focusing Abilities of Metasurface-Based 250 GHz Lenses,

67th International Open Readings Conference 2024, O3.1, 55 (2024). Vilnius, Lithuania. **Oral presentation.**

[D14] Karolis Redeckas, Kasparas Stanaitis, **Vladislovas Čižas**, and Linas Minkevičius. THz Metalenses with Different Split Ring Resonator Geometries, *67th International Open Readings Conference 2024*, 133 (2024). Vilnius, Lithuania. **Poster presentation.**

[D15] Barbora Škėlaitė, **Vladislovas Čižas**, Kęstutis Ikamas, Vytautas Jakštas, Domas Jokubauskis, Andrius Bičiūnas, Andrzej Urbanowicz, Marius Treideris, Renata Butkutė, Linas Minkevičius and Ignas Grigelionis. Comparison of Spectral Properties of Semiconductor Structures Equipped with Metallic (Ti/Au) or N-type GaAs Metasurfaces, *67th International Open Readings Conference 2024*, 168 (2024). Vilnius, Lithuania. **Poster presentation.**

Contribution of the author

In publication [A1] and subsequent patent [A2] author participated in the analysis of the data acquired from the waveguide-based experimental setup. Conducted I-V measurements. Performed simulations of the small signal gain leading to the estimation of the bias AC electric field strength in the superlattice structure. Participated in the preparation for the publications: writing, editing. Representation (figures and graphs).

In publication [A3] author performed required small and large signal gain model based simulations. Performed data analysis. Participated in the preparation for the publications: writing. Representation (graphs).

In publication [A4] author performed required large signal gain model based simulations. Performed data analysis. Participated in the preparation for the publications: writing. Representation (graphs).

The particular thesis is separated into 5 chapters. Chapter 1 provides the introduction into the long-lasting theoretical investigation and experimental achievements, including ones performed in bulk semiconductors, supplementing an understanding on the significance of the further presented results. Chapter 2 supplements structural and experimental techniques employed during the research. Chapter 3 presents evidence of the first experimental observation of the dissipative parametric generation in the DC and microwave biased GaAs/AlGaAs superlattice. Expansion of the investigation is presented in Chapter 4 by introduction of the large-signal gain model contributing to the evidence on the coexistence of Bloch and parametric gain in biased semiconductor superlattices. Finally, chapter 5 describes the first experimental evidence on the stable Bloch gain in electrically biased GaAs/AlGaAs superlattice.

1. LITERATURE OVERVIEW

1.1. High-frequency generation and amplification effects in bulk semiconductors

One of the first experimental evidences of the nonlinear mobility dependency on the applied electric field strength was achieved in bulk germanium samples by Ryder et al. [66]. Significant current density deviation from linear Ohmic dependency was observed (see Figure 6.1), after the applied electric field strength exceeds some threshold value. Explicit theoretical explanation of the achieved data is further presented in the works of Shockley and Kroemer, introducing the theoretical model, which fits the experimental results [67, 68].

The observed effect was attributed to the appearance of carriers featured by negative effective mass. It is known that such carriers, being under influence of electric field, are accelerated to the opposite direction. As the result, the electrical current is directed against the direction of the electric field (negative mobility) [69]. In the case of above-mentioned Ge samples the formation of negative effective mass region is expounded by degenerate valence band structure, predicting the possibility to achieve generation up to the frequencies of several terahertz (THz) [70].

Works of Kroemer [69, 70] have been expanded by the mathematical explanation on the appearance of negative resistance in displaced energy bands [71]. One of the first experimental evidence of the negative differential resistance effects in bulk III-V semiconductors was observed by Hilsum in GaAs and GaSb [72]. Application of the electric field to system with two conduction valleys is analysed (the effective mass of the upper valley minima exceeds the effective mass of the bottom valley minima). The electric field causes redistribution of the charge carriers, compared to the zero field case. Higher energy electrons are scattered to the upper valley, exhibiting smaller mobility, resulting in conductivity decrease and appearance of negative differential resistance [72]. At this moment of the investigation, the formation of instabilities leading to the domain formation has been predicted, leading to the electric field instabilities inside the samples, wherein negative differential resistance was expected. It is also noted that the domain formation is expected to destructively affect the effects leading to appearance of negative differential resistance [71]. The effect was fully elucidated in the monumental works of Gunn, wherein the microwave generation from bulk GaAs sample biased by electric field strength, exceeding some critical value, has been observed [73–75]. The radiation period was found to correspond to the transit time between the electrodes. The physical explanation was predicted by Ridley [76] and later implemented by Kroemer [77] explaining that the generation occurs due to appearance of pe-

riodic space charge domain instabilities, occurring due to the above discussed non-linear drift velocity - electric field strength relation (see Figure 1.1). Note that the peak drift velocity v_p is achieved under application of critical electric field strength E_{cr} . The fact that the appearance of the Gunn effect is related to the inter-valley charge transfer was very quickly experimentally confirmed by multiple groups [78–80].

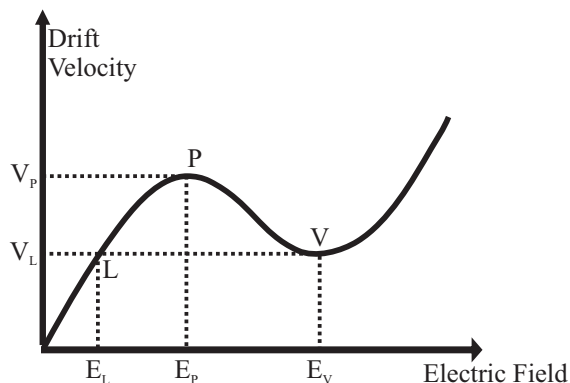


Figure 1.1: Principal N-type drift velocity dependency on the applied electric field for bulk semiconductor sample. Note the appearance of the non-linearity [77] ©1964 IEEE.

If the Ohms' laws can be applied to the sample, space charge damping, occurring due to Coulombian interaction of the charges in domain is exponential with the characteristic relaxation time equal

$$\tau_m = \frac{\varepsilon_r \varepsilon_0}{\sigma} = \frac{\varepsilon_r \varepsilon_0}{e \mu N}. \quad (1.1)$$

Here N is charge carrier density, $\varepsilon = \varepsilon_r \varepsilon_0$ - dielectric constant of the sample, e - elementary charge, σ - conductivity, and μ - charge mobility. The latter in the non-Ohmic case should be changed to the differential mobility $\mu = dv_d/dE_{tot}$. It is quite obvious that in the case of negative differential mobility ($\mu < 0$) the time constant will also be negative resulting in charge accumulation. Thus, in order for the domain to form $|\tau_m|/T_0 < 1$, ($T_0 = L/v_d$ - oscillation period, L - sample length, and v_d - charge drift velocity). As a result one may derive the sample-dependent $(NL)_{cr}$ coefficient describing the minimal doping (N) and sample length (L) value combination, required for the domain formation:

$$(NL)_{cr} > \frac{\varepsilon v_d}{4\pi e |\mu|}. \quad (1.2)$$

As will be noted further, the same domain formation boundary logic (with different equation) can be applied to the subject of the superlattices. To proceed, several modes of operation can be clearly distinguished depending on the

applied electric field strength and (NL) criterion of the structure.

Regardless on the applied electric field strength no "mature" domain corresponding to Gunn operational mode can be formed in the $(NL) < (NL)_{cr}$ region. If the electric field strength is small ($E < E_{cr}$), the structure may be treated as a simple linear Ohmic resistance. However, it is important to note that for the conditions $E > E_{cr}$ differential conductivity becomes negative close to the transit frequency, resulting in stable amplification regime, derived limited space-charge accumulation mode (LSA) [77, 81]. The latter mode, transferred to the physics of quantum semiconductor superlattices, is the most interesting, covering the majority of the presented results.

If one would apply electric field to the sample, current density $j > eNv_d(E)$ is expected to be constant throughout the whole sample. Still, non-uniformity occurs close to the cathode. While $E < E_{cr}$ (close to cathode), one may observe excess charge carriers injected from the cathode to compensate decrease in drift velocity (see Figure 6.5 (b)). After electric field strength $E = E_{cr}$ is reached, with the further increase of electric field strength, the drift velocity decreases, leading to the increase of excess charge carriers, which in turn leads to further increase of electric field strength and even further decrease of the drift velocity [82]. This results in saturation of the VACh if $E > E_{cr}$ is applied. Under these conditions as it was shown by Shockley, in the case of weak doping the domain is not able to form but extends throughout the whole structure, making the whole structure a uniform accumulation layer [83]. As a result, by additionally biasing the structure with oscillations of transit frequency or higher, space charge formation may be observed, which would increase while travelling through the structure amplifying the signal [84].

The operation under LSA mode is employed in Thim microwave amplifiers. It is shown in the work of McCumber and Chynoweth [85] that two operation modes are available: the well known Gunn mode, wherein $(NL)_{cr}$ criterion is exceeded and domain formation proceeds. On the other hand, operation under $(NL)_{cr}$ criterion provides second distinct operation mode for the two-valley devices via LSA. Samples being too short or less doped, result in high conductivity preventing space charge accumulation leading to domain formation. In contrast to Gunn-based oscillators, Thim amplifiers are DC stable, as the device facilitates positive differential DC resistance [86]. Generation under these conditions has been experimentally revealed in the work of Thim and Haaki revealing generation possibilities reaching sub-THz frequency range [87–89]. Moreover, such oscillations were shown to be highly temperature dependent and available only in a small range of doping or in other terms (NL) criterion [90].

The above-discussed effects are still being a subject of research in many different fields including, Esaki diodes [91], thin-film transistors [92], implementation of graphene layers [93, 94], GaN photoconductive switches [95, 96], and superlattices [97]. Being discussed in bulk semiconductors, the same prin-

ciples may be applied to the devices employing the negative differential drift velocity. To summarize the section:

- NDV regime, appearing in bulk III-V semiconductors, leads to the vast amount of possible operational modes, depending on different aspects like doping, length, bias strength, type, and frequency etc. High-frequency signal generation and/or amplification effects may or may not be achieved.
- In long structures $(NL) > (NL)_{cr}$ Gunn oscillator-like mechanism is expected, while in short structures $(NL) < (NL)_{cr}$ Thin amplifier behaviour is expected.
- Operation on the boundary of critical Kroemer criterion, is expected to result in intriguing mixture of both of the effects, which are extensively explored within this thesis.

1.2. High-frequency generation and amplification effects in quantum semiconductor superlattices

1.2.1. On the nature of negative differential velocity in superlattices

With the appearance and evolution of the molecular beam epitaxy technology [98] exploration of new much more complicated structures became possible. One of these: quantum semiconductor superlattice, consisting of huge amount (at specific researches more than several hundred periods may be met) of periodic layers of at least two different semiconductors [99, 100]. Exploiting different techniques (eg. different doping/material/composition for different layers) fence-like bandgap profile may be achieved, consisting of repetitive wells and barriers [101], resulting in intriguing effects. Literature analysis of the superlattices imminently should start with the foundation laying work of Esaki and Tsu [63], who were the first to notice that in the case of periodically arranged layers, resulting in periodic potential, unique quantum mechanical properties arise. If the periodicity of the potential is significantly smaller compared to the mean free path of the electron, narrow allowed and forbidden bands form due to the formation of the minizones in the Brillouin zones [102]. This effect is depicted at Figure 1.2 (a). The original first Brillouin zone of the bulk crystal (π/a in k -space) is separated in the minizones as π/d , where a denotes the lattice constant of the bulk crystal and d is the period of the superlattice.

The same research [63] reveals another essentially important feature of the superlattice which is affected by an external electric field. Making an assumption $k_x = eEt/\hbar$, where E is applied electric field strength, and employing the potential profile-dependent velocity equation $v_x(V_x) = \hbar^{-1} \partial V_x / \partial k_x$ it is shown that

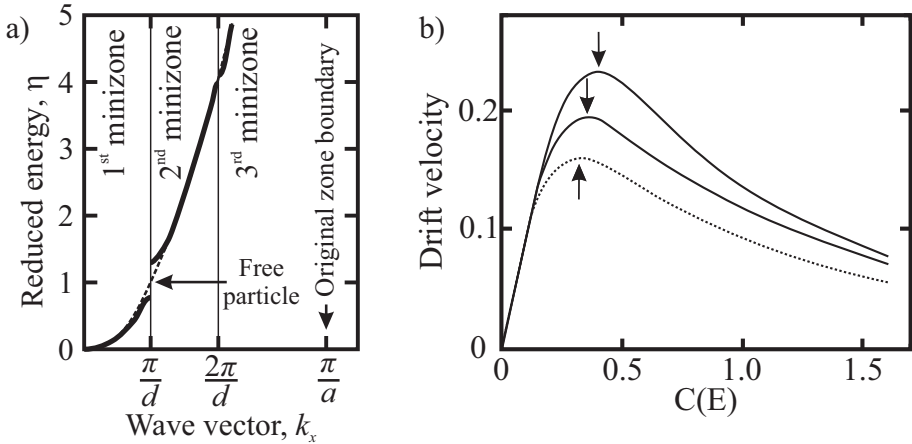


Figure 1.2: (a) Reduced energy η dependency on wavevector k_x . Hereby, $\eta = (V_x - V_1)/V_0$, where V_1 is the amplitude of periodic potential and $V_0 = \hbar^2\pi^2/2m^*d^2$, d being the period of the superlattice and m^* being the effective mass. Note the separation of original Brillouin zone of the bulk crystal into series of minizones for the case of periodic superlattice structure. Adapted from [63]. (b) Drift velocity amplitude dependency on the applied electric field strength via $C(E) = eE\tau d/\hbar\pi$. Dependencies are presented for sinusoidal potential (dashed line) and square-well potential with different $V - k$ shape (solid lines). Arrows depict peak drift velocity position. Adapted from [63].

$$\frac{dk_x}{dt} = \frac{eE}{\hbar} \quad \rightarrow \quad \frac{dv_x}{dt} = \frac{\partial v_x}{\partial k_x} \frac{\partial k_x}{\partial t} = \frac{1}{\hbar} \frac{\partial^2 V_x}{\partial k_x^2} \frac{eE}{\hbar} = \frac{eE}{\hbar^2} \frac{\partial^2 V_x}{\partial k_x^2}. \quad (1.3)$$

Describing average drift velocity, including the relaxation time τ , results in

$$v_d = \int_0^\infty \exp\left(-\frac{t}{\tau}\right) dv_x = \frac{eE}{\hbar^2} \int_0^\infty \frac{\partial^2 V_x}{\partial k_x^2} \exp\left(-\frac{t}{\tau}\right) dt. \quad (1.4)$$

The integral is solved employing field sinusoidal approximation, which is reasonable for low-doped superlattices $V_x \approx 0.5V_1(1 - \cos(k_x d))$. Such approximation results in final drift velocity dependence (see Appendix 6.1.6):

$$v_d = \frac{eEV_1 d^2 \tau}{2(e^2 E^2 d^2 \tau^2 + \hbar^2)}. \quad (1.5)$$

As a result, under the impact of the external electric field, drift velocity function on the electric field strength dependency experiences maximum and starts decreasing, resulting in negative differential velocity and thus, negative differential conductivity (Figure 1.2 (b)) which is claimed to lead to the Bloch oscillations in the superlattice. Note similarities of the given graph with one for the bulk semiconductor (see Figure 1.1), exploiting different physical effect,

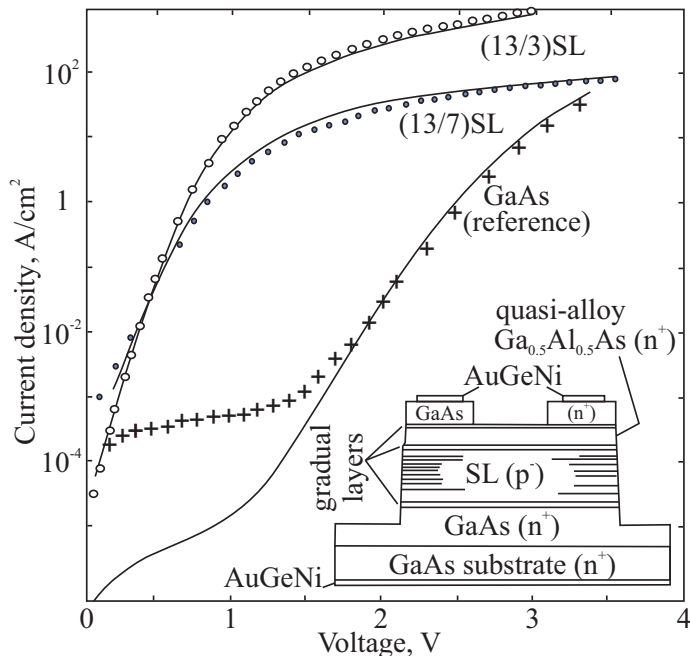


Figure 1.3: I-V characteristic of bulk GaAs and two superlattices of different period, acquired at room temperature conditions. Dots depict experimental data and lines represent theoretical simulations. The structure of the superlattice-comprising samples is depicted in the inset. Reprinted from [103], with the permission of AIP Publishing.

but resulting in the similar-looking dependency. Making analogy to the case of bulk semiconductor, the NDV region onsets after peak drift velocity (v_p) is reached at the electric field strength further denoted as the Esaki-Tsu critical electric field

$$E_{cr} = \frac{\hbar}{ed\tau}. \quad (1.6)$$

Experimental works performed by Sibille group making an undeniable contribution to the understanding of negative differential conductivity effect in the semiconductor superlattice are worth a short special note [104]. Employing the GaAs/AlGaAs superlattice structure, the acquired I-V characteristics (see Figure 1.3), depict the same saturation as the I-V characteristics theoretically estimated in [105]. Moreover, in the cited articles diffusion and Poisson equations are used to emulate the I-V characteristics employing the velocity-field dependencies of Esaki-Tsu [63]. The theoretically obtained I-V characteristics were found to ideally correspond to the experimentally acquired curves [103]. The group uses Ohmic contact, which, according to their own admittance, result in non-uniform electric field distribution, allowing to obtain NDV, but

not NDC at room temperature conditions [106] (see Appendix 6.1.2 on the matter of appropriate contact selection). The NDC has been observed in later works, by employment of the equivalent RLC contour schematic and doping the previously undoped structure of the proper length, still satisfying the above-mentioned Kroemer criterion, in order to achieve increased electric field uniformity. Experimental NDC at room temperature conditions was shown [107].

The work of Esaki and Tsu [63] exposed the process of the NDC formation, however, did not cover its spectral dependency. This was performed later in the ground-breaking work of Ktitorov, Simin and Sindalovskij [14]. The particular work solves the Boltzmann transport equation to achieve high-frequency conductivity dependency when the electron relaxation time is sufficiently long for Bloch oscillations to have a significant impact

$$\sigma(\omega) = \sigma_0 \frac{1 - \omega_E^2 \tau_p \tau_e - i\omega \tau_e}{(\omega_E^2 - \omega^2) \tau_p \tau_e + 1 - i\omega(\tau_p + \tau_e)}; \quad \sigma_0 = \frac{\sigma_{00}}{1 + \omega_E^2 \tau_p \tau_e}. \quad (1.7)$$

In these equations $\omega_E = eEd/\hbar$ - Wannier-Stark frequency (E applied electric field strength, d - period of the superlattice); $\tau_{p,e}$ - momentum and energy relaxation times; σ_{00} - DC conductivity. It is shown, that the real part of this equation increases with an increase of the frequency, experiencing negative peak just below Bloch frequency (see Figure 1.4 (a)). To summarize:

- Semiconductor superlattices feature NDC under bias exceeding Esaki-Tsu critical electric field strength, leading to the Bloch oscillations.
- Spectral conductivity analysis reveals NDC should be expected for the frequencies below Bloch oscillation frequency.
- Electric field non-uniformity problem, appearing partially due to the employment of Ohmic contacts is highlighted, leading to the understanding of the necessity of non-Ohmic contacts.

1.2.2. On the matter of Bloch oscillations in superlattices.

The behaviour of the electrons in the periodic potential (lattice) under uniform electric field was first described in the fundamental work of Bloch [108] and later clarified by Zener [109], revealing the appearance of periodic oscillations, later called by "Bloch oscillations". The period of such oscillations was estimated to be $T_B = h/eEd$.

Considering the Bloch oscillations from energy band point of view, in ideal world, electrons can move freely throughout the sample without changing its energy. Under the application of electric field said energy band becomes tilted. As a result, electrons become more confined (see Figure 1.4 (b)), but if no energy is lost during the collision with boundary of the band, it remains on the same energy level. Still, in the reality losses appear [68]. Electron energy

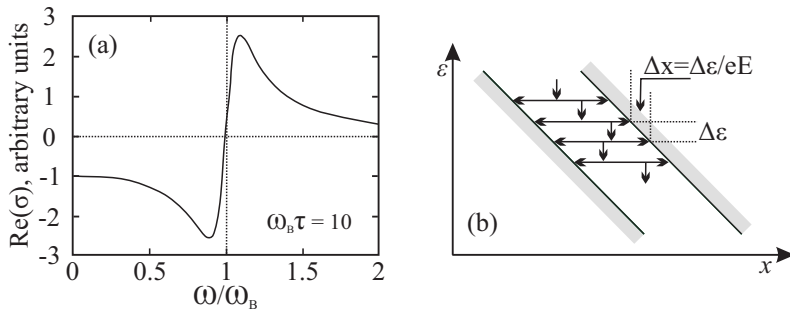


Figure 1.4: (a) Dependence of the real part of the differential conductivity on frequency according to theoretical estimations of [14] ($\omega_B\tau = 10$). Note that the conductivity for the frequencies smaller than the Bloch frequency, to be negative with a peak just below the Bloch frequency and positive for the frequencies above it. (b) Schematic example of the Bloch oscillations in a miniband of DC biased superlattice in real space. Depicted inelastic scattering provides electric field strength dependent mechanism for the decrease of drift velocity. Adapted from [112].

losses of $\Delta\varepsilon$ (scattering event), would result in displacement of the horizontal oscillation by $\Delta x = \Delta\varepsilon/eE$, which may look like hopping down the steps of the stairs. Thus, if the scattering event occurs often enough ($f = 1/\Delta t$) the displacement can be treated as electron drift.

$$v_d = \frac{1}{eE} \overline{\left(\frac{\Delta\varepsilon}{\Delta t}\right)}. \quad (1.8)$$

When the applied electric field strength (band tilt) is big enough, collision frequency and the corresponding decrease of drift velocity saturates becoming inversely proportional at some electric field strength interval [110]. The nonlinearity of the collision probability is one of the main causes for the appearance of the negative differential velocity effects, leading to the amplification/generation processes [111]. The discovered effect claims the way for the observation of Bloch oscillations up to several THz.

Considering the k -space point of view, under the bias electric field electron travels through the minizone-representing k -space until the boundary is reached at $\pm\pi/d$ [110]. By reaching the boundary, Umklapp process (Bragg reflection) occurs, making electron "to appear" at the opposite side of the k -space period [113,114]. In the case of only DC electric field being applied, electrons travelling with a uniform speed will spread across the Brillouin zone with average current contribution zero, however, due to scattering weak current flow is expected to appear. The much more interesting effects are expected upon biasing the superlattice with DC and AC electric fields. The combination of AC bias and inelastic scattering results in formation of the travelling waves [112]. First of all, biasing superlattice with AC electric field of Bloch frequency, would result

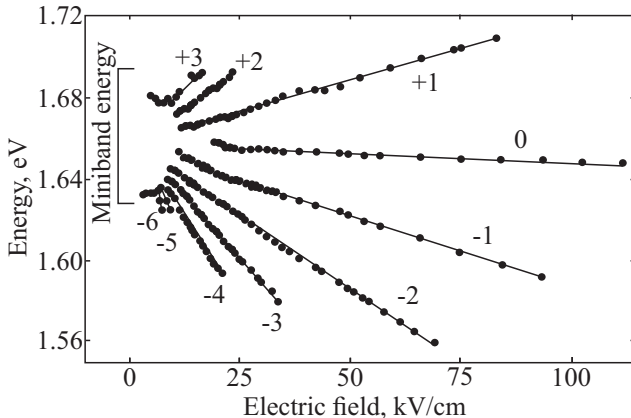


Figure 1.5: Dependence of the interband transition energy on the applied electric field strength for the case of GaAs/AlGaAs superlattice, acquired at 5 K temperature conditions. Numbers correspond to Wannier-Stark states involved in the transition. Spatial coherence of 13 periods is observed. Adapted from [116].

in non-uniform speed of the electrons within the k -space (below average on the negative part of the AC bias cycle, and above average on the positive part). This non-uniformity results in the peak of negative conductivity visible on the Figure 1.4 (a) [14]. Under AC bias below Bloch frequency the electrons would not be able to travel the full k -period within one cycle, resulting in some phase-shift and being located in the below-average speed part of the cycle results in appearance of negative conductivity [115].

Formation of the above-mentioned steps are called Wannier-Stark ladder. First of all it is worth mentioning that all of the discussed effects appear under application of an external bias of different type (AC, DC, or both). This appliance contorts the miniband in strength-dependent different ways, resulting in different charge transport properties. To properly address this issue one may treat the miniband of the unbiased superlattice as a closely packed set of allowed energy levels. In the case of electric bias application, it was shown by Wannier that if the Schrodinger equation results is wavefunction of $\psi(z)$ for an energy V_0 , wavefunction of $\psi(z - nd)$ is also solution for the energy $V_0 + Ne\epsilon d$. This results in electric field-dependent set of energy levels separated by

$$\Delta_s = eEd = \hbar\omega_B. \quad (1.9)$$

One should also note the Bloch frequency being dependent on the strength of the applied electric field [117]. The experiment of optical observation of the Wannier-Stark ladder in the GaAs superlattice (see Figure 1.5) obviously discloses the change of the charge localization with the change of the electric field strength of the bias [118]. Indeed, with the increase of the electric field

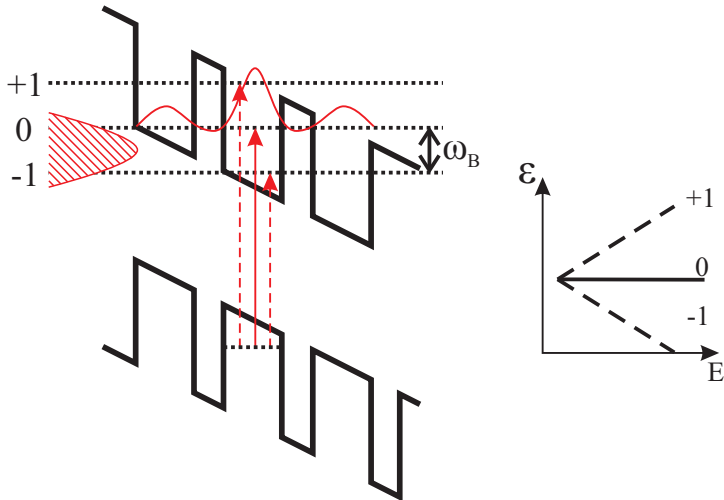


Figure 1.6: Sketch depicting the occurrence of the Bloch oscillations in the biased semiconductor superlattice. Under bias electric field the superlattice miniband splits into Wannier-Stark ladder. The wavepacket can be excited by spectrally-broad femtosecond laser pulse to perform Bloch oscillations in the structure.

strength the transition to the more distant Stark steps vanish as the charge becomes more and more localized in one quantum well, making the superlattice to act as a set of single distant quantum wells [116]. In the proposed example, results achieved from the superlattice, comprising 4 nm GaAs wells and 2 nm $\text{Al}_{0.35}\text{Ga}_{0.65}\text{As}$ barriers at 5 K. This results in an important conclusion - charge carriers in the superlattice under different bias are differently localized. This result in different dominating charge transport. Three main types of the latter can be distinguished in scientific literature: miniband conduction [63], Wannier-Stark hopping [119], and sequential tunnelling [120,121]. Experimental evidence of the latter type are presented in the works of Allen group [122] employing the free electron laser for the intense high-frequency application ($\omega\tau > 1$; $eE_{ac}d/\hbar\omega \geq 1$). Localization of the Wannier-Stark levels occurs when the energy levels are fully resolved. This means that due to the applied bias, the energetic separation between levels exceeds collision broadening ($eEd > \hbar\omega$) [123,124].

Significant influence to the understanding of Bloch oscillations is attributed to the K. Leo group, famous for the observations of the Bloch oscillations in superlattices by means of different detection methods. These include Degenerate Four-Wave Mixing technique (DFWM) [5, 65, 125], THz spectroscopy [6, 126], and transmittive electro-optic sampling (TEOS) [127–129]. First of all, Bloch oscillations have been experimentally evidenced at room temperature conditions. Secondly, Bloch oscillations were attributed to the localization at

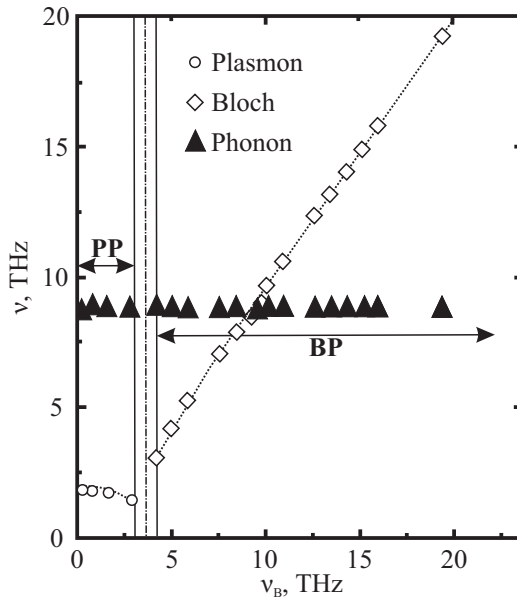


Figure 1.7: Three coexisting modes dependency on Bloch frequency in the superlattice: coupled plasmon-phonon modes for frequencies $f < 2f_p$, and Bloch-phonon modes for $f > 2f_p$. Dotted line represents predictions of the pendulum Equation 1.10 while symbols depict numerical solutions of the modified equation of [131]. Sharp transition between the modes is expected in the absence of collisions. Aperiodic electron motion allows to resolve only frequencies outside the solid vertical lines. Reprinted figure with permission from [131]. Copyright 2000 by the American Physical Society.

Wannier-Stark levels, depicting the linear dependency of the Bloch frequency on the applied DC bias. The latter evidence is of particular importance.

The possibility to control Bloch oscillation frequency with the applied bias reveals its importance due to the possibility of resonance with other oscillation modes. These include plasmonic oscillations and longitudinal optical phonons [130]. Behaviour of the coupled modes totally differs, compared to the individual oscillations. For the case of Bloch and plasmon modes, the pendulum interaction-describing equation is

$$\ddot{\eta} + \omega_p^2 \sin(\eta) = 0, \quad (1.10)$$

wherein η denotes pendulum displacement, $\omega_p = \sqrt{4\pi N e^2 / m^*}$ - plasma frequency, and N - charge carrier concentration [132, 133]. The effective mass in semiconductor superlattices is expressed as $m^* = 2\hbar^2 / \Delta d^2$ [134]. Initial conditions are proposed for the instant excitation and absence of initial displacement $\eta(0) = 0$ and displacement velocity set by the Bloch oscillation frequency $\dot{\eta}(0) = \omega_B = edE/\hbar$. The coherent case when $j = 0$ is considered.

The solution of the Equation 1.10 results in the motion of classical particle in periodic potential $V(\eta) = \omega_P^2(1 - \cos(\eta))$ with energy $\omega_B^2/2$. For the cases when energy is much smaller compared to the maximal potential energy particle is trapped in the one period of potential as plasmonic screening of the external electric field occurs due the Bloch period is larger than the plasmon oscillation period. If the energy is larger than the potential barrier, particles go above the potential oscillating with the Bloch frequency [135]. As a result a change in behaviour is expected at $\omega_B = 2\omega_P$ frequency. Figure 1.7 illustrates the transition from plasmon-phonon mode (low frequency region) to Bloch-phonon mode (high-frequency region) at Bloch frequencies below 5 THz. The sharp transfer is expected in the ideal conditions, however, due to scattering the transfer interval is expected to widen. In the appearing transition interval, motion is aperiodic, leading to the broad frequency spectrum [131].

To summarize this section:

- Appearance of Bloch oscillations is expected (and have experimentally been shown during optical experiments) in the DC biased superlattice due to the formation of Wannier-Stark ladders.
- Different Bloch oscillations types are revealed via different Wannier Stark localization types, changing with the change of applied DC electric field.
- Bloch frequency, being DC bias dependent is shown to feature appearance of Bloch-phonon-plasmon mode with distinctive transition at $\omega_B = 2\omega_P$ as revealed during optical experiments.

1.2.3. Parametric gain in superlattices

The parametric gain effects, occurring in non-linear medium in common and semiconductor superlattices in particular, are known for more than 50 years. First of all, it is worth noting the coherent mixing of the commensurate frequencies resulting in generation of DC current [136]. The appearance of the effect under mixing AC electric field and its second harmonic with a specific phase-shift has theoretically been predicted by Seeger [137] and further expanded to any even harmonic by Alekseev [138]. The theoretically shown effect is similarly attributed to the formation of Wannier-Stark ladder [139].

Secondly, the possibility of odd harmonics generation under application of pure AC electric field is revealed in the theoretical work by Alekseev et al. [140]. Such generation is allowed at THz frequencies and operates in domainless regime, suppressing space-charge instabilities [141]. Moreover, it is shown that under application of the DC and AC pump generation of even harmonics becomes possible (Figure 1.8 (a)) [142].

Theoretical feasibility of the half sub-harmonics generation in AC biased superlattice has also been predicted (see Figure 1.8 (b)) [143]. Furthermore, the

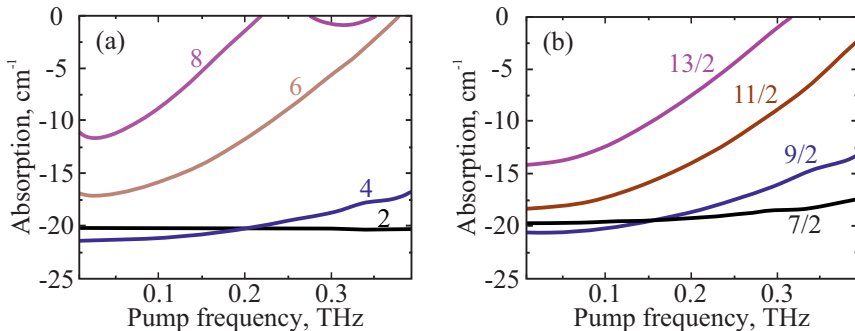


Figure 1.8: (a) Dependency of the small signal gain magnitude at even harmonics $\omega_1 = n\omega_0$ (n=2,4,6,8) for fixed amplitude $E_{ac} = 6.5 E_{cr}$ at $\varphi = \varphi_{opt}$ [143]. (b) Dependency of the small signal gain magnitude at half-harmonics $7\omega_0/2, 9\omega_0/2, 11\omega_0/2, 13\omega_0/2$ for fixed amplitude $E_{ac} = 6.5 E_{cr}$, DC bias $E_{dc} = E_{cr}$ at $\varphi = \varphi_{opt}$ [143]. © 2007 IEEE.

work analyses down-conversion processes, predicting that the half-harmonics may be generated from the AC pump of higher frequency. Same theoretical results are obtained by independent research of Romanov [144–147]. Moreover, the works of Romanov et al. reveal generation possibility on the frequencies other than half sub-harmonics [148]. The importance of the domainless operation for the achievement of successful parametric generation in the superlattices is highlighted in the above-mentioned publications. Still, despite more than 50 years of theoretical research, no experimental evidence of the generation in biased semiconductor superlattices has been provided.

- Predicted appearance of bias - dependent wave-mixing effects in AC and DC biased superlattices is expected to feature gain at harmonics and sub-harmonics of the excitation frequency.

2. Samples and Experimental Techniques

2.1. Architecture of the superlattice

The superlattice comprising 30 periods of moderately Si doped GaAs quantum wells (5 nm; 10^{16} cm^{-3}) and $\text{Al}_{0.3}\text{Ga}_{0.7}\text{As}$ quantum barriers (1 nm) was chosen for the experimental part (see Figure 2.1) resulting in the superlattice length of $L = 180 \text{ nm}$. The structure is grown by molecular beam epitaxy technique (MBE) on the n -doped ($\sim 500 \mu\text{m}$; 10^{18} cm^{-3}) GaAs substrate. Such combination of wells and barriers results in a wide miniband reaching 104 meV. According to the Sec. 1.4.1 of [149], the superlattice of selected parameters feature the critical Kroemer coefficient at $NL_{\text{cr}} = 2.7 \cdot 10^{11} \text{ cm}^{-2}$. As the absence of domain formation was required for the particular experiment, doping of $N = 10^{16} \text{ cm}^{-3}$ was selected. Thus, the resulting NL coefficient of the current structure is found to be at $NL = 1.8 \cdot 10^{11} \text{ cm}^{-2}$, indicating that formation of high-field travelling domains is not expected. To achieve uniform electric field across the superlattice structure, AuTi Schottky controlling contact was

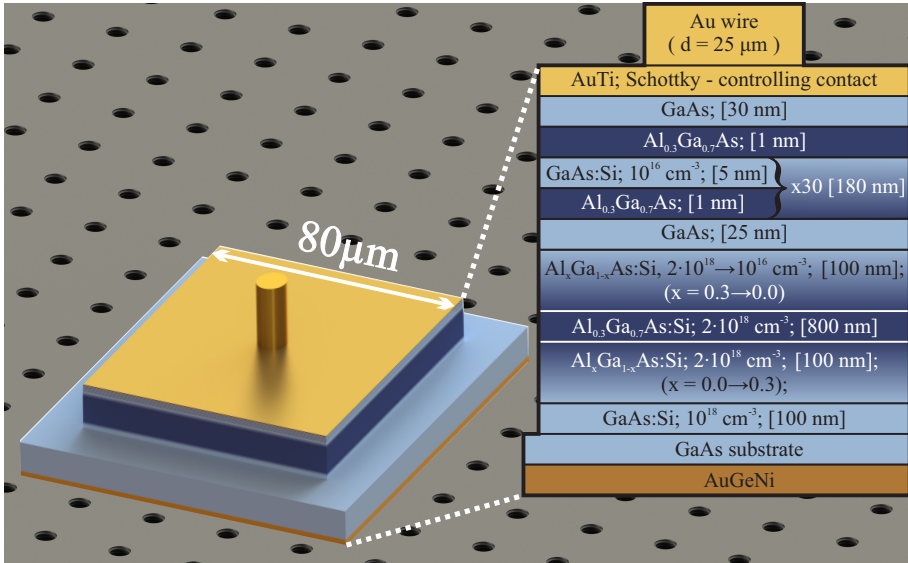


Figure 2.1: The enlarged view of the investigated GaAs/AlGaAs superlattice device. The superlattice is sandwiched between the AuTi Schottky controlling contact at the top and the heterojunction from the bottom. Au wire of $25 \mu\text{m}$ in diameter is connected to the top contact to direct AC pump electric field into the superlattice and for DC biasing. The Ohmic contact is deposited at the bottom of the substrate. Mesas of $80 \mu\text{m} \times 80 \mu\text{m}$ were used in the presented experiment. Reprinted figure with permission from [1]. Copyright 2022 by the American Physical Society.

placed on the top of the superlattice with a 30 nm GaAs buffer layer, sandwiched between the superlattice and the contact (see Section 6.1.2 for more details on the proper contact selection). Moreover, heterojunction injection contact is formed at the bottom of the superlattice (gradient alloy and concentration layer of 100 nm). The employment of the asymmetric non-Ohmic contact (the Schottky from top and heterojunction one from the bottom of the superlattice), as will be fundamental by the experimental results, allowed us to achieve uniform electric field inside the superlattice. Finally, Ohmic AuGeNi contact was annealed at the bottom of the structure, to act as a second contact. Wet etching was applied to achieve square mesas of different area. The experiment was performed on the mesas of $80 \mu\text{m} \times 80 \mu\text{m}$.

In order to couple the incident AC electric field, golden wire ($d = 25 \mu\text{m}$) was connected to the top Schottky controlling contact. Similar solution was already used by Guimaraes [122], however, open air experiment was performed, adjusting the angle of incidence for different frequencies in order to achieve higher coupling strength. There are also other open-air solutions, e.g. exploiting the bow-tie design antenna for coupling the incident AC field [150]. Employment of the open air solutions has already proved its operability, however, weaker

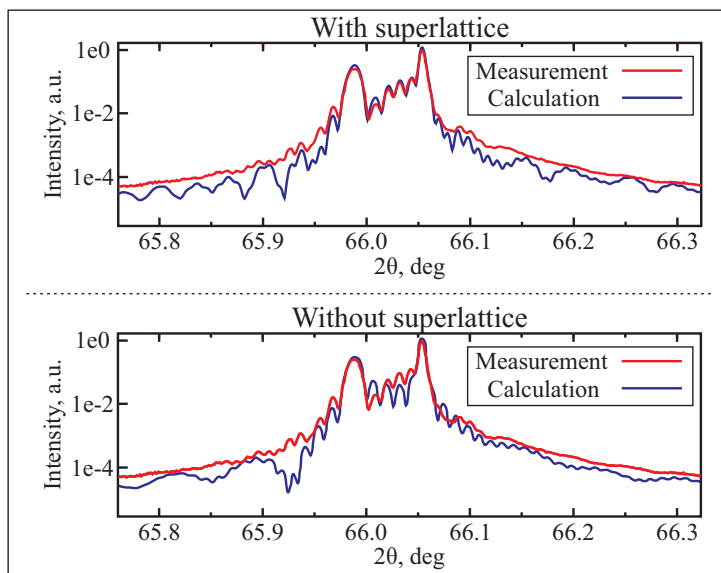


Figure 2.2: The simulated (blue) and experimentally acquired (red) XRD rocking curves. Simulated curve depicted at the upper half represent structure with the superlattice comprising 4.5 nm GaAs wells and 1.15 nm $\text{Al}_{0.41}\text{Ga}_{0.59}\text{As}$ barriers. The particular parameters selected for the best match with experimentally acquired curve. Simulated curve depicted at the bottom half represent structure without superlattice. One should note the close match between the simulated and experimental results of the superlattice-based structure.

coupling strength is expected thus, waveguide-friendly solution was selected for the proof-of-concept experiment.

In order to insure the congruence of the fabricated design with the performed theoretical estimation, structures have been evaluated using transmission electron microscopy (TEM) and the X-Ray diffraction (XRD). The XRD analysis obtained by drilling a throughout hole was achieved using Smartlab x-ray diffractometer with high resolution optics (Ge (400)x2 monochromator) and 9 kW power x-ray tube with rotating Cu anode. The rocking curves, presented in Figure 2.2. The upper graph of the figure depicts strong match with the curve obtained for structure including the superlattice, while the rocking curve, depicted at the bottom part of the figure represents comparison of the experimental curve with the one simulated for the same structure, but without the superlattice. Sample for TEM imaging prepared using field emission SEM (FESEM-FIB Helios NanoLab 650, FEI Company, Netherlands). TEM images depicted on Figure 2.3 were achieved by microscope (Tecnai G2 F20 X-TWIN by FEI Company, Netherlands) also confirm the successful formation of the superlattice.

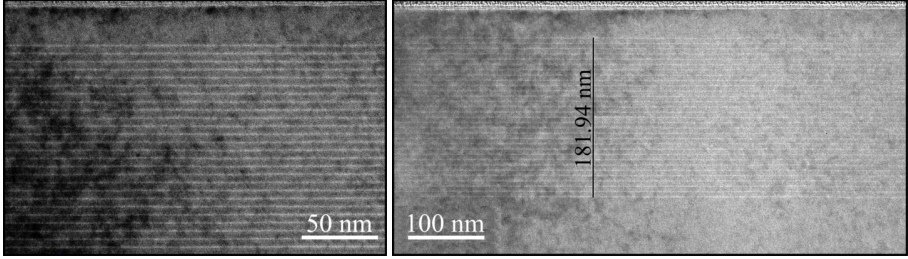


Figure 2.3: Transmission electron microscopy (TEM) images of the analysed superlattices. Specified length of 181.94 nm results in 6.06 nm superlattice period. Samples achieved by Tecnai G2 F20 X-TWIN microscope by FEI Company, Netherlands. Reprinted figure with permission from [1]. Copyright 2022 by the American Physical Society.

2.2. Experimental technique and the setup

A waveguide-based setup was employed for the experiment. The superlattice structure was placed into a single-ridged waveguide (17 mm \times 6 mm). This type of the waveguide is selected to ensure increased AC electric field strengths in the coupling area of the sample. The sample is placed along the wide wall of the waveguide for the TE_{10} mode. The golden wire, acting as an antenna was connected to the waveguide, whilst the bottom Ohmic contact was connected to the isolated coaxial line via filter (see Figure 2.4).

Experiment relies on the change of the transmitted and reflected microwaves, induced by the processes inside the sample [151]. Setup is presented

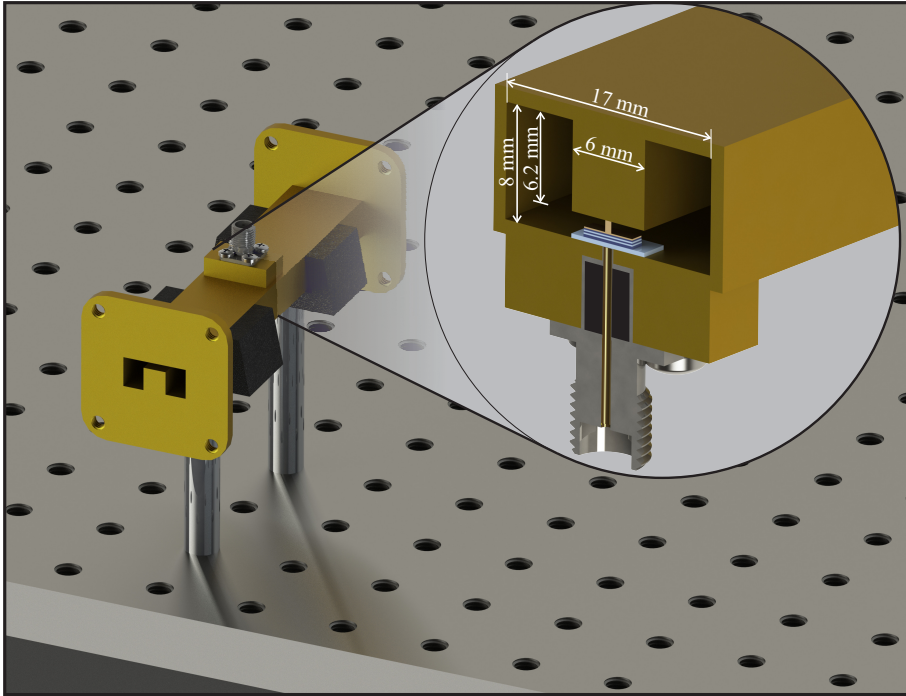


Figure 2.4: Part of the measurement setup, depicting the sample holding part of the waveguide. The sample (not to scale) is placed along the wide wall of the single-ridged waveguide with inner dimensions of $17\text{ mm} \times 8\text{ mm}$. $25\text{ }\mu\text{m}$ diameter golden wire, bonded to the top contact to direct the AC bias and for DC biasing. Bottom Ohmic contact was connected to the coaxial line via filter. Final thickness of the structure (excluding substrate) was $\approx 1.3\text{ }\mu\text{m}$. Mesas of $80\text{ }\mu\text{m} \times 80\text{ }\mu\text{m}$ was employed in the particular research. Reprinted figure with permission from [1]. Copyright 2022 by the American Physical Society.

in Figure 2.5. Two microwave radiation generators (MWGS) were used. The first one was klystron generator, which can emit power of 10 mW in the range of $8.2\text{ GHz} - 12.4\text{ GHz}$. The second generator was magnetron, operating at 9.4 GHz with power of 30 mW . After passing the low-pass filter (LPF), eliminating the second and third harmonics from the generator, microwave excitation via ferrite circulator (FC) is transferred into the sample line. Next, impedance transformer is inserted (IT) into the sample line. The impedance transformer comprises two quartz quarter wave plates, which can be translated together, changing their position in the waveguide line, or separately, changing the distance between them. It allows to minimize the reflected signals in the line beyond the impedance transformer and adjust the phase. The importance of phase adjustment will be explained in the result section. The impedance transformer was manually adjusted to achieve the desired amplitude on the selected frequency. Waveguide switch (WS) was inserted after the sample with differ-

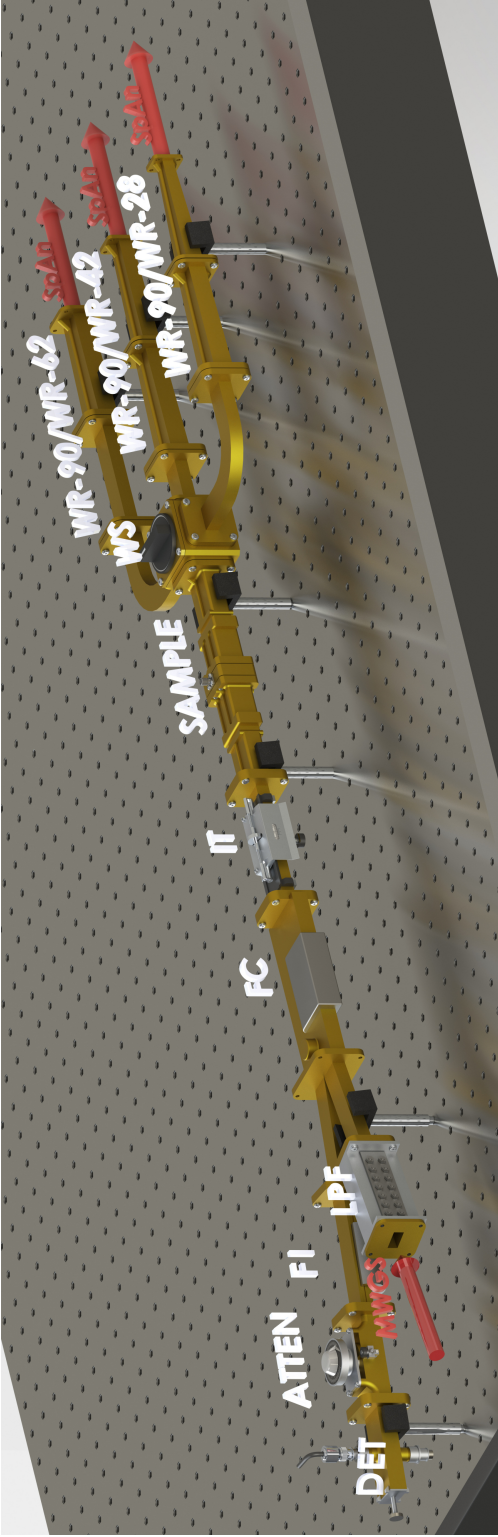


Figure 2.5: Experimental setup. Microwave radiation generated by klystron (8.2 - 12.4 GHz frequency range) or magnetron (9.53 GHz) inputted at MWGS is transferred via low pass filter (LPF) to the main line via ferrite circulator (FC). The low pass filter is required to remove parasitic high-frequency components. Impedance transformer (IT) adjusted to the excitation frequency is introduced to suppress reflections of the excitation signal, ensuring optimal phase at the sample. Adjustment is performed by analysing output signal in the search of maximum. A waveguide switch (WS) is used to connect three WR-90/WR-XX waveguide adapters (WR-XX: WR-62, WR-42, WR-28), allowing expand frequency range which can be recorded without interfering into setup. Transient spectrum was recorded using C4-27 spectrum analyser (SpAn). Reflected wave change analysis was performed by a Schottky diode detector (DET), connected to the LeCroy Waverunner digital oscilloscope via attenuator (ATTEN) and isolator (FI). Reprinted figure with permission from [1]. Copyright 2022 by the American Physical Society.

ent waveguide adapters connected to its branches. In particular these include WR-90 (X-band: 8 GHz - 12 GHz) to WR-62 (K_u-band: 12 GHz - 18 GHz), WR-42 (K-band: 18 GHz - 27 GHz), and WR-28 (K_a-band: 27 GHz - 40 GHz). Such interconnection allows to increase the frequency range to be detected without interfering into the setup. The reflected part of the signal was also analysed, as the generation effect of the superlattice structure is not directed, thus, should be expected in the both detection lines. Ferrite circulator allows to redirect the "reflected" signal into reflection line without interference with the signal from microwave generator. The signal is detected with Schottky-diode detector (DET) with a time constant of ~ 10 ns. The attenuator (ATTEN) is used for the sensitivity calibration The frequency response was explored with the C4-27 spectrum analyser (SpAn). Except when highlighted otherwise, all the experiments were carried out at room temperature conditions.

2.3. Theoretical Models

As will be shown in the result part, during the experiment successful generation of harmonics ($\omega_1 = n\omega_0$), half-harmonics ($\omega_1 = n\omega_0/2$), and sub-harmonics ($\omega_1 = p\omega_0/q$) was recorded (n, p, q - integers). Theoretically, single miniband model is explored, thus, no miniband interaction effects are taken into account. Parameters of the superlattice, employed in experiment, are taken as reference. It is assumed that the electric field, directed along the growth axis of the superlattice is expressed as

$$E_{\text{tot}}(t) = E_{\text{pump}} + E_{\text{probe}}. \quad (2.1)$$

One may see an analogy of the pump-probe experiment definitions. In this research, probe electric field strength can be either small, compared to the pump electric field strength (small-signal gain model), or become at least comparable (large-signal gain model). The majority of theoretical research stick to the small-signal gain model, however, as will be shown later, breaking these boundaries is not only necessary due to experimentally achieved values of amplification coefficient, but also allows to reveal the physics beyond the boundaries of the small-signal gain model. Returning to the pump field, one may further be expressed as

$$E_{\text{pump}}(t) = E_{\text{dc}} + E_{\text{ac}} \cos(\omega_0 t), \quad (2.2)$$

here E_{dc} is an electric field strength of the DC bias, E_{ac} is the electric field strength of the AC bias, and ω_0 is frequency of the AC bias. Two types of probe electric field may be employed. Probe electric field may comprise one probe frequency (other than the pump) leading to the degenerate gain processes or two probe frequencies, leading to non-degenerate gain processes. Thus

$$\begin{aligned}
E_{\text{probe-deg}}(t) &= E_1 \cos(\omega_1 t + \varphi_1); \\
E_{\text{probe-nondeg}}(t) &= E_1 \cos(\omega_1 t + \varphi_1) + E_2 \cos(\omega_2 t + \varphi_2),
\end{aligned}
\tag{2.3}$$

where φ_1 , and φ_2 are relative phase differences, further to be shown as essential for the observation of the parametric generation or amplification processes. For the sake of clarity, it is reasonable to first modify drift velocity expression 1.5 aiming to separate structure and experiment related components. To do that, one should first define critical electric field strength, under which peak drift velocity is reached. The derivation for the latter is achieved via differentiation over E_{tot} of the expression 1.5, resulting in

$$E_{\text{cr}} = \frac{\hbar}{ed\tau}, \tag{2.4}$$

resulting in the peak velocity

$$v_{\text{p}} = \frac{\Delta d}{4\hbar}. \tag{2.5}$$

Exact derivation is given in Appendix 6.2.1. Taking these equations into account Equation 1.5 can be reorganized as

$$v_{\text{d}}(E_{\text{tot}}) = 2v_{\text{p}} \frac{E_{\text{tot}}/E_{\text{cr}}}{1 + (E_{\text{tot}}/E_{\text{cr}})^2} = 2v_{\text{p}} \frac{F_{\text{tot}}}{1 + F_{\text{tot}}^2}, \tag{2.6}$$

Note the introduction of the dimensionless electric field strength describing variable $F = E/E_{\text{cr}}$ introduced for simplification. It is also important to note, that the above-derived equations are valid only in the quasistatic approximation ($\omega_i\tau \ll 1$) [152]. This condition implies that the drift velocity follows the change of the alternating component of the electric field. This allows to use equations, derived for the case when only DC electric field is applied for the cases of mixed electric fields. However, such conditions enable frequency range limitations. Characteristic relaxation time is estimated as $\tau \approx 200$ fs. Thus, the below presented consideration cover frequencies below ≈ 300 GHz.

Depending on the probe electric field strength small or large signal model should be applied. Small-signal gain model may be employed to qualify if the superlattice would start generating signal under particular biasing conditions, while the large signal model can be employed to estimate gain limits in the superlattice.

3. Experimental Observation of Dissipative parametric gain in doped GaAs/AlGaAs superlattices and small signal approach

Parametric generation is known to be realized in various physical systems like electronic circuits, nonlinear optics, and Josephson mesoscopic device for quantum information processing [153–155]. There exists a less popular dissipative parametric gain mechanism, responsible for the generation of sub-harmonics in systems featured by nonlinear oscillators [64]. Having the AC pump applied, negative differential resistance mode should be reached by the system during part of the bias pump period [64, 156]. Superlattice being placed within the limits of strong dissipation ($\omega_0\tau \ll 1$) reveals intriguing operation. Regenerative amplification, still relying on the periodic switching to the NDV state, may be supplied not only by the down-conversion processes, but also by the up-conversion [140, 157]. Superlattices are found to meet the above-described conditions [158, 159]. However despite 50 years of studies, no experimental evidence of the parametric gain in the superlattices have been provided yet.

The electromagnetic wave, successfully coupled with the superlattice by the golden wire, modulates electron drift velocity and excites coherent emission by the means of parametric gain process. Frequency of 8.45 GHz was selected to be generated by the klystron with additional DC bias of 0.3 V. The second experiment was performed on the 9.53 GHz frequency using the magnetron as

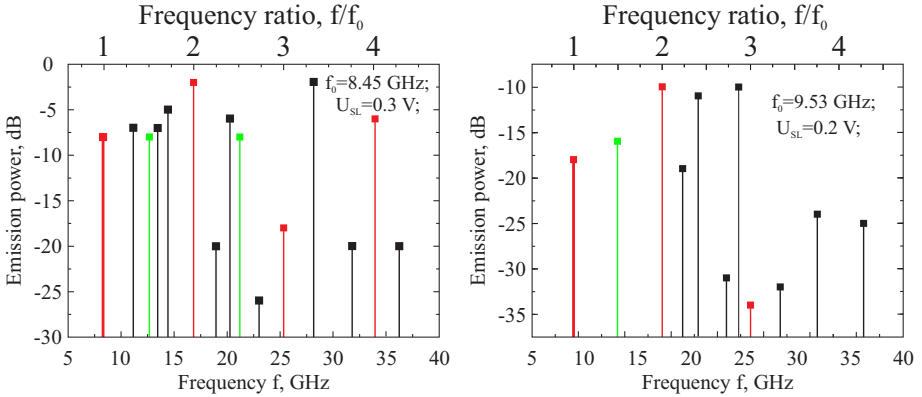


Figure 3.1: Recorded multi-frequency spectra, obtained from the superlattice structure. Left graph depicts frequency obtained by the excitation employing klystron generator at 8.45 GHz frequency, right spectra obtained using magnetron at 9.53 GHz. Different colours depict different types of recorded frequencies. Red thick line correspond to the excitation frequency and thin red lines correspond to harmonics of the excitation frequency. Green lines represent half-harmonics. Note that the $\omega_0/2$ frequency not detected. Black lines correspond to the fractional sub-harmonics.

an AC source and additional 0.2 Volts of DC bias. The recorded spectra are presented in Figure 3.1.

Three different types of frequencies that have been recorded. The first one (marked red) are the harmonics of the primary frequency $\omega_1 = n\omega_0$, n being integer. The second type are the half sub-harmonics (marked green) $\omega_1 = n\omega_0/2$. And, finally, the sub-harmonics (marked black) $\omega_1 = p\omega_0/q$ have been observed; p, q also being integer. It is important to underline the wave-guide setup does not allow to observe $\omega_0/2$ half harmonic generation due to waveguide cut-off frequency. However, generation is expected in the case when other half-harmonics are visible. The recorded multi-frequency spectra is particularly rare and interesting from the scientific point of view as it depicts possibility to generate fractional frequencies. The recorded frequencies were found to be connected to the pump frequency as

$$\omega_1 \pm \omega_2 = n_{\pm}\omega_0; \quad \omega_1 = n_0\omega_0, \quad (3.1)$$

representing non-degenerate or degenerate processes respectively. The recorded frequencies and corresponding non-degenerate equations are presented in table 3.1 and 3.2. Frequencies were asserted to the fractions with 2.5% deviation limit.

One should note the significant amount of relations corresponding to $n_- \geq 1$. The existence of such relations involving the up-conversion processes ($\omega_1 + n\omega_0 = \omega_2$) are devoted to remarkably represent the dissipative mechanism [157,158]. On the other hand, down-conversion processes ($n\omega_0 = \omega_1 + \omega_2$) marked by n_+ is a universal signature of the parametric gain in the superlattice [142]. The latter is further justified by the process dependency on the phase of the incoming radiation, which was adjusted by the impedance transformer. Analysing the relations presented in tables 3.1 and 3.2, one could note that almost any of the recorded frequencies may participate in several different relations. Not only one can observe response, being result of the multi-photon processes upon particular biasing conditions, but **the multiplicity of the simultaneously occurring multi-photon processes**. All the relations depicted in tables 3.1 and 3.2 are shown in Figure 3.2

For example, in the case of 8.45 GHz AC bias (left of Figure 3.2), one may note red dashed lines marking five simultaneously occurring 28.2 GHz frequency-related amplification processes. One may further note the different amount of pump photons participating in the reaction.

Table 3.1: Possible $\omega_1 + \omega_2 = n_+\omega_0$ (top) and $\omega_1 - \omega_2 = n_-\omega_0$ (bottom) relations of gain processes acquired from the multi-frequency spectra excited by 8.45 GHz klystron generator. 2.5% deviation for the frequency estimation is applied. Reprinted table with permission from [1]. Copyright 2022 by the American Physical Society.

Freq.	Fraction		Freq.	Fraction		$n_+; n_-$		Excitation frequency
11.20	(4/3)	+	23.05	(8/3)	=	4	×	8.45
12.67	(3/2)	+	21.20	(5/2)	=	4	×	8.45
14.46	(7/4)	+	18.98	(9/4)	=	4	×	8.45
13.45	(8/5)	+	20.30	(12/5)	=	4	×	8.45
18.98	(9/4)	+	23.05	(11/4)	=	5	×	8.45
13.45	(8/5)	+	28.20	(17/5)	=	5	×	8.45
23.05	(8/3)	+	28.20	(10/3)	=	6	×	8.45
14.46	(7/4)	+	36.25	(17/4)	=	6	×	8.45
18.98	(9/4)	+	31.80	(15/4)	=	6	×	8.45
18.98	(11/5)	+	31.80	(19/5)	=	6	×	8.45
23.05	(8/3)	+	36.25	(13/3)	=	7	×	8.45
23.05	(11/4)	+	36.25	(17/4)	=	7	×	8.45
31.80	(15/4)	+	36.25	(17/4)	=	8	×	8.45
31.80	(19/5)	+	36.25	(21/5)	=	8	×	8.45
36.25	(13/3)	-	28.20	(10/3)	=	1	×	8.45
21.20	(5/2)	-	12.67	(3/2)	=	1	×	8.45
31.80	(15/4)	-	23.05	(11/4)	=	1	×	8.45
23.05	(11/4)	-	14.46	(7/4)	=	1	×	8.45
28.20	(17/5)	-	20.30	(12/5)	=	1	×	8.45
28.20	(10/3)	-	11.20	(4/3)	=	2	×	8.45
36.25	(17/4)	-	18.98	(9/4)	=	2	×	8.45
36.25	(21/5)	-	18.98	(11/5)	=	2	×	8.45
31.80	(15/4)	-	14.46	(7/4)	=	2	×	8.45
36.25	(13/3)	-	11.20	(4/3)	=	3	×	8.45

Table 3.2: Possible $\omega_1 + \omega_2 = n_+\omega_0$ (top) and $\omega_1 - \omega_2 = n_-\omega_0$ (bottom) relations of gain processes acquired from the multi-frequency spectra excited by 9.53 GHz magnetron generator. 2.5% deviation for the frequency estimation is applied.

Freq.	Fraction		Freq.	Fraction		$n_+; n_-$		Excitation frequency
21.25	(11/5)	+	27.32	(14/5)	=	5	×	9.53
21.25	(9/4)	+	26.00	(11/4)	=	5	×	9.53
21.25	(9/4)	+	35.80	(15/4)	=	6	×	9.53
21.25	(11/5)	+	35.80	(19/5)	=	6	×	9.53
26.00	(8/3)	+	31.80	(10/3)	=	6	×	9.53
26.00	(11/4)	+	40.80	(17/4)	=	7	×	9.53
26.00	(8/3)	+	40.80	(13/3)	=	7	×	9.53
31.80	(10/3)	+	35.80	(11/3)	=	7	×	9.53
35.80	(11/3)	+	40.80	(13/3)	=	8	×	9.53
35.80	(15/4)	+	40.80	(17/4)	=	8	×	9.53
35.80	(11/3)	-	26.00	(8/3)	=	1	×	9.53
40.80	(13/3)	-	31.80	(10/3)	=	1	×	9.53
35.80	(15/4)	-	26.00	(11/4)	=	1	×	9.53
31.80	(17/5)	-	22.95	(12/5)	=	1	×	9.53
35.80	(19/5)	-	27.32	(14/5)	=	1	×	9.53
40.80	(17/4)	-	21.25	(17/4)	=	2	×	9.53

$$\left\{ \begin{array}{l} \mathbf{28.20} + 23.05 = 6 \times 8.45 \text{ GHz (8-photons)}, \\ \mathbf{28.20} + 13.45 = 5 \times 8.45 \text{ GHz (7-photons)}, \\ \mathbf{28.20} - 11.20 = 2 \times 8.45 \text{ GHz (4-photons)}, \\ \mathbf{28.20} - 20.30 = 1 \times 8.45 \text{ GHz (3-photons)}, \\ 36.25 - \mathbf{28.20} = 1 \times 8.45 \text{ GHz (3-photons)}. \end{array} \right. \quad (3.2)$$

The amount of photons included in one process is in sharp contrast to the classical cases of parametric generation within optical systems, wherein the Manley-Rowe equation may be applied to all of the occurring processes. Not only the recorded processes brake the Manley-Rowe relations, but the generation involving up-conversion processes ($n_- = 2, 3$) are also not realizable in conventional parametric generation systems. It is important to note, that the non-compliance to the Manley-Rowe relations is expected to be observed only under the limit of strong dissipation $\omega_0\tau \ll 1$. In the limit of small dissipation $\omega_0\tau \gg 1$, Manley-Rowe relations will be satisfied [158]. More information on the Manley-Rowe relation is provided in Appendix 6.1.3

To further understand the nature of the effect, I-V curves of the SL device

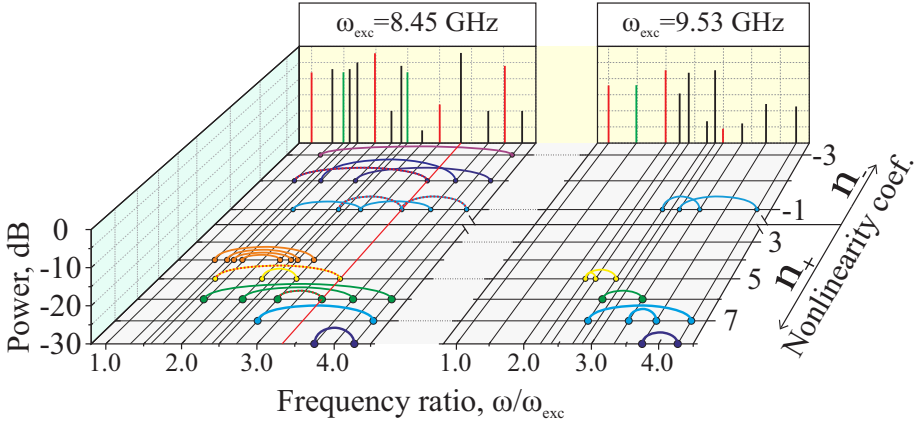


Figure 3.2: Relations of the frequencies corresponding to the gain processes acquired from the experimental spectra. 8.45 GHz excitation on the left and 9.53 GHz magnetron excitation on the right. Frequencies are scaled to pump excitation frequency. Spectral line on the back of each graph correspond to harmonics (red), half sub-harmonics (green), and fractional sub-harmonics (black). Links in the horizontal plane correspond to the Equation 3.1 with color depicting different non-linearity coefficient. Thick red line on the horizontal plane depict several processes involving 28.20 GHz frequency, depicting the theoretical possibility of several simultaneous multiphoton processes to occur at the same time see Equation 3.2 for detailed info. Adapted from [1]. Reprinted figure with permission from [1]. Copyright 2022 by the American Physical Society.

have been obtained by applying electrical pulses of 20 ns. The results are displayed by the thick black line in Figure 3.3 (a). Positive slope of the I-V curve refers to the typical electronic system with NDV, operating in stable transport regime. One may find analogies with the I-V curves, described in the literature overview [106, 107]. The red line on the main graph depicts neutral I-V characteristic, which directly follows $v(E)$ dependence of Esaki-Tsu [63] and allows to gain an additional information on the nature of the contacts in the structure. It was shown that superlattices with Ohmic contacts are prone to saturate at the peak Esaki-Tsu current or above it (see inset in Figure 3.3) [105]. As one may note, the achieved I-V curve runs significantly below the peak current, indicating the non-Ohmic nature of the contacts employed. The built-in voltage of 0.65 V due to this non-Ohmicity was taken into account into further calculations.

Power input-output dependencies have been additionally recorded. The acquirement of such curves is classical in non-linear optical systems, leading to comparison with proposed theoretical models, the simplest of which implies

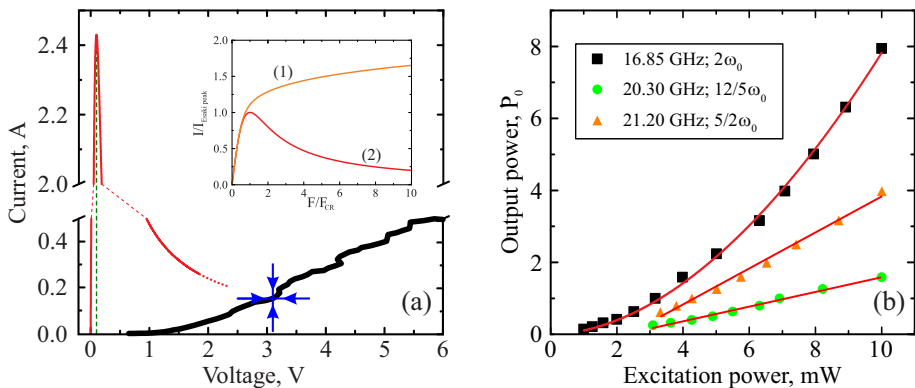


Figure 3.3: (a) Experimentally acquired I-V characteristic of the described superlattice structure (thick black line). Vertical green dashed line represent voltage of $E_{\text{cr}}L \approx 0.1$ V, marking the critical voltage, corresponding to peak Esaki-Tsu current depicted by red line and reaching peak current of $I_p \approx 2.4$ A. Inset depicts the calculated I-V characteristics for the superlattice with Ohmic contacts (orange line marked (1)) compared to the Esaki-Tsu curve (red line marked (2)). One should note significant differences between the orange line and experimental IV, marking an importance of non-Ohmic contact selection. (b) Input-output power dependencies for the above-discussed superlattice in the experimental setup. No DC pump was applied for the particular experiment. AC pump of 8.45 GHz was used. Note the differences of the approximated dependencies. Quadratic dependency may be found for the harmonics, while in the case of half sub-harmonics and fractional sub-harmonics linear dependency with different gradient may be observed [1]. Reprinted figure with permission from [1]. Copyright 2022 by the American Physical Society.

that the corresponding n^{th} harmonic should be featured by the n^{th} power function dependency on the excitation power [60, 61]. However, in contrast to the above-cited optical experiments, linear dependencies have been observed in a medium with quadratic nonlinearity [160, 161]. The recorded dependencies for different types of frequencies (second harmonic $2\omega_0$, half-harmonic $5\omega_0/2$, and fractional harmonic $12\omega_0/5$) are depicted at Figure 3.3 (b). The input-output dependencies of the second harmonic generation process is non-linear, while the sub-harmonics dependency is linear, but with different slopes. This result once again depicts the complexity of the system. The discrepancies from the mature optical theoretical models is explained by the emphasis that the superlattice structure in the microwave electric field can not be treated as a pure optical system, but **nonlinear optoelectronic system operating in negative differential velocity regime with predominating multiphoton generation/amplification process**. It is the complexity of the system resulting in juvenile theoretical model, arising from huge amount of different aspects, only partially covered within the presented results.

Small signal gain model

Small signal gain model was proposed in order to roughly estimate the AC bias electric field strength in the superlattice. The process is based on the application of the small signal gain model, which may be described in terms of high-frequency complex mobility $\mu = \mu_r + i\mu_i$. For the mathematical simplicity analysing the degenerate process, the response to the probe AC electric field

$$\begin{aligned} v_d &= \Re[\mu E_1 e^{-i\omega_1 t + \varphi_1}] = \Re \left[E_1 \left((\mu_r + i\mu_i) (\cos(\omega_1 t + \varphi_1) - i \sin(\omega_1 t + \varphi_1)) \right) \right] = \\ &= E_1 (\mu_r \cos(\omega_1 t + \varphi_1) + \mu_i \sin(\omega_1 t + \varphi_1)) \end{aligned} \quad (3.3)$$

wherein

$$\mu_r = \frac{2}{E_1} \langle v_d(E_{\text{tot}}) \cos(\omega_1 t) \rangle_t; \quad \mu_i = \frac{2}{E_1} \langle v_d(E_{\text{tot}}) \sin(\omega_1 t) \rangle_t. \quad (3.4)$$

In these equations $\langle \dots \rangle_t$ denotes averaging over the common period of all the AC electric fields involved (pump and probe). Dimensionless units are introduced by scaling the mobility to Drude mobility $\mu_0 = e\tau/m^*$. In this equation $m^* = 2\hbar^2/\Delta d^2$ being the effective mass on the bottom of the miniband results in

$$\mu_0 = \frac{e\tau}{m^*} = \frac{e\tau\Delta d^2}{2\hbar^2} = \frac{2v_p}{E_{\text{cr}}}. \quad (3.5)$$

Equations 3.4 and 3.5 combined result in

$$\frac{\mu_r}{\mu_0} = \frac{E_{\text{cr}}}{v_p E_1} \langle v_d(E_{\text{tot}}) \cos(\omega_1 t + \varphi_1) \rangle_t; \quad \frac{\mu_i}{\mu_0} = \frac{E_{\text{cr}}}{v_p E_1} \langle v_d(E_{\text{tot}}) \sin(\omega_1 t + \varphi_1) \rangle_t. \quad (3.6)$$

To proceed further, taking into account that the probe electric field strength is negligibly small, one should use Taylor series to the drift velocity Equation 2.6

$$v_d(E_{\text{tot}}) = v_d(E_{\text{pump}} + E_{\text{probe}}) \approx v_d(E_{\text{pump}}) + v'_d(E_{\text{pump}}) E_1 \cos(\omega_1 t + \varphi_1). \quad (3.7)$$

Note the introduction of the dimensionless electric field strength derived as $F = E/E_{\text{cr}}$. Extended analysis of the mobility components given in the Appendix 6.2.2 reveals that under averaging over common period, imaginary component converges to zero, thus, only real part is left for the net mobility. Moreover, real mobility component is shown to be equal to

$$\frac{\mu_r}{\mu_0} = \frac{1}{v_p F_1} (A_h + A_{\text{inc}} + A_{\text{coh}}), \quad (3.8)$$

wherein

$$\begin{cases} A_h = 0; \\ A_{\text{inc}} = \langle v'_d(E_{\text{pump}}) \rangle_T \cdot E_1/2; \\ A_{\text{coh}}(\varphi_1) = \langle v'_d(E_{\text{pump}}) \cos(\omega_1 t) \rangle_T \cdot \cos(2\varphi_1) \cdot (E_1/2). \end{cases} \quad (3.9)$$

One may note the existence of phase independent incoherent component and phase-dependent coherent component, influence of each will be further analysed in the result section. Proceeding further, one would achieve final mobility components:

$$\begin{cases} \mu_{\text{inc}} = \mu_0 \left\langle \frac{(1-F_{\text{pump}}^2)}{(1+F_{\text{pump}}^2)^2} \right\rangle_T; \\ \mu_{\text{coh}}(\varphi_1) = \mu_0 \left\langle \frac{(1-F_{\text{pump}}^2)}{(1+F_{\text{pump}}^2)^2} \cos(\omega_1 t) \right\rangle_T \cos(\varphi_1) \end{cases} \quad (3.10)$$

where the total mobility is the sum of the latter $\mu = \mu_{\text{inc}} + \mu_{\text{coh}}(\varphi_1)$ [159,162]. Interesting note about the incoherent mobility component should be done at this point. If one would imagine the pump electric field to comprise only the DC component, the incoherent mobility component would look like

$$\mu_{\text{inc}}(E_{\text{dc}}, E_{\text{ac}} = 0) = \mu_0 \frac{1 - F_{\text{dc}}^2}{(1 + F_{\text{dc}}^2)^2}. \quad (3.11)$$

One may note that μ_{inc} would become negative right after the applied bias electric field strength would exceed Esaki-Tsu critical field $F_{\text{dc}} = E_{\text{dc}}/E_{\text{cr}} > 1$)

leading to the canonical description of the Bloch gain (see Equation 11 in [14]). This is also supplemented by the fact that for the case when only AC bias electric field is applied

$$\mu_{\text{inc}}(E_{\text{dc}} = 0, E_{\text{ac}}) = \mu_0(1 + F_{\text{ac}}^2)^{-3/2} \quad (3.12)$$

leading that the incoherent mobility will always be positive, thus, no gain processes are expected.

To summarize, for the case of the gain mechanism, described by incoherent component, the power which is gained by probe electric field comes from the DC source, while the AC pump electric field provides control for the energy transfer. Thus, the incoherent processes may be treated like Bloch gain mechanism, modified by the alternating electric field [163]. At the same time, the coherent component displays more a parametric nature, wherein gain is caused by a periodic variation of the differential velocity, affected by the alternating pump electric field. In this case, the power of the probe electric field has its origin in the AC pump electric field, while the DC power provides power transfer control. This is the reason one may observe parametric gain effects even under small DC bias values being much lower than the critical electric field strength E_{cr} . It is obvious that peak of coherent mobility depends on the relative phase φ_1 , thus, the cosine term can be omitted by employing optimal phase φ_{opt} so that $\mu^{\text{opt}}(\varphi_{\text{opt}}) = \max(-|\mu_{\text{coh}}(\varphi_1)|)$. As a result the final mobility equation looks like

$$\mu^{\text{opt}} = \mu_0 \left\langle \frac{(1 - F_{\text{pump}}^2)}{(1 + F_{\text{pump}}^2)^2} \right\rangle_T + \mu_0 \left\langle \frac{(1 - F_{\text{pump}}^2)}{(1 + F_{\text{pump}}^2)^2} \cos(\omega_1 t) \right\rangle_T. \quad (3.13)$$

In order to achieve gain processes the latter equation should be negative. The parameters to reach those conditions varying for different types of frequencies will be analysed in chapter 4. In order to reach match with the already published equation the averaging should be rewritten as integral and change conversion to the dimensionless units ($\omega t \rightarrow x$) and ($T \rightarrow 2\pi$) should be made. The latter will not be done for now, due to universality considerations. Thus, the final equation is

$$\mu^{\text{opt}} = \frac{\mu_0}{2\pi} \int_0^T \frac{(1 - F_{\text{pump}}^2)}{(1 + F_{\text{pump}}^2)^2} dt + \frac{\mu_0}{2\pi} \int_0^T \frac{(1 - F_{\text{pump}}^2)}{(1 + F_{\text{pump}}^2)^2} \cos(\omega_1 t) dt. \quad (3.14)$$

Applying the $\omega_1 = n\omega_0$ equation, corresponding to the amount of pump photons, participating in the process, one should achieve different photon amount dependent generation pictures (see Figure 3.4). One should note a presence of no generation gap appearing for $n > 1$ cases (marked white). The existence of

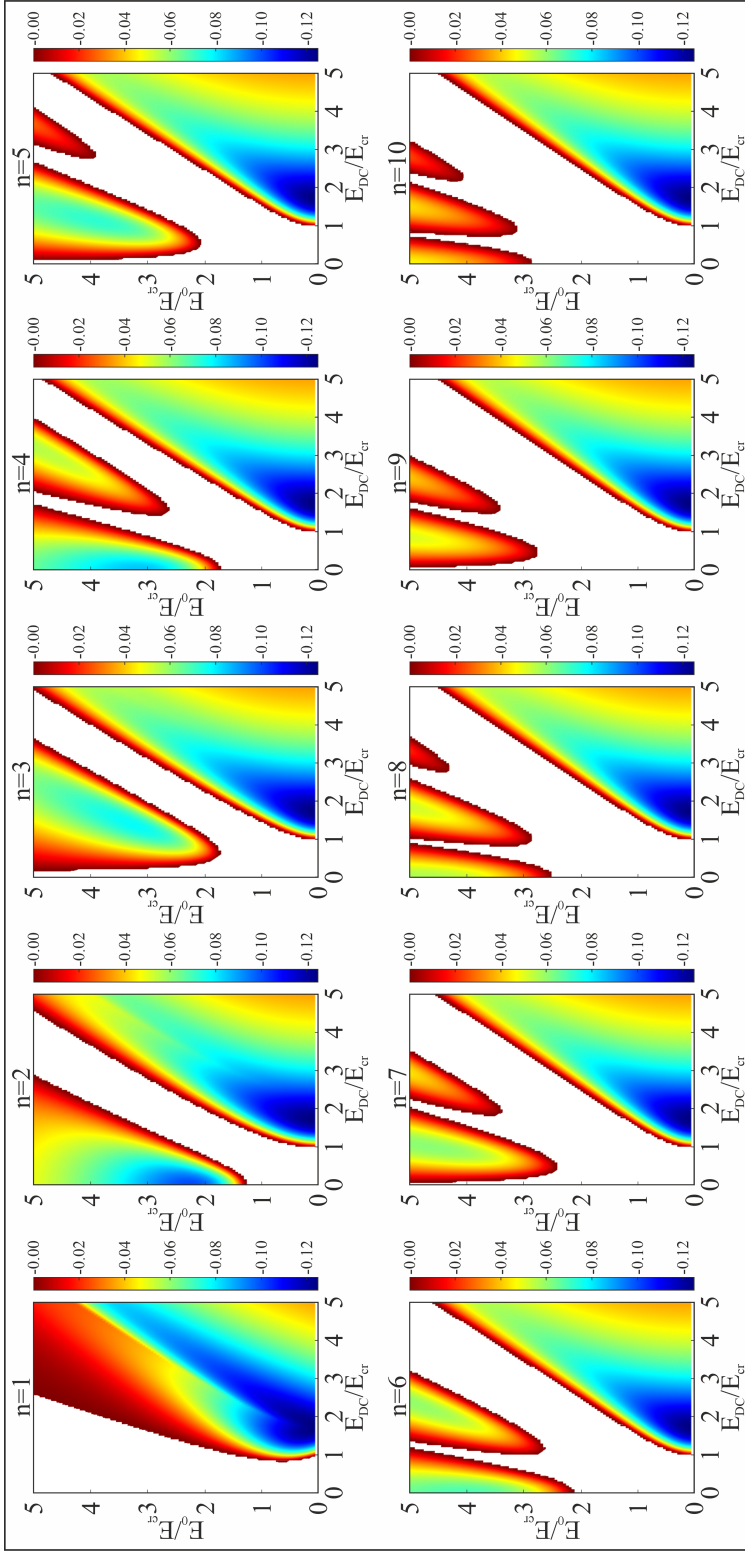


Figure 3.4: Negative mobility areas of μ^{opt}/μ_0 for different $\omega_1 = n\omega_0$ frequencies, wherein n describes the amount of pump photons participating in the gain process. Areas are presented in a 2D plots as a dependencies of the applied DC and AC pump electric fields, derived in terms of Esaki-Tsu critical electric field. Blank areas correspond to positive mobility values, depicting conditions wherein generation is not possible. Coloured areas depict magnitude of the relative mobility. One should note single area for the $n = 1$ case and clearly separated regions for the $n > 1$ cases. Reprinted figure with permission from [1]. Copyright 2022 by the American Physical Society.

this gap for the single process is important as during the experiment no gap will be recorded. This absence in the experimental data will nicely fit into an explanation of the multiplicity of the processes occurring in the superlattice. As the $n = 1$ generation area is obviously larger, after the superposition of several processes of different amount of participating photons, the areas overlap in such way that no-generation gap vanishes.

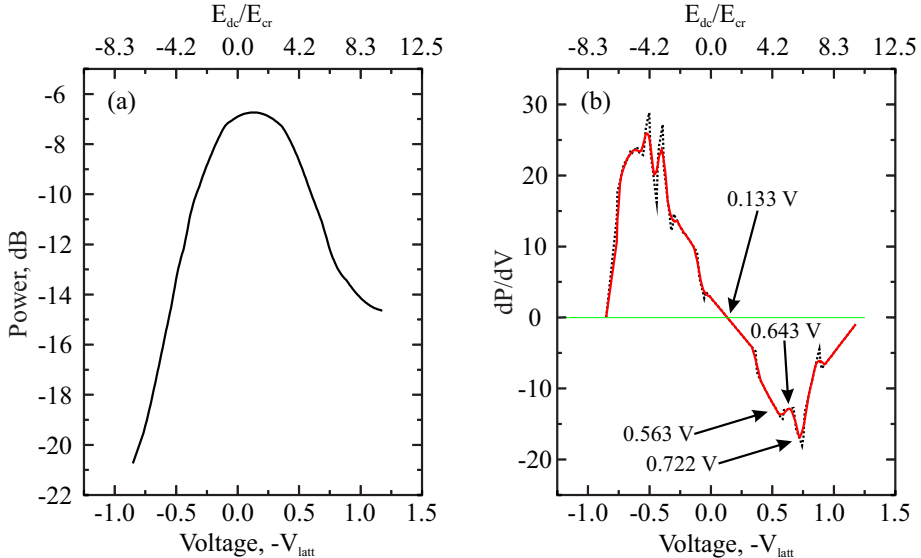


Figure 3.5: (a) Exemplary experimentally acquired power - voltage profile acquired for the $5\omega_{\text{exc}}/2$ half sub-harmonics being excited by 8.45 GHz klystron generator. (b) Derivative of the power - voltage profile presented at Figure 3.5 (a). Note appearance of four points marked by arrows. Such shape of derivative was found to be typical for the analysed superlattice (analysis was performed by tweaking incident power). Relative distance between the points was employed to estimate the AC pump electric field strength, applied during the spectra-recording experiment.

Turning back to the experimental research, in order to roughly estimate the AC bias electric field strength in the superlattice we recorded several power – DC voltage characteristics varying the AC bias (see Figure 3.5 (a) for the exemplary dependency). It has been noticed that the derivatives of such dependencies feature a distinctive local and global peaks (marked by values at Figure 3.5 (b)). Turning back to the previously verified small signal gain model, taking into account the already known conclusion on the multiplicity of simultaneously occurring multiphoton processes primary assumption was made that the recorded profile is a linear superposition of multiphoton processes. Moreover, based on the laws of classical optical experiments, it was decided that the amount of photons participating in the process has a reverse influence on the superpositioned profile (i.e. more photons - smaller linear co-

efficient). This assumptions allowed us to limit our superposition equation up to $n < 4$ leading to

$$\frac{\mu}{\mu_{0 \text{ final}}} = C_1 \cdot \frac{\mu}{\mu_0}(n = 1) + C_2 \cdot \frac{\mu}{\mu_0}(n = 2) + C_3 \cdot \frac{\mu}{\mu_0}(n = 3) \quad (3.15)$$

wherein μ/μ_0 are separate relative mobility components, calculated for particular amount of pump photons according to the equations presented in the Section 3. Only negative relative mobility is taken into account during the superposition as in the case of relative mobility being positive, the particular generation/amplification process will not proceed, however, it will not be disturbing other processes. Thus, positive relative mobility was zeroed during the superposition. In particular case we can clearly see the global peak to be located at 0.133 V (influence of the non-Ohmic contacts included) resulting in 5.51 kV/cm electric field strength or $1.013E_{\text{cr}}$ in terms of critical Esaki-Tsu field. This data is a good starting point as we can limit ourselves to the combination of coefficient and AC bias values wherein the global peak position is known. Moreover, one may find out that the superpositioned profiles feature similar shape with the local peaks changing their relative distance depending on the applied AC bias (see Figure 3.6). As a result, we managed to acquire C_2 and C_3 coefficients by finding proper peak distance (C_1 was achieved by adjusting peak relative magnitude) resulting in final relation to be

$$\frac{\mu}{\mu_{0 \text{ final}}} = 119 \cdot \frac{\mu}{\mu_0}(n = 1) + 18.85 \cdot \frac{\mu}{\mu_0}(n = 2) + 1 \cdot \frac{\mu}{\mu_0}(n = 3) \quad (3.16)$$

corresponding to AC bias of $8.61E_{\text{cr}}$. The reason for the selection of the small signal gain model for the particular research was our pure interest in approximate bias electric field strength. Moreover, as mentioned earlier, the small-signal model has been known for a long time at the moment the particular experiment was conducted, thus, it was deduced to stick with the small signal gain model for simplicity. The even larger complexity of the large signal gain model from the theoretical (numerical) point of view will be discussed in the section below. The performed superpositioning operation resulted in considerably good match of experimental and theoretical data. Also one should note, that such superpositioning process removed the no generation gap, visible in the majority of single multiphoton processes once again being a proof of the multiplicity of the processes, occurring inside the superlattice.

The origin of the amplification resulting in the observation of enormous gain in the superlattice structure is worth additional comment. Basically our logic follows the work of Hyart [142] wherein the generated components were assumed to be transverse electromagnetic modes of external cavity. However, in the ex-

perimental structure there is no cavity. Thus, the generation/amplification processes are believed to rely on intrinsic longitudinal modes inside the superlattice, appearing and growing from the fluctuations of electron plasma. The electromagnetic wave travelling across the waveguide with the speed of light couples with electron plasma and converts into the slow longitudinal mode, propagating with the drift velocity of electrons [113,164] along the superlattice structure. As a result if such a wave is formed at the frequency corresponding to one of the "allowed" processes and relative mobility is negative, small fluctuations will grow exponentially with the electron flow through the superlattice structure. The gain may be expressed with the standard Beer law ($I_{\text{out}} = I_{\text{in}} \exp(-\beta_n z)$) resulting in the gain coefficient β_n to be concentration, mobility and drift velocity dependent [165]:

$$\beta_n = \frac{2eN\mu_n}{\varepsilon v}. \quad (3.17)$$

It is essentially important to note that the gain is inversely proportional to

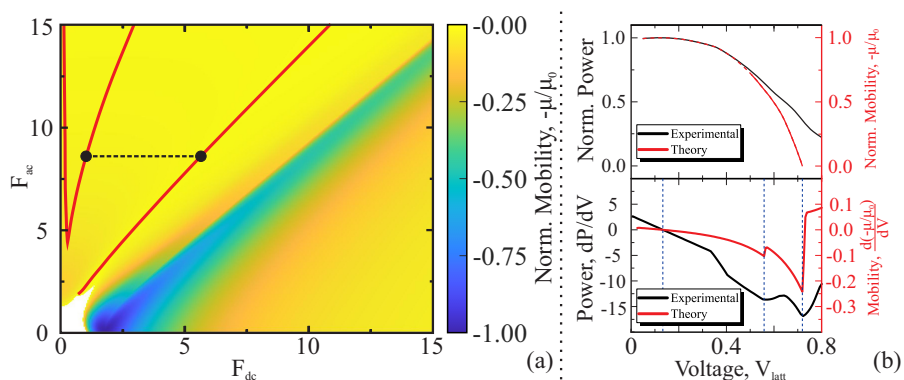


Figure 3.6: (a) Normalized negative mobility areas of μ^{opt}/μ_0 for the superpositioned mobility dependency on DC and AC bias for the case of $\omega_1 = 5\omega_0/2$ frequency. Thick red lines represent mobility peak positioned for each profile of single AC pump value. Distance between these peaks was one of the parameters employed for the determination of superpositioning coefficients. Dotted black line, located at $F_{\text{ac}} \approx 8.61$ represent the distance, corresponding to the experimental profile. (b) Comparison of the output power and its derivative dependencies on the voltage (black) and theoretical mobility and its derivative dependency on the voltage (red). Experimental and theoretical profile corresponding to the black dotted line in Figure 3.6 (a) are analysed. One should note considerable correspondence of the profiles, allowing to make conclusion on the approximate AC electric field strength in the superlattice. Blue vertical dashed lines correspond to the position of peaks of interest, employed for the determination of the superpositioning coefficients. Adapted from [1]. Reprinted figure with permission from [1]. Copyright 2022 by the American Physical Society.

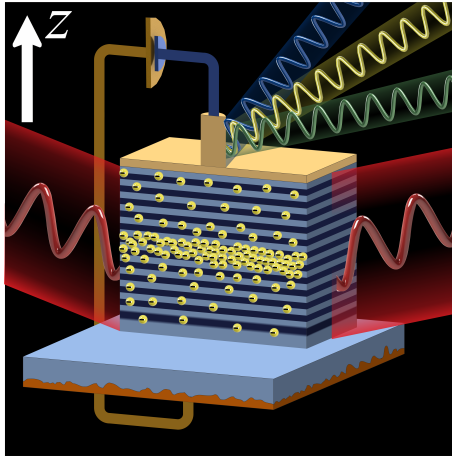


Figure 3.7: Sketch depicting the finger physics of the parametric generation in the above-described superlattice structure. High-frequency AC pump being coupled with the superlattice via the golden wire antenna is directed along the z axis. Wave interacts with the electrons in the miniband exciting growing waves at the recorded frequencies. The generated longitudinal electrostatic wave travels through the superlattice at the electron drift velocity. Schematics depict spatial modulation of the electron density related to one of the slow waves. Copyright 2022 by the American Physical Society.

the wave velocity. In contrary to the case of electromagnetic wave, which is propagating with the speed of light, longitudinal wave propagates with drift velocity. Using the calculated relative mobility $\mu_1/\mu_0 \approx -0.02$ the values of gain coefficient $\beta \gtrsim 10^4 \text{ cm}^{-1}$ are expected for the slow modes (see Figure 3.7). Finally, the generated electrostatic modes are transformed back to electromagnetic waves, which continue propagation through the waveguide to the spectrum analyser.

In summary, following findings can be underlined:

- DC biased superlattice structure in the microwave electric field can not be treated as pure optical system, but must be considered as nonlinear optoelectronic system operating in negative differential velocity regime with predominating multiphoton generation/amplification process.
- Stable coherent parametric gain at various harmonics and sub-harmonics of the pump frequency was observed from the DC biased GaAs/AlGaAs superlattice at room temperature.
- The observed parametric amplification is explained via formation of slow longitudinal waves, travelling with the drift velocity, thus, ensuring gain coefficients exceeding 10^4 cm^{-1} .
- Multiplicity of simultaneously occurring multiphoton processes was revealed. The frequencies of the analysed spectra were found to be connected via up- or down-conversion equations ($\omega_1 \pm \omega_2 = n_{\pm}\omega_0$). The existence of both of the types of the processes was found to be a remarkable property of the dissipative mechanism for the superlattices operating in the Esaki-Tsu NDV regime.
- Processes involving up to 8 excitation photons participating in the reaction were recorded.
- Under dissipative parametric gain conditions ($\omega_0\tau \ll 1$), Manley-Rowe relations, describing the power transfer in the nonlinear elements, are broken for the superlattices operating in the Esaki-Tsu NDV regime.

These findings allow to formulate the following statements for defence:

- **Statement 1:** Dissipative parametric gain under intense microwave pumping in biased sub-critically doped quantum GaAs/AlGaAs superlattices at room temperature manifests itself as a coherent emission at various fractional sub-harmonics of the pump frequency via multiplicity of simultaneously occurring up-conversion and down-conversion processes.
- **Statement 2:** Manley-Rowe relations are not valid for description of dissipative parametric gain in biased and subcritically doped GaAs/AlGaAs superlattices.

4. Degenerate and Non-Degenerate Large Signal Gain in GaAs Superlattices

A new insight in the matter of phase-dependent parametric gain revealed in [A1] raised a new wave of interest on the particular subject. The experimental findings [A1] depicted good consistency with the prediction of the semiclassical model [142,147,158,159,166,167]. The previous theoretical considerations comprised several disadvantages, limiting their applicability to the experimental approach. First of all, the overwhelming majority of the works employed the small signal approximation for the calculation. Secondly, phase-independent effects of the DC-AC Bloch gain and its interaction with the parametric gain processes are usually omitted [163,168].

In this chapter we expand the boundaries of previous investigations. First of all, overview of the small signal gain conditions is presented, highlighting the differences of the main focus of the large signal gain model. Afterwards the analysis of the degenerate and non-degenerate generation processes is presented employing the large signal gain approach.

4.1. Influence of the Large Signal Gain Model on the Degenerate Gain Processes

As described above, the superlattice structure is prone to generation and or amplification of the signal up to the values far exceeding the limit of small signal gain model. Thus, obvious interest in analysis of the processes under the large signal gain model exists.

It is obvious that upon analysis of the large-signal gain model, wherein the probe electric field strength is at least comparable to the pump electric field strength, employment of the small signal gain model, described in previous chapter, would result in inconsistent solutions. The calculation via mobility calculation presented in the previous section is possible. However, analysis via power density is about to be proposed as an alternative. Upon the limits of the small-signal gain model standard classical equation may be applied $P = 0.5eN\mu E_1^2$, wherein N denotes the electron volume density. Once again, it is obvious that the positive gain condition $P < 0$ is achieved only under $\mu < 0$. For the large-signal gain model, the power density equation is

$$P = eN \langle v_d(E_{tot}) E_{probe}(t) \rangle_t \quad (4.1)$$

So the gain logic is the same as in the small-signal gain model. Upon favourable biasing conditions, P becomes negative and power flow is directed out of the superlattice into external circuit [169]. With the growth of the power density P , probe electric field E_{probe} strength also increases. The situation continues

until the P becomes positive resulting in steady state oscillations (saturation of gain). The introduction of the dimensionless units is also reasonable, especially for the case of numerical analysis, thus, the resultant equation

$$\bar{P} = \frac{F_1}{2\pi n} \int_0^{2\pi n} \frac{2F_{\text{tot}}(x)}{1 + F_{\text{tot}}^2(x)} dx, \quad F_{\text{tot}}(x) = F_{\text{dc}} + F_{\text{ac}} \cos(x) + F_1 \cos\left(\frac{p}{q}x + \varphi_1\right). \quad (4.2)$$

In this equation $\bar{P} = P/P_0$; $P_0 = env_p E_{\text{cr}}$; $x = \omega_0 t$; $p\omega_0/q = \omega_1$; p and q – integers. This equation covers the degenerate case with one probe frequency participating in the reaction. If one would consider the non-degenerate process comprising two probe frequencies the relative power equation becomes

$$\bar{P}_{1,2} = \frac{F_{1,2}}{2\pi(q_1 q_2)} \int_0^{2\pi q_1 q_2} \frac{2F_{\text{tot}}(x)}{1 + F_{\text{tot}}^2(x)} dx \cos\left(\frac{p_{1,2}}{q_{1,2}}x + \varphi_{1,2}\right). \quad (4.3)$$

wherein

$$F_{\text{tot}}(x) = F_{\text{dc}} + F_{\text{ac}} \cos(x) + F_1 \cos\left(\frac{p_1}{q_1}x + \varphi_1\right) + F_2 \cos\left(\frac{p_2}{q_2}x + \varphi_2\right) \quad (4.4)$$

is the total applied electric field strength. Under such electric field, the total relative power would be the result of two:

$$\bar{P}(\varphi_1, \varphi_2, E_1, E_2) = \bar{P}_1 + \bar{P}_2. \quad (4.5)$$

Being interested in large-signal gain model small addition by the small-signal gain model is worth mentioning. Figure 4.1 depicts the mobility components of different frequencies calculated by the small signal gain Equations 3.10. These include incoherent (left), coherent (center), and total (right) mobilities of half-harmonics of $3\omega_0/2$ and $\omega_0/2$ and sub-harmonics of $5\omega_0/3$. One should instantly note that the incoherent component, does not depend on the frequency analysed. This component qualitatively is negative (resulting in generation) in the $F_{\text{dc}} > F_{\text{ac}}$ area, which will be denoted as "type I biasing conditions". On the other side, for the case of $F_{\text{ac}} > F_{\text{dc}}$ area, which will be denoted as "type II biasing conditions" the incoherent component is positive, meaning no incoherent gain is possible. The coherent gain, depicted in the central column is shown to be negative throughout the whole range of biasing conditions for the case of both sub-harmonics. One should note on the different distribution (colour) of the mobilities for $3\omega_0/2$, classical for the majority of the half-harmonics and $\omega_0/2$, uniqueness of which will be further discussed below. One should also note that for the case of fractional sub-harmonics (bottom center graph), no coherent generation is expected as mobility is positive (blank) under all the biasing conditions. As a result, the net gain in the case of fractional sub-harmonics is fully defined by the incoherent mobility component,

while both mobilities have effect in the case of half-harmonics. In the case of $3\omega_0/2$ the net mobility results in two well separated areas of generation. The

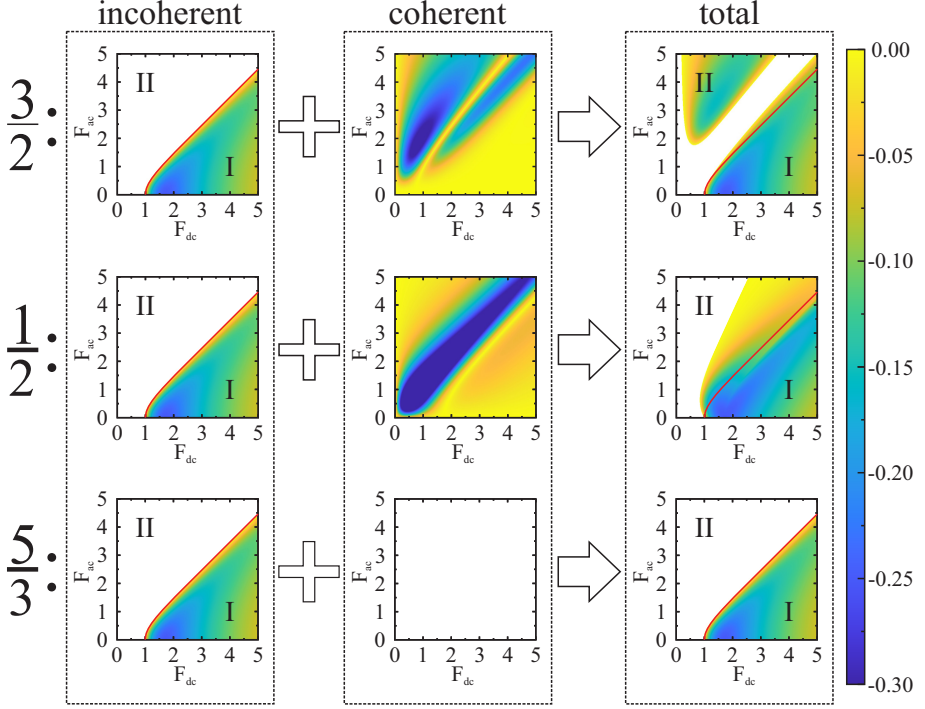


Figure 4.1: Incoherent (left column), coherent (center column), and net (right column; sum of the former two) negative mobility components μ^{opt}/μ_0 calculated using the small-signal gain model. The dependency on the applied DC and AC electric field strengths is presented (electric fields are scaled to the Esaki-Tsu critical electric field and mobility is scaled to Drude mobility). Colour represent areas of negative mobility, while blank areas represent conditions of positive mobility, wherein no gain is expected. The dependencies are given for three different types of frequency: first row represent $3\omega_0/2$ frequency of half sub-harmonic type; second row represent $\omega_0/2$ frequency (importance of this frequency will be discussed below); third row represent $5\omega_0/3$ being a typical example of fractional sub-harmonic. Solid red lines represent boundaries of the incoherent gain areas. It is important to note, the incoherent mobility is frequency independent. Furthermore, net gain in the case of $3\omega_0/2$ being typical for all the half sub-harmonics, facilitate two well-separated areas marked by I (bottom right; $F_{\text{dc}} > F_{\text{ac}}$) and II (upper left; $F_{\text{ac}} > F_{\text{dc}}$). This separation will be very important in future analysis. One should also note single net negative mobility area in the case of $\omega_0/2$. Finally, one should note absence of negative area of coherent mobility component in the case of fractional sub-harmonic. All of the presented diagrams provide a basic understanding, essentially important for the analysis under large signal gain model, as small-signal gain model may be used to determine conditions for the generation to start [3].

area of the type II biasing occurs for the biasing conditions when $|\mu_{\text{coh}}| > \mu_{\text{inc}}$, while in the area of type I biasing conditions, both components are negative ($\mu_{\text{coh}} < 0, \mu_{\text{inc}} < 0$).

The understanding of the differences under small-signal gain conditions is extremely important because, as already been discussed above, small-signal gain describes the generation from fluctuations (seeding) abilities. Another non-obvious advantage lies under possibility to separate phase-dependent coherent and phase-dependent incoherent components, under the small-signal gain mode linking the existence of them to two different processes parametric and Bloch gain respectively. Although such separation is not mathematically available in the large-signal gain model, one will soon notice, that all the above discussed features will have a significant effect.

The large signal gain case operates the Equation 4.2. The importance of the relative phase should be addressed first (phase difference between the AC pump and probe electric field of the frequency of interest). Several of the typical generated electric field strength - relative phase dependencies are presented in Figure 4.2 (colour depicts the \bar{P} value). In the figure colour indicated positive gain wherein $P < 0$ condition is satisfied and blank depicts no gain conditions ($P > 0$). Most simple dependence, typical to harmonics and half-harmonics is presented at Figure 4.2 (a) ($2\omega_0$ is taken for particular example). One can clearly distinct optimal phase (0.5π and 1.5π) which is probe electric field strength independent. Also there is a range of relative phase, wherein no generation is allowed at all. Both these findings is an fundamental proof of requirement of phase control possibility in the experimental setups. Within the particular example probe electric field strength up to $3E_{\text{cr}}$ is predicted. One should note that the largest power \bar{P} is achieved at considerably lower probe electric field strengths.

Turning to the Figure 4.2 (b) and (c) depicting $5\omega_0/3$ and $7\omega_0/5$ fractional sub-harmonics, typical for the majority of fractional sub-harmonics one should instantly note the differences, resulting in the formation of amplification islands. Under the presented biasing conditions, fractional sub-harmonics can not start amplification from negligibly small signal, as the probe electric field strength has to be larger than some threshold value. In order for the superlattice structure to start amplification, some external mechanism or factor has to make influence (this is depicted by the red arrow). After the probe electric field strength exceeds the threshold value, superlattice start amplification, until peak values are reached (green arrows). The formation of the amplification islands is found to be independent of the DC bias and can form even with the absence of the one. One should note the change of the periodicity of the formed islands, corresponding to the denominator of the fractional sub-harmonic. Having in mind the typical relative phase dependencies, further in this chapter (unless stated otherwise) we will proceed analysis on the optimal relative phase-shift.

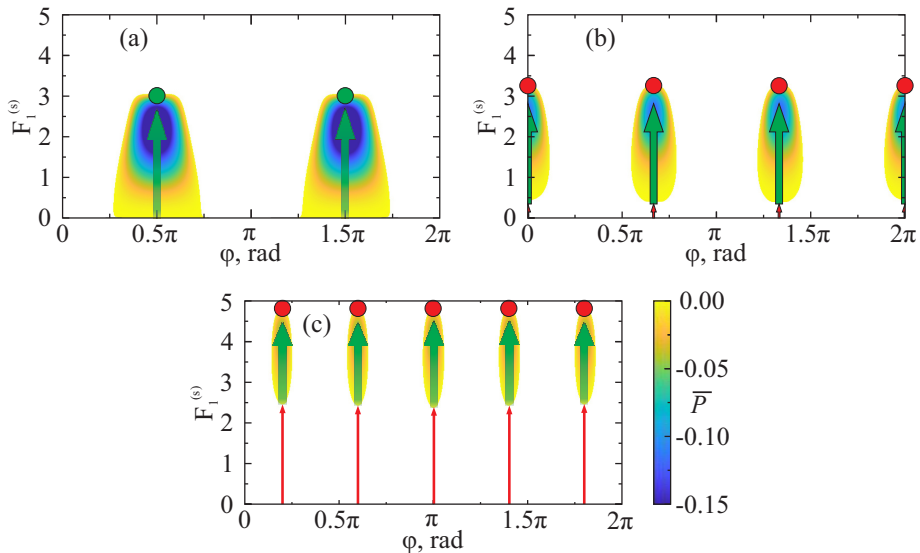


Figure 4.2: Exemplary dependencies of relative probe power on probe electric field strength and relative phase, calculated for several characteristic frequency ratios and fixed pump electric field strength components employing large signal gain model. (a) $\omega_1/\omega_0 = 2$, $F_{dc} = 0$, $F_{ac} = 5$. One can clearly see two separate generation/amplification areas, corresponding to $\varphi_{opt} = \pi/2$ and $3\pi/2$. Electric field strengths up to $3E_{cr}$ can be reached (see green circle, meaning generation is available, starting from negligibly small probe electric field strength). (b) $\omega_1/\omega_0 = 5/3$, $F_{dc} = 0$, $F_{ac} = 5$. Calculation based on large signal gain model results in negative values (amplification) at some optimal phases only after exceeding some threshold of the probe electric field strength. The process is marked by red circle (amplification, starting from large probe electric field strength is available). In order to achieve amplification in the superlattice, one should somehow supply probe electric field strength above the threshold (red arrow) and afterwards amplification onsets (green arrow). The areas of amplification are named "amplification islands". (c) $\omega_1/\omega_0 = 7/5$, $F_{dc} = 1$, $F_{ac} = 10$. Note the increase of the threshold with the increase of denominator and change of periodicity of the amplification islands. Colour indicates relative power $\bar{P} = P/P_0$ and blank areas depict areas of positive relative power (no generation or amplification) [3].

Starting from the half-harmonic $3\omega_0/2$ depicted at Figure 4.3 (A) represent maximal \bar{P} value for each set of biasing conditions F_{dc}, F_{ac} at the optimal relative phase shift. As have already been shown above, only two net gain mechanisms are possible: hybrid combination of coherent parametric gain and incoherent Bloch gain or pure parametric gain mechanism. In the analysed figure, the latter may be attributed to the area of type II biasing conditions. This is clearly depicted by the upper inset, representing probe-phase dependencies for the biasing condition marked by the red points. One can note the obvious

increase of the maximum probe electric field strength and generated power with the increase of the applied AC bias pump electric field. The generated power for the biasing conditions $(F_{\text{dc}}, F_{\text{ac}}) = (0.5, 4)$ is estimated to be of 3.2 mW at $E_1 \approx 9.7$ kV/cm.

Situation becomes different considering the fractional sub-harmonics. The typical example covering the fractional frequency of $5\omega_0/3$ is depicted at Figure 4.3 (B). Considering the already known information on the absence of the

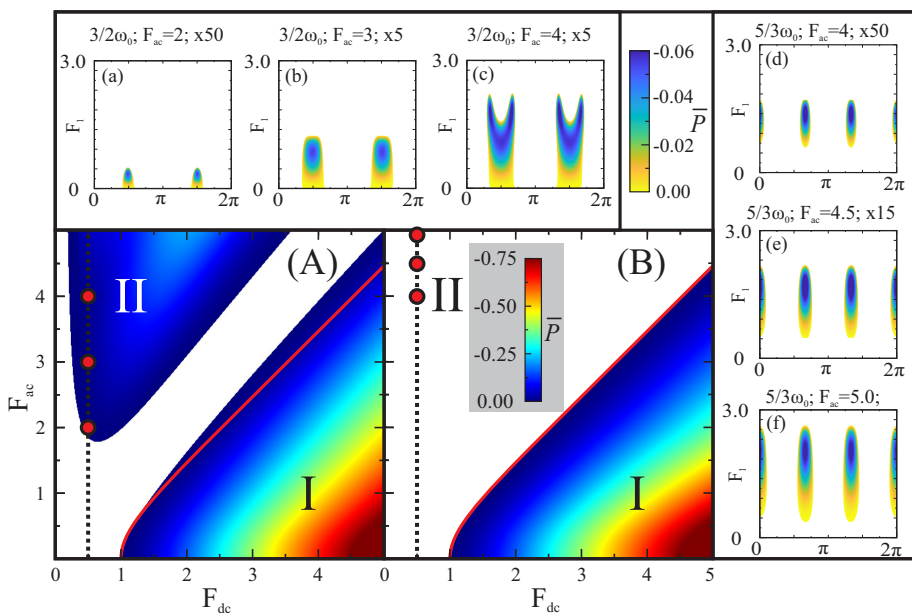


Figure 4.3: (A) Maximal available generation power for particular pump biasing conditions, calculated at optimal phase employing large signal gain method and $3\omega_0/2$ probe frequency (half sub-harmonic). Colour areas represent relative power \bar{P} and blank areas represent biasing conditions, wherein no gain is available. Black dashed line and red circles corresponding to type II biasing conditions further expanded in the upper inset (a) - (c), depicting relative power dependency on probe electric field strength and relative probe phase shift ($F_{\text{dc}} = 0.5$ and $F_{\text{ac}} = 2 : 1 : 4$). One should note the range of phases wherein no gain is available at all. This depicts the observed process has a pure parametric nature. One should also note significant pump AC threshold ($F_{\text{ac}} > 2$) which has to be overcome in order to get into pure parametric generation regime. (B) Maximal available generation power for particular pump biasing conditions, calculated at optimal phase employing large signal gain method and $5\omega_0/3$ probe frequency (fractional sub-harmonic). Black dashed line and red circles corresponding to type II biasing conditions further expanded in the right inset (d) - (f), depicting relative power dependency on probe electric field strength and on the relative probe phase shift ($F_{\text{dc}} = 0.5$ and $F_{\text{ac}} = 4 : 0.5 : 5$). Formation of amplification island may be observed, meaning no generation is available from small probe signal [3].

coherent gain component in the case of fractional sub-harmonics resulting in no signal generation in the area of type II biasing conditions (marked blank as Figure 4.3 depict maximal power achievable from small probe signal i.e. generation). Amplification after reaching specific threshold probe electric field strength is available in the form of amplification islands as depicted in the right inset. As example, for the biasing conditions $(F_{dc}, F_{ac}) = (0.5, 4)$ represented in Figure 4.3 (d), amplification starts at $F_1 \approx 0.75$ extending up to $F_1 \approx 2$. At this particular example power up to 3.3 mW can be reached at probe electric field strength $E_1 \approx 8.8$ kV/cm, being comparable to the power levels demonstrated for the same biasing conditions at $3\omega_0/2$ frequencies. Naturally the amplification threshold of the island increases with an increase of the denominator of the fractional frequency.

Totally different picture may be seen for the type I biasing conditions ($F_{dc} > F_{ac}$). Under these conditions, significant influence of the incoherent processes takes place. As the numerical simulations are performed with the above described superlattice structure, there are no formal limitation to assign the observed incoherency to the Bloch gain processes. To analyse type I biasing conditions the case of the $\omega_0/2$ is presented at Figure 4.4. First of all one should note that the particular picture depicts maximal power (Figure 4.4 (A) left) and probe electric field strength (Figure 4.4 (A) right), which can be achieved from small probe signal (generation). The obvious difference between the both distributions should be noted. One should also note the differences of the type I biasing areas as seen at Figure 4.4 and Figure 4.3. Basically, the type I biasing conditions area was found to be almost identical to all the cases as depicted in Figure 4.3 making the case of $\omega_0/2$ comparably unique. The physical results of such uniqueness will be separately discussed below.

By applying considerably high DC bias ($F_{dc} = 4$) and sweeping the AC bias one can clearly determine the transition from pure phase-independent Bloch gain to phase-dependent parametric gain (see upper inset of Figure 4.4). Notably, Bloch generation exists even without AC pump, resulting in a domination competition of the two gain mechanisms in the range of moderate AC pump bias. Bloch mechanism being dominating at low AC pump bias, diminishes up until pure parametric gain takes over. Here and afterwards, we call pure parametric gain the effect when no gain is available at some relative phase interval (see Figure 4.4 (f)). It is important to note, that for the majority of frequencies analysed, the pure parametric gain is available in a very small interval of biasing conditions, thus, case of small Bloch influence is more likely to be determined (see Figure 4.4 (e)). It the discrepancies of the $\omega_0/2$ providing a significant range of biasing conditions featured with pure parametric gain.

In the case of type I biasing, the generated power is considerably larger compared to the pure parametric generation achieved within type II biasing conditions. The most powerful output is naturally expected in the case of $\omega_0/2$.

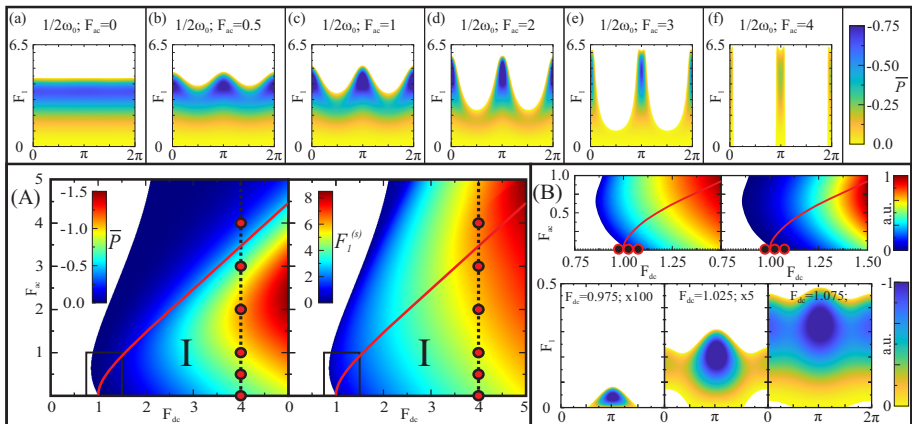


Figure 4.4: (A) Maximal available generation power (left) and electric field strength (right) for particular pump biasing conditions, calculated at optimal phase employing large signal gain method and $\omega_0/2$ probe frequency (half sub-harmonic). Colour areas represent relative power \bar{P} or electric field strength normalised to Esaki-Tsu critical electric field $F_1^{(s)}$ and blank areas represent generation, wherein no gain is available. Black dashed line and red circles corresponding to type I biasing conditions further expanded in the upper inset (a) - (f), depicting relative power dependency on probe electric field strength and relative probe shift ($F_{dc} = 4$ and $F_{ac} = 0 : 1 : 4$). Red lines represent boundaries of the incoherent gain calculated by the small signal gain model. The inset clearly expose the coexistence of phase-independent Bloch and phase-dependent parametric mechanism. The dominating process changes with the increase of the pump AC electric field: being dominant at low AC bias, Bloch gain (a) surrenders domination to the parametric gain, up until pure parametric process is reached (f). One should note the pure parametric process is achieved after crossing the incoherent gain boundary. Moreover, pure parametric gain conditions as will be shown below, can be achieved specifically in the case of $\omega_0/2$ frequency, attributed to specific distribution, analysed within small signal gain conditions (see Figure 4.1). (B) The upper part represent zoomed view of the Figure 4.4 (A), located at low AC bias and $F_{dc} \approx 1$. Three red circles correspond to $F_{ac} = 10^{-3}$ and F_{dc} values that are slightly above and below critical electrical field strength and are intended to depict evolution of the gain processes under small DC electric field change. One should note peculiarities of such small range transition from pure parametric to Bloch gain. The $\omega_0/2$ case is the only one featured with such transition possibility [3].

For example, the use of the pump electric field strengths $(F_{dc}, F_{ac}) = (4, 2)$ corresponding to Figure 4.4 (d), results in the power of 257 mW and in the maximum generated signal of 31.5 kV/cm ($F_1 \approx 5.75$).

Unique feature of the $\omega_0/2$, appearing due to specific small signal coherent gain component (see middle column, middle row picture of Figure 4.1) is anomalously low threshold of conversion between Bloch and pure parametric

generation modes, appearing via small ($\Delta F_{\text{dc}} < 10^{-3}$) DC pump electric field shift depicted at Figure 4.4 (B). Such a small electric field shift supplements simple switching between different generation mechanisms, keeping the AC pump negligibly small. Furthermore, this small interval of biasing conditions is the only case wherein pure parametric generation is available from extremely small AC pump electric field values, inlining an analogy to the seeding based optically pumped parametric oscillators. This effect is to the large contrast of other harmonic and half-harmonic frequencies wherein pure parametric oscillation is allowed only within type II biasing conditions.

Proceeding with the type I biasing conditions, one should analyse the fractional sub-harmonics. One should remember that unlike the other type of frequencies, the fractional sub-harmonics under small signal gain model resulted in the absence of the coherent mobility components. Making a direct analogue, one would expect no phase-relative dependencies transferred to the large signal gain model. Phase - probe electric field strength dependencies, corresponding to the biasing conditions marked by red circles in Figure 4.4 clearly reveal the coexistence of the parametric and Bloch gains (see Figure 4.5). Importantly, this applies to both presented $5\omega_0/3$ and $5\omega_0/4$ comprising odd and even denominators (the differences between these types of fractional sub-harmonics are not analysed in detail within the current scope). Such quantitative analysis allows to make an assumption of the formation of parametric amplification island, forming on considerably large AC pump bias. Due to the saturation of the Bloch at quite large probe signal electric field strengths [163, 170], overlapping of the parametric and Bloch gain processes is expected resulting in the hybridization of the net gain within the biasing conditions, resulting in a formation amplification island. This in turn results in the appearance of the phase-dependency of the net gain. This simple approach, despite being quite illuminating, is far from completion due to the complexity of the hybrid generation mode appearing not to be a direct overlap of two uncombined processes and. One of the concern includes different probe electric field amplitude saturation values for the hybrid mode and Bloch gain itself.

Employing the same biasing conditions as for the above described cases, $(F_{\text{dc}}, F_{\text{ac}}) = (4, 2)$ to the case of $5\omega_0/3$ we estimated the maximal generated power to reach 43.2 mW and the maximal achievable probe electric field strength ≈ 20 kV/cm. The power generated for the fractional sub-harmonic is expectedly lower compared to the above discussed case of sub-harmonics, however, it is still an order larger compared to the case of pure parametric amplification within the amplification islands in the type I biasing conditions.

As have been discussed above, the amplification via amplification island may be started by igniting the probe electric field to reach the threshold electric field strength values. Some external process was suggested to achieve these conditions. However, ignition process by changing the biasing conditions is

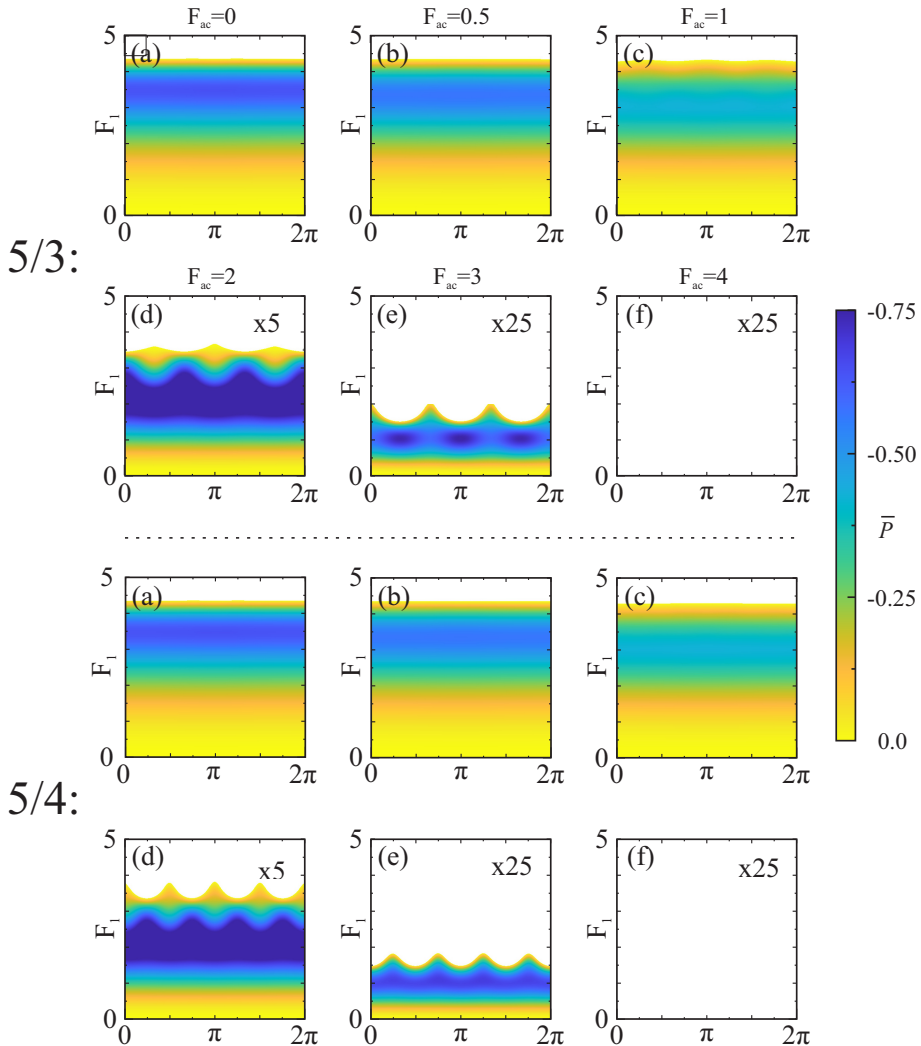


Figure 4.5: Transition of the phase-independent Bloch gain to the hybrid process of Bloch and parametric gain with an increase of AC pump electric field strength ($F_{dc} = 4, F_{ac} = 0 : 1 : 4$). The presented examples are given for the case of $5\omega_0/3$ and $5\omega_0/4$ frequencies by presenting relative probe power dependency on relative phase and probe electric field strength. Colour represent conditions corresponding to negative relative power meaning generation is allowed, while blank means relative power is positive, thus, no gain is expected. One should note the transition from pure Bloch to parametric process. Also pure parametric mode can not be achieved under type I biasing condition, as this was shown to be the feature of $\omega_0/2$ solely. Such approach allows to claim formation of parametric amplification islands. This is additionally supplemented by the fact one may not achieve generation at high AC pump ($F_{ac} > 4$) [3].

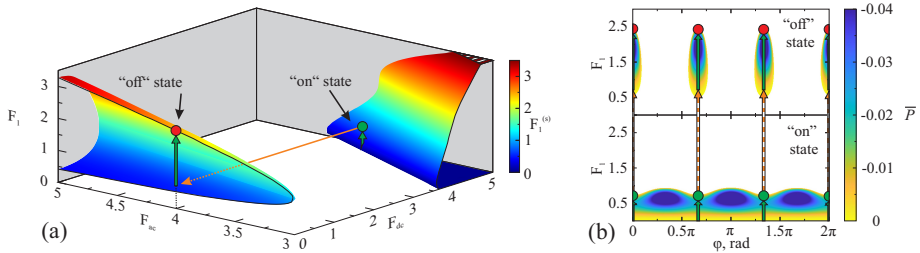


Figure 4.6: (a) Probe electric field strength dependency on the applied pump DC, pump AC, and probe electric field strengths depicted as the boundaries for the gain areas. Case of $5\omega_0/3$ frequency is presented, illustrating the proposed ignition process by switching the DC pump electric field. The orange arrow represents transition from the "on" state ($F_{dc} = 4.7, F_{ac} = 4$; supplementing generation from negligibly small probe signal) to "off" state ($F_{dc} = 0, F_{ac} = 4$), representing amplification island with the threshold lower than probe electric field strength achievable within "on" state conditions. This allows to reach pure parametric amplification without applying external AC ignition. b) Probe relative phase dependency on the probe electric field strength and relative phase for the internal ignition process via DC switching. Green arrows depict generation/amplification occurring inside the superlattice and dashed orange line represent transfer between the two above-described states [3].

also feasible. The advantages of this process is that it does not require any additional setup components. The process is depicted at Figure 4.6. Two biasing conditions are observed. In the "on" condition (Figure 4.6 (B) bottom part), generation from the small signal is allowed and will proceed to some specific electric field strength value. This value is above the threshold for the amplification island at the "off" state (Figure 4.6 (B) upper part), wherein pure parametric generation, at higher electric field strengths may be achieved.

In the particular case, depicted at Figure 4.6, $5\omega_0/3$ frequency is taken as example. The "on" state corresponds to $(F_{dc}, F_{ac}) = (4.7, 4)$ biasing conditions, while the "off" state corresponds to $(F_{dc}, F_{ac}) = (0, 4)$ biasing conditions. One should also note the "on" state is employed in non-optimal relative phase, as there is a $\pi/3$ optimal phase shift between the states. In the "on" state probe electric field can reach strength exceeding $0.5E_{cr}$, while in the "off" state probe electric field strength of $2.5E_{cr}$ is reachable. Another advantage, is the single use requirement - once probe electric field was ignited to operate in the interval of amplification island, superlattice structure is expected to be self-sustaining i.e. one should not use DC switching algorithm periodically unless the probe electric field strength went below the threshold electric field strength.

4.2. Influence of the Large Signal Gain Model on the Non-Degenerate Gain Processes

Analysis of the non-degenerate gain processes in basics is very similar to the degenerate processes, described in the previous chapter. However, it adds even more variables, making analysis more complicated and longer. Several peculiarities that have been noticed are worth noticing. To start with, one should consider the case of two different fractional sub-harmonics $\omega_1 = p_1\omega_0/q_1$ and $\omega_2 = p_2\omega_0/q_2$. As have been described above processes covered by $\omega_1 + \omega_2 = n_+\omega_0$ or $\omega_1 - \omega_2 = n_-\omega_0$ can proceed. One can represent the time-dependent phases in the form of

$$\omega_1 t + \varphi_1 = \frac{(\omega_1 + \omega_2)t + (\omega_1 - \omega_2)t}{2} + \varphi_1 = \left(\frac{n_+ + n_-}{2}\right)\omega_0 t + \varphi_1 \quad (4.6)$$

and

$$\omega_2 t + \varphi_2 = \frac{(\omega_1 + \omega_2)t - (\omega_1 - \omega_2)t}{2} + \varphi_2 = \left(\frac{n_+ - n_-}{2}\right)\omega_0 t + \varphi_2. \quad (4.7)$$

Inserting these equations into the relative power Equations 4.3 and 4.4 and assuming the electric field strengths equal, one would achieve the same degenerate process equations with the corresponding results discussed in the previous chapter. Within the quasistatic approximation non-degenerate large-signal gain effects can be simplified to the several separate degenerate processes. This individual case will not be further analysed aside of the common analysis. In this part the effect on the electric field strength of one of the probes F_1 to the predefined set of parameters is evaluated. The set includes, DC (F_{dc}) and AC (F_{ac}) biasing conditions, frequencies (ω_1, ω_2) and relative phase-shifts (φ_1, φ_2) of both probes, electric field strength of the second probe (F_2). Such approach allows us for now neglect the differences between the up- and down-conversion processes. Due to the large amount of variables, current stage of analysis includes only two non-degenerate processes: $4/3 + 8/3$ serving an example of fractional sub-harmonics gain and $1/2 + 3/2$ serving an example for half sub-harmonics. To avoid misunderstanding, here and beyond the lower frequency be labelled as probe 1, and higher will be indicated as probe 2.

Figure 4.7 depicts the change of the dependency of the probe 1 relative power on relative phase-shift and probe 1 electric field strength for different probe 2 relative phase shift. The process analysed is $4/3 + 8/3$, and the biasing conditions are $F_{dc} = 4, F_{ac} = 3, F_2 = 2$. As is the pictures above, coloured areas depict conditions under which probe 1 will be amplified and blank areas represent conditions wherein amplification is not possible. One should compare the presented figure with the degenerate case depicted in the right inset of Figure 4.3. First of all, in the degenerate case Π -symmetry is expected for any

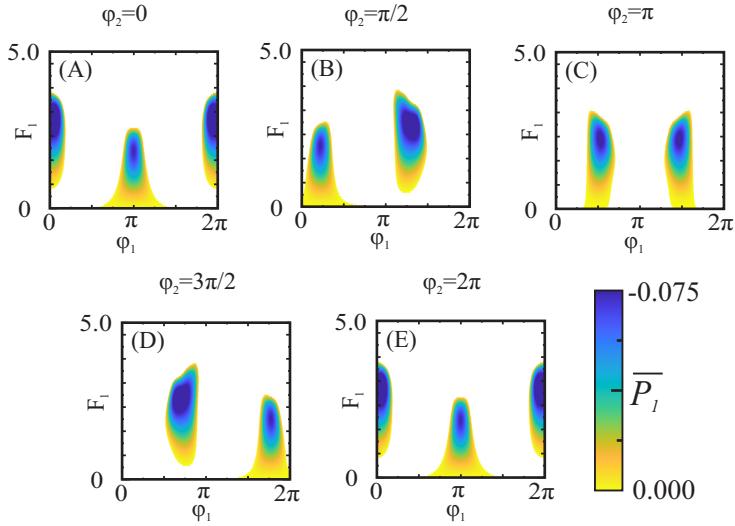


Figure 4.7: Probe 1 relative power dependency on relative phase 1 and probe 1 electric field strength for the case of different relative probe 2 phases. Non-degenerate process of $8/3+4/3$ is analysed. Constant biasing conditions $F_{dc} = 4; F_{ac} = 3; F_2 = 2$. Coloured area depict the set of conditions wherein generation or amplification is available and blank areas depict set of conditions with positive relative probe 1 power resulting in absorption. One should note the appearance the loss of symmetry of the dependencies, which is to strong difference with the previously analysed degenerate processes. One should also note the existence of both area types in one dependency: generation from negligibly small probe signal and formation of amplification islands.

of the cases. It is considerably obvious to predict that in the non-degenerate case, such symmetry will break except for some specific cases. This conclusion is supplemented by the proposed figure. As one may note the amplification islands typical for the degenerate case change their shape. Moreover, in contrary to the previously analysed degenerate process relations, one may note the formation of generation areas and amplification islands, occurring in same power-phase dependency. This means for the non-degenerate case one can achieve generation of the fractional sub-harmonic from negligibly small probe signal under type II biasing conditions. This is an exclusively important finding, explaining the experimental results of the first section, wherein the generation was observed under considerably low DC bias and high AC bias (type II biasing conditions).

Differences between the degenerate and non-degenerate processes are revealed at Figure 4.8 depicting maximal achievable relative probe 1 power (P_1) for particular pump and probe 2 electric field strengths. In particular example, both phases (φ_1, φ_2) are kept optimal for maximal relative power. The figure discloses the case of non-degenerate fractional sub-harmonic process ($4/3+8/3$). The upper inset of the graph discloses probe 1 electric field strength - phase

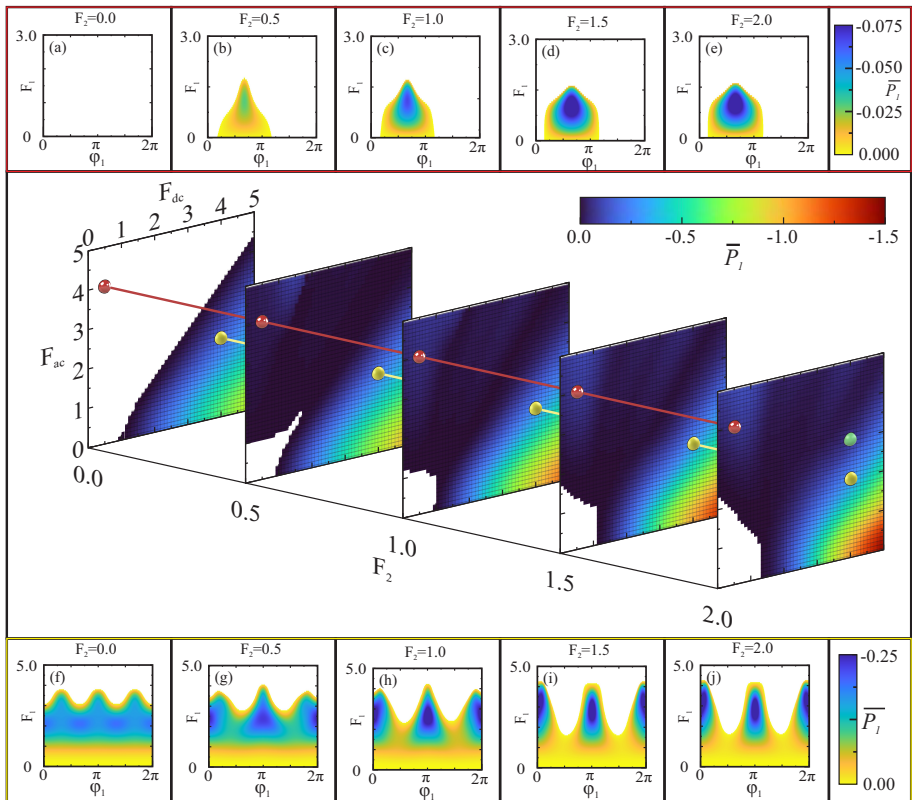


Figure 4.8: Main figure (center): maximal probe 1 relative power dependency on the pump biasing conditions and probe 2 electric field strength for the case of $4/3+8/3$ non-degenerate process. Each set of conditions correspond to the maximal achievable probe 1 power at optimal probe 1 and probe 2 relative phase. Coloured area depict conditions when generation is available, while blank areas depict conditions when generation is absent. Upper insets ((a)-(e)): probe 1 relative power dependency on the probe 1 relative phase and electric field strength for different probe 2 electric field strengths. Biasing conditions correspond to the red dots on the central figure ($F_{dc} = 0.5; F_{ac} = 4; F_2 = 0 : 0.5 : 2$ - type II biasing conditions). One should note that in the contrary to the case of fractional sub-harmonics in the degenerate process, the formation of generation area can be observed, supporting the experimental results of chapter 3. Bottom insets ((f)-(j)): probe 1 relative power dependency on the probe 1 relative phase and electric field strength for different probe 2 electric field strengths. Biasing conditions correspond to the yellow dots on the central figure ($F_{dc} = 4; F_{ac} = 3; F_2 = 0 : 0.5 : 2$ - type I biasing conditions). One should note the persistence of the coexistence of two gain mechanisms and the increase of the parametric gain influence with the increase of probe 2 electric field strength. Green dot on the main figure correspond to the biasing conditions depicted at Figure 4.7.

dependencies depicted by red spheres on the main graph, corresponding to type II biasing conditions ($F_{ac} > F_{dc}$). Confirming the results of Figure 4.7 one may note the possibility to start fractional sub-harmonic generation under type II biasing conditions. The generation process being phase-dependent reveals the parametric nature of the observed generation process. On the other hand, bottom inset of Figure 4.8 reveals changes of the probe 1 field strength - phase dependencies for the case of non-degenerate process in the case of biasing type I conditions ($F_{dc} > F_{ac}$). The dependencies depicted in the inset correspond to the position of yellow spheres on the main figure. One may note, that the above discussed coexistent of two generation mechanisms (Bloch and parametric) remains in the case of non-degenerate process. Moreover, the dependencies seem to be more affected by the domination of the parametric gain mechanism with the increase of probe 2 electric field strength (see Figure 4.8 (f)-(j)) highlighting an increased necessity of the optimal phase selection for the successful conduction of the experiment.

The increased influence of the parametric generation is found to remain in the case of non-degenerate half-harmonic generation process (see Figure 4.9 (a)). Even more interesting for the analysis is the power transfer between probes revealed via analysis of the relative power of each of the probes and total power, being sum of the latter. Figure 4.9 (b) left depict the maximal achievable probe 1 relative power and corresponding probe 2 relative power is depicted second left of the figure. One may note that under particular range of biasing conditions relative power of probe 2 is either negative (representing emission at probe 2 frequency) or positive (representing absorption at probe 2 frequency). Obviously this reflects on the net relative power of both probes, allowing to distinguish three zones as depicted on the most right graph of the figure.

Zone 1 correlates to the set of biasing conditions wherein the relative power of both probes is negative ($\overline{P_1} < 0, \overline{P_2} < 0$) resulting in generation of both frequencies. At this point of research it is impossible to determine the interchange processes between two probe electric fields, however, as both of them are generating (emitting energy) one can claim with firm confidence that the energy for the generation is taken from the pump. Zone 2 covers the range of biasing conditions wherein probe 1 is in generation mode (emitting energy) and probe 2 is in absorption mode, but probe 1 emits more than probe 2 absorbs $\overline{P_1} < 0, \overline{P_2} > 0, |\overline{P_1}| > |\overline{P_2}|$. Under these conditions, energy absorbed by probe 2 is not enough for the probe 1 to emit, thus, one can claim that the power for probe 1 is supplied both by probe 2 and pump electric field. Finally, zone 3 represents conditions when probe 1 emits less power than is absorbed by probe 2 $\overline{P_1} < 0, \overline{P_2} > 0, |\overline{P_1}| < |\overline{P_2}|$, showing that all the power for the generation of probe 1 may be supplied solely by the probe 2. This conclusion is also supplemented by the fact that no generation is available in the absence

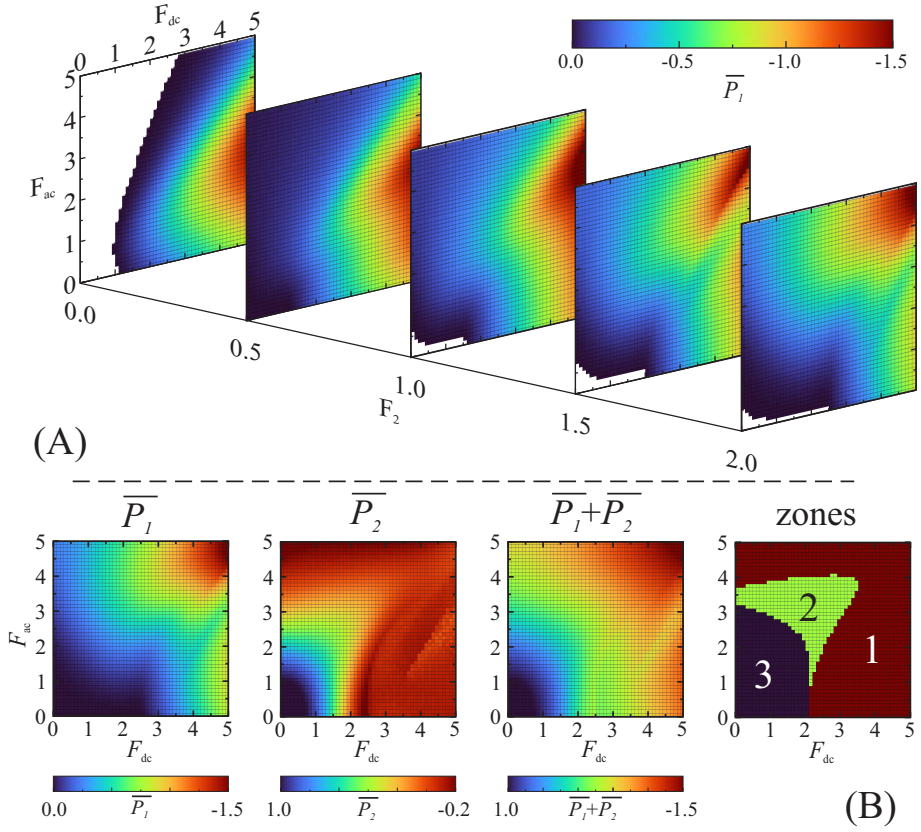


Figure 4.9: (A): Maximal probe 1 relative power dependency on the pump biasing conditions and probe 2 electric field strength for the case of $1/2+3/2$ non-degenerate process. Each set of conditions correspond to the maximal achievable probe 1 power at optimal probe 1 and probe 2 relative phase. Coloured area depict conditions when generation is available, while blank areas depict conditions when generation is absent. Note the formation of the increasing generation area with the increase of the probe 2 electric field strength. (B): The leftmost graph corresponds to the maximal probe 1 relative power for the case of $F_2 = 2$, the second left graph depict the probe 2 relative power dependency on the pump electric field strength, corresponding to the probe 1 maximal relative power conditions. Note the existence of energy absorbing positive relative power area. The third graph depict the total relative power of the pronounced non-degenerate process, being the sum of the two latter. The effect of both relative powers result in formation of three different regions, representing possible ways of the energy exchange during the process for particular set of biasing conditions. The areas are depicted at the most right figure. One would found further discussion and information on the matter in text.

of probe 2. On the other hand, in the case of biasing conditions, covered by zone 3, electric field of probe 2 may be employed as a controlling element to deliver pump energy to the probe 1. Further analysis is required for clarification,

which is not covered in the current scope.

Summarizing, following findings can be underlined:

- Importance of proper probe electric field phase selection was addressed, revealing the existence of optimal relative phase, supplementing significantly larger gain in comparison to the non-optimal relative phase, which under several biasing conditions may result in the total absence of gain.
- Formation of the amplification islands have been shown, wherein amplification from the threshold probe electric field strength is allowed for specific selection of biasing conditions and frequencies.
- Coexistence of phase-independent Bloch gain and phase-dependent parametric gain may be observed under DC bias exceeding critical Esaki-Tsu electric field conditions. The dominance between the two processes changes with the change of AC pump electric field strength.
- For the case of $\omega_0/2$ frequency generated by degenerate process, pure parametric mode can be achieved at high AC pump electric field strength (effect unavailable for any other frequency).
- Possibility to achieve pure parametric gain for any other frequency was suggested by placing the superlattice into amplification island mode via DC switch, allowing to achieve pure parametric generation without applying the external AC source of particular frequency to overcome the threshold electric field strength.
- For the case of non-degenerate process, generation possibility (from negligibly small probe signal) of fractional sub-harmonics in the area of $F_{ac} > F_{dc}$ is available.

These findings allow to formulate the following statements for defence:

- **Statement 3:** High-frequency gain in sub-critically doped semiconductor quantum superlattices is coexistence of Bloch and parametric mechanisms. The interplay and contribution of these gain mechanisms can be adjusted by the sweeping the pump strength and leveraging a proper phase between the pump and strong probe electric fields.
- **Statement 4:** Transition of the dominating gain mechanism from the Bloch to the parametric one in sub-critically doped semiconductor superlattices with an increase of probe electric field is conserved in both degenerate and non-degenerate gain processes. In case of strong signal and two probe frequencies in the parametric gain, the energy can be transferred not only from the bias, but also between the probes.

5. Signatures of Stable Bloch Gain Observed via Hybrid Bloch Plasmon Modes in Injector-Controlled Strongly-Coupled GaAs/AlGaAs Superlattice

It is well known that the operational physics of any type of laser employs population inversion in the system aiming to generate a coherent stimulated emission [171,172]. Consequently, the main focus in the laser design is to find the best ways to achieve such inversion as the light gain is directly proportional to the difference in the occupation level as shown in Figure 5.1 (a) [173].

However, this paradigm can be broken if the energy levels are inhomogeneously broadened which often happens in real systems due to the scattering effects as depicted in Figure 5.1 (a). In such circumstances, due to the blurring of both energy levels and different carrier occupation probabilities, the gain characteristics are extended, and the gain then displays a so-called dispersive feature via strong frequency dependence with a change of the sign around the resonance frequency. In other words, in this situation, for a given pair of levels, the incident light with a red-shifted frequency exhibits gain, while the blue-shifted illumination frequency exposes absorption. It deserves to be underlined that the total occupancy of both levels is approximately equal, i. e. there is no population inversion in this case (see Figure 5.1 (b)).

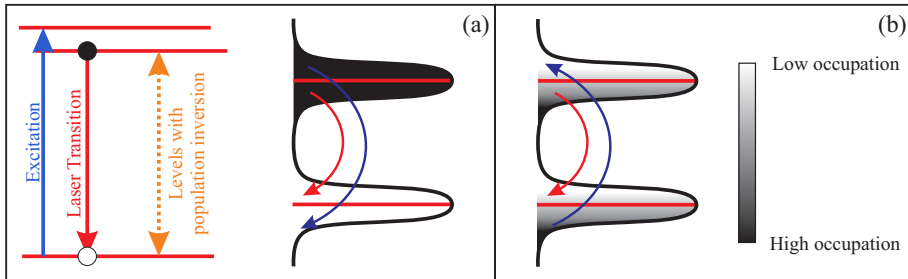


Figure 5.1: (a) Classical laser operation via inversion of the charge carriers – three energy level schematics (left panel) and broadened energy levels due to the scattering (right panel). (b) Inversionless gain appearing due to the uneven charge carrier occupation of each energy level [15].

To specify the aforesaid situation to semiconductor quantum superlattices, the quantum levels are Wannier–Stark states that are equally spaced in energy and have an equal occupation in the superlattice. The resonance frequency in this case is the Bloch frequency. This particular situation which possibly can be realized in superlattices attracts wide attention and long-standing scientific debate [174–177], whether inversionless gain – so-called – Bloch gain – can be possible to resolve. The main issue is to realize a homogenous electric field in

the superlattice structure.

To circumvent this challenging obstacle a large variety of approaches – including technological means and experimental tricks – were engaged and tested. Technologically, modification of unstable gain profile can be brought about, for instance, by placing periodic highly-doped layers in SL – creating thus, so-called super-superlattice [178, 179]. Such structures illuminated with a free-electron laser enable to observe a frequency-dependent crossover from loss to gain – the gain below the Bloch frequency and absorption above it – can be also explicated in a specially designed quantum cascade structure for infrared [15] illustrating the effect via tuning the laser operation in conditions from weak to vanishing population inversion. The problem of electric field inhomogeneity can also be resolved by applying special experimental techniques, e.g., a time-domain approach in studying the effect within a very short time scale, e.g., within 10 ps, until the homogeneity of the electric field is not disturbed by the redistribution of optically excited carriers [177]. Some experimental signatures of the dispersive Bloch gain were demonstrated employing time-domain THz electro-optic sampling technique in optically excited undoped SLs [180]. The aforementioned approaches rely on sequential tunneling transport regimes in weakly coupled structures.

In strongly-coupled SLs including conventional Bloch gain miniband transport regime often suffers from the occurrence of the electrical instabilities like moving high-electric field domains of the Gunn origin [71, 77] i.e., the SL becomes unstable resulting to the suppression of the gain. As is revealed in previous chapters, the coupling of the incident microwave into the superlattice converts the electromagnetic wave into a slow plasmon-like electrostatic wave which propagates in the structure providing a significant enhancement of the gain coefficient reaching the values of 10^4 cm^{-1} [A1]. As theory predicts [131], this electrostatic wave can exhibit remarkable features – it can couple to the Bloch oscillating electrons and longitudinal optical phonons, expressing a sharp electric field-dependent transition from coupled plasmon-phonon to Bloch-phonon modes.

In this part of the study, we resolved the issue of the inhomogeneous electric field via the placement of the silicon-doped strongly-coupled GaAs/AlGaAs superlattice between the specially designed asymmetric injecting/blocking contacts. It allowed the demonstration injector-controlled broadband amplifier based on a stable Bloch gain manifesting itself via hybrid Bloch-plasmon-phononic modes at room temperature. Moreover, the experiments in microwave range within 8.4 GHz–11.5 GHz allowed to discriminate plasmon damping, hybrid Bloch-plasmon-phonon related gain in the miniband regime confirming thus, theoretical prediction by Avik W. Ghosh and co-workers [131]. In other words, we evidenced experimentally so-called Epshtein modes [181] for the first time. Furthermore, it is shown that the extremely

higher electric field-induced interminiband-related electron-hopping transport (non-resonant tunneling) [182] still preserves the high-frequency gain. It is indicated that the gain can reach values of 1200 cm^{-1} and thus, could serve as a promising avenue in further development of room temperature sub-THz–THz amplifiers based on quantum semiconductor superlattice.

The superlattice sample was of the same architecture as in previous experimental studies. For the sake of clarity and convenience, its design with a special underline of asymmetric contact features is presented and specified in Figure 5.2.

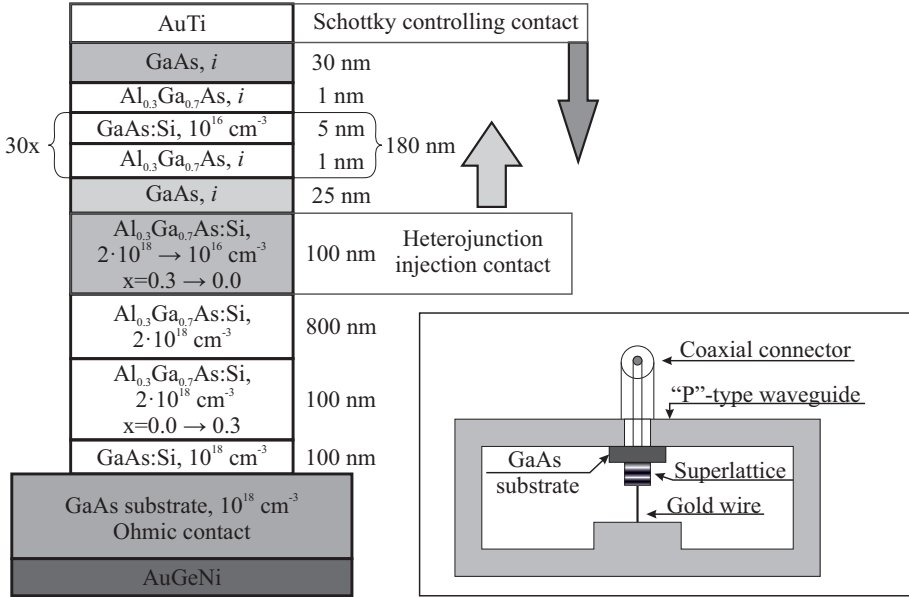


Figure 5.2: The architecture of the sample for the Bloch gain experiment. Wide miniband GaAs/AlGaAs superlattice structure is placed between Au/Ti top contact (Schottky barrier) and GaAs/AlGaAs heterojunction barrier with variable Al content. In the forward-biased SL, the latter one serves for carrier injection, while the Schottky contact – is the controlling electrode; in the reverse bias, their roles are exchanged – Schottky contact plays the role of the injecting contact, while heterojunction provides the control over transport in the entirely depleted SL. Inset: sample mounting scheme in P-type waveguide: golden wire allows coupling of the incident microwave radiation into the mesa of the sample.

It is shown that inversionless gain can be observed in a two-level system due to the broadened optical transition width, allowing for phase-lock uneven distribution of charge carrier distribution on each energy level (see Figure 5.3 (a)), for instance, in quantum cascade structures [15, 16]. The excitation of the Bloch oscillations in optical experiments observed by several independent research groups [5–7, 65, 127], was found to manifest strong sensitivity to excitation conditions, especially, on the spectral position or shape of the exciting

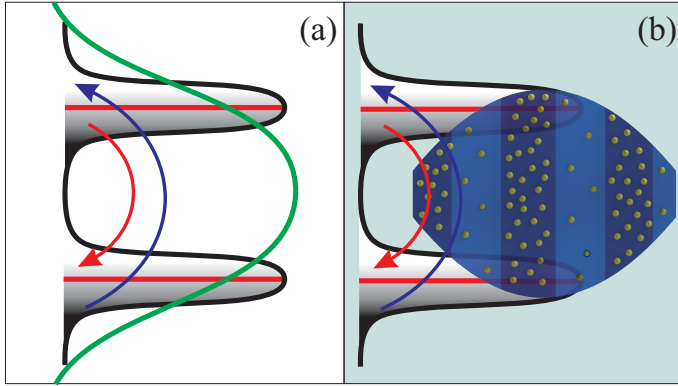


Figure 5.3: Different coupling mechanisms leading to the Bloch gain. (a) Inversionless Bloch gain and coupling via broadened laser excitation spectra (green line). Note the "inversionlessness" featured due to the uneven distribution of the charge carriers on one energy level. (b) Inversionless Bloch gain wherein coupling is featured by the plasmonic mode resulting in plasmonic phase-locking and hybridized Bloch-plasmon (Epshtein) mode. This coupling method corresponds to the light green zone biasing conditions depicted below.

laser, leading to simultaneous excitation of several neighbouring Wannier-Stark ladders [183–185].

It is worth highlighting that in optical experiments, the Bloch wavepackets are excited via spanning the Wannier-Stark levels by a spectrally-broad femtosecond laser as schematically depicted in Figure 5.3 leading to the phase locking between the incident light and intraband polarization in the biased superlattice [6, 184]. In contrast to optical experiments, our approach here is exclusively electrical and is based on the excitation of an electrostatic wave in AC and DC electric fields driven quantum semiconductor superlattice. As was indicated in the previous chapters, the slow plasmonic wave is excited in the structure and can serve as a coupling mechanism between the Wannier-Stark states. Moreover, the coupling itself changes the properties of the propagating wave which experiences transformation into a hybrid Bloch-plasmon mode (see Figure 5.3(b)).

The signal amplification induced in the superlattice operating under NDV regime exhibits a resonant nature [83] and depends on so-called electric field-dependent transit angle

$$\theta(F) = \omega T_L = \frac{\omega L}{v(E)} = \theta_0 \frac{1 + F^2}{F}, \quad (5.1)$$

where $T_L = L/v_d$ is the electron transit time, ω labels oscillation frequency, L stands for the sample length, $\theta_0 = \omega L/v_p$, and v_p is the maximal miniband velocity. When θ approaches zero, amplification is absent however, amplifi-

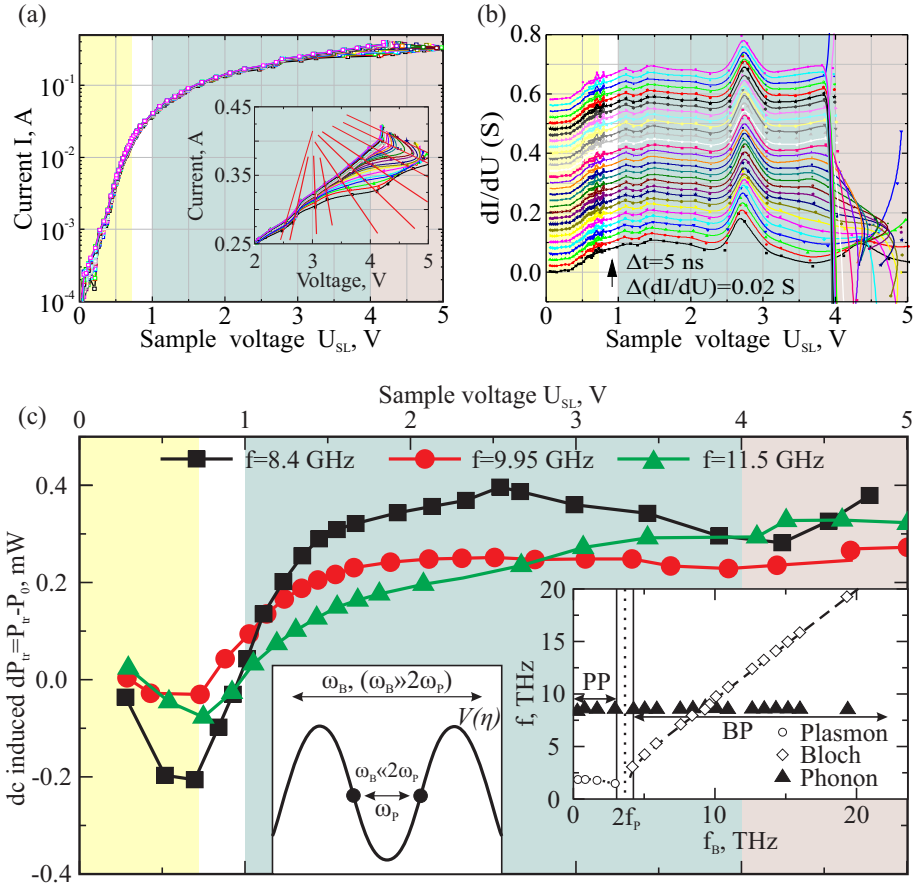


Figure 5.4: Panel (a) I-V characteristics of the semiconductor superlattice measured by application of DC pulses of nanosecond duration and data recording after every 5 ns. Inset: enlarged part of the I-V dependence to illustrate the appearance of the Wannier-Stark states with the increasing bias. Red lines serve as a guide for an eye to indicate induced Wannier-Stark levels (see Figure 1.5). Panel (b) – conductivity extracted from the I-V measurement (shifted for clarity in the y-axis). Note a spike around 2.7 V which is probably related to the EL2 defect in GaAs and unstable region above 4 V. In both graphs differently coloured areas correspond to the different gain mechanisms: light yellow - plasmonic absorption, light green - Wannier-Stark – Bloch gain, light brown - interminiband tunneling-based gain. Panel (c) – gain as a function of the applied voltage. Note plasma-related absorption in the Ohmic region and stable Bloch gain in the remainder part of the characteristics. Left inset: schematics of Bloch oscillations in a plasmonic potential; right inset: illustration of coexistence of the coupled plasmonic-Bloch-phonon modes in semiconductor superlattices according to A. W. Ghosh et al [131].

cation can arise with the increase of θ . In the case of strong electric fields ($F \gg 1$), the equation experiences modification so that θ becomes linearly pro-

portional to both, frequency, ω and, the electric field strength, F . Therefore, if the DC electric field profile is close to uniform, the gain can be expected, and its features, according to Equation 5.1, can be examined either varying the frequency or the electric field strength.

The same setup and wave-guide-based positioning technique was employed, as discussed in Section 2.1. Initially, to characterize the sample, the I-V characteristics were measured by applying nanosecond time-scale DC pulses allowing thus, to analyse the evolution of the processes by changing the time of data collection from the leading edge of the pulse by 5 ns each time up to 150 ns (see Figure 5.4(a)). As one can see, no distinct peculiarities are observed below 2 V, and the curves overlap each other. With further increase of the voltage, the curves start to slightly deviate from each other, and begin to saturate, while at higher voltages, exceeding 4 V, notable discrepancies between the curves are observable as the superlattice becomes unstable. In particular, it is strongly pronounced in the conductivity dependence given in Figure 5.4 (b). Note that only saturation but not NDV region is observed in I-V curves due to the screening effects as indicated in the Shockley theorem [111], however, the electrically-induced Wannier-Stark ladder can be resolved within the range of 2–5 V as depicted in the inset of Figure 5.4 (a).

Measured microwave transmission as a function of the applied using the klystron generator is given in Figure 5.4 (c). The setup was aligned in minimal levels of reflection, therefore, all the observed changes in the transmission can be attributed to the physical processes occurring in the biased superlattice. As one can see, the function is non-monotonic: initially, at low bias below 1 V, a weak absorption is observed; with further increase in bias voltage the gain is observed which remains stable within all studied range. Note that the observed instabilities above 4 V do not destroy the general gain picture.

To get an understanding of the physics behind and get a deeper insight into the processes involved, one needs to recall that the propagating wave is electrostatic, i. e. of plasmonic origin, and the superlattice is tuned into NDV regime, i. e. it operates under the Esaki-Tsu nonlinearity regime where the Bloch oscillations can be observed. In this context, it is reasonable to consider the possibility of controlling the interplay and coexistence of different oscillation modes. These include, for instance, plasmonic oscillations and longitudinal optical phonons [130]. The behaviour of the coupled modes differs if compared to individual oscillations. For example, in the case of Bloch and plasmon modes, the pendulum interaction-describing equation is

$$\ddot{\eta} + \omega_{\text{P}}^2 \sin(\eta) = 0, \quad (5.2)$$

wherein η denotes pendulum displacement, $\omega_{\text{P}} = \sqrt{4\pi N e^2 / m^*}$ - plasma frequency, and N - charge carrier concentration [132, 133]. The effective mass in semiconductor superlattices is expressed as $m^* = 2\hbar^2 / \Delta d^2$ [134]. Initial

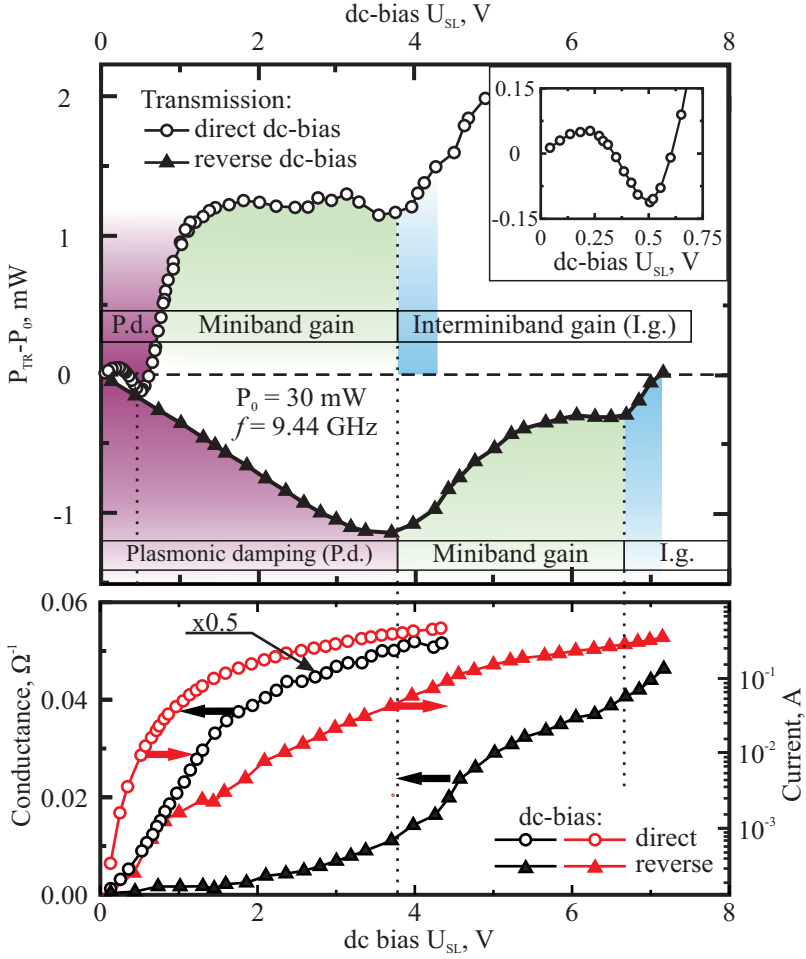


Figure 5.5: The dependence of transmitted power on the DC bias voltage (applied direct and reverse), measured under microwave excitation delivered by magnetron generator. Note three different regions in the transmission curve. At voltage bias – below 0.6 V – plasmonic absorption (damping) is visible; within 0.6 – 3.8 V stable Bloch gain within the miniband becomes strongly pronounced; further increase in the gain above 4 V is related to non-resonant interminiband (Zener) tunneling. For the case of reverse bias, the plasmonic damping region is more expressed and the stable Bloch gain region is more narrowed due to the asymmetric nature of the structure contacts.

conditions are proposed in the instant excitation and absence of an initial displacement $\eta(0) = 0$ and displacement velocity set by Bloch oscillation frequency $\dot{\eta}(0) = \omega_B = edE\hbar$. The solution of the Equation 5.2 results in the motion of classical particle in periodic potential $V(\eta) = \omega_P^2(1 - \cos(\eta))$ with energy $\omega_P^2/2$. In fact, the pendulum equation describes the transition from plasma oscillations to Bloch oscillations. When energy is much smaller than the maximal

potential energy, the particle is trapped in the one period of potential as plasmonic screening of the external electric field occurs due to the Bloch period being larger than the plasmon oscillation period. If the energy is larger than the potential barrier, particles go above the potential oscillating with the Bloch frequency [135]. As a result behaviour change is expected at $\omega_B = 2\omega_P$ frequency. The behaviour is depicted in the right inset of Figure 5.4 (c). As it is seen, three different modes – plasmon, Bloch, and phonon – can coexist in the superlattice. Theory predicts the transition from plasmon-phonon mode (low frequencies) to Bloch-phonon mode (high-frequency); further, a sharp transition from plasmon to Bloch mode is expected in the absence of collisions, and the electron motion should be aperiodic near the transition point [131].

If one compares the experimental dependence of the transmission power presented at Figure 5.5 with the theoretical estimates by Ghosh (see Figure 1.7) [131], their good correlation is evident. One may note that the experimentally observed transition from plasmon to Bloch mode is smoothed due to collisions. The obvious analogy between the experimental observations and theoretical predictions allows us to infer that the experimentally observed gain profile represents **plasmonic Epshtein effect** via coupled hybrid Bloch-plasmon-phonon modes (see right inset of Figure 5.4 (c)). As far as our knowledge goes, it is the first experimental observation of this effect.

To complete the physical picture, we measure the gain in direct and reverse bias employing magnetron as a high source at 9.44 GHz with emitted powers reaching 30 mW. The results are presented in Figure 5.5. As one can see, dependencies are quite similar, only shifted in the bias scale due to different origins of the contacts in the structure. In the reverse bias, the plasmonic absorption (damping) part is much more extended (up to 3.8 V in comparison to 0.5 V in the direct bias) due to the higher electric field needed to inject sufficient electrons for the Bloch gain. The miniband-related gain area displays weakly electric field-dependent features, while at 3.8 V and 6.7 V in the reverse bias, the second Bloch gain area becomes pronounced. Importantly, NDM and its direct consequence the high-frequency gain, arise within both miniband and interminiband hopping transport models [186], but in the case of the hopping model, the drift velocity decreases with the field faster $v_d \sim E^{-n}$ (the value of n depends on the dominant scattering mechanism but it is always $n > 1$) [187]. This difference in the behaviour of $v_d(E)$ can explain the observed gain increases when the bias crosses the boundary between these two transport regimes. In other words, the hopping can be attributed to interminiband non-resonant (Zener) tunneling, hence, the increase in the gain can be an indication of the phase conservation between intraminiband and interminiband-related transport mechanisms. It is worth underlining that the Bloch gain saturation in the intraminiband regime can be associated with the scattering and dispersion-free phonon modes coupling with the Bloch oscillations.

To support the experimental observation of the plasmonic Epshtein effect and its features, we have estimated frequency values of the transition from plasma-phonon to the Bloch-phonon modes. It is known that the plasma frequency in the semiconductor superlattice can be described as

$$f_P = \sqrt{\frac{e^2 N}{m^* \epsilon_0 \epsilon_r}} \quad (5.3)$$

wherein $m^* = 2\hbar^2/\Delta d^2$ is the effective mass [131, 188]. This results in plasma frequency of $f_P \approx 1.24$ THz. One may also note the plasmon-phonon to Bloch-phonon transition in the performed experiment was observed at the DC bias level of 0.5 V (see upper right inset of Figure 5.5). Such biasing voltage corresponds to the electric field strength of 21.6 kV/cm. Taking into account the Bloch frequency relation

$$f_B = \frac{edE}{2\pi\hbar}$$

one would achieve $f_B = 3.14$ THz Bloch frequency. If one assumes that the superlattice is placed between conductive layers representing capacitor plates, both plasmon and Bloch frequencies need to be modified (see [15] of [131]). The correction to the frequencies can be expressed as

$$f_B = f_B \epsilon_\infty / \epsilon_r; \quad f_P = f_P \sqrt{\epsilon_\infty / \epsilon_r} \quad (5.4)$$

for the Bloch and plasmon frequencies respectively. In equations, ϵ_∞ and ϵ_r represent high and low frequency dielectric constants. For GaAs, the values are 10.9 and 12.9. The correction results in the final frequencies of $f_P = 1.14$ THz and $f_B = 2.65$ THz. The ratio of these frequencies amounts to ($f_B/f_P \approx 2.33$) which is close to the theoretically expected value of 2. The observed deviation can be attributed to the non-zero current in the experiment due to the bias electric field which is not taken into account in the theoretical model. Despite this fact, one can underline that the observed gained curves present a manifestation of the plasmonic Epshtein effect via coupled hybrid Bloch-plasmon-phonon (Epshtein) modes. The gain features a sharp transition from plasmonic absorption to the Bloch gain which is still preserved in both intraminiband transport and non-resonant interminiband (Zener) tunnelling regimes.

The results considered above allow the drawing of a general view and resolve peculiarities of carrier transport mechanisms in semiconductor quantum superlattice varying the applied voltage. The illustration following the scheme [182] is depicted in Figure 5.6. As it is seen, with the increase of the bias, the carrier transport mechanisms in semiconductor quantum superlattices can be tuned from Ohmic mode, via Bloch gain/oscillations up to interminiband transport domination via the manifestation of non-resonant Zener tunneling effects at high applied DC voltages.

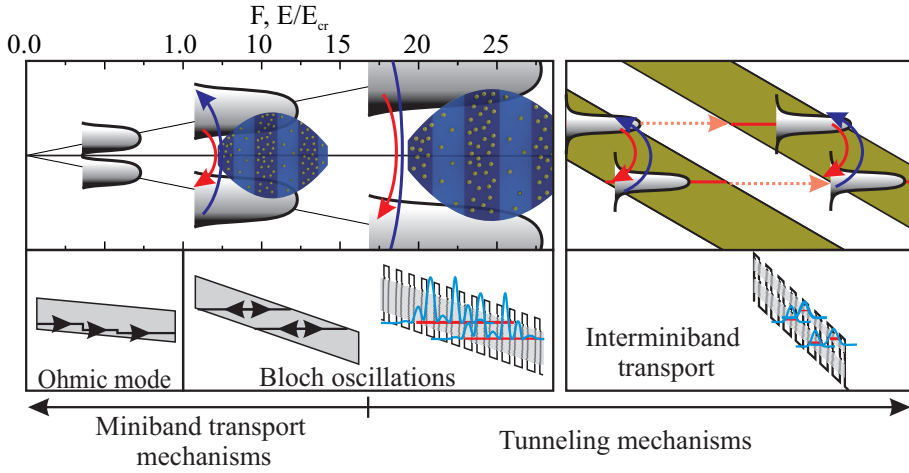


Figure 5.6: Variation of the dominating charge carrier transport mechanisms versus applied DC bias. Beyond the critical Esaki-Tsu electric field, the Ohmic regime is observed. With the increase of the bias, exceeding the critical electric field, the Bloch oscillations can be observed, and the hybridized plasmon-phonon mode experiences a transition to the stable Bloch gain regime. At large DC bias, interminiband transport dominates via the manifestation of non-resonant Zener tunnelling effects (according to [182]).

In summary, following findings can be summarized:

- The coupled Bloch-plasmon-phonon (Epshtein) modes were experimentally demonstrated in semiconductor quantum superlattice for the first time.
- The gain mechanism from the coupled plasmon-phonon to the stable Bloch gain displays the sharp transition with the applied DC voltage.
- Stable inversionless Bloch gain can be observed in GaAs/AlGaAs superlattice in microwaves at room temperature. The gain mechanism is preserved in both miniband transport and non-resonant interminiband (Zener) tunneling regimes.
- Carrier transport mechanisms in semiconductor quantum superlattices from Ohmic mode, via Bloch gain/oscillations up to interminiband transport domination can be tuned by variation of the applied voltage.

The aforesaid findings allow us to formulate the following statement for defense:

- **Statement 5:** Inversionless Bloch gain can be observed in biased GaAs/AlGaAs superlattice in microwaves at room temperature via manifestation of coupled Bloch-plasmon-phonon (Epshtein) modes. The gain

features a sharp transition from plasmonic absorption to the Bloch gain which is preserved in both miniband transport and non-resonant inter-miniband (Zener) tunneling regimes.

APPENDICES

6.1. Appendix A. Additions to the literature review section

6.1.1. Addition to the matter of negative differential velocity effects in bulk materials

This appendix will provide additional information to supplement broadened understanding of the negative differential velocity based effects in bulk semiconductors. The accent will be made on operation and devices not directly related to the ones presented in the results section. One will find out that NDV as an effect comprehends significantly to other than superlattice-based generators and/or amplifiers, thus, it is very important to clearly distinguish the similarities and differences between these devices and their operational principles.

Specifically, in the discussed field of solid state oscillators, negative differential velocity relates to the case when the drift velocity in the structure decreases under the influence of increasing electric field ($dv_d/dE < 0$). Before proceeding further, it is important to understand that the term negative differential mobility (NDM) being $\mu = v_d/E$ is an indistinguishable consequence of NDV, while negative differential conductivity (NDC) being $\sigma = eN\mu$, negative differential resistivity (NDR) ($\rho = 1/\sigma$), and negative differential resistivity (NDR) $R = \rho L/S$ may differ due to non-uniform charge carrier distribution within the structure ($dN/dx \neq 0$). One should be aware during literature analysis as these terms, met equally often, can be treated as quasi-commensurate depending on the particular subject. One should also be aware of "non-differential" negative units, that may be found in several articles.

As described in the literature analysis section, the first investigation of the NDV effects has been conducted by Ryder [66]. Ryder managed to overcome the outer heating problem, occurring due to the high energy transfer rate by employing short and low repetition rate pulses of electric fields to avoid accumulative heating. Furthermore, sample of specific geometry was employed to supply constant carrier density and avoid the influence of the holes injected from positive electrode. Combination of the solutions resulted in significant current density deviation from linear ohmic dependency (see Figure 6.1), resulting in three distinguished dependency areas: at low electric field correspondence to the Ohm law was observed ($\mu = \text{const}$), but after exceeding some electric field value mobility becomes electric field dependent ($\mu \propto E^{-1/2}$) until current density reaches saturation range ($\mu \propto E^{-1}$) [189].

It is mathematically shown in the works of Kroemer, that formation of the negative effective mass may possibly lead to the generation effects in high-frequency leading up to several THz [69]. In that case, generation effect

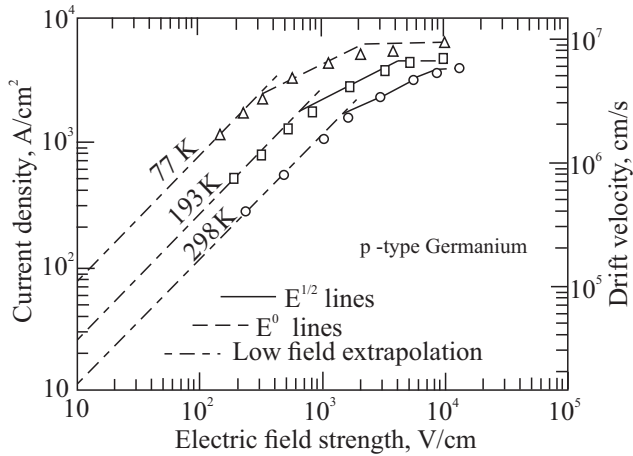


Figure 6.1: Current density dependency on external electric field for the case of bulk p-type germanium sample. Note the deviation from the linear ohmic dependency at higher electric field strengths, resulting in electron mobility becoming field dependent and leading to the saturation of current density. Reprinted figure with permission from [189]. Copyright 1953 by the American Physical Society.

can be expressed via time-dependent component of the work per unit time. Employing DC and AC bias field and assuming the effective mass to be constant within the k -space, work per unit time equation can be expressed via three components. These are energy, acquired from DC field, AC field contribution at the moment of collision, and energy acquired from the AC field. The latter term is the most interesting, as being negative results in charge carrier (electron or hole) delivering energy to the field than acquiring [70]. Thus, generation or amplification will arise if one of the main effective masses (diagonal) will be negative and the direction of the signal field is close or corresponding to that negative mass. The properly directed bias field should also be strong enough to supply sufficient amount of charge carriers into the k -space area of negative effective mass [69].

The above discussed considerations regarding the directions of the bias and signal fields results in parallel (longitudinal effective mass component becomes negative) and cross-field (transverse effective mass component becomes negative) cases (see Figure 6.2). In the parallel case, negative effective mass region is defined by the nonparabolicity of the band structure. In the cross-field case (which the case of Ge and Si - most investigated materials at that time) negative effective mass region is defined by the degeneracy of the energy bands, resulting in splitting, granting negative effective mass regions to be highly directive and spanning up to $k = 0$. The above-described cases are the two extreme ones, while others should be treated as a result of superposition of the two [70].

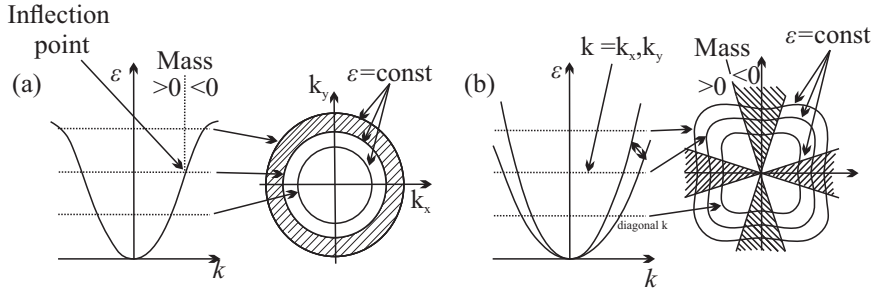


Figure 6.2: (a) Schematic band structure depicting the cases when energy remains isotropic as for free electrons, but is nonparabolic. Longitudinal mass becomes negative above the inflection point (shaded regions) [70]. (b) Schematic band structure depicting the cases when energy remains parabolic as for the case of free electrons, but depends on the direction. If the energy contours become re-entrant, transverse mass becomes negative within re-entrant section (shaded regions) [70]. ©1959 IEEE.

Before proceeding, an important note must be taken on the types of negative differential effects in bulk semiconductors should be made. The two types are voltage-controlled and current-controlled negative differential resistances Figure 6.3. The first one, being much more common to the related studies can also be contributed to the Gunn effect, discussed below. The current-controlled case is non the less interesting for the study of hysteresis effects in the superlattices, however, the results of other groups will be shortly mentioned. Furthermore, the current- controlled nonlinearities can be met at impact ionization is shallow impurity levels in bulk semiconductors [190]. It is considerably simple to notice, that in the case of voltage-controlled nonlinearity, electric field is multi-valued i.e. we can achieve several electric field values under the same current value, whilst in current-controlled case current is multi-valued leading to the material instabilities. Such instability may lead to the formation of hysteresis and other scientifically attractive effects [76]. In articles the voltage-controlled nonlinearity may be found by the name of N-type characteristic, while the current-controlled nonlinearity may be found by the name S-type characteristic.

Further research on the NDV effects in bulk semiconductors resulted in publication of the fundamental work of Gunn [73]. The nature of the intervalley transfer was quickly experimentally confirmed by different groups employing different experiments. In these experiments the energetic separation between the valley minima have been modified in different ways. The Gunn effect implies that the critical electric field depends on the energy difference between the valleys, thus, such modification was intended to correlated the observed effects to the explanation. To achieve different energies Allen et al. employ sweeping from GaAs ($\Delta\epsilon \approx 0.36$ meV) to GaAs_{0.5}P_{0.5} ($\Delta\epsilon \approx 0$ meV) [78]; Hutson et

al. apply hydro-static pressure to the samples of GaAs (9 meV/kbar) [79]; and Shyam et al. apply the uniaxial stress [80]. In all of these considerably unrelated and physically diverse experiments, the decrease of the energy separation between the minima resulted in decrease of the threshold voltage, required to observe the above-described Gunn oscillations.

Assume one apply the electric field exceeding critical E_{cr} to the sample with pronounced region of negative differential resistance. If the field is ideally uniform along the whole sample, one will achieve constant flow of electrons from cathode to anode. However, in the real world, instabilities may occur due to several reasons causing field fluctuations which may lead to formation either of accumulation or depletion layer of the space charge. Several types of uniformity may be distinguished. The first one, is an inevitable formation of the accumulation layer near the cathode, which under the below-discussed conditions plays a primary role for the operational case named "stable amplification regime". The second type, related to the "real" Gunn effect, arising mostly due to structural non-uniformities or statistical fluctuations, usually lead to the formation of a coupled accumulation and depletion layers, called domain. In domain, the charge carrier density in accumulation layer is increased and the charge carrier density in depletion layer is decreased. This in turn results, that electric field inside the domain is larger compared to the outside. Taking into account that according to the N-type drift velocity dependency on the applied electric field (see Figure 6.3), the drift velocity inside the domain will be smaller compared to the outside. As the drift velocity outside will be larger the charge density in accumulation layer of slowly moving domain will increase being caught up by the aback electrons, drifting from cathode with the higher speed. At the same time the charge density of depletion layer of the domain will further decrease due to charge carriers rushing towards anode with speed, larger compared to the inside of the domain. Both these factors result in the further increase of the space charge of the domain and its field, resulting in further decrease of

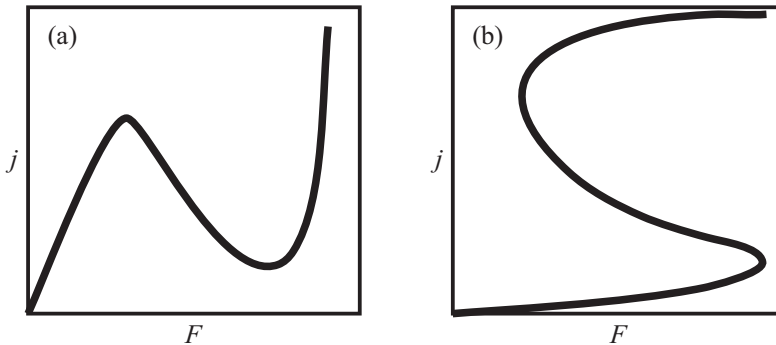


Figure 6.3: Two type of negative differential resistances. (a) N-type voltage controlled and (b) S-type current controlled dependencies. Adapted from [76]

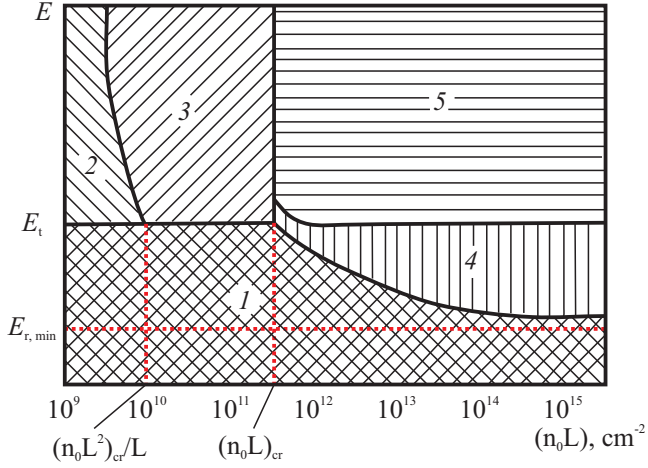


Figure 6.4: Gunn diode operational mode dependency on the Kroemers (NL) criterion and applied DC bias [81]. Area labeled "1" depict condition for Ohmic resistance mode, "2" - positive differential resistance mode, "3" - domainless negative differential resistance mode, "4" - trigger mode, and "5" - domain generator mode. Adapted from [81].

drift velocity [191].

If in the voltage (field) applied to the sample is kept constant, with the increase of the space charge domain (electric field in domain also increases), the decrease in the field outside the domain may be observed as well as the drift velocity. When the drift velocities inside and outside space charge layer levels up, space charge layer stops growing as there are no quick enough electrons to catch up the moving domain, thus, the domain proceeds unchanged until reaches the contact and disappears [81].

Existence of the $(NL)_{cr}$ criterion is one of the most important things for the explanation of the observed effect. The criterion describes the threshold conditions for the domain formation in the structure. For the bulk case this results in several different operation modes depicted at Figure 6.4. Before discussing this graph, one may additionally note the highlighted $(NL^2)_{cr}/L$ criterion, which marks the influence of diffusion. Diffusion itself, having a destructive effect on domain formation is usually omitted in GaAs environment as diffusion time constant $\tau_d = L^2/4\pi^2 m^2 D$ is much larger compared to the characteristic dipole formation time D - diffusion coefficient. The marked $(NL^2)_{cr}$ can be simply shown to be equal as

$$(NL^2)_{cr} = \frac{\pi \epsilon D m^2}{q |\mu_d|}. \quad (\text{A.1})$$

Operation modes under $(NL) > (NL)_{cr}$ conditions may not be too much related, as all the structures involved in the presented research do not fulfil do-

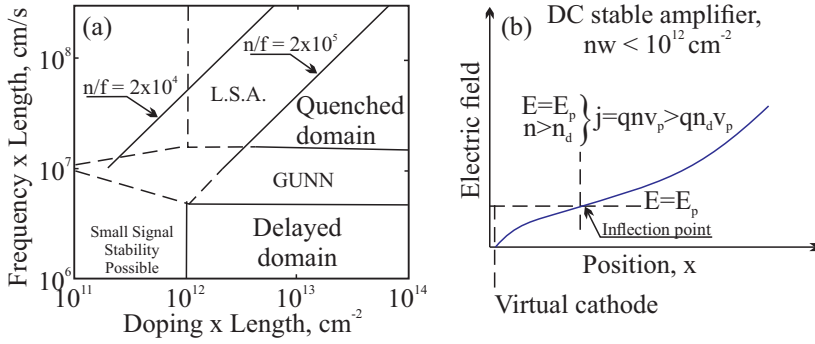


Figure 6.5: (a) Modes of GaAs for different conditions of Kroemers (NL) criterion and (fL) criterion. Reprinted from [192], with the permission of AIP Publishing. (b) Field distribution in sub-critically doped semiconductor [82]. © 1968 IEEE

main formation criteria, however, they are worth a short mention. Area 5 represents the case of classical Gunn effect described above. In this mode frequency is defined by transit time and external circuit tuning has comparably low effect. Furthermore, in this mode low biasing effect is expected as the formed domain absorb any voltage above critical. Here $NL > (NL)_{cr}$ and $E > E_{cr}$. Area 4 represent operation in "trigger mode". This regime employs the fact that the critical electric field strength required for domain formation E_{cr} may be considerably larger compared to the electric field strength E_q under which the formed domain can be sustained. This creates some sort of hysteresis, which is employed by biasing the structure with electric field strength $E_q < E < E_{cr}$ and sending short single pulses (shorter than transit time, but longer than characteristic domain formation time) to exceed E_{cr} , allowing to create single domain resulting in single pulse of generated signal.

In stable amplification regime, corresponding to $E > E_{cr}$, the applied AC field is expected to be "small signal" i.e. when the electric field strength of the AC field is much smaller compared to the DC electric field strength. As will be shown below, such assumptions results in significantly transparent mathematical background, still being sufficiently precise to describe conditions for the amplification processes to start. For the case when AC electric field strength becomes comparable ("large signal gain") one would have to introduce another, frequency-dependent fL criterion (see Figure 6.5 (a)) [192]. Again, depending on the applied DC electric field strength one may achieve a bunch of different effects. If frequency is small and $E_{dc} - E_p < E_{ac} < E_{dc} - E_q$, at the moment domain reaches anode, the total electric field strength is smaller than E_p , thus, some AC cycle should pass until field becomes equal to E_p . This means, there will be some delay before new domain formation will start. This operation mode is called "delayed domain mode" [193]. With the further increase of the

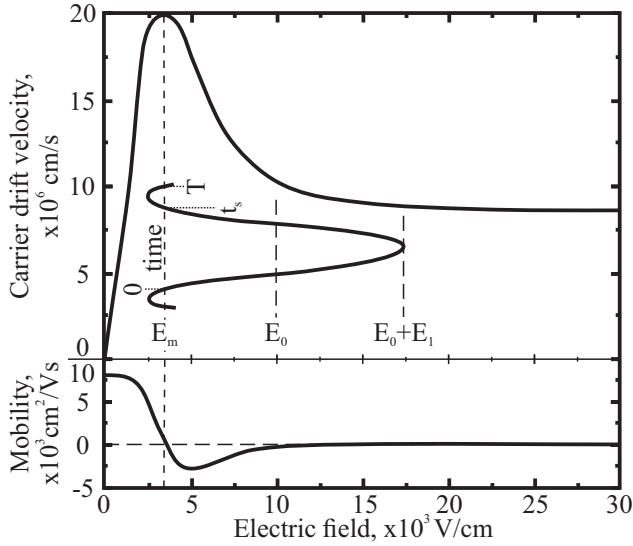


Figure 6.6: Drift velocity dependency of the bias electric field strength for the case of n-GaAs in LSA mode. Bottom inset represent corresponding mobility. Reprinted from [192], with the permission of AIP Publishing.

AC electric field strength $E_{dc} - E_0 < E_{ac}$, the domain would disappear before reaching the anode - the "quenched domain mode" [194]. However, both of the described operation modes are mostly typical to high (NL) criterion values and only for comparably low fL criterion values. In the case of $(NL) < (NL)_{cr}$ and high frequency, limited space-charge accumulation (LSA) mode becomes dominating.

In the LSA mode the period of the connected bias AC electric field is much higher compared to the characteristic domain formation time. As the frequency is so high, domains in the structure do not have enough time to form fully, as negative part of the AC cycle occurs, resulting in total field to be below critical, initiating domain quenching [195]. While the total field E_{cr} is above critical structure amplifies signal, however, there is a part of the period (marked t_s on Figure 6.6), wherein total field is below critical (Figure 6.6). During this time interval, structure should be treated as the above describe linear element quenching the formed accumulation layer. It is also worth noticing that if the quenching period would be too short to fully quench the accumulation layer, the latter would grow within each cycle, resulting in exiting of the LSA mode.

To observe the amplification of the AC signal carrier absorbed power should be estimated. The latter may be separated into

$$P_{dc} = \frac{eE_{dc}}{T} \int_0^T v dt \quad (A.2)$$

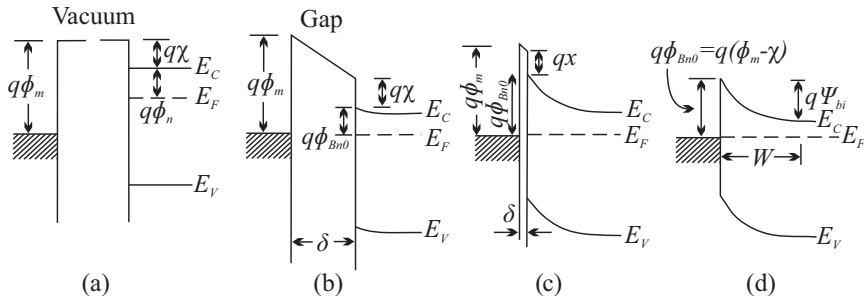


Figure 6.7: Energy diagrams of metal-semiconductor interfaces. (a) Metal and semiconductor as separated systems; (b) connected into one system; (c) with reduced gap; (d) with removed gap. Adapted from [201].

for the power, absorbed from the DC field and

$$P_{ac} = \frac{eE_{ac}}{T} \int_0^T v \sin(2\pi ft) dt \quad (\text{A.3})$$

for the power, absorbed from the AC field [192]. It is shown that there is a range of combinations of the DC and AC field strength wherein P_{ac} is negative, showing that the energy flows into the AC field. This is a clear evidence of the generation and/or amplification process possibility in the structure under the above-mentioned conditions [196]. As the result, the main peculiarity of the LSA operation mode arises, resulting in that the resonant frequency is described by the external oscillator circuit and has a significantly lower dependency on the transit time, typical for standard-based Gunn amplifiers [197]. The experimental results prove to be in a significant agreement with the proposed theoretical description by the ice-breakers [198–200].

6.1.2. On the matter of proper contact selection

This subsection is mostly devoted to the physical nature of Ohmic and Schottky contacts and the importance of the proper contact selection for the case of generation and/or amplification processes in the superlattice. At first, the physics and differences between the contacts is presented following the considerations and researches related particularly to the case of the superlattices. The majority of the section is devoted to the physics of Schottky contact as the employment of the latter considered to be very important. It is supposed that selection of the correct (and different compared to the typical superlattice-related research) type of contacts resulted in successful observation of the subsequently presented results.

Considering the semiconductor-metal connection interface it is considered to be useful to recall the contact relevant physical properties which would be mentioned below. The first one is Fermi level E_F , representing the energy level

which is occupied with 50% probability presented in Fermi-Dirac distribution function

$$F(E) = \frac{1}{1 + \exp((E - E_F)/kT)} \quad (\text{A.4})$$

and the second one is the work function, being equal to energy difference between the vacuum level and the Fermi level, representing the amount of energy required to remove electron to the infinite distance. At the next step the remainder of the classical picture (Figure 6.7), representing the disturbances in energy levels by connecting metal and semiconductor. If the materials are selected as depicted in the inset (a), after connection of the two materials into one system, charge redistribution would start, creating an electron flow from the semiconductor into metal until the Fermi level would not become equal to the work function of the metal (see Figure 6.7 (b)) [202]. This redistribution creates an electric field in the gap between the two materials which increases the field by decreasing the gap as the negative charge is build up at the metal (see Figure 6.7 (c)). As the gap becomes negligibly small we obtain a barrier of $e(\phi_m - \chi)$ height (see Figure 6.7 (d)), wherein $e\phi_m$ is the work functions of metal, and $e\chi$ is electron affinity (energy between the vacuum level and conduction band of the semiconductor). It also worth of additional notice on the formation of contact potential (Volta potential) which is formed on the interface of metal and semiconductor. The formation of the contact potential and its behaviour under forward or reverse biasing has a significant effect on the quantitative results of the experiments. The influence of this potential on the presented research and the necessity of taking it into account will be explained in result section. The above-presented equation describing the height of the formed barrier is titled Schottky-Mott Rule and the barrier is denoted as Schottky barrier [203]. The Schottky-Mott rule however, does not take into account interaction of the interfaces. In real life two interfaces being brought close to each other result in modification of the surface states. The change itself is mostly dependent on the atomic structure of the interfaces and can be accounted by inclusion of additional "interface dipole" component eD_{int} [204]. From the applicational point of view the barrier height may be either deduced by experiment or taken from pre-evaluated tables [205]. In case of the non-contact-related studies this solution may even considered preferential due to harsh reality event, leading to unaccountable changes. There is a lot of scientific literature to get into the subject of contacts starting from the all-time classical Sze textbooks [201] ending with the catchall review articles [206] and references therein.

On the other hand, in the case of Ohmic contacts, the metal-semiconductor interface is fabricated employing such materials that the formation of the barrier is avoided, resulting in contact which does not perturb the performance

of the connected device. Thus, employment of the Ohmic contacts, although being considerably more difficult in fabrication, is widely expected to be preferential for the majority of modern semiconductor devices. That is why understanding that generation and/or amplification process in the superlattices is one of the exceptions, is one of the key factors, resulting in achievement of new scientific milestones. The idea behind the employment of the Schottky contacts lies beneath the target to achieve as uniform electric field as possible in the superlattice structure. According to the Mott-Gurney law, the electric field distribution in the sample is described by the Poisson and continuity equations [207, 208]

$$\frac{\partial E}{\partial x} = e(N - N_D)/\varepsilon_0\varepsilon_r; \quad j = eNv_d(E). \quad (\text{A.5})$$

The similar work has been done by Kroemer [209], showing that uniform field is achievable by specific boundary conditions. In our case, however, the biggest interest is the results presented by Maksimenko [105], wherein the boundary analysis of the superlattices are thoroughly analysed. It is shown that by employing the Esaki-Tsu drift velocity equation [63] one may achieve a differential equation

$$\frac{dF}{dx} = \alpha \left(\frac{J(1 + F^2)}{F} - 1 \right). \quad (\text{A.6})$$

In this equation F , J , and x is a dimensionless representation of the electric field strength, current, and coordinate which respectively are equal to $F = E/E_{cr}$, $J = j/eN_Dv_p$, and $x = X/L$ (j - current density, N - doping density, $v_p = \Delta d/2\hbar$ - drift velocity peak value, L - superlattice length). Furthermore, $\alpha = eLN_D/E_{cr}\varepsilon_0\varepsilon_r$ represent the (NL) Kroemer' coefficient [209]. The solution of the Equation A.6 leads to two stationary points, one belonging to the positive differential conductivity and one to negative differential conductivity

$$F_{\pm} = \frac{1 \pm \sqrt{1 - 4J^2}}{2J}. \quad (\text{A.7})$$

It is important to note that the above-mentioned standing points representing the external biasing conditions are only existing if $J \leq 0.5$ (see Figure 6.8 or Figure 1 of [105] for enhanced understanding). Note that the referenced Figure 6.8 depicts the field distribution recalculated according to the equation given in [105], but using structure parameters of the samples, used within the particular research. Under this condition by applying the field three types behaviour are possible (see Figure 6.9). If the applied field $F < F_-$, field strength quickly increases until it reaches F_- value and then continues to be constant along the residuary part of the superlattice. If the strength of the applied electric field is between two stationary points ($F_- < F < F_+$), the field strength

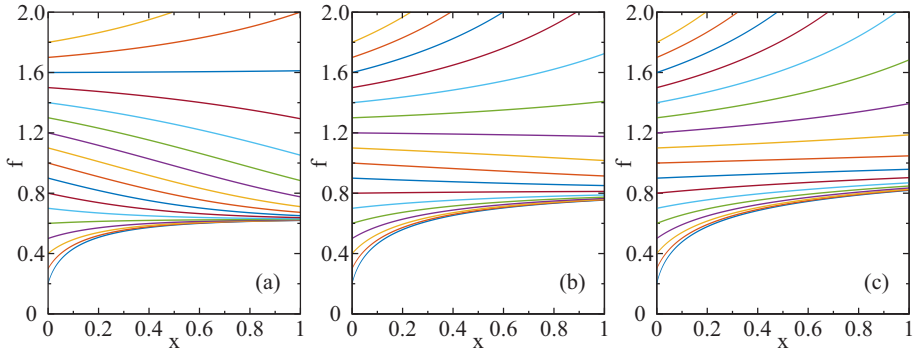


Figure 6.8: Spatial electric field distribution for different field strengths at the emitter. Simulations performed according to the theoretical estimations of [105] for the superlattice employed in the current research (see Section 2.1 for more data on the structure). Currents $J = 0.45$ (a), $J = 0.49$ (b), and $J = 0.505$ (c) are employed.

gradually decreases with an increase of the coordinate. If the current is close to the peak values, distance between the two stationary points is small, thus, the decrease is considerably slow. Finally when electric field strength is high $F > F_+$, strength quickly increases reaching very high values at the end of the structure.

One should also note that for the case when the peak current is reached or exceeded ($J \geq 0.5$) the stationary points disappear (Figure 6.8 (c)). Herein the field strength increases on the whole length of the superlattice structure.

Considering the realistic scenario wherein the current through the structure is electric field strength dependent, one may achieve contact characteristic (Figure 6.9 (a)). In the currently discussed research, linear dependency $J = sF_e$ is used. In this equation s is the dimensionless conductivity parameter describing the contact ($s \gg 1$ is ideal ohmic contact; $s \ll 1$ - blocking Schottky contact). On the picture one may note three linear dependencies intersecting the Esaki-Tsu curve. The intersection of these two lines depicts the conditions to achieve uniform electric field. One may note, that line (1), representing ohmic contacts does not intersect Esaki-Tsu curve, meaning it is impossible to achieve uniform electric field employing ideal Ohmic contacts. Furthermore, the case depicted with the line (2) shows intersection with F_+ , meaning that uniform field conditions are met when the superlattice is in the positive differential mobility state - operation mode, undesirable for the current research. Finally the line (3) shows a nice intersection with the F_- part of Esaki-Tsu curve, representing negative differential mobility regime. This research shows that in order to avoid or reduce domain formation in the superlattice, operating in negative differential mobility regime by creation a uniform electric field along the superlattice, one should not use Ohmic contacts, but fabricate

Schottky blocking contacts instead.

One should note the IV dependencies presented at Figure 6.9 (b) expressed in non-dimensional variables ($u = U/F_{cr}L$ and $U = \int_L^0 F(x)dx$). For the case of Schottky contact one may note the saturation, not representing the initial Esaki-Tsu curve [103].

Alternative to the proposed contact solution is presented in the work of Beltram [210]. The proposed solution is to use three-terminal structure to supply the bias-independent constant-flux current. This is achieved by an addition of the forward biased p-n heterojunction, controlling the current and reverse biased heterojunction to control the electric field in the superlattice (see Figure 6.10). Such a solution is claimed to allow achievement of uniform electric field, still using the Ohmic contacts. The achieved I-V characteristics clearly depict the formation of the NDC region. Moreover, several peaks are observed on the increasing part under higher bias. These peaks are attributed to Wannier-Stark localization (WSL) states mixing with the states belonging to other minibands or to the continuum above the barriers. These peaks in real-life conditions also includes the accountancy for the electron coherence length (evaluated via electron mean path). The proposed mathematical model for the transmission is claimed to fit experimental results with mean free path $\lambda = 30$ nm [210]. This article has additional importance, as it proposes an employment of the heterojunctions to achieve uniform electric field much earlier than the works of Maksimenko.

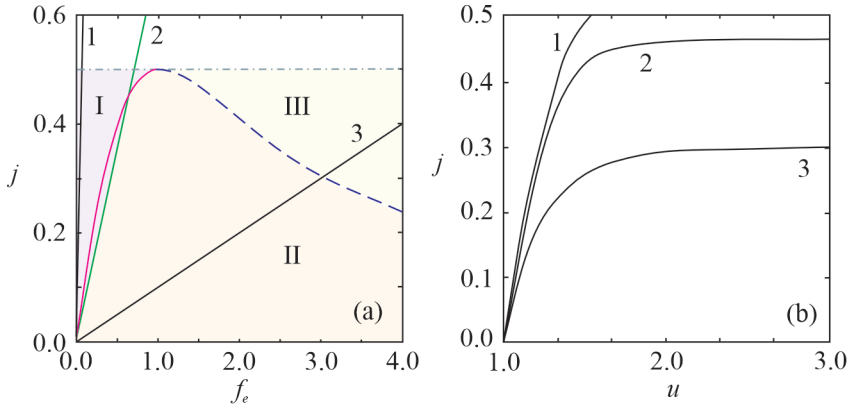


Figure 6.9: Three regions, corresponding to different types of field distribution marked I,II, and III. Red and blue dashed line mark Esaki-Tsu curve. Number 1,2, and 3 represent linear emitters with dimensionless conductances of 17, 0.7, and 0.1 respectively. Graphic clearly depicts inability to get into NDV regime of Esaki-Tsu curve employing ideal Ohmic contacts in the superlattice structure. b) I-V characteristics corresponding to contact characteristics 1-3. [105]. Reproduced with permission from Springer Nature.

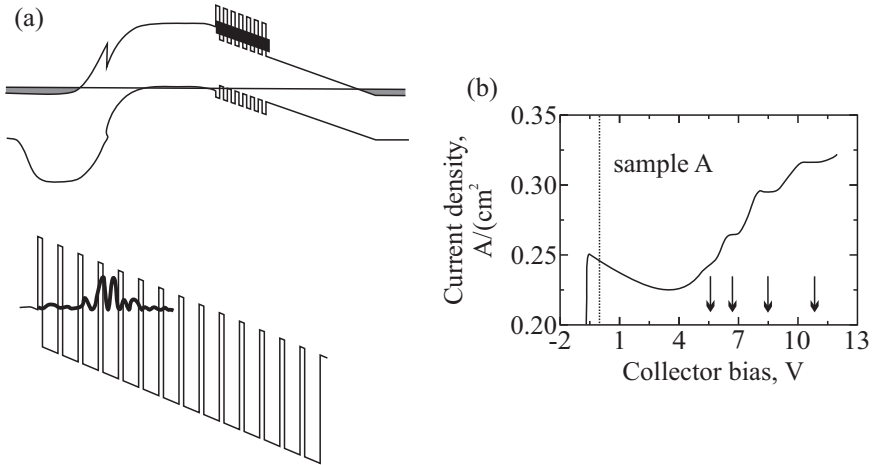


Figure 6.10: (a) Energy diagram of the samples studied in [210]. Employment of the three-terminal structure allow to supply bias independent constant flux current and achieve uniform electric field across the superlattice. (b) Formation of the NDC region visible at the I-V characteristics along with several peaks, attributed to the intraband interaction of Wannier-Stark localization states [210].

6.1.3. Comment on the Manley-Rowe relations

Manley-Rowe relations is a set of equation, describing the power transfer of the non-linear element, affected by at least one alternating power source (modulators, demodulators, mixers) [211]. For the inductive or capacitive nonlinearities, the set consists of two independent equations, relating power at two different frequencies. Such relations are treated to be general i.e. independent on amplitude of the frequency, or the external circuit. Moreover, the relations consider the possibility of generation of subharmonics or multiples of subharmonics lower or larger than the applied frequency making the application of the relations even more attractive for the discussed subject of fractional sub-harmonic generation effect in the semiconductor superlattices.

Non-linear capacitor is analysed to derive the Manley-Rowe relations. Applying frequencies $f_{m,n} = mf_x + nf_y$, wherein m and n are positive and negative integers and omitting the full derivation (can be found at [211]), one would achieve the resultant equation of

$$\begin{aligned} \sum_{m=0}^{\infty} \sum_{n=-\infty}^{\infty} \frac{mP_{m,n}}{mf_x + nf_y} &= \frac{1}{2\pi} \int_0^{2\pi} d\omega_y t \int_{q(0,\omega_y)}^{q(2\pi,\omega_y t)} V(q) dq \\ \sum_{m=-\infty}^{\infty} \sum_{n=0}^{\infty} \frac{nP_{m,n}}{mf_x + nf_y} &= \frac{1}{2\pi} \int_0^{2\pi} d\omega_x t \int_{q(\omega_x t, 0)}^{q(\omega_x t, 2\pi)} V(q) dq \end{aligned} \quad (\text{A.8})$$

wherein $P_{m,n}$ is the average power flowing into the nonlinear element at fre-

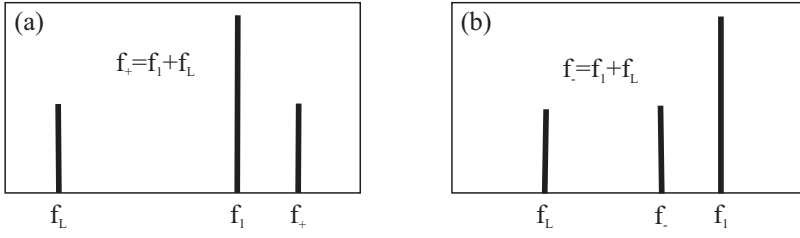


Figure 6.11: Signal and local oscillator frequencies for modulators and demodulators. (a) Non-inverting modulator and demodulator; (b) inverting modulator and demodulator. f_L marks local oscillator frequency [211]. © 1956 IEEE

frequencies $\pm|mf_x + nf_y|$, e - charge flowing into the nonlinear capacitor, and $V(q)$ voltage. The achieved equations are universal, still if one would like to achieve Manley-Rowe equations of classic shape, one should introduce the hysteresislessness of the nonlinear capacitor. Absence of the hysteresis in the nonlinear characteristics result in the right integrals to be equal to zero, thus

$$\begin{aligned} \sum_{m=0}^{\infty} \sum_{n=-\infty}^{\infty} \frac{mP_{m,n}}{mf_x + nf_y} &= 0 \\ \sum_{m=-\infty}^{\infty} \sum_{n=0}^{\infty} \frac{nP_{m,n}}{mf_x + nf_y} &= 0 \end{aligned} \quad (\text{A.9})$$

providing two independent relation for the powers flowing into the capacitor at the analysed frequencies. The solution of these equations is expected to depict the power flow in or out of the nonlinear element. The research of the Manley and Peterson [212,213] show that in the case of two frequencies, two solutions are possible: one resulting in positive power entering the nonlinear element (stable absorption) and second, resulting in unstable solution, wherein one of the power flows is negative, representing emission from the nonlinear element on one of the frequencies.

Consider participation of only two frequencies one of which has a much larger amplitude. The latter is called pump field and the small one - probe field. In the analysis of Manley [211] the pump frequency is called "local oscillator", we will use this term in the current chapter. Assuming we have only two frequencies, the instability (gain) of the smaller one is of particular interest for us representing the case of the presented experiment. Figure 6.11 depict output duality for the above-described case, resulting in "inverting" (f_-) and "non-inverting" (f_+) processes wherein $f_{\pm} = f_1 \pm f_L$, and f_L depicts local oscillator frequency.

For the case of "non-inverting" processes Equations A.9 can be further simplified to

$$\begin{aligned}\frac{P_1}{f_1} + \frac{P_+}{f_+} &= 0 \\ \frac{P_L}{f_L} + \frac{P_+}{f_+} &= 0\end{aligned}\tag{A.10}$$

This equation system reveals that for the case of positive P_1 and P_L , P_+ is negative, representing gain from the nonlinear element. For the case of inverting process

$$\begin{aligned}\frac{P_1}{f_1} + \frac{P_-}{f_-} &= 0 \\ \frac{P_L}{f_L} - \frac{P_-}{f_-} &= 0\end{aligned}\tag{A.11}$$

situation is a bit different. P_1 is positive and P_L, P_- - negative. Power from the oscillator flows at frequencies f_L and f_- resulting in instability of the device. Under such operating conditions device can feature any gain, depending on the external impedances [211].

It is also important to note, that all the equations below Equation A.8 are given assuming the absence of hysteresis in the analysed non-linear structure. This note is very important as during the research the non-compliance of the analysed structure to classical Manley-Rowe equations, typical for the non-linear structures and devices was revealed. Our primary researches do show the existence of the hysteresis in the analysed structure. This research is currently in the very early stage of development, thus, neither results on the appearance of the hysteresis in the proposed structure, nor the influence of the latter on the Maley-Rowe equations will not be presented or discusses.

6.1.4. Evolution and negative differential velocity effect of the quantum semiconductor superlattices

As is mentioned everywhere along the manuscript, superlattices are the main subject of this research. The peculiarity of such a structure, which leads to immense physical effects, lies in its composition of at least two different periodic materials. Although the overwhelming majority of the manuscripts typically commences the introduction with the fundamental work of Esaki and Tsu [63] as the initial ice-breaking, however, taking the advantage of the extensive manuscript, even older and not so famous works are worth uncovering in order to deliver an expanded knowledge on the subject of superlattices in common and semiconductor superlattices in particular.

One of the earliest studies on the development of the synthetic modulated structures was performed almost half a century earlier by Johansson and Linde [214]. However, the first works on the periodic structure involved metal-metal (Au-Cu and Pd-Cu) periodic structures, later labelled as metal super-

lattices. The metal-metal superlattice structure was considered attractive due to its specific electric parameters [215], including but not limited to thermoelectric power [216] and superconductivity [217] or magnetic parameters [218], including but not limited to perpendicular magnetic anisotropy [219] and giant magneto-resistance [220].

Taking into account the early stage of the deposition technology at the time of first metal-metal superlattice related studies, one may find a significant part of works dedicated to the high-quality fabrication of the periodic layered structures [221–223]. Although, these works nowadays may be considered outdated, they are widely acknowledged for the development of deposition methods and techniques, laying a robust foundation and determining a rapid evolutionary growth of the subsequent research related to semiconductor superlattices.

Due to the differences between physics and properties of metal and semiconductor superlattices (the latter will be extensively discussed below), considerably soon after the discovery, studies related to semiconductor superlattices seceded into separate research branch. Both types of superlattices managed to maintain the scientific interest. Considerably recent researches of metallic superlattice explore high-temperature superconductivity possibilities [224], Fano lineshape control [225], unique electronic properties by addition of graphene [226, 227], magnetic properties [228], and thermoelectric energy conversion [229].

As disclosed in the main part of the text, Esaki and Tsu [63] claim the formation of negative differential velocity range in the DC biased superlattice. The whole multiplicity of the experimental works by Sibille group experimentally prove this claim by solving the Poisson equation with the only drift velocity dependency of Esaki Tsu allowing to achieve good match with the experimental I-V characteristics. To further analyse the NDC formation mechanism, superlattices of different miniband width have been fabricated and analysed [230, 231]. As Esaki mechanism claimed $edE = \hbar/\tau$ [63] and WSL mechanism claimed $edE \sim \Delta$ [119]. Although claimed differently in the article, transition between the two dependencies is clearly depicted (see Figure 6.12 (B)). This branch of the research is being finalized by combined optical and electrical experiments, confirming the WSL and Esaki mechanisms being expressions of one phenomena - electron localization, occurring due to Bragg reflection under the application of external electric field [232, 233]. It was shown that critical field for the WSL mechanism and the critical electric field for the onset of Esaki mechanism are almost equivalent, demonstrating the fundamental link between both mechanisms. In particular, it is mathematically shown that the electric field required for the complete localization of the Stark ladder, meaning that the electric field is so strong that the wave-function is shrunk to one well (i.e. separate quantum wells) is equal to the onset of Esaki NDV mechanism. The latter conclusion is also a result of another independent

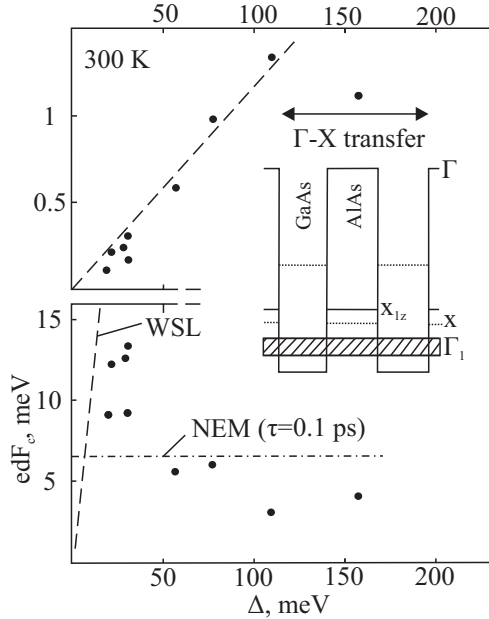


Figure 6.12: Peak velocity per superlattice period dependency on the mini-band width. One should note difference between two mechanisms: NEM and WSL. Reprinted figure with permission from [230]. Copyright 1990 by the American Physical Society.

work [210].

6.1.5. On the matter of Bloch oscillations in semiconductor superlattices

There is a big amount of theoretical research on the matter of Bloch oscillations including but not limited by [234, 235], still particular attention on the works of Bouchard should be paid [135]. In the article authors deviate from the classical single-band tight-binding model, but choose the numerical solving of the time-dependent Schrodinger equation, applying different initial wave functions. Such an approach is thought to be favourable as it allows to avoid the typical Hamiltonian approximations and include interminiband transmissions. During the particular research, authors manage to show the appearance of Bloch oscillations in different modes.

The above-mentioned Bloch oscillation modes include "center-of-mass oscillations" and "breathing oscillations" appearing due to different initial wavefunction applied. One of the examples for the initial wavefunction (via probability) and probability density (time and positioned dependent) for the former mode is depicted at Figure 6.13. The selected initial wavefunction is of particular interest as it corresponds to the one achievable within experiment, wherein electrons are excited by laser from the valence band. The wavefunction repre-

sents a set of Wannier functions providing approximately equal probability for 6 neighbouring wells. One may note periodic probability density oscillations in time representing the classical picture of the Bloch oscillations. Moreover, such oscillations supplement initial statement of the ice-breaking works of Esaki and Tsu [63, 236]. On the other hand, breathing mode is shown to be achieved by the wavefunctions comprising single Wannier state or the sum of separate Wannier states (occupied well is separated by at least one substantially empty well). In the breathing mode motion of the particles is found periodic, but lacking center-of-mass oscillatory behaviour (charges move to the both sides in the lattice; compare to Figure 6.13 depicting center-of-mass oscillations). The requirements to achieve breathing mode are considered as highly restrictive and unlikely to be met in actual experiment conditions.

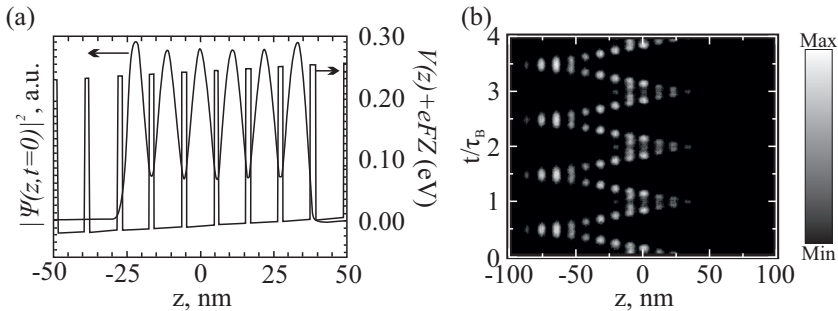


Figure 6.13: (a) Initial electron density probability and total potential energy as a function of z for the periodic GaAs/AlGaAs superlattice under DC bias. (b) Probability density as function of z and t/τ_B for the initial state and potential energy depicted in (a). The lighter the colour, the larger the probability density. Reprinted figure with permission from [236]. Copyright 1993 by the American Physical Society.

Moreover, the research considers a significant background of previously conducted Bloch oscillations experiments, fulfilling the gaps in the theoretical parts of the experiments. Employment of the described method reveals no-decay oscillations for at least 25 periods. In particular, quick decay, observed in the above-described experimental works [5, 6, 128, 237] is explained not by the interminiband hopping as claimed but some other effect not included within the model of independent electron Hamiltonian or due to the experimental imperfections (structure, setup etc.). The structural uncertainty is also partially addressed [236]. First of all, small random amount (up to 0.5%) addition of Aluminium to the GaAs wells was performed resulting in not strictly periodic profile and rounded well/barrier corners. Center-of-mass oscillations on frequency close to Bloch have been detected, due to small influence of random profile variation, that averages on the analysed large distance. It is stated that small profile roughening would not affect Bloch oscillation experiment and re-

sults are expected to be indistinguishable. On the other hand, contaminating one of the wells result periodic function wherein probability density described as an infinite Fourier series of incommensurate frequencies. Authors employ this effect and scattering to explain the quick dephasing in the work of Feldmann denying the provided assumption of interband transmission [5].

Considering the evolution of understanding the physics of Bloch oscillation, it is also important to note that at the early stages of the research, the above discussed negative effective mass mechanism of the electrons being accelerated beyond the inflection point of the Brillouin zone [63] and mechanism based on the electron localization of the Wannier-Stark states [123,124] were treated as physically different. It was shown that in case of WSL, transition probability decreases being inversely proportional to the square of the applied electric field strength, resulting in the appearance of the NDC [119]. As considerably wide-miniband superlattices are exploited in our research, especially high bias electric field would be expected to be required for this mechanism to become dominating. For example for the miniband $\Delta = 110$ meV, electric field strength of $E \approx 200$ kV/cm is expected for the Wannier-Stark ladder hopping mechanism [238]. It was experimentally proofed, considerably quickly, that both WSL and Esaki mechanisms are manifestations of the one physical effect: localization of electronic states by Bragg reflection [232,233]. Moreover, employment of the quantum theory of transport transition between the latter two mechanisms was show depicted via Green functions [239] and revealed experimentally [240,241]. However, this early-stage (before 1990-ies) misunderstanding is worth mentioning as considerable amount of articles, treating WSL and Esaki mechanisms as separate may be met.

As was mentioned in the main part of the text, K.Leo group concentrated on the optical excitation of the Wannier-Stark ladder and analysis of the generated Bloch oscillations using different methods. One of the methods is Degenerate Four-Wave Mixing (DFWM) technique [125]. During the DFWM two coherent pulses of two different wave vectors (k_1 and k_2) are sent with a specific time difference between the pulses (τ). To perform the DFWM mixing, photon-echo signal $k_3 = 2k_2 - k_1$ at 2τ is analysed for different τ . The degeneracy of the DFWM is featured by employment of two different initial pulses, one of which is used twice [242]. Considering the biased superlattice as a plurality of two-level systems, representing high localization level, first excitation excites all the systems with the same macroscopic phase of the dipole moment. With time, due to different evolution, dephasing occurs, but in the case of no bias applied second pulse at τ result in zero phase shift at $t = 2\tau$, recovering the initial macroscopic polarization leading to the emission of photon echo [5]. In the case of biased electric field, due to momentum time dependency (see Equation 1.3), not all excited electrons will feature zero phase shift interaction of dipole moments at $t = 2\tau$ with the second pulse. It is shown that only elec-

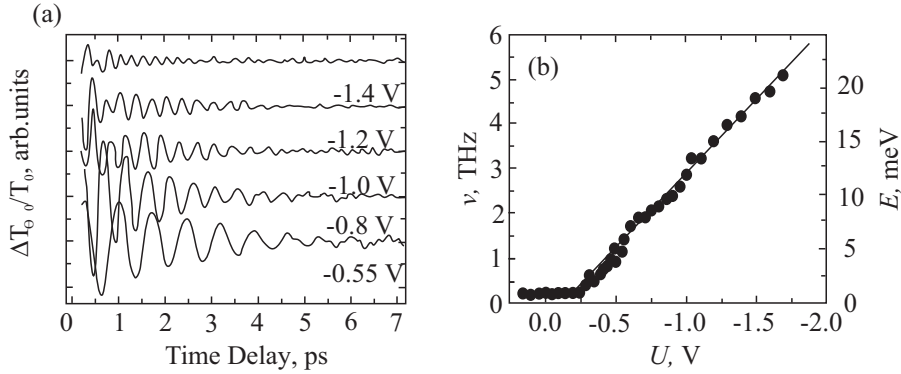


Figure 6.14: (a) TEOS oscillatory traces of transmission change in the superlattice for different reverse bias. (b) Frequency of Bloch oscillations changing with the change of DC bias voltage achieved from the Fourier transformation of the TEOS experimental data. Reprinted figure with permission from [127]. Copyright 1994 by the American Physical Society.

trons which travelled throughout the whole Brillouin zone between the pulses (τ equal to Bloch period) will be in phase after 2τ . It is mathematically and experimentally shown in the work of Plessen [125], that by sweeping the τ , strong photon echo peak may be observed at delay times corresponding to n -th Bloch oscillation period. Thus, detection of signal, modulated to Bloch period is expected. The correlation of the observed peaks to the Bloch oscillation have been shown by changing the electric field strength, thus, changing the Bloch oscillation period [5]. Moreover, the biasing sweep reveals response to the excitation on different not fully localized Wannier states [65].

Another method, widely employed at primary stages of the research of Bloch oscillations is the transmittive electro-optic sampling (TEOS). In difference to the above-discussed DFWM method, wherein Bloch oscillations are observed due to the interband modulation of polarization, the TEOS method allows to record Bloch oscillations, associated to the intraband modulation of polarisation [243]. Method exploits the linear electro-optics effect resulting in an induction of the optical anisotropy (birefringence) in GaAs/AlGaAs, which can be detected by the pump-probe system [244]. The polarization of the transmitted probe becomes elliptical and the degree is analysed by the differential comparison of the intensity along two main axes [128, 245]. Resultant image for different bias voltages omitting the instantaneous part is depicted at Figure 6.14 (a). One may see periodic Bloch oscillations with frequency being voltage dependent. Applying the Fourier transformation to the achieved oscillatory dependencies one may finally get the Bloch frequency voltage dependency as depicted at Figure 6.14 (b). One should note two regions: linear dependency above -0.25 V and flat dependency below -0.25 V. Both of the regions are of

extreme importance. First of all the linear dependency, corresponds to the above-disclosed theoretical considerations. The differences between the theoretically predicted and experimental slopes are explained by the appearance of the screening effects. Secondly, the flat dependency attributed to the excitonic-biexcitonic effects and inability of proper resolvancy, thus, is not fully disclosed in the discussed researches [127]. It will be shown in the further discussion and subsequent result section, that this biasing range supplement intriguing physical effects leading to the understanding on the effects inside the superlattice. It is important to note that the above discussed method also reveals existence of Bloch oscillations at room temperature conditions [129]. Increased temperature results in increased dephasing (dephasing time decreases three times), resulting in much quicker decreasing amount of TEOS amplitude

THz emission spectroscopy, being one of the most classical methods [246, 247], is worth mentioning in order to get the full picture on the research, related to the detection of Bloch oscillations [6]. Method is shown to allow direct observation of the Bloch oscillations in the superlattice featuring the same dependencies as discussed within the employment of other detection methods [126, 248].

6.1.6. Esaki-Tsu drift velocity/electric field dependency derivation

This appendix covers mathematical steps between Equation 1.4 and Equation 1.5. For the simplicity first lets simplify the derivative part by inserting sinusoidal approximation of E_x resulting in

$$\frac{\partial^2 E_x}{\partial k_x^2} = 0.5\Delta d^2 \cdot \cos(k_x d). \quad (\text{A.12})$$

Thus, the final integral (with k_x value included) to be solved is

$$v_d = \frac{eE_{tot}\Delta d^2}{2\hbar^2} \int_0^\infty \cos\left(\frac{eE_{tot}d}{\hbar}t\right) \exp\left(-\frac{t}{\tau}\right) dt. \quad (\text{A.13})$$

For simplicity $eE_{tot}d/\hbar$ will be treated as C_1 and $1/\tau$ will be treated as C_2 . To solve the integral basic $\int u dv = uv - \int v du$ rule is employed two times. First time with

$$\begin{aligned} u &= \cos(C_1 t) \rightarrow du = -C_1 \cdot \sin(C_1 t) dt \\ dv &= \exp(-C_2 t) dt \rightarrow v = -\frac{1}{C_2} \exp(-C_2 t) \end{aligned} \quad (\text{A.14})$$

results in

$$I = -\frac{1}{C_2} \cos(C_1 t) \exp(-C_2 t) - \frac{C_1}{C_2} \int_0^\infty \exp(-C_2 t) \sin(C_1 t) dt. \quad (\text{A.15})$$

Second time (based on the integral in Equation A.15) with

$$\begin{aligned} u &= \sin(C_1 t) \rightarrow du = C_1 \cdot \cos(C_1 t) dt \\ dv &= \exp(-C_2 t) dt \rightarrow v = -\frac{1}{C_2} \exp(-C_2 t) \end{aligned} \quad (\text{A.16})$$

the employment of the integration rule results in

$$\begin{aligned} I &= -\frac{1}{C_2} \cos(C_1 t) \exp(-C_2 t) - \frac{C_1}{C_2} \left[-\frac{1}{C_2} \sin(C_1 t) \exp(-C_2 t) \right] - \\ &\quad - \frac{C_1^2}{C_2^2} \left[\int_0^\infty \cos(C_1 t) \exp(-C_2 t) dt \right] \end{aligned} \quad (\text{A.17})$$

or

$$I = -\frac{1}{C_2} \cos(C_1 t) \exp(-C_2 t) + \frac{C_1}{C_2^2} \sin(C_1 t) \exp(-C_2 t) - \frac{C_1^2}{C_2^2} \cdot I. \quad (\text{A.18})$$

Moving I to the left side results in

$$I = \frac{-C_2 \cos(C_1 t) \exp(-C_2 t) + C_1 \sin(C_1 t) \exp(-C_2 t)}{C_1^2 + C_2^2} \Bigg|_0^\infty. \quad (\text{A.19})$$

Application of the boundaries gives the final integral equation

$$I = \frac{C_2}{C_1^2 + C_2^2}, \quad (\text{A.20})$$

and thus, the final drift velocity function is

$$v_d = \frac{e E_{tot} \Delta d^2}{2 \hbar^2} \frac{\frac{1}{\tau}}{\frac{e^2 E_{tot}^2 d^2}{\hbar^2} + \frac{1}{\tau^2}} = \frac{e E_{tot} \Delta d^2 \tau}{2(e^2 E_{tot}^2 d^2 \tau^2 + \hbar^2)} \quad (\text{A.21})$$

6.2. Appendix B. Additions to the methods section

6.2.1. Derivation of the critical electric field equation

The main task of this appendix is to derive critical electric field equation, which defines the electric field strength upon which peak drift velocity is reached. To start with one should take Esaki-Tsu drift velocity equation (cf. Equation 1.5)

$$v_d = \frac{eE_{\text{tot}}\Delta d^2\tau}{2(e^2E_{\text{tot}}^2d^2\tau^2 + \hbar^2)}. \quad (\text{B.1})$$

For simplicity imply $A = e\Delta d^2\tau$, $B = 2e^2d^2\tau^2$, $C = 2\hbar^2$. This results in $v_d = AE_{\text{tot}}/(BE_{\text{tot}}^2 + C)$. Differentiating the simplified equation over E_{tot} , and equating numerator to zero gives

$$\begin{aligned} (AE_{\text{tot}})'(BE_{\text{tot}}^2 + C) - (BE_{\text{tot}}^2 + C)'(AE_{\text{tot}}) &= A(BE_{\text{tot}}^2 + C) - 2BE_{\text{tot}}(AE_{\text{tot}}) = \\ &= ABE_{\text{tot}}^2 + AC - 2ABE_{\text{tot}}^2 = AC - ABE_{\text{tot}}^2 = A(C - BE_{\text{tot}}^2) = 0. \end{aligned} \quad (\text{B.2})$$

Thus

$$E_{\text{cr}} = \sqrt{\frac{C}{B}} = \sqrt{\frac{2\hbar^2}{2e^2d^2\tau^2}} = \frac{\hbar}{ed\tau}. \quad (\text{B.3})$$

Moreover, this equation allows to define peak velocity, based only on the parameters of the superlattice

$$v_p = \frac{e\frac{\hbar}{ed\tau}\Delta d^2\tau}{2e^2\frac{\hbar^2}{e^2d^2\tau^2}d^2\tau^2 + 2\hbar^2} = \frac{\hbar\Delta d}{4\hbar^2} = \frac{\Delta d}{4\hbar}. \quad (\text{B.4})$$

This result in drift velocity equation to take the final form of

$$v(E_{\text{tot}}) = 2v_p \frac{E_{\text{tot}}/E_{\text{cr}}}{1 + (E_{\text{tot}}/E_{\text{cr}})^2} = 2v_p \frac{F_{\text{tot}}}{1 + F_{\text{tot}}^2}, \quad (\text{B.5})$$

For the future, derivative of the latter equation will be found

$$\begin{aligned} \frac{\partial v}{\partial E_{\text{tot}}} &= 2v_p \frac{1/E_{\text{cr}} \cdot (1 + (E_{\text{tot}}/E_{\text{cr}})^2) - 2/E_{\text{cr}} * (E_{\text{tot}}/E_{\text{cr}})^2}{(1 + (E_{\text{tot}}/E_{\text{cr}})^2)^2} = \\ &= \frac{2v_p}{E_{\text{cr}}} \frac{1 - (E_{\text{tot}}/E_{\text{cr}})^2}{(1 + (E_{\text{tot}}/E_{\text{cr}})^2)^2} \end{aligned} \quad (\text{B.6})$$

6.2.2. Derivation of the high-frequency mobility equations for the degenerate case

The analysed integrals (averaging) are found to be considerably complicated, some are impossible to solve analytically. This appendix will provide the expanded info on the required integrals, employing analytic and numerical solving methods in order to supplement the conclusions given in the main text. To start with, one would like to gather all the required and already derived equations in one place. These include drift velocity and its derivative equations (cf. Equations 2.6 and B.6; in this case given in dimensionless type):

$$v_d(F_{\text{tot}}) = 2v_p \frac{F_{\text{tot}}}{1 + F_{\text{tot}}^2}; \quad \frac{\partial v_d}{\partial E_{\text{tot}}} = \frac{2v_p}{E_{\text{cr}}} \frac{1 - F_{\text{tot}}^2}{(1 + F_{\text{tot}}^2)^2}. \quad (\text{B.7})$$

Furthermore, Taylor series of the drift velocity is given as (cf. Equation 3.7)

$$v_d(E_{\text{tot}}) = v_d(E_{\text{pump}} + E_{\text{probe}}) \approx v_d(E_{\text{pump}}) + v'_d(E_{\text{pump}})E_1 \cos(\omega_1 t + \varphi_1). \quad (\text{B.8})$$

The next step is insertion of the above equations into different equations of the method section and solving the integral over specified amount of common periods. As one will note, the majority of the integrals can not be solved analytically, thus, only numerical solution remains. Two ways can be chosen: inserting everything into one long equation or dividing into small integrals, diminishing those equal to zero. The second way will be depicted in the current appendix.

Imaginary Mobility Component

First, lets apply the Taylor series equation to the imaginary mobility component of Equation 3.6. In this appendix if not stated otherwise common variable C will be used, demarking out-of-integral variables. Note that C may have different values within one equation. Equation

$$\begin{aligned} \frac{\mu_i}{\mu_0} &= \frac{E_{\text{cr}}}{v_p E_1} \langle v_d(E_{\text{tot}}) \sin(\omega_1 t + \varphi_1) \rangle_t = C \int_0^{2T} v_d(E_{\text{tot}}) \sin(\omega_1 t + \varphi_1) dt = \\ &= C \int_0^{2T} \left(v_d(E_{\text{pump}}) + v'_d(E_{\text{pump}})E_1 \cos(\omega_1 t + \varphi_1) \right) \sin(\omega_1 t + \varphi_1) dt \end{aligned} \quad (\text{B.9})$$

results in two independent integrals

$$\begin{aligned} &C \int_0^{2T} v_d(E_{\text{pump}}) \sin(\omega_1 t + \varphi_1) dt + \\ &+ C \int_0^{2T} v'_d(E_{\text{pump}}) \cos(\omega_1 t + \varphi_1) \sin(\omega_1 t + \varphi_1) dt. \end{aligned} \quad (\text{B.10})$$

For the simplicity the integrals will be analysed separately. Starting from the first one, inserting the drift velocity and $F_{\text{pump}} = F_{\text{dc}} + F_{\text{ac}} \cos(\omega_0 t)$ equations result in

$$\begin{aligned} I_1 &= C \int_0^{2T} \frac{F_{\text{pump}}}{1 + F_{\text{pump}}^2} \sin(\omega_1 t + \varphi_1) dt = \\ &= C \int_0^{2T} \frac{F_{\text{dc}} + F_{\text{ac}} \cos(\omega_0 t)}{1 + (F_{\text{dc}} + F_{\text{ac}} \cos(\omega_0 t))^2} \sin(\omega_1 t + \varphi_1) dt. \end{aligned} \quad (\text{B.11})$$

The integral itself can be divided into two simplified integrals

$$\begin{aligned} I_1 &= C \int_0^{2T} \frac{F_{\text{dc}}}{1 + (F_{\text{dc}} + F_{\text{ac}} \cos(\omega_0 t))^2} \sin(\omega_1 t + \varphi_1) dt + \\ &+ C \int_0^{2T} \frac{F_{\text{ac}} \cos(\omega_0 t)}{1 + (F_{\text{dc}} + F_{\text{ac}} \cos(\omega_0 t))^2} \sin(\omega_1 t + \varphi_1) dt, \end{aligned} \quad (\text{B.12})$$

leading to

$$\begin{aligned} I_{1.1} &= C \int_0^{2T} \frac{\sin(\omega_1 t + \varphi_1)}{1 + (F_{\text{dc}} + F_{\text{ac}} \cos(\omega_0 t))^2} dt; \\ I_{1.2} &= C \int_0^{2T} \frac{\cos(\omega_0 t) \sin(\omega_1 t + \varphi_1)}{1 + (F_{\text{dc}} + F_{\text{ac}} \cos(\omega_0 t))^2} dt. \end{aligned} \quad (\text{B.13})$$

Expanding the sine sum one should obtain

$$I_{1.1} = C \int_0^{2T} \frac{\sin(\omega_1 t) \cos(\varphi_1) + \cos(\omega_1 t) \sin(\varphi_1)}{1 + (F_{\text{dc}} + F_{\text{ac}} \cos(\omega_0 t))^2} dt \quad (\text{B.14})$$

or sum of two maximally simplified integrals

$$I_{1.1} = C \int_0^{2T} \frac{\sin(\omega_1 t) \cos(\varphi_1)}{1 + (F_{\text{dc}} + F_{\text{ac}} \cos(\omega_0 t))^2} dt + C \int_0^{2T} \frac{\cos(\omega_1 t) \sin(\varphi_1)}{1 + (F_{\text{dc}} + F_{\text{ac}} \cos(\omega_0 t))^2} dt. \quad (\text{B.15})$$

In both cases function is periodic over double common period, and the integral can not be solved analytically. Still it is easy to show numerically that both integrals converge to zero for any set of $F_{\text{dc}}, F_{\text{ac}}, \omega_1, \omega_0$. For the future applications these will be marked as

$$\begin{aligned} I_a &= C \int_0^{2T} \frac{\sin(\omega_1 t)}{1 + (F_{\text{dc}} + F_{\text{ac}} \cos(\omega_0 t))^2} dt \approx 0; \\ I_b &= C \int_0^{2T} \frac{\cos(\omega_1 t)}{1 + (F_{\text{dc}} + F_{\text{ac}} \cos(\omega_0 t))^2} dt \approx 0. \end{aligned} \quad (\text{B.16})$$

Considering integral $I_{1.2}$ of Equation B.13, same expansion of the sine sum results in

$$I_{1,2} = C \int_0^{2T} \frac{\cos(\omega_0 t) \left(\sin(\omega_1 t) \cos(\varphi_1) + \cos(\omega_1 t) \sin(\varphi_1) \right)}{1 + (F_{dc} + F_{ac} \cos(\omega_0 t))^2} dt \quad (\text{B.17})$$

or sum of two integrals

$$I_{1,2} = C \int_0^{2T} \frac{\cos(\omega_0 t) \sin(\omega_1 t) \cos(\varphi_1)}{1 + (F_{dc} + F_{ac} \cos(\omega_0 t))^2} dt + C \int_0^{2T} \frac{\cos(\omega_0 t) \cos(\omega_1 t) \sin(\varphi_1)}{1 + (F_{dc} + F_{ac} \cos(\omega_0 t))^2} dt. \quad (\text{B.18})$$

Both of the above most simplified integrals, also converges to zero

$$\begin{aligned} I_c &= C \int_0^{2T} \frac{\cos(\omega_0 t) \sin(\omega_1 t)}{1 + (F_{dc} + F_{ac} \cos(\omega_0 t))^2} dt \approx 0; \\ I_d &= C \int_0^{2T} \frac{\cos(\omega_0 t) \cos(\omega_1 t)}{1 + (F_{dc} + F_{ac} \cos(\omega_0 t))^2} dt \approx 0. \end{aligned} \quad (\text{B.19})$$

These considerations gives us understanding that integrals $I_{1,1}$, $I_{1,2}$ and consequently I_1 is zero.

Turning back to I_2 insertion of drift velocity derivative results in

$$\begin{aligned} I_2 &= C \int_0^{2T} \frac{1 - F_{\text{pump}}^2}{(1 + F_{\text{pump}}^2)^2} \cos(\omega_1 t + \varphi_1) \sin(\omega_1 t + \varphi_1) dt = \\ &= C \int_0^{2T} \frac{1 - (F_{dc} + F_{ac} \cos(\omega_0 t))^2}{(1 + (F_{dc} + F_{ac} \cos(\omega_0 t))^2)^2} \cos(\omega_1 t + \varphi_1) \sin(\omega_1 t + \varphi_1) dt. \end{aligned} \quad (\text{B.20})$$

Applying double angle trigonometry equations and further expanding the first half one would achieve

$$I_2 = \frac{C}{2} \int_0^{2T} \frac{1 - (F_{dc}^2 + 2F_{dc}F_{ac} \cos(\omega_0 t) + F_{ac}^2 \cos^2(\omega_0 t))}{(1 + (F_{dc} + F_{ac} \cos(\omega_0 t))^2)^2} \sin(2\omega_1 t + 2\varphi_1) dt \quad (\text{B.21})$$

resulting in three separate integrals

$$\begin{aligned} I_2 &= C \int_0^{2T} \frac{1 - F_{dc}^2}{(1 + (F_{dc} + F_{ac} \cos(\omega_0 t))^2)^2} \sin(2\omega_1 t + 2\varphi_1) dt + \\ &+ C \int_0^{2T} \frac{2F_{dc}F_{ac} \cos(\omega_0 t)}{(1 + (F_{dc} + F_{ac} \cos(\omega_0 t))^2)^2} \sin(2\omega_1 t + 2\varphi_1) dt + \\ &+ C \int_0^{2T} \frac{F_{ac}^2 \cos^2(\omega_0 t)}{(1 + (F_{dc} + F_{ac} \cos(\omega_0 t))^2)^2} \sin(2\omega_1 t + 2\varphi_1) dt. \end{aligned} \quad (\text{B.22})$$

Expanding double angle sine sum three independent integrals are achieved

$$\begin{aligned}
I_2 = & C \int_0^{2T} \frac{1}{(1 + (F_{dc} + F_{ac} \cos(\omega_0 t))^2)^2} \sin(2\omega_1 t) \cos(2\varphi_1) + \cos(2\omega_1 t) \sin(2\varphi_1) dt + \\
& + C \int_0^{2T} \frac{\cos(\omega_0 t)}{(1 + (F_{dc} + F_{ac} \cos(\omega_0 t))^2)^2} \sin(2\omega_1 t) \cos(2\varphi_1) + \cos(2\omega_1 t) \sin(2\varphi_1) dt + \\
& + C \int_0^{2T} \frac{\cos^2(\omega_0 t)}{(1 + (F_{dc} + F_{ac} \cos(\omega_0 t))^2)^2} \sin(2\omega_1 t) \cos(2\varphi_1) + \cos(2\omega_1 t) \sin(2\varphi_1) dt.
\end{aligned} \tag{B.23}$$

The final equation can be represented as 6 independent integrals

$$\begin{aligned}
I_2 = & C \int_0^{2T} \frac{\sin(2\omega_1 t) \cos(2\varphi_1)}{(1 + (F_{dc} + F_{ac} \cos(\omega_0 t))^2)^2} dt + \\
& + C \int_0^{2T} \frac{\cos(2\omega_1 t) \sin(2\varphi_1)}{(1 + (F_{dc} + F_{ac} \cos(\omega_0 t))^2)^2} dt + \\
& + C \int_0^{2T} \frac{\cos(\omega_0 t) \sin(2\omega_1 t) \cos(2\varphi_1)}{(1 + (F_{dc} + F_{ac} \cos(\omega_0 t))^2)^2} dt + \\
& + C \int_0^{2T} \frac{\cos(\omega_0 t) \cos(2\omega_1 t) \sin(2\varphi_1)}{(1 + (F_{dc} + F_{ac} \cos(\omega_0 t))^2)^2} dt + \\
& + C \int_0^{2T} \frac{\cos^2(\omega_0 t) \sin(2\omega_1 t) \cos(2\varphi_1)}{(1 + (F_{dc} + F_{ac} \cos(\omega_0 t))^2)^2} dt + \\
& + C \int_0^{2T} \frac{\cos^2(\omega_0 t) \cos(2\omega_1 t) \sin(2\varphi_1)}{(1 + (F_{dc} + F_{ac} \cos(\omega_0 t))^2)^2} dt
\end{aligned} \tag{B.24}$$

or

$$\begin{aligned}
I_{2.1} = & C \int_0^{2T} \frac{\sin(2\omega_1 t)}{(1 + (F_{dc} + F_{ac} \cos(\omega_0 t))^2)^2} dt \approx 0 \\
I_{2.2} = & C \int_0^{2T} \frac{\cos(2\omega_1 t)}{(1 + (F_{dc} + F_{ac} \cos(\omega_0 t))^2)^2} dt \approx 0 \\
I_{2.3} = & C \int_0^{2T} \frac{\cos(\omega_0 t) \sin(2\omega_1 t)}{(1 + (F_{dc} + F_{ac} \cos(\omega_0 t))^2)^2} dt \approx 0 \\
I_{2.4} = & C \int_0^{2T} \frac{\cos(\omega_0 t) \cos(2\omega_1 t)}{(1 + (F_{dc} + F_{ac} \cos(\omega_0 t))^2)^2} dt \approx 0 \\
I_{2.5} = & C \int_0^{2T} \frac{\cos^2(\omega_0 t) \sin(2\omega_1 t)}{(1 + (F_{dc} + F_{ac} \cos(\omega_0 t))^2)^2} dt \approx 0 \\
I_{2.6} = & C \int_0^{2T} \frac{\cos^2(\omega_0 t) \cos(2\omega_1 t)}{(1 + (F_{dc} + F_{ac} \cos(\omega_0 t))^2)^2} dt \approx 0.
\end{aligned} \tag{B.25}$$

All components being zero, result in total imaginary mobility component approaching zero. This shows that the imaginary component can be omitted for the total mobility calculation.

Real Mobility Component

To proceed, further analysis of the real mobility component is required. Applying Taylor series to the drift velocity equation, the real mobility component (cf. Equation 3.4) transforms into

$$\begin{aligned} \frac{\mu_r}{\mu_0} &= \frac{E_{cr}}{v_p E_1} \langle v_d(E_{tot}) \cos(\omega_1 t + \varphi_1) \rangle_t = \\ &= C \int_0^{2T} \left(v_d(E_{pump}) + v'_d(E_{pump}) E_1 \cos(\omega_1 t + \varphi_1) \right) \cos(\omega_1 t + \varphi_1) dt. \end{aligned} \quad (\text{B.26})$$

From now unless stated otherwise $C = 1/v_p F_1$. The integral can be expanded in order to achieve the separation into components as depicted in Equation 3.8

$$\begin{aligned} \frac{\mu_r}{\mu_0} &= C \int_0^{2T} v_d(E_{pump}) \cos(\omega_1 t + \varphi_1) dt + \\ &+ C \int_0^{2T} v'_d(E_{pump}) E_1 \cos(\omega_1 t + \varphi_1) \cos(\omega_1 t + \varphi_1) dt. \end{aligned} \quad (\text{B.27})$$

Applying double angle trigonometry equations

$$\begin{aligned} \frac{\mu_r}{\mu_0} &= C \int_0^{2T} v_d(E_{pump}) \cos(\omega_1 t + \varphi_1) dt + \\ &+ \frac{C E_1}{2} \int_0^{2T} v'_d(E_{pump}) (1 + \cos(2\omega_1 t + 2\varphi_1)) dt = \\ &= C \int_0^{2T} v_d(E_{pump}) \cos(\omega_1 t + \varphi_1) dt + \frac{C E_1}{2} \int_0^{2T} v'_d(E_{pump}) dt + \\ &+ \frac{C E_1}{2} \int_0^{2T} v'_d(E_{pump}) \cos(2\omega_1 t + 2\varphi_1) dt = A_h + A_{inc} + A_{coh}. \end{aligned} \quad (\text{B.28})$$

One note the match of the latter equation with the Equation 12 of the supplementary of [A1]. Next the components will be analysed separately.

A_h real mobility component analysis

Starting from the A_h , expanding sine sum and inserting the drift velocity relation:

$$\begin{aligned}
 A_h &= C \int_0^{2T} v_d(E_{\text{pump}}) \cos(\omega_1 t + \varphi_1) dt = \\
 &= C \int_0^{2T} 2v_p \frac{F_{\text{pump}}}{1 + F_{\text{pump}}^2} \left(\cos(\omega_1 t) \cos(\varphi_1) + \sin(\omega_1 t) \sin(\varphi_1) \right) dt = \\
 &= \frac{2 \cos(\varphi_1)}{F_1} \int_0^{2T} \frac{F_{\text{pump}}}{1 + F_{\text{pump}}^2} \cos(\omega_1 t) dt + \frac{2 \sin(\varphi_1)}{F_1} \int_0^{2T} \frac{F_{\text{pump}}}{1 + F_{\text{pump}}^2} \sin(\omega_1 t) dt.
 \end{aligned} \tag{B.29}$$

Inserting $F_{\text{pump}} = F_{\text{dc}} + F_{\text{ac}} \cos(\omega_0 t)$ results in

$$\begin{aligned}
 A_h &= \frac{2 \cos(\varphi_1)}{F_1} \int_0^{2T} \frac{F_{\text{dc}} + F_{\text{ac}} \cos(\omega_0 t)}{1 + (F_{\text{dc}} + F_{\text{ac}} \cos(\omega_0 t))^2} \cos(\omega_1 t) dt + \\
 &+ \frac{2 \sin(\varphi_1)}{F_1} \int_0^{2T} \frac{F_{\text{dc}} + F_{\text{ac}} \cos(\omega_0 t)}{1 + (F_{\text{dc}} + F_{\text{ac}} \cos(\omega_0 t))^2} \sin(\omega_1 t) dt
 \end{aligned} \tag{B.30}$$

or

$$\begin{aligned}
 A_h &= \frac{2 \cos(\varphi_1)}{F_1} \int_0^{2T} \frac{F_{\text{dc}} \cos(\omega_1 t)}{1 + (F_{\text{dc}} + F_{\text{ac}} \cos(\omega_0 t))^2} dt + \\
 &+ \frac{2 \cos(\varphi_1)}{F_1} \int_0^{2T} \frac{F_{\text{ac}} \cos(\omega_0 t) \cos(\omega_1 t)}{1 + (F_{\text{dc}} + F_{\text{ac}} \cos(\omega_0 t))^2} dt + \\
 &+ \frac{2 \sin(\varphi_1)}{F_1} \int_0^{2T} \frac{F_{\text{dc}} \sin(\omega_1 t)}{1 + (F_{\text{dc}} + F_{\text{ac}} \cos(\omega_0 t))^2} dt + \\
 &+ \frac{2 \sin(\varphi_1)}{F_1} \int_0^{2T} \frac{F_{\text{ac}} \cos(\omega_0 t) \sin(\omega_1 t)}{1 + (F_{\text{dc}} + F_{\text{ac}} \cos(\omega_0 t))^2} dt
 \end{aligned} \tag{B.31}$$

or

$$\begin{aligned}
 A_h &= \frac{2F_{\text{dc}} \cos(\varphi_1)}{F_1} \int_0^{2T} \frac{\cos(\omega_1 t)}{1 + (F_{\text{dc}} + F_{\text{ac}} \cos(\omega_0 t))^2} dt + \\
 &+ \frac{2F_{\text{ac}} \cos(\varphi_1)}{F_1} \int_0^{2T} \frac{\cos(\omega_0 t) \cos(\omega_1 t)}{1 + (F_{\text{dc}} + F_{\text{ac}} \cos(\omega_0 t))^2} dt + \\
 &+ \frac{2F_{\text{dc}} \sin(\varphi_1)}{F_1} \int_0^{2T} \frac{\sin(\omega_1 t)}{1 + (F_{\text{dc}} + F_{\text{ac}} \cos(\omega_0 t))^2} dt + \\
 &+ \frac{2F_{\text{ac}} \sin(\varphi_1)}{F_1} \int_0^{2T} \frac{\cos(\omega_0 t) \sin(\omega_1 t)}{1 + (F_{\text{dc}} + F_{\text{ac}} \cos(\omega_0 t))^2} dt.
 \end{aligned} \tag{B.32}$$

The derived integrals correspond to the already analyzed I_{a-d} and are equal to zero. Resulting $A_h = 0$ and Equation B.28 to be modified as

$$\begin{aligned}
\frac{\mu_r}{\mu_0} &= \frac{CE_1}{2} \int_0^{2T} v'_d(E_{\text{pump}}) dt + \frac{CE_1}{2} \int_0^{2T} v'_d(E_{\text{pump}}) \cos(2\omega_1 t + 2\varphi_1) dt = \\
&= A_{\text{inc}} + A_{\text{coh}}.
\end{aligned} \tag{B.33}$$

A_{inc} real mobility component analysis

Proceeding with the incoherent part inserting drift velocity derivative equation results in

$$\begin{aligned}
A_{\text{inc}} &= \frac{CE_1}{2} \int_0^{2T} v'_d(E_{\text{pump}}) dt = \frac{E_1}{2v_p F_1} \int_0^{2T} \frac{2v_p}{E_{\text{cr}}} \frac{1 - F_{\text{pump}}^2}{(1 + F_{\text{pump}}^2)^2} dt = \\
&= \int_0^{2T} \frac{1 - (F_{\text{dc}} + F_{\text{ac}} \cos(\omega_0 t))^2}{(1 + (F_{\text{dc}} + F_{\text{ac}} \cos(\omega_0 t))^2)^2} dt = \\
&= \int_0^{2T} \frac{1 - (F_{\text{dc}}^2 + 2F_{\text{dc}}F_{\text{ac}} \cos(\omega_0 t) + F_{\text{ac}}^2 \cos^2(\omega_0 t))}{(1 + (F_{\text{dc}} + F_{\text{ac}} \cos(\omega_0 t))^2)^2} dt = \\
&= \int_0^{2T} \frac{1 - F_{\text{dc}}^2}{(1 + (F_{\text{dc}} + F_{\text{ac}} \cos(\omega_0 t))^2)^2} dt - \\
&\quad - \int_0^{2T} \frac{2F_{\text{dc}}F_{\text{ac}} \cos(\omega_0 t)}{(1 + (F_{\text{dc}} + F_{\text{ac}} \cos(\omega_0 t))^2)^2} dt - \\
&\quad - \int_0^{2T} \frac{F_{\text{ac}}^2 \cos^2(\omega_0 t)}{(1 + (F_{\text{dc}} + F_{\text{ac}} \cos(\omega_0 t))^2)^2} dt
\end{aligned} \tag{B.34}$$

or

$$\begin{aligned}
A_{\text{inc}} &= (1 - F_{\text{dc}}^2) \int_0^{2T} \frac{1}{(1 + (F_{\text{dc}} + F_{\text{ac}} \cos(\omega_0 t))^2)^2} dt - \\
&\quad - 2F_{\text{dc}}F_{\text{ac}} \int_0^{2T} \frac{\cos(\omega_0 t)}{(1 + (F_{\text{dc}} + F_{\text{ac}} \cos(\omega_0 t))^2)^2} dt - \\
&\quad - F_{\text{ac}}^2 \int_0^{2T} \frac{\cos^2(\omega_0 t)}{(1 + (F_{\text{dc}} + F_{\text{ac}} \cos(\omega_0 t))^2)^2} dt.
\end{aligned} \tag{B.35}$$

Numerical solution reveals all the integrals not to be equal to zero, thus, none of these can be omitted.

A_{coh} real mobility component analysis

Proceeding with the coherent part, applying the same procedure

$$\begin{aligned}
 A_{\text{coh}} &= \frac{CE_1}{2} \int_0^{2T} v'_d(E_{\text{pump}}) \cos(2\omega_1 t + 2\varphi_1) dt = \\
 &= \frac{CE_1}{2} \int_0^{2T} v'_d(E_{\text{pump}}) \left(\cos(2\omega_1 t) \cos(2\varphi_1) - \sin(2\omega_1 t) \sin(2\varphi_1) \right) dt = \\
 &= \frac{CE_1}{2} \int_0^{2T} v'_d(E_{\text{pump}}) \cos(2\omega_1 t) \cos(2\varphi_1) dt - \\
 &\quad - \frac{CE_1}{2} \int_0^{2T} v'_d(E_{\text{pump}}) \sin(2\omega_1 t) \sin(2\varphi_1) dt = \\
 &= \frac{E_1 \cos(2\varphi_1)}{2v_p F_1} \int_0^{2T} v'_d(E_{\text{pump}}) \cos(2\omega_1 t) dt - \\
 &\quad - \frac{E_1 \sin(2\varphi_1)}{2v_p F_1} \int_0^{2T} v'_d(E_{\text{pump}}) \sin(2\omega_1 t) dt.
 \end{aligned} \tag{B.36}$$

Inserting the derivative of the drift velocity corresponding to the Equation B.6 results in

$$\begin{aligned}
 A_{\text{coh}} &= \frac{E_1 \cos(2\varphi_1)}{2v_p F_1} \int_0^{2T} \frac{2v_p}{E_{\text{cr}}} \frac{1 - F_{\text{pump}}^2}{(1 + F_{\text{pump}}^2)^2} \cos(2\omega_1 t) dt - \\
 &\quad - \frac{E_1 \sin(2\varphi_1)}{2v_p F_1} \int_0^{2T} \frac{2v_p}{E_{\text{cr}}} \frac{1 - F_{\text{pump}}^2}{(1 + F_{\text{pump}}^2)^2} \sin(2\omega_1 t) dt = \\
 &= \cos(2\varphi_1) \int_0^{2T} \frac{1 - F_{\text{pump}}^2}{(1 + F_{\text{pump}}^2)^2} \cos(2\omega_1 t) dt - \\
 &\quad - \sin(2\varphi_1) \int_0^{2T} \frac{1 - F_{\text{pump}}^2}{(1 + F_{\text{pump}}^2)^2} \sin(2\omega_1 t) dt.
 \end{aligned} \tag{B.37}$$

Inserting $F_{\text{pump}} = F_{\text{dc}} + F_{\text{ac}} \cos(\omega_0 t)$ results in

$$\begin{aligned}
 A_{\text{coh}} &= \cos(2\varphi_1) \int_0^{2T} \frac{1 - (F_{\text{dc}} + F_{\text{ac}} \cos(\omega_0 t))^2}{(1 + (F_{\text{dc}} + F_{\text{ac}} \cos(\omega_0 t))^2)^2} \cos(2\omega_1 t) dt - \\
 &\quad - \sin(2\varphi_1) \int_0^{2T} \frac{1 - (F_{\text{dc}} + F_{\text{ac}} \cos(\omega_0 t))^2}{(1 + (F_{\text{dc}} + F_{\text{ac}} \cos(\omega_0 t))^2)^2} \sin(2\omega_1 t) dt = I_3 + I_4.
 \end{aligned} \tag{B.38}$$

Next, separation into two independent integrals results in

$$\begin{aligned}
I_3 &= \cos(2\varphi_1) \int_0^{2T} \frac{1 - \left(F_{\text{dc}}^2 + 2F_{\text{dc}}F_{\text{ac}} \cos(\omega_0 t) + F_{\text{ac}}^2 \cos^2(\omega_0 t) \right)}{\left(1 + (F_{\text{dc}} + F_{\text{ac}} \cos(\omega_0 t))^2 \right)^2} \cos(2\omega_1 t) dt = \\
&= \cos(2\varphi_1) \int_0^{2T} \frac{1 - F_{\text{dc}}^2}{\left(1 + (F_{\text{dc}} + F_{\text{ac}} \cos(\omega_0 t))^2 \right)^2} \cos(2\omega_1 t) dt - \\
&- \cos(2\varphi_1) \int_0^{2T} \frac{2F_{\text{dc}}F_{\text{ac}} \cos(\omega_0 t)}{\left(1 + (F_{\text{dc}} + F_{\text{ac}} \cos(\omega_0 t))^2 \right)^2} \cos(2\omega_1 t) dt - \\
&- \cos(2\varphi_1) \int_0^{2T} \frac{F_{\text{ac}}^2 \cos^2(\omega_0 t)}{\left(1 + (F_{\text{dc}} + F_{\text{ac}} \cos(\omega_0 t))^2 \right)^2} \cos(2\omega_1 t) dt.
\end{aligned} \tag{B.39}$$

Expanding double cosine one achieve final 6 most simplified integrals to analyse

$$\begin{aligned}
I_3 &= \cos(2\varphi_1) \int_0^{2T} \frac{1 - \left(F_{\text{dc}}^2 + 2F_{\text{dc}}F_{\text{ac}} \cos(\omega_0 t) + F_{\text{ac}}^2 \cos^2(\omega_0 t) \right)}{\left(1 + (F_{\text{dc}} + F_{\text{ac}} \cos(\omega_0 t))^2 \right)^2} \cos(2\omega_1 t) dt = \\
&= (1 - F_{\text{dc}}^2) \cos(2\varphi_1) \int_0^{2T} \frac{\cos^2(\omega_1 t)}{\left(1 + (F_{\text{dc}} + F_{\text{ac}} \cos(\omega_0 t))^2 \right)^2} dt - \\
&- (1 - F_{\text{dc}}^2) \cos(2\varphi_1) \int_0^{2T} \frac{\sin^2(\omega_1 t)}{\left(1 + (F_{\text{dc}} + F_{\text{ac}} \cos(\omega_0 t))^2 \right)^2} dt - \\
&- 2F_{\text{dc}}F_{\text{ac}} \cos(2\varphi_1) \int_0^{2T} \frac{\cos^2(\omega_1 t) \cos(\omega_0 t)}{\left(1 + (F_{\text{dc}} + F_{\text{ac}} \cos(\omega_0 t))^2 \right)^2} dt + \\
&+ 2F_{\text{dc}}F_{\text{ac}} \cos(2\varphi_1) \int_0^{2T} \frac{\sin^2(\omega_1 t) \cos(\omega_0 t)}{\left(1 + (F_{\text{dc}} + F_{\text{ac}} \cos(\omega_0 t))^2 \right)^2} dt - \\
&- F_{\text{ac}}^2 \cos(2\varphi_1) \int_0^{2T} \frac{\cos^2(\omega_1 t) \cos^2(\omega_0 t)}{\left(1 + (F_{\text{dc}} + F_{\text{ac}} \cos(\omega_0 t))^2 \right)^2} dt + \\
&+ F_{\text{ac}}^2 \cos(2\varphi_1) \int_0^{2T} \frac{\sin^2(\omega_1 t) \cos^2(\omega_0 t)}{\left(1 + (F_{\text{dc}} + F_{\text{ac}} \cos(\omega_0 t))^2 \right)^2} dt.
\end{aligned} \tag{B.40}$$

Neither of these integrals equals to zero, thus, none of these can be omitted.

All of the above consideration prove that the final mobility equation is

$$\frac{\mu}{\mu_0} = \frac{1}{v_p F_1} \int_0^{2T} \left(v_d(E_{\text{pump}}) + v'_d(E_{\text{pump}}) E_1 \cos(\omega_1 t + \varphi_1) \right) \cos(\omega_1 t + \varphi_1) dt. \tag{B.41}$$

REFERENCES

- [1] V. Čižas, L. Subačius, N. V. Alexeeva, D. Seliuta, T. Hyart, K. Köhler, K. N. Alekseev, G. Valušis, Dissipative parametric gain in a GaAs/AlGaAs superlattice, *Physical Review Letters* **128**(23), 236802 (2022), <https://doi.org/10.1103/PhysRevLett.128.236802>.
- [2] G. Valušis, K. Alekseev, V. Čižas, L. Minkevičius, N. Alexeeva, D. Seliuta, L. Subačius, Broadband high-frequency radiation generating/amplifying device based on quantum semiconductor superlattice, *Lithuanian Patent* 7000 (2023).
- [3] V. Čižas, N. V. Alexeeva, K. N. Alekseev, G. Valušis, Coexistence of Bloch and parametric mechanisms of high-frequency gain in doped superlattices, *Nanomaterials* **13**(13), 1993 (2023), <https://doi.org/10.3390/nano13131993>.
- [4] V. Čižas, N. V. Alexeeva, K. Alekseev, G. Valušis, Sum-frequency generation and amplification processes in semiconductor superlattices, *Lithuanian Journal of Physics* **63**(3), 148–154 (2023), <https://doi.org/10.3952/physics.2023.63.3.5>.
- [5] J. Feldmann, K. Leo, J. Shah, D. A. Miller, J. Cunningham, T. Meier, G. Von Plessen, A. Schulze, P. Thomas, S. Schmitt-Rink, Optical investigation of Bloch oscillations in a semiconductor superlattice, *Physical Review B* **46**(11), 7252 (1992), <https://doi.org/10.1103/PhysRevB.46.7252>.
- [6] C. Waschke, H. G. Roskos, R. Schwedler, K. Leo, H. Kurz, K. Köhler, Coherent submillimeter-wave emission from Bloch oscillations in a semiconductor superlattice, *Physical Review Letters* **70**(21), 3319 (1993), <https://doi.org/10.1103/PhysRevLett.70.3319>.
- [7] V. G. Lyssenko, G. Valušis, F. Löser, T. Hasche, K. Leo, M. M. Dignam, K. Köhler, Direct measurement of the spatial displacement of Bloch-oscillating electrons in semiconductor superlattices, *Physical Review Letters* **79**, 301–304 (1997), <https://doi.org/10.1103/PhysRevLett.79.301>.
- [8] T. Bauer, J. Kolb, A. B. Hummel, H. G. Roskos, Y. Kosovich, K. Köhler, Coherent Hall effect in a semiconductor superlattice, *Physical Review Letters* **88**, 086801 (2002), <https://doi.org/10.1103/PhysRevLett.88.086801>.
- [9] J. Y. Romanova, E. Demidov, L. Mourokh, Y. A. Romanov, Zener tunneling in semiconductor superlattices, *Journal of Physics: Condensed Matter* **23**(30), 305801 (2011).
- [10] W. Shi, S. Kahn, N. Leconte, T. Taniguchi, K. Watanabe, M. Crommie, J. Jung, A. Zettl, High-order fractal quantum oscillations in graphene/BN superlattices in the extreme doping limit, *Physical Review Letters* **130**, 186204 (2023), <https://doi.org/10.1103/PhysRevLett.130.186204>.

- [11] M. A. Belkin, F. Capasso, New frontiers in quantum cascade lasers: high performance room temperature terahertz sources, *Physica Scripta* **90**(11), 118002 (2015).
- [12] K. F. Renk, B. I. Stahl, A. Rogl, T. Janzen, D. G. Pavel'ev, Y. I. Koshurinov, V. Ustinov, A. Zhukov, Subterahertz superlattice parametric oscillator, *Physical Review Letters* **95**, 126801 (2005), <https://doi.org/10.1103/PhysRevLett.95.126801>.
- [13] K. Renk, A. Rogl, B. Stahl, Semiconductor-superlattice parametric oscillator for generation of sub-terahertz and terahertz waves, *Journal of Luminescence* **125**(1), 252–258, festschrift in Honor of Academician Alexander A. Kaplyanskii (2007), <https://doi.org/https://doi.org/10.1016/j.jlumin.2006.08.037>.
- [14] S. Ktitorov, G. Simin, V. Sindalovskij, Влияние Брэгговских отражений на высокочастотную проводимость электронной плазмы твердого тела, *Soviet Physics of Solid State* **13**(8), 2230–2233 (1971).
- [15] R. Terazzi, T. Gresch, M. Giovannini, N. Hoyler, N. Sekine, J. Faist, Bloch gain in quantum cascade lasers, *Nature Physics* **3**(5), 329–333 (2007), <https://doi.org/10.1038/nphys577>.
- [16] A. Wacker, Coexistence of gain and absorption, *Nature Physics* **3**(5), 298–299 (2007), <https://doi.org/10.1038/nphys603>.
- [17] C. Chaccour, M. N. Soorki, W. Saad, M. Bennis, P. Popovski, M. Debbah, Seven defining features of terahertz (THz) wireless systems: A fellowship of communication and sensing, *IEEE Communications Surveys & Tutorials* **24**(2), 967–993 (2022).
- [18] H. Sameddeen, M.-S. Alouini, T. Y. Al-Naffouri, An overview of signal processing techniques for terahertz communications, *Proceedings of the IEEE* **109**(10), 1628–1665 (2021).
- [19] M. Koch, D. M. Mittleman, J. Ornik, E. Castro-Camus, Terahertz time-domain spectroscopy, *Nature Reviews Methods Primers* **3**(1), 48 (2023).
- [20] E. Castro-Camus, M. Koch, D. M. Mittleman, Recent advances in terahertz imaging: 1999 to 2021, *Applied Physics B* **128**(1), 12 (2022).
- [21] G. Valušis, A. Lisauskas, H. Yuan, W. Knap, H. G. Roskos, Roadmap of terahertz imaging 2021, *Sensors* **21**(12), 4092 (2021).
- [22] A. Leitenstorfer, A. S. Moskalenko, T. Kampfrath, J. Kono, E. Castro-Camus, K. Peng, N. Qureshi, D. Turchinovich, K. Tanaka, A. G. Markelz, et al., The 2023 terahertz science and technology roadmap, *Journal of Physics D: Applied Physics* **56**(22), 223001 (2023).
- [23] J. F. Federici, D. Gary, R. Barat, D. Zimdars, Terahertz imaging using an interferometric array, in *Terahertz for Military and Security Applications III* (SPIE, 2005), volume 5790, 11–18.

- [24] Q. Song, Y. Zhao, A. Redo-Sanchez, C. Zhang, X. Liu, Fast continuous terahertz wave imaging system for security, *Optics Communications* **282**(10), 2019–2022 (2009).
- [25] D. Zimdars, J. S. White, Terahertz reflection imaging for package and personnel inspection, in *Terahertz for Military and Security Applications II* (SPIE, 2004), volume 5411, 78–83.
- [26] Y. Morita, A. Dobroiu, K. Kawase, C. Otani, Terahertz technique for detection of microleaks in the seal of flexible plastic packages, *Optical Engineering* **44**(1), 019001–019001 (2005).
- [27] K. W. Kim, K.-S. Kim, H. Kim, S. H. Lee, J.-H. Park, J.-H. Han, S.-H. Seok, J. Park, Y. Choi, Y. I. Kim, et al., Terahertz dynamic imaging of skin drug absorption, *Optics express* **20**(9), 9476–9484 (2012).
- [28] G. Choi, D.-H. Lee, I. Park, D. Kang, H. K. Lee, J. Rhie, Y.-M. Bahk, Evaluation of moisturizing cream using terahertz time-domain spectroscopy, *Current Applied Physics* **39**, 84–89 (2022).
- [29] L. Afsah-Hejri, P. Hajeb, P. Ara, R. J. Ehsani, A comprehensive review on food applications of terahertz spectroscopy and imaging, *Comprehensive Reviews in Food Science and Food Safety* **18**(5), 1563–1621 (2019).
- [30] Y. Zhang, C. Wang, B. Huai, S. Wang, Y. Zhang, D. Wang, L. Rong, Y. Zheng, Continuous-wave THz imaging for biomedical samples, *Applied Sciences* **11**(1), 71 (2020).
- [31] X. G. Peralta, D. Lipscomb, G. J. Wilmink, I. Echchgadda, Terahertz spectroscopy of human skin tissue models with different melanin content, *Biomedical optics express* **10**(6), 2942–2955 (2019).
- [32] Y. Wang, H. Minamide, M. Tang, T. Notake, H. Ito, Study of water concentration measurement in thin tissues with terahertz-wave parametric source, *Optics Express* **18**(15), 15504–15512 (2010), <https://doi.org/10.1364/OE.18.015504>.
- [33] R. Ivaškevičiūtė-Povilauskienė, V. Čižas, E. Nacius, I. Grigelionis, K. Re-deckas, M. Bernatonis, S. Orlov, G. Valušis, L. Minkevičius, Flexible terahertz optics: light beam profile engineering via C-shaped metallic metasurface, *Frontiers in Physics* **11**, 1196726 (2023).
- [34] R. Ivaškevičiūtė-Povilauskienė, P. Kizevičius, E. Nacius, D. Jokubauskis, K. Ikamas, A. Lisauskas, N. Alexeeva, I. Matulaitienė, V. Jukna, S. Orlov, et al., Terahertz structured light: nonparaxial Airy imaging using silicon diffractive optics, *Light: Science & Applications* **11**(1), 326 (2022).
- [35] S. Orlov, R. Ivaškevičiūtė-Povilauskienė, K. Mundrys, P. Kizevičius, E. Nacius, D. Jokubauskis, K. Ikamas, A. Lisauskas, L. Minkevičius, G. Valušis, Light engineering and silicon diffractive optics assisted nonparaxial terahertz imaging, *Laser & Photonics Reviews* 2301197 (2024).

- [36] K. Stanaitis, K. Redekas, A. Bielevičiūtė, M. Bernatoniš, D. Jokubauskis, V. Čizas, L. Minkevičius, Study of the low-cost HIPS and paraffin-based terahertz optical components, *Lithuanian Journal of Physics* **63**(4) (2023).
- [37] I. Gayduchenko, G. Fedorov, M. Moskotin, D. Yagodkin, S. Seliverstov, G. Goltsman, A. Y. Kuntsevich, M. Rybin, E. Obraztsova, V. Leiman, et al., Manifestation of plasmonic response in the detection of sub-terahertz radiation by graphene-based devices, *Nanotechnology* **29**(24), 245204 (2018).
- [38] A. Ahmadvand, R. Sinha, B. Gerislioglu, M. Karabiyik, N. Pala, M. Shur, Transition from capacitive coupling to direct charge transfer in asymmetric terahertz plasmonic assemblies, *Optics letters* **41**(22), 5333–5336 (2016).
- [39] A. Arlauskas, P. Svidovsky, K. Bertulis, R. Adomavičius, A. Krotkus, GaAsBi photoconductive terahertz detector sensitivity at long excitation wavelengths, *Applied Physics Express* **5**(2), 022601 (2012).
- [40] D. V. Lavrukhin, A. E. Yachmenev, Y. G. Goncharov, K. I. Zaytsev, R. A. Khabibullin, A. M. Buryakov, E. D. Mishina, D. S. Ponomarev, Strain-induced InGaAs-based photoconductive terahertz antenna detector, *IEEE Transactions on Terahertz Science and Technology* **11**(4), 417–424 (2021).
- [41] A. Shurakov, Y. Lobanov, G. Goltsman, Superconducting hot-electron bolometer: from the discovery of hot-electron phenomena to practical applications, *Superconductor Science and Technology* **29**(2), 023001 (2015).
- [42] V. Ryzhii, I. Khmyrova, M. Ryzhii, V. Mitin, Comparison of dark current, responsivity and detectivity in different intersubband infrared photodetectors, *Semiconductor science and technology* **19**(1), 8 (2003).
- [43] V. Ryzhii, Negative differential photoconductivity in quantum-dot infrared photodetectors, *Applied Physics Letters* **78**(21), 3346–3348 (2001).
- [44] V. Desmaris, H. Rashid, A. Pavolotsky, V. Belitsky, Design, simulations and optimization of micromachined Golay-cell based THz sensors operating at room temperature, *Procedia Chemistry* **1**(1), 1175–1178 (2009).
- [45] R. Müller, B. Gutschwager, J. Hollandt, M. Kehrt, C. Monte, R. Müller, A. Steiger, Characterization of a large-area pyroelectric detector from 300 GHz to 30 THz, *Journal of Infrared, Millimeter, and Terahertz Waves* **36**, 654–661 (2015).
- [46] F. Simoens, Thz bolometer detectors, *Physics and Applications of Terahertz Radiation* 35–75 (2014).
- [47] Y. Shin, G. Park, G. Scheitrum, G. Caryotakis, Circuit analysis of an extended interaction klystron, *Journal-Korean Physical Society* **44**(2), 1239–1245 (2004).

- [48] B. Knyazev, G. Kulipanov, N. Vinokurov, Novosibirsk terahertz free electron laser: instrumentation development and experimental achievements, *Measurement Science and Technology* **21**(5), 054017 (2010).
- [49] C. Sung, S. Y. Tochitsky, S. Reiche, J. Rosenzweig, C. Pellegrini, C. Joshi, Seeded free-electron and inverse free-electron laser techniques for radiation amplification and electron microbunching in the terahertz range, *Physical Review Special Topics-Accelerators and Beams* **9**(12), 120703 (2006).
- [50] L.-A. Yang, Y. Hao, Q. Yao, J. Zhang, Improved negative differential mobility model of GaN and AlGa_N for a terahertz Gunn diode, *IEEE Transactions on Electron Devices* **58**(4), 1076–1083 (2011).
- [51] S. Pérez, T. González, D. Pardo, J. Mateos, Terahertz Gunn-like oscillations in InGaAs/InAlAs planar diodes, *Journal of applied physics* **103**(9) (2008).
- [52] W. Knap, J. Lusakowski, T. Parenty, S. Bollaert, A. Cappy, V. Popov, M. Shur, Terahertz emission by plasma waves in 60 nm gate high electron mobility transistors, *Applied Physics Letters* **84**(13), 2331–2333 (2004).
- [53] M. S. Shur, J.-Q. Lu, Terahertz sources and detectors using two-dimensional electronic fluid in high electron-mobility transistors, *IEEE Transactions on microwave theory and techniques* **48**(4), 750–756 (2000).
- [54] J. Darmo, V. Tamosiunas, G. Fasching, J. Kröll, K. Unterrainer, M. Beck, M. Giovannini, J. Faist, C. Kremser, P. Debbage, Imaging with a terahertz quantum cascade laser, *Optics express* **12**(9), 1879–1884 (2004).
- [55] L. Bosco, M. Franckić, G. Scalari, M. Beck, A. Wacker, J. Faist, Thermoelectrically cooled THz quantum cascade laser operating up to 210 K, *Applied Physics Letters* **115**(1) (2019).
- [56] H.-W. Hübers, A. Semenov, K. Holldack, U. Schade, G. Wüstefeld, G. Gol'tsman, Time domain analysis of coherent terahertz synchrotron radiation, *Applied Physics Letters* **87**(18) (2005).
- [57] Y. J. Ding, Progress in terahertz sources based on difference-frequency generation, *JOSA B* **31**(11), 2696–2711 (2014).
- [58] M. A. Belkin, F. Capasso, F. Xie, A. Belyanin, M. Fischer, A. Wittmann, J. Faist, Room temperature terahertz quantum cascade laser source based on intracavity difference-frequency generation, *Applied Physics Letters* **92**(20) (2008).
- [59] K. Kawase, J. Shikata, M. Sato, T. Taniuchi, H. Ito, Widely tunable coherent terahertz-wave generation using nonlinear optical effect, *Electronics and Communications in Japan (Part II: Electronics)* **81**(7), 10–18 (1998).

- [60] H. Zhao, Q. An, X. Ye, B. Yu, Q. Zhang, F. Sun, Q. Zhang, F. Yang, J. Guo, J. Zhao, Second harmonic generation in AB-type LaTiO₃/SrTiO₃ superlattices, *Nano Energy* **82**, 105752 (2021), <https://doi.org/10.1016/j.nanoen.2021.105752>.
- [61] C. Wang, M. J. Burek, Z. Lin, H. A. Atikian, V. Venkataraman, I.-C. Huang, P. Stark, M. Lončar, Integrated high quality factor lithium niobate microdisk resonators, *Optics Express* **22**(25), 30924–30933 (2014), <https://doi.org/10.1364/OE.22.030924>.
- [62] M. Asada, S. Suzuki, Thz resonant tunneling devices, *Fundamentals of Terahertz Devices and Applications* 447–477 (2021).
- [63] L. Esaki, R. Tsu, Superlattice and negative differential conductivity in semiconductors, *IBM Journal of Research and Development* **14**(1), 61–65 (1970), <https://doi.org/10.1147/rd.141.0061>.
- [64] L. Mandelstam, N. Papalexii, Über resonanzerscheinungen bei frequenzteilung, *Zeitschrift für Physik* **73**(3), 223–248 (1932), <https://doi.org/10.1007/BF01351217>.
- [65] K. Leo, J. Feldmann, J. Shah, G. von Plessen, P. Thomas, S. Schmitt-Rink, J. Cunningham, Optical investigation of Bloch oscillations in semiconductor superlattices, *Superlattices and Microstructures* **13**(1), 55–60 (1993), <https://doi.org/10.1103/PhysRevB.46.7252>.
- [66] E. J. Ryder, W. Shockley, Mobilities of electrons in high electric fields, *Physical Review* **81**(1), 139–140 (1951), <https://doi.org/10.1103/PhysRev.81.139.2>.
- [67] W. Shockley, Hot electrons in germanium and Ohm’s law, *The Bell System Technical Journal* **30**(4), 990–1034 (1951), <https://doi.org/10.1002/j.1538-7305.1951.tb03693.x>.
- [68] H. Kröemer, Zur theorie des germaniumgleichrichters und des transistors, *Zeitschrift für Physik* **134**, 435–450 (1953), <https://doi.org/10.1007/BF01332747>.
- [69] H. Krömer, Proposed negative-mass microwave amplifier, *Physical Review* **109**(5), 1856–1856 (1958), <https://doi.org/10.1103/PhysRev.109.1856>.
- [70] H. Krömer, The physical principles of a negative-mass amplifier, *Proceedings of the IRE* **47**(3), 397–406 (1959), <https://doi.org/10.1109/JRPROC.1959.287175>.
- [71] B. K. Ridley, T. B. Watkins, The possibility of negative resistance effects in semiconductors, *Proceedings of the Physical Society* **78**(2), 293 (1961), <https://doi.org/10.1088/0370-1328/78/2/315>.
- [72] C. Hilsum, Transferred electron amplifiers and oscillators, *Proceedings of the IRE* **50**(2), 185–189 (1962), <https://doi.org/10.1109/JRPROC.1962.288025>.

- [73] J. Gunn, Microwave oscillations of current in III–V semiconductors, *Solid State Communications* **1**(4), 88–91 (1963), [https://doi.org/https://doi.org/10.1016/0038-1098\(63\)90041-3](https://doi.org/https://doi.org/10.1016/0038-1098(63)90041-3).
- [74] J. B. Gunn, Instabilities of current in III–V semiconductors, *IBM Journal of Research and Development* **8**(2), 141–159 (1964), <https://doi.org/10.1147/rd.82.0141>.
- [75] P. Guetin, Contribution to the experimental study of the Gunn effect in long GaAs samples, *IEEE Transactions on Electron Devices* **14**(9), 552–562 (1967), <https://doi.org/10.1109/T-ED.1967.16003>.
- [76] B. K. Ridley, Specific negative resistance in solids, *Proceedings of the Physical Society* **82**(6), 954 (1963), <https://doi.org/10.1088/0370-1328/82/6/315>.
- [77] H. Kröemer, Theory of the Gunn effect, *Proceedings of the IEEE* **52**(12), 1736–1736 (1964), <https://doi.org/10.1109/PROC.1964.3476>.
- [78] J. W. Allen, M. Shyam, Y. S. Chen, G. L. Pearson, Microwave oscillations in GaAs_xP_{1-x} alloys, *Applied Physics Letters* **7**(4), 78–80 (1965), <https://doi.org/10.1063/1.1754320>.
- [79] A. R. Hutson, A. Jayaraman, A. G. Chynoweth, A. S. Coriell, W. L. Feldman, Mechanism of the Gunn effect from a pressure experiment, *Physical Review Letters* **14**(16), 639–641 (1965), <https://doi.org/10.1103/PhysRevLett.14.639>.
- [80] M. Shyam, J. W. Allen, G. L. Pearson, Effect of variation of energy minima separation on Gunn oscillations, *IEEE Transactions on Electron Devices* **ED-13**(1), 63–67 (1966), <https://doi.org/10.1109/T-ED.1966.15636>.
- [81] M. E. Levinshstein, J. K. Pozhela, M. S. Shur, *The Gunn Effect (rus.)* (Sov. Radio, 1975).
- [82] H. Kröemer, Negative conductance in semiconductors, *IEEE Spectrum* **5**(1), 47–56 (1968), <https://doi.org/10.1109/MSPEC.1968.5215632>.
- [83] W. Shockley, Negative resistance arising from transit time in semiconductor diodes, *Bell System Technical Journal* **33**(4), 799–826 (1954), <https://doi.org/10.1002/j.1538-7305.1954.tb03742.x>.
- [84] B. W. Hakki, S. Knight, M. Uenohara, Active modes of interaction in bulk GaAs, *IEEE Transactions on Electron Devices* **12**(9), 503–503 (1965), <https://doi.org/10.1109/T-ED.1965.15546>.
- [85] D. McCumber, A. Chynoweth, Theory of negative-conductance amplification and of Gunn instabilities in "two-valley" semiconductors, *IEEE Transactions on Electron Devices* **ED-13**(1), 4–21 (1966), <https://doi.org/10.1109/T-ED.1966.15629>.

- [86] H. Thim, Series-connected bulk GaAs amplifiers and oscillators, *Proceedings of the IEEE* **56**(7), 1245–1245 (1968), <https://doi.org/10.1109/PROC.1968.6548>.
- [87] B. Hakki, S. Knight, Phenomenological aspects of CW microwave oscillations in GaAs, *Solid State Communications* **3**(5), 89–91 (1965), [https://doi.org/10.1016/0038-1098\(65\)90228-0](https://doi.org/10.1016/0038-1098(65)90228-0).
- [88] H. Thim, M. Barber, Microwave amplification in a GaAs bulk semiconductor, *IEEE Transactions on Electron Devices* **ED-13**(1), 110–114 (1966), <https://doi.org/10.1109/T-ED.1966.15642>.
- [89] H. Rees, Hot electron effects at microwave frequencies in GaAs, *Solid State Communications* **7**(2), 267–269 (1969), [https://doi.org/10.1016/0038-1098\(69\)90396-2](https://doi.org/10.1016/0038-1098(69)90396-2).
- [90] H. Thim, Temperature effects in bulk GaAs amplifiers, *IEEE Transactions on Electron Devices* **14**(2), 59–62 (1967), <https://doi.org/10.1109/T-ED.1967.15899>.
- [91] C.-Y. Liu, K.-Y. Tien, P.-Y. Chiu, Y.-J. Wu, Y. Chuang, H.-S. Kao, J.-Y. Li, Room-temperature negative differential resistance and high tunneling current density in GeSn Esaki diodes, *Advanced Materials* **34**(41), 2203888 (2022), <https://doi.org/10.1002/adma.202203888>.
- [92] Y.-S. Shiah, K. Sim, Y. Shi, K. Abe, S. Ueda, M. Sasase, J. Kim, H. Hosono, Mobility–stability trade-off in oxide thin-film transistors, *Nature Electronics* **4**(11), 800–807 (2021), <https://doi.org/10.1038/s41928-021-00671-0>.
- [93] S. R. Figarova, E. M. Aliyev, R. G. Abaszade, R. I. Alekberov, V. R. Figarov, Negative differential resistance of graphene oxide/sulphur compound, *Journal of Nano Research* **67**(1), 25–31 (2021), <https://doi.org/10.4028/www.scientific.net/JNanoR.67.25>.
- [94] M. Lee, T. W. Kim, C. Y. Park, K. Lee, T. Taniguchi, K. Watanabe, M.-g. Kim, D. K. Hwang, Y. T. Lee, Graphene bridge heterostructure devices for negative differential transconductance circuit applications, *Nano-Micro Letters* **15**(1), 22 (2023), <https://doi.org/10.1007/s40820-022-01001-5>.
- [95] S. Rakheja, K. Li, K. M. Dowling, A. M. Conway, L. F. Voss, Design and simulation of near-terahertz GaN photoconductive switches–operation in the negative differential mobility regime and pulse compression, *IEEE Journal of the Electron Devices Society* **9**(1), 521–532 (2021), <https://doi.org/10.1109/JEDS.2021.3077761>.
- [96] K. Dowling, Y. Dong, D. Hall, S. Mukherjee, J. D. Schneider, S. Hau-Riege, S. E. Harrison, L. Leos, A. Conway, S. Rakheja, L. Voss, Pulse compression photoconductive switching using negative differential mobility, *IEEE Transactions on Electron Devices* **69**(2), 590–596 (2022), <https://doi.org/10.1109/TED.2021.3136500>.

- [97] M. F. Pereira, Harmonic generation in biased semiconductor superlattices, *Nanomaterials* **12**(9) (2022), <https://doi.org/10.3390/nano12091504>.
- [98] A. Y. Cho, J. Arthur, Molecular beam epitaxy, *Progress in Solid State Chemistry* **10**, 157–191 (1975), [https://doi.org/10.1016/0079-6786\(75\)90005-9](https://doi.org/10.1016/0079-6786(75)90005-9).
- [99] A. P. Silin, Semiconductor superlattices, *Soviet Physics Uspekhi* **28**(11), 972 (1985), <https://doi.org/10.1070/PU1985v028n11ABEH003967>.
- [100] F. Capasso, Band-gap engineering: from physics and materials to new semiconductor devices, *Science* **235**(4785), 172–176 (1987), <https://doi.org/10.1126/science.235.4785.172>.
- [101] H. T. Grahn, *Semiconductor superlattices: growth and electronic properties* (World Scientific, 1995).
- [102] L. Brillouin, Les électrons libres dans les métaux et le rôle des réflexions de Bragg, *Journal de Physique et Le Radium* **1**(11), 377–400 (1930), <https://doi.org/10.1051/jphysrad:01930001011037700>.
- [103] A. Sibille, J. Palmier, C. Minot, F. Mollot, High-field perpendicular conduction in GaAs/AlAs superlattices, *Applied Physics Letters* **54**(2), 165–167 (1989), <https://doi.org/10.1063/1.101217>.
- [104] A. Sibille, J. Palmier, C. Minot, F. Mollot, High field perpendicular transport in GaAs/AlAs superlattices, *Superlattices and Microstructures* **5**(3), 431–435 (1989), [https://doi.org/10.1016/0749-6036\(89\)90328-5](https://doi.org/10.1016/0749-6036(89)90328-5).
- [105] V. A. Maksimenko, V. V. Makarov, A. A. Koronovskii, A. Hramov, R. Venckevičius, G. Valušis, A. G. Balanov, F. Kusmartsev, K. N. Alekseev, Electric-field distribution in a quantum superlattice with an injecting contact: Exact solution, *JETP letters* **103**, 465–470 (2016), <https://doi.org/10.1134/S0021364016070080>.
- [106] A. Sibille, J. F. Palmier, F. Mollot, H. Wang, J. C. Esnault, Negative differential conductance in GaAs/AlAs superlattices, *Physical Review B* **39**(9), 6272–6275 (1989), <https://doi.org/10.1103/PhysRevB.39.6272>.
- [107] A. Sibille, J. Palmier, H. Wang, J. Esnault, F. Mollot, dc and microwave negative differential conductance in GaAs/AlAs superlattices, *Applied Physics Letters* **56**(3), 256–258 (1990), <https://doi.org/10.1063/1.102821>.
- [108] F. Bloch, Quantum mechanics of electrons in crystal lattices, *Z. Phys* **52**, 555–600 (1929).
- [109] C. Zener, A theory of the electrical breakdown of solid dielectrics, *Proceedings of the Royal Society of London. Series A, Containing Papers of a Mathematical and Physical Character* **145**(855), 523–529 (1934), <https://doi.org/10.1098/rspa.1934.0116>.

- [110] H. Kröemer, On the nature of the negative-conductivity resonance in a superlattice Bloch oscillator, arXiv preprint cond-mat/0007482 (2000).
- [111] W. Shockley, W. Mason, Dissected amplifiers using negative resistance, *Journal of Applied Physics* **25**(5), 677–677 (1954), <https://doi.org/10.1063/1.1721712>.
- [112] H. Kröemer, Large-amplitude oscillation dynamics and domain suppression in a superlattice Bloch oscillator, arXiv preprint cond-mat/0009311 (2000).
- [113] M. Büttiker, H. Thomas, Current instability and domain propagation due to Bragg scattering, *Physical Review Letters* **38**(2), 78 (1977), <https://doi.org/0.1103/PhysRevLett.38.78>.
- [114] N. Ashcroft, N. Mermin, *Solid State Physics* (Cengage Learning, 1976).
- [115] F. G. Bass, A. P. Tetervov, High-frequency phenomena in semiconductor superlattices, *Physics Reports* **140**(5), 237–322 (1986), [https://doi.org/10.1016/0370-1573\(86\)90083-9](https://doi.org/10.1016/0370-1573(86)90083-9).
- [116] E. E. Mendez, G. Bastard, Wannier-Stark ladders and Bloch oscillations in superlattices, *Physics Today* **46**(6), 34–42 (1993), <https://doi.org/10.1063/1.881353>.
- [117] G. H. Wannier, Wave functions and effective Hamiltonian for Bloch electrons in an electric field, *Physical Review* **117**(2), 432 (1960), <https://doi.org/10.1103/PhysRev.117.432>.
- [118] F. Agulló-Rueda, E. Mendez, J. Hong, Quantum coherence in semiconductor superlattices, *Physical Review B* **40**(2), 1357 (1989), <https://doi.org/10.1103/PhysRevB.40.1357>.
- [119] R. Tsu, G. Döhler, Hopping conduction in a superlattice, *Physical Review B* **12**(2), 680 (1975), <https://doi.org/10.1103/PhysRevB.12.680>.
- [120] A. Wacker, A.-P. Jauho, Microscopic modelling of perpendicular electronic transport in doped multiple quantum wells, *Physica Scripta* **1997**(T69), 321 (1997), <https://doi.org/10.1088/0031-8949/1997/T69/070>.
- [121] A. Wacker, A.-P. Jauho, S. Zeuner, S. J. Allen, Sequential tunneling in doped superlattices: Fingerprints of impurity bands and photon-assisted tunneling, *Physical Review B* **56**(20), 13268 (1997), <https://doi.org/10.1103/PhysRevB.56.13268>.
- [122] P. Guimaraes, B. J. Keay, J. P. Kaminski, S. Allen Jr, P. Hopkins, A. Gosard, L. Florez, J. Harbison, Photon-mediated sequential resonant tunneling in intense terahertz electric fields, *Physical Review Letters* **70**(24), 3792 (1993), <https://doi.org/10.1103/PhysRevLett.70.3792>.

- [123] P. Voisin, J. Bleuse, C. Bouche, S. Gaillard, C. Alibert, A. Regreny, Observation of the Wannier-Stark quantization in a semiconductor superlattice, *Physical Review Letters* **61**(14), 1639–1642 (1988), <https://doi.org/10.1103/PhysRevLett.61.1639>.
- [124] E. E. Mendez, F. Agulló-Rueda, J. M. Hong, Stark localization in GaAs/GaAlAs superlattices under an electric field, *Physical Review Letters* **60**(23), 2426–2429 (1988), <https://doi.org/10.1103/PhysRevLett.60.2426>.
- [125] G. Von Plessen, P. Thomas, Method for observing Bloch oscillations in the time domain, *Physical Review B* **45**(16), 9185 (1992), <https://doi.org/10.1103/PhysRevB.45.9185>.
- [126] C. Waschke, P. Leisching, P. H. Bolivar, R. Schwedler, F. Brüggemann, H. G. Roskos, K. Leo, H. Kurz, K. Köhler, Detection of Bloch oscillations in a semiconductor superlattice by time-resolved terahertz spectroscopy and degenerate four-wave mixing, *Solid-State Electronics* **37**(4-6), 1321–1326 (1994), [https://doi.org/10.1016/0038-1101\(94\)90417-0](https://doi.org/10.1016/0038-1101(94)90417-0).
- [127] T. Dekorsy, P. Leisching, K. Köhler, H. Kurz, Electro-optic detection of Bloch oscillations, *Physical Review B* **50**(11), 8106 (1994), <https://doi.org/10.1103/PhysRevB.50.8106>.
- [128] T. Dekorsy, P. Leisching, C. Waschke, K. Kohler, K. Leo, H. Roskos, H. Kurz, Terahertz Bloch oscillations in semiconductor superlattices, *Semiconductor Science and Technology* **9**(11S), 1959 (1994), <https://doi.org/10.1088/0268-1242/9/11S/017>.
- [129] T. Dekorsy, R. Ott, H. Kurz, K. Köhler, Bloch oscillations at room temperature, *Physical Review B* **51**(23), 17275 (1995), <https://doi.org/10.1103/PhysRevB.51.17275>.
- [130] T. Dekorsy, A. Bartels, H. Kurz, K. Köhler, R. Hey, K. Ploog, Coupled Bloch-phonon oscillations in semiconductor superlattices, *Physical Review Letters* **85**(5), 1080 (2000), <https://doi.org/10.1103/PhysRevLett.85.1080>.
- [131] A. W. Ghosh, L. Jönsson, J. W. Wilkins, Bloch oscillations in the presence of plasmons and phonons, *Physical Review Letters* **85**, 1084–1087 (2000), <https://doi.org/10.1103/PhysRevLett.85.1084>.
- [132] B. J. Keay, S. Zeuner, S. Allen Jr, K. D. Maranowski, A. C. Gossard, U. Bhattacharya, M. J. Rodwell, Dynamic localization, absolute negative conductance, and stimulated, multiphoton emission in sequential resonant tunneling semiconductor superlattices, *Physical Review Letters* **75**(22), 4102 (1995), <https://doi.org/10.1103/PhysRevLett.75.4102>.
- [133] G. Shmelev, I. Ciiikovskii, V. Pavlovich, Plasma oscillations in a superlattice, *Physica Status Solidi (b)* **82**(1), 391–395 (1977), <https://doi.org/10.1002/pssb.2220820145>.

- [134] A. W. Ghosh, M. C. Wanke, S. J. Allen, J. W. Wilkins, Third harmonic generation by Bloch-oscillating electrons in a quasi-optical array, *Applied Physics Letters* **74**(15), 2164–2166 (1999), <https://doi.org/10.1063/1.123788>.
- [135] A. Bouchard, M. Luban, Bloch oscillations and other dynamical phenomena of electrons in semiconductor superlattices, *Physical Review B* **52**(7), 5105 (1995), <https://doi.org/10.1103/PhysRevB.52.5105>.
- [136] H. Carlin, Y. Pozhela, Some remarks on microwave excitation of dc by hot electrons in germanium, *Proceedings of the IEEE* **53**(11), 1788–1790 (1965), <https://doi.org/10.1109/PROC.1965.4412>.
- [137] K. Seeger, High-frequency-induced phase-dependent dc current by Bloch oscillator non-ohmicity, *Applied Physics Letters* **76**(1), 82–84 (2000), <https://doi.org/10.1063/1.125663>.
- [138] K. N. Alekseev, F. V. Kusmartsev, Direct current generation due to harmonic mixing: from bulk semiconductors to semiconductor superlattices, arXiv preprint cond-mat/0012348 (2000).
- [139] K. N. Alekseev, E. H. Cannon, F. V. Kusmartsev, D. K. Campbell, Fractional and unquantized dc voltage generation in THz-driven semiconductor superlattices, *Europhysics Letters* **56**(6), 842 (2001), <https://doi.org/10.1209/epl/i2001-00596-9>.
- [140] K. N. Alekseev, M. V. Gorkunov, N. V. Demarina, T. Hyart, N. V. Alexeeva, A. V. Shorokhov, Suppressed absolute negative conductance and generation of high-frequency radiation in semiconductor superlattices, *Europhysics Letters* **73**(6), 934 (2006), <https://doi.org/10.1209/epl/i2005-10484-4>.
- [141] T. Hyart, N. V. Alexeeva, A. Leppänen, K. N. Alekseev, Terahertz parametric gain in semiconductor superlattices in the absence of electric domains, *Applied Physics Letters* **89**(13) (2006), <https://doi.org/10.1063/1.2357579>.
- [142] T. Hyart, A. V. Shorokhov, K. N. Alekseev, Theory of parametric amplification in superlattices, *Physical Review Letters* **98**(22), 220404 (2007), <https://doi.org/10.1103/PhysRevLett.98.220404>.
- [143] T. Hyart, A. V. Shorokhov, K. N. Alekseev, Terahertz parametric gain in semiconductor superlattices, in *2007 Joint 32nd International Conference on Infrared and Millimeter Waves and the 15th International Conference on Terahertz Electronics* (IEEE, 2007), 472–473.
- [144] Y. A. Romanov, J. Y. Romanova, L. G. Mourokh, N. J. Horing, Nonlinear terahertz oscillations in a semiconductor superlattice, *Journal of Applied Physics* **89**(7), 3835–3840 (2001), <https://doi.org/10.1063/1.1350978>.
- [145] Y. A. Romanov, On the differential conductivity of semiconductor superlattices, *Physics of the Solid State* **45**, 559–565 (2003), <https://doi.org/10.1134/1.1562247>.

- [146] Y. A. Romanov, Y. Y. Romanova, On a superlattice Bloch oscillator, *Physics of the Solid State* **46**, 164–169 (2004), <https://doi.org/10.1134/1.1641945>.
- [147] Y. Y. Romanova, Parametric generation of high-frequency harmonics in semiconductor superlattices, *Semiconductors* **46**(11), 1451–1459 (2012), <https://doi.org/10.1134/S1063782612110164>.
- [148] Y. A. Romanov, Y. Y. Romanova, Spectra of the field and current oscillations in superlattices exposed to terahertz laser radiation, *Semiconductors* **35**, 204–208 (2001), <https://doi.org/10.1134/1.1349933>.
- [149] B. Rieder, *Semiclassical transport in semiconductor superlattices with boundaries*, Ph.D. thesis, University of Regensburg (2004).
- [150] S. Allen, U. Bhattacharya, K. Campman, H. Drexler, A. Gossard, B. Keay, K. Maranowski, G. Medeiros-Ribeiro, M. Rodwell, J. Scott, et al., Photon assisted transport through semiconductor quantum structures in intense terahertz electric fields, *Physica B: Condensed Matter* **227**(1-4), 367–372 (1996), [https://doi.org/10.1016/0921-4526\(96\)00446-2](https://doi.org/10.1016/0921-4526(96)00446-2).
- [151] L. Subačius, K. Jarašiūnas, P. Ščajev, M. Kato, Development of a microwave photoconductance measurement technique for the study of carrier dynamics in highly-excited 4H-SiC, *Measurement Science and Technology* **26**(12), 125014 (2015), <https://doi.org/10.1088/0957-0233/26/12/125014>.
- [152] S. Winnerl, E. Schomburg, J. Grenzer, H.-J. Regl, A. Ignatov, A. Semenov, K. Renk, D. Pavel'ev, Y. Koschurinov, B. Melzer, et al., Quasistatic and dynamic interaction of high-frequency fields with miniband electrons in semiconductor superlattices, *Physical Review B* **56**(16), 10303 (1997), <https://doi.org/10.1103/PhysRevB.56.10303>.
- [153] C. Ockeloen-Korppi, E. Damskägg, J.-M. Pirkkalainen, T. Heikkilä, F. Massel, M. Sillanpää, Low-noise amplification and frequency conversion with a multiport microwave optomechanical device, *Physical Review X* **6**(4), 041024 (2016), <https://doi.org/10.1103/PhysRevX.6.041024>.
- [154] W. Wustmann, V. Shumeiko, Parametric effects in circuit quantum electrodynamics, *Low Temperature Physics* **45**(8), 848–869 (2019), <https://doi.org/10.1063/1.5116533>.
- [155] Z. Lin, K. Inomata, K. Koshino, W. Oliver, Y. Nakamura, J.-S. Tsai, T. Yamamoto, Josephson parametric phase-locked oscillator and its application to dispersive readout of superconducting qubits, *Nature Communications* **5**(1), 4480 (2014), <https://doi.org/10.1038/ncomms5480>.
- [156] V. Migulin, V. Medvedev, E. Mustel, V. Parygin, *Основы теории колебаний* (Nauka, Moscow, 1978).

- [157] L. Orlov, Y. A. Romanov, Parametric mixing of electromagnetic waves in superlattices, *Radiophysics and Quantum Electronics* **25**(6), 506–510 (1982), <https://doi.org/10.1007/BF01034646>.
- [158] T. Hyart, K. N. Alekseev, Nondegenerate parametric amplification in superlattices and the limits of strong and weak dissipation, *International Journal of Modern Physics B* **23**(20n21), 4403–4413 (2009), <https://doi.org/10.1142/S0217979209063559>.
- [159] Y. A. Romanov, J. Y. Romanova, L. G. Mouroukh, Semiconductor superlattice in a biharmonic field: Absolute negative conductivity and static electric-field generation, *Journal of Applied Physics* **99**(1), 013707 (2006), <https://doi.org/10.1063/1.2158497>.
- [160] R. L. Byer, Quasi-phasematched nonlinear interactions and devices, *Journal of Nonlinear Optical Physics & Materials* **6**(04), 549–592 (1997), <https://doi.org/10.1142/S021886359700040X>.
- [161] Y. Du, S. Zhu, Y. Zhu, P. Xu, C. Zhang, Y. Chen, Z. Liu, N. Ming, X. Zhang, F. Zhang, et al., Parametric and cascaded parametric interactions in a quasiperiodic optical superlattice, *Applied Physics Letters* **81**(9), 1573–1575 (2002), <https://doi.org/10.1063/1.1502007>.
- [162] C. Torrey, C. Whitmer, *Crystal Rectifiers* (McGraw-Hill Book Company Inc., 1948).
- [163] T. Hyart, K. N. Alekseev, E. V. Thuneberg, Bloch gain in dc-ac-driven semiconductor superlattices in the absence of electric domains, *Physical Review B* **77**(16), 165330 (2008), <https://doi.org/10.1103/PhysRevB.77.165330>.
- [164] M. A. Lampert, Plasma oscillations at extremely high frequencies, *Journal of Applied Physics* **27**(1), 5–11 (1956), <https://doi.org/10.1063/1.1722195>.
- [165] W. Heinle, Principles of a phenomenological theory of Gunn-effect domain dynamics, *Solid-State Electronics* **11**(6), 583–598 (1968), [https://doi.org/10.1016/0038-1101\(68\)90011-7](https://doi.org/10.1016/0038-1101(68)90011-7).
- [166] Y. A. Romanov, Y. Y. Romanova, Self-oscillations in semiconductor superlattices, *Journal of Experimental and Theoretical Physics* **91**, 1033–1045 (2000), <https://doi.org/10.1134/1.1334994>.
- [167] A. V. Shorokhov, K. N. Alekseev, Theoretical backgrounds of nonlinear thz spectroscopy of semiconductor superlattices, *International Journal of Modern Physics B* **23**(20n21), 4448–4458 (2009), <https://doi.org/10.1142/S0217979209063584>.
- [168] Y. A. Romanov, V. Bovin, L. Orlov, Nonlinear amplification of electromagnetic oscillations in semiconductors with superlattices, *Soviet Physics. Semiconductors* **12**(9), 987–989 (1978).

- [169] G. I. Haddad, R. J. Trew, Microwave solid-state active devices, *IEEE Transactions on Microwave Theory and Techniques* **50**(3), 760–779 (2002), <https://doi.org/10.1109/22.989960>.
- [170] A. A. Ignatov, K. Renk, E. Dodin, Esaki-Tsu superlattice oscillator: Josephson-like dynamics of carriers, *Physical Review Letters* **70**(13), 1996 (1993), <https://doi.org/10.1103/PhysRevLett.70.1996>.
- [171] J. Faist, F. Capasso, D. L. Sivco, C. Sirtori, A. L. Hutchinson, A. Y. Cho, Quantum cascade laser, *Science* **264**(5158), 553–556 (1994), <https://doi.org/10.1126/science.264.5158.553>.
- [172] M. S. Vitiello, G. Scamarcio, V. Spagnolo, B. S. Williams, S. Kumar, Q. Hu, J. L. Reno, Measurement of subband electronic temperatures and population inversion in THz quantum-cascade lasers, *Applied Physics Letters* **86**(11) (2005), <https://doi.org/doi.org/10.1063/1.1886266>.
- [173] M. D. Frogley, J. Dynes, M. Beck, J. Faist, C. Phillips, Gain without inversion in semiconductor nanostructures, *Nature Materials* **5**(3), 175–178 (2006), <https://doi.org/10.1038/nmat1586>.
- [174] H. Willenberg, G. Döhler, J. Faist, Intersubband gain in a Bloch oscillator and quantum cascade laser, *Physical Review B* **67**(8), 085315 (2003), <https://doi.org/10.1103/PhysRevB.67.085315>.
- [175] T. Hyart, N. V. Alexeeva, J. Mattas, K. N. Alekseev, Terahertz Bloch oscillator with a modulated bias, *Physical Review Letters* **102**(14), 140405 (2009), <https://doi.org/10.1103/PhysRevLett.102.140405>.
- [176] A. Lisauskas, M. Dignam, N. Demarina, E. Mohler, H. Roskos, Examining the terahertz signal from a photoexcited biased semiconductor superlattice for evidence of gain, *Applied Physics Letters* **93**(2) (2008), <https://doi.org/10.1063/1.2957040>.
- [177] A. Lisauskas, C. Blöser, R. Sachs, H. G. Roskos, A. Juozapavičius, G. Valušis, K. Köhler, Time-resolved photocurrent spectroscopy of the evolution of the electric field in optically excited superlattices and the prospects for Bloch gain, *Applied Physics Letters* **86**(10) (2005), <https://doi.org/10.1063/1.1867552>.
- [178] P. G. Savvidis, B. Kolasa, G. Lee, S. Allen, Resonant crossover of terahertz loss to the gain of a Bloch oscillating InAs/AlSb superlattice, *Physical Review Letters* **92**(19), 196802–196802 (2004), <https://doi.org/10.1109/NANO.2004.1392365>.
- [179] P. Robrish, J. Xu, S. Kobayashi, P. G. Savvidis, B. Kolasa, G. Lee, D. Mars, S. J. Allen, Loss and gain in Bloch oscillating super-superlattices: THz Stark ladder spectroscopy, *Physica E: Low-dimensional Systems and Nanostructures* **32**(1-2), 325–328 (2006), <https://doi.org/10.1016/j.physe.2005.12.060>.

- [180] N. Sekine, K. Hirakawa, Dispersive terahertz gain of a non-classical oscillator: Bloch oscillation in semiconductor superlattices, *Physical Review Letters* **94**(5), 057408 (2005), <https://doi.org/10.1103/PhysRevLett.94.057408>.
- [181] E. M. Epshtein, Nonlinear plasma oscillations in a semiconductor with a superlattice, *Solid State Physics* **11**(7), 1386–1388 (1977).
- [182] S. Rott, P. Binder, N. Linder, G. Döhler, Combined description for semiclassical and quantum transport in superlattices, *Physical Review B* **59**(11), 7334 (1999), <https://doi.org/10.1103/PhysRevB.59.7334>.
- [183] P. Leisching, P. H. Bolivar, W. Beck, Y. Dhaibi, F. Brüggemann, R. Schwedler, H. Kurz, K. Leo, K. Köhler, Bloch oscillations of excitonic wave packets in semiconductor superlattices, *Physical Review B* **50**(19), 14389 (1994), <https://doi.org/10.1103/PhysRevB.50.14389>.
- [184] G. Valušis, V. Lyssenko, M. Sūdžius, F. Löser, T. Hasche, K. Leo, K. Köhler, Dynamics of Bloch oscillations: influence of excitation conditions, *Physica Scripta* **1999**(T79), 183 (1999), <https://doi.org/10.1238/Physica.Topical.079a00183/meta>.
- [185] M. M. Dignam, J. E. Sipe, Exciton Stark ladder in GaAs/Ga_{1-x}Al_xAs superlattices, *Physical Review Letters* **64**, 1797–1800 (1990), <https://doi.org/10.1103/PhysRevLett.64.1797>.
- [186] R. Tsu, L. Esaki, Stark quantization in superlattices, *Physical Review B* **43**(6), 5204 (1991).
- [187] S. Rott, N. Linder, G. Döhler, Field dependence of the hopping drift velocity in semiconductor superlattices, *Physical Review B* **65**(19), 195301 (2002).
- [188] Y. A. Kosevich, Anomalous Hall velocity, transient weak supercurrent, and coherent Meissner effect in semiconductor superlattices, *Physical Review B* **63**, 205313 (2001), <https://doi.org/10.1103/PhysRevB.63.205313>.
- [189] E. J. Ryder, Mobility of holes and electrons in high electric fields, *Physical Review* **90**(5), 766–769 (1953), <https://doi.org/10.1103/PhysRev.90.766>.
- [190] J. Yamashita, Low-temperature electrical breakdown in germanium, *Journal of the Physical Society of Japan* **16**(4), 720–732 (1961), <https://doi.org/10.1143/JPSJ.16.720>.
- [191] M. P. Shaw, H. L. Grubin, P. R. Solomon, *The Gunn-Hilsum Effect* (Academic Press Inc. (London) LTD, 1979).
- [192] J. A. Copeland, LSA oscillator-diode theory, *Journal of Applied Physics* **38**(8), 3096–3101 (2004), <https://doi.org/10.1063/1.1710069>.
- [193] J. B. Gunn, Properties of a free, steadily travelling electrical domain in GaAs, *IBM Journal of Research and Development* **10**(4), 300–309 (1966), <https://doi.org/10.1147/rd.104.0300>.

- [194] J. E. Carroll, Oscillations covering 4 Gc/s to 31 Gc/s from a single Gunn diode, *Electronics Letters* **2**(4), 141 (1966), <https://doi.org/10.1049/el:19660113>.
- [195] J. A. Copeland, A new mode of operation for bulk negative resistance oscillators, *Proceedings of the IEEE* **54**(10), 1479–1480 (1966), <https://doi.org/10.1109/PROC.1966.5158>.
- [196] J. A. Copeland, Doping uniformity and geometry of LSA oscillator diodes, *IEEE Transactions on Electron Devices* **14**(9), 497–500 (1967), <https://doi.org/10.1109/T-ED.1967.15993>.
- [197] I. B. Bott, C. Hilsum, An analytic approach to the LSA mode, *IEEE Transactions on Electron Devices* **14**(9), 492–497 (1967), <https://doi.org/10.1109/T-ED.1967.15992>.
- [198] W. K. Kennedy, L. F. Eastman, R. J. Gilbert, LSA operation of large volume bulk GaAs samples, *IEEE Transactions on Electron Devices* **14**(9), 500–504 (1967), <https://doi.org/10.1109/T-ED.1967.15994>.
- [199] A. J. Shuskus, M. P. Shaw, Current instabilities in gallium arsenide, *Proceedings of the IEEE* **53**(11), 1804–1805 (1965), <https://doi.org/10.1109/PROC.1965.4430>.
- [200] M. P. Shaw, A. J. Shuskus, Current instability above the Gunn threshold, *Proceedings of the IEEE* **54**(11), 1580–1581 (1966), <https://doi.org/10.1109/PROC.1966.5198>.
- [201] S. Sze, K. Kwok, *Physics of semiconductor devices* (John Wiley & Sons, 2006).
- [202] N. F. Mott, The theory of crystal rectifiers, *Proceedings of the Royal Society of London. Series A. Mathematical and Physical Sciences* **171**(944), 27–38 (1939), <https://doi.org/10.1098/rspa.1939.0051>.
- [203] W. Schottky, Zur halbleitertheorie der sperrschicht-und spitzengleichrichter, *Zeitschrift für Physik* **113**, 367–414 (1939), <https://doi.org/10.1007/BF01340116>.
- [204] J. Waldrop, Schottky-barrier height of ideal metal contacts to GaAs, *Applied Physics Letters* **44**(10), 1002–1004 (1984), <https://doi.org/10.1063/1.94599>.
- [205] R. Tung, Schottky barrier height—do we really understand what we measure?, *Journal of Vacuum Science & Technology B: Microelectronics and Nanometer Structures Processing, Measurement, and Phenomena* **11**(4), 1546–1552 (1993), <https://doi.org/10.1116/1.586967>.
- [206] R. T. Tung, The physics and chemistry of the Schottky barrier height, *Applied Physics Reviews* **1**(1), 011304 (2014), <https://doi.org/10.1063/1.4858400>.

- [207] M. A. Lampert, R. B. Schilling, Chapter 1 current injection in solids: The regional approximation method, in R. Willardson, A. C. Beer (eds.), *Injection Phenomena* (Elsevier, 1970), volume 6 of *Semiconductors and Semimetals*, 1–96.
- [208] N. Mott, R. Gurney, *Electronic Processes in Ionic Crystals*, Dover Books. S (Dover Publications, 1964).
- [209] H. Kröemer, The Gunn effect under imperfect cathode boundary conditions, *IEEE Transactions on Electron Devices* **15**(11), 819–837 (1968), <https://doi.org/10.1109/T-ED.1968.16523>.
- [210] F. Beltram, F. Capasso, D. L. Sivco, A. L. Hutchinson, S.-N. G. Chu, A. Y. Cho, Scattering-controlled transmission resonances and negative differential conductance by field-induced localization in superlattices, *Physical Review Letters* **64**(26), 3167 (1990), <https://doi.org/10.1103/PhysRevLett.64.3167>.
- [211] J. Manley, H. Rowe, Some general properties of nonlinear elements-part I. General energy relations, *Proceedings of the IRE* **44**(7), 904–913 (1956), <https://doi.org/10.1109/JRPROC.1956.275145>.
- [212] J. Manley, E. Peterson, Negative resistance effects in saturable reactor circuits, *Electrical Engineering* **65**(12), 870–881 (1946), <https://doi.org/10.1109/T-AIEE.1946.5059263>.
- [213] J. Manley, Some general properties of magnetic amplifiers, *Proceedings of the IRE* **39**(3), 242–251 (1951), <https://doi.org/10.1109/JRPROC.1951.231835>.
- [214] C. H. Johansson, J. O. Linde, Röntgenographische bestimmung der atomanordnung in den mischkristallreihen Au-Cu und Pd-Cu, *Annalen der Physik* **383**(21), 439–460 (1925), <https://doi.org/https://doi.org/10.1002/andp.19253832104>.
- [215] B. Y. Jin, J. B. Ketterson, Artificial metallic superlattices, *Advances in Physics* **38**(3), 189–366 (1989), <https://doi.org/10.1080/00018738900101112>.
- [216] L. Friedman, Thermopower of superlattices as a probe of the density of states distribution, *Journal of Physics C: Solid State Physics* **17**(22), 3999 (1984), <https://doi.org/10.1088/0022-3719/17/22/018>.
- [217] I. Banerjee, Q. Yang, C. M. Falco, I. K. Schuller, Superconductivity of Nb/Cu superlattices, *Solid State Communications* **41**(11), 805–808 (1982), [https://doi.org/10.1016/0038-1098\(82\)91253-4](https://doi.org/10.1016/0038-1098(82)91253-4).
- [218] I. K. Schuller, S. Kim, C. Leighton, Magnetic superlattices and multilayers, *Journal of Magnetism and Magnetic Materials* **200**(1-3), 571–582 (1999), [https://doi.org/10.1016/S0304-8853\(99\)00336-4](https://doi.org/10.1016/S0304-8853(99)00336-4).
- [219] P. F. Carcia, A. D. Meinhaldt, A. Suna, Perpendicular magnetic anisotropy in Pd/Co thin film layered structures, *Applied Physics Letters* **47**(2), 178–180 (1985), <https://doi.org/10.1063/1.96254>.

- [220] M. N. Baibich, J. M. Broto, A. Fert, F. N. Van Dau, F. Petroff, P. Etienne, G. Creuzet, A. Friederich, J. Chazelas, Giant magnetoresistance of (001)Fe/(001)Cr magnetic superlattices, *Physical Review Letters* **61**(21), 2472–2475 (1988), <https://doi.org/10.1103/PhysRevLett.61.2472>.
- [221] C. P. Flynn, Constraints on the growth of metallic superlattices, *Journal of Physics F: Metal Physics* **18**(9), L195 (1988), <https://doi.org/10.1088/0305-4608/18/9/005>.
- [222] J. L. Makous, C. M. Falco, Integer monolayer metallic superlattices, *Solid State Communications* **68**(4), 375–378 (1988), [https://doi.org/https://doi.org/10.1016/0038-1098\(88\)90298-0](https://doi.org/https://doi.org/10.1016/0038-1098(88)90298-0).
- [223] J. W. M. DuMond, J. P. Youtz, Selective X-ray diffraction from artificially stratified metal films deposited by evaporation, *Physical Review* **48**(8), 703–703 (1935), <https://doi.org/10.1103/PhysRev.48.703>.
- [224] J. Son, J. M. LeBeau, S. J. Allen, S. Stemmer, Conductivity enhancement of ultrathin LaNiO₃ films in superlattices, *Applied Physics Letters* **97**(20), 202109 (2010), <https://doi.org/10.1063/1.3511738>.
- [225] Z. L. Deng, N. Yogesh, X. D. Chen, W. J. Chen, J. W. Dong, Z. Ouyang, G. P. Wang, Full controlling of Fano resonances in metal-slit superlattice, *Scientific Reports* **5**(1), 18461 (2015), <https://doi.org/10.1038/srep18461>.
- [226] X. D. Li, S. Yu, S. Q. Wu, Y. H. Wen, S. Zhou, Z. Z. Zhu, Structural and electronic properties of superlattice composed of graphene and monolayer MoS₂, *The Journal of Physical Chemistry C* **117**(29), 15347–15353 (2013), <https://doi.org/10.1021/jp404080z>.
- [227] Y. Sakai, T. Koretsune, S. Saito, Electronic structure and stability of layered superlattice composed of graphene and boron nitride monolayer, *Physical Review B* **83**(20), 205434 (2011), <https://doi.org/10.1103/PhysRevB.83.205434>.
- [228] J. Hoffman, I. C. Tung, B. B. Nelson-Cheeseman, M. Liu, J. W. Freeland, A. Bhattacharya, Charge transfer and interfacial magnetism in (LaNiO₃)_n/(LaMnO₃)₂ superlattices, *Physical Review B* **88**(14), 144411 (2013), <https://doi.org/10.1103/PhysRevB.88.144411>.
- [229] B. Saha, T. D. Sands, U. V. Waghmare, First-principles analysis of ZrN/ScN metal/semiconductor superlattices for thermoelectric energy conversion, *Journal of Applied Physics* **109**(8), 083717 (2011), <https://doi.org/10.1063/1.3569734>.
- [230] A. Sibille, J. Palmier, H. Wang, F. Mollot, Observation of Esaki-Tsu negative differential velocity in GaAs/AlAs superlattices, *Physical Review Letters* **64**(1), 52 (1990), <https://doi.org/10.1103/PhysRevLett.64.52>.
- [231] M. Hadjazi, A. Sibille, J. Palmier, F. Mollot, Negative differential conductance in GaAs/AlAs superlattices, *Electronics Letters* **27**(12), 1101–1103 (1991), <https://doi.org/10.1049/el:19910684>.

- [232] A. Sibille, J. Palmier, F. Mollot, Coexistence of Wannier–Stark localization and negative differential velocity in superlattices, *Applied Physics Letters* **60**(4), 457–459 (1992), <https://doi.org/10.1063/1.106633>.
- [233] G. Bastard, R. Ferreira, *Wannier-Stark Quantization and Bloch Oscillator in Biased Semiconductor Superlattices* (Springer US, Boston, MA, 1989), 333–345.
- [234] A. Rabinovitch, J. Zak, Does a Bloch electron in a constant electric field oscillate?, *Physics Letters A* **40**(3), 189–190 (1972), [https://doi.org/10.1016/0375-9601\(72\)90649-4](https://doi.org/10.1016/0375-9601(72)90649-4).
- [235] J. Krieger, G. Iafrate, Time evolution of Bloch electrons in a homogeneous electric field, *Physical Review B* **33**(8), 5494 (1986), <https://doi.org/10.1103/PhysRevB.33.5494>.
- [236] A. M. Bouchard, M. Luban, Semiconductor superlattices as terahertz generators, *Physical Review B* **47**(11), 6815 (1993), <https://doi.org/10.1103/PhysRevB.47.6815>.
- [237] K. Leo, P. H. Bolivar, F. Brüggemann, R. Schwedler, K. Köhler, Observation of Bloch oscillations in a semiconductor superlattice, *Solid State Communications* **84**(10), 943–946 (1992), [https://doi.org/10.1016/0038-1098\(92\)90798-E](https://doi.org/10.1016/0038-1098(92)90798-E).
- [238] A. Sibille, J. Palmier, H. Wang, J. Esnault, F. Mollot, Negative differential perpendicular velocity in GaAs/AlAs superlattices, *Solid-State Electronics* **32**(12), 1461–1465 (1989), [https://doi.org/10.1016/0038-1101\(89\)90257-8](https://doi.org/10.1016/0038-1101(89)90257-8).
- [239] A. Wacker, A.-P. Jauho, Quantum transport: The link between standard approaches in superlattices, *Physical Review Letters* **80**(2), 369 (1998), <https://doi.org/10.1103/PhysRevLett.80.369>.
- [240] A. Sibille, C. Minot, F. Laruelle, Transport in excited states of semiconductor superlattices, *International Journal of Modern Physics B* **14**(09), 909–942 (2000), <https://doi.org/10.1142/S0217979200001394>.
- [241] L. Esaki, L. Chang, New transport phenomenon in a semiconductor superlattice, *Physical Review Letters* **33**(8), 495 (1974), <https://doi.org/10.1103/PhysRevLett.33.495>.
- [242] M. Fok, P. Prucnal, Switching based on optical nonlinear effects, in B. Li, S. J. Chua (eds.), *Optical Switches* (Woodhead Publishing, 2010), Woodhead Publishing Series in Electronic and Optical Materials, 181–205.
- [243] T. Dekorsy, R. Ott, P. Leisching, H. Bakker, C. Waschke, H. Roskos, H. Kurz, K. Köhler, Time-resolved optical investigations of Bloch oscillations in semiconductor superlattices, *Solid-State Electronics* **40**(1-8), 551–554 (1996), [https://doi.org/10.1016/0038-1101\(95\)00288-X](https://doi.org/10.1016/0038-1101(95)00288-X).
- [244] S. E. Ralph, F. Capasso, R. J. Malik, New photorefractive effect in graded-gap superlattices, *Physical Review Letters* **63**(20), 2272 (1989), <https://doi.org/10.1103/PhysRevLett.63.2272>.

- [245] T. Dekorsy, P. Leisching, W. Beck, R. Ott, Y. Dhaibi, R. Schwedler, H. G. Roskos, H. Kurz, K. Köhler, Internal field dynamics of coherent Bloch oscillations in superlattices, *Superlattices and Microstructures* **15**(1), 11 (1994), <https://doi.org/10.1006/spmi.1994.1003>.
- [246] J. Neu, C. A. Schmuttenmaer, Tutorial: An introduction to terahertz time domain spectroscopy (THz-TDS), *Journal of Applied Physics* **124**(23) (2018), <https://doi.org/10.1063/1.5047659>.
- [247] W. Withayachumnankul, M. Naftaly, Fundamentals of measurement in terahertz time-domain spectroscopy, *Journal of Infrared, Millimeter, and Terahertz Waves* **35**, 610–637 (2014), <https://doi.org/10.1007/s10762-013-0042-z>.
- [248] C. Waschke, H. Roskos, K. Leo, H. Kurz, K. Kohler, Experimental realization of the Bloch oscillator in a semiconductor superlattice, *Semiconductor Science and Technology* **9**(5S), 416 (1994), <https://doi.org/10.1088/0268-1242/9/5S/002>.

SANTRAUKA LIETUVIŲ KALBA

7.1. Įvadas

Puslaidininkinės supergardelės – kvantinės struktūros, sudarytos iš mažiausiai dviejų skirtingų medžiagų, taip užtikrinant energijos miniuostų formavimąsi [63]. Tokie dariniai pasižymi išskirtine krūvininkų pernašos valdymo galimybe, todėl supergardelės laikomos patrauklia terpe tyrinėti įvairius fizikinius reiškinius. Dešimtmečius trukusių intensyvių tyrimų metu buvo pastebėti įvairūs efektai: Blocho osciliacijos [5–7], koherentinis Holo efektas [8], Zenerio tuneliavimas [9] ir aukštos eilės fraktalinės kvantinės osciliacijos grafeno/BN supergardelėse [10]. Taip pat buvo pademonstruotas supergardelių pritaikomumas prietaisams, veikiantiems terahercų (THz) ir sub-terahercų (sub-THz) dažnių ruože [A1]. Supergardelės yra plačiai naudojamos šiuolaikiniuose elektronikos ir optoelektronikos įrenginiuose, pavyzdžiui, kvantiniuose kaskadiniuose lazeriuose [11]. Be to, teorinių tyrimų metu yra parodyta, kad supergardelės gali veikti kaip stiprintuvai, naudojantys parametrinės generacijos [12, 13] arba beinversinį Blocho [14–16] stiprinimo mechanizmus.

THz dažnio spinduliuotė, kurios dažnių ruožas apima nuo 0,1 THz iki 10 THz, šiuo metu sulaukia didelio mokslinio susidomėjimo, kas lemia intensyvią taikymo galimybių plėtrą. THz dažnių ruožas yra naudojamas naujos kartos duomenų perdavimui, spektroskopijoje ir vaizdinime [17–22]. Pastarojo taikymo galimybės vertos papildomo dėmesio, dėl plačių taikymo galimybių tokių kaip saugumas [23, 24], pakuočių inspekcija [25, 26], farmacija [27], kosmetika [28] ir maisto kontrolė [29]. THz kvantai turi mažą energiją (nuo 0,4 meV iki 40 meV), tad THz spinduliuotė iš esmės yra nekenksminga gyvoms būtybėms ir šis dažnių diapazonas yra patrauklus medicininio vaizdinimo taikymams [30], suteikiant naujų galimybių, tokių kaip tiesioginis skenavimas ar vandens kiekio analizė skirtinguose audiniuose [31, 32]. Bet kurio taikymo atveju, kompaktiška, efektyvi ir ekonomiškai THz vaizdinimo sistema yra būtina sėkmingam plačiam naudojimui. Paprasčiausią vaizdinimo sistemą sudaro THz šaltinis, detektorius ir keletas spinduliuotės formavimo elementų. Geras sistemos dydžio sumažinimo pavyzdys yra didelių optinių komponentų pakeitimas moderniais metapaviršių pagrindu veikiančiais difrakciniais optikos elementais [33–35]. Taip pat verta paminėti darbus su naujomis medžiagomis, tokiomis kaip 3D spausdinimui tinkantis smūgiams atsparus polistirenas (angl. *high-impact polystyrene*), leidžiantis gaminti itin pigius spinduliuotės formavimo elementus, naudojant sąlyginai paprastą gamybos procesą [36]. Ženklaus indėlis jau padarytas jautrių, greitaveikių THz detektorių tyrimuose. Tyrimų metu yra nagrinėjami didelio elektronų judrio tranzistoriai [37, 38], fotolaidžios THz antenos [39, 40],

superlaidininkai [41], kvantinių struktūrų pagrindu sukurti sprendimai [42, 43], Golay celės [44], piroelektriniai detektoriai [45] ir bolometrai [46]. Kiekviena technologija pasižymi savo privalumais ir trūkumais. Atsižvelgiant į taikymo poreikį galima išsirinkti vieną iš daugelio sukurtų THz šaltinių technologijų tokių kaip kvantiniai vakuuminės elektronikos šaltiniai (klistronai [47], laisvųjų elektronų lazeriai [48, 49]), kietojo kūno šaltiniai (Gunn diodai [50, 51], aukšto dažnio tranzistoriai [52, 53]), lazeriniai šaltiniai (kvantiniai kaskadiniai lazeriai (QCL) [54, 55], puslaidininkiniai lazeriai [56]), skirtuminio dažnio generatoriai [57, 58], kristaliniai parametriniai osciliatoriai [59–61]. Nepaisant didelio šaltinių ir kitų vaizdavimo sistemų komponentų pasirinkimo įvairovės, kiekvienas THz šaltinis gali būti tobulinamas atsižvelgiant į konkretaus taikymo reikalavimus. Teorinis kvantinių puslaidininkinių struktūrų panaudojimas kuriant kompaktišką, derinamą ir efektyvų THz dažnio ruožo šaltinį buvo aprašytas daugiau nei prieš 50 metų [63]. Siūlomos kvantinės supergardenės struktūra suteikia papildomo patrauklumo dėl galimybės veikti kambario temperatūros sąlygomis. Tačiau nepaisant ilgamečių teorinių tyrimų, stabilus stiprinimas supergardenėje eksperimento metu vis dar nėra registruotas.

Taigi pagrindinis šio tyrimo tikslas buvo **eksperimentiškai ir teoriškai ištirti aukšto dažnio stiprinimo mechanizmus puslaidininkinėse kvantinėse supergardenėse kambario temperatūros sąlygomis, siekiant atskleisti jų savybes bei jų valdymo parametrus ir nustatyti optimalias eksperimentines sąlygas stabiliam stiprinimui registruoti.**

Blocho ir parametrinio stiprinimo mechanizmų atsiradimas supergardenėse buvo numatytas dėl parodyto neigiamo krūvinikų diferencialinio greičio (angl. *negative differential drift velocity - NDV*) režimo į kurį supergardenė patenka, kai yra veikama tinkamu priešįtampiu. Esaki ir Tsu darbuose yra parodyta [63], kad nuolatinės įtampos šaltiniu veikiamoje supergardenėje dreifo greitis pasiekia maksimumą ir pradeda mažėti. Efektas yra paaiškinamas elektronų Braggo atspindžiu periodinėje k -erdvėje. Disipatyvaus parametrinio stiprinimo atveju, pasireiškiančiu supergardenę veikiant kintama ir nuolatinė įtampa, dalį kintamo elektrinio lauko periodo supergardenė praleis NDV būsenoje, dėl ko pradės vykti išsigimę ir neišsigimę generacijos procesai [64]. Dėl pridėto priešįtampio supergardenėje susiformuoja Wannier-Starko lygmenys, užtikrinantys Blocho stiprinimą puslaidininkinėse supergardenėse [5]. Valdant priešįtampį galima kontroliuoti plačiajuosčių disipatyvių parametrinio stiprinimo procesų spektrines charakteristikas ir Blocho dažnį. Nepaisant ilgalaikių teorinių tyrimų, iki šiol nebuvo pateikta jokių eksperimentinių disipatyvaus parametrinio stiprinimo supergardenėje įrodymų. Be to, beinversinis Blocho stiprinimas buvo registruotas tik naudojant optinius eksperimentus, kuriuose Wannier-Starko lygmenys buvo susieti naudojant optinį žadinančio lazerio spinduliuotės išplė-

timą [65]. Galiausiai, minėtuose tyrimuose nebuvo analizuojamas nei dviejų stiprinimo mechanizmų sambūvis nei didelio signalo stiprinimo efektai, į kuriuos yra būtina atsižvelgti, nes eksperimentai, atlikti šio tyrimo metu, parodė generacijos lygius, kurie gerokai viršija įprastai naudojamo mažo signalo stiprinimo modelio ribas.

Ši disertacija yra suskirstyta į 5 skyrius. Skyriuje 1 pateikiama prieš tai kitų mokslininkų grupių atliktų teorinių tyrimų ir eksperimentinių pasiekimų, įskaitant atliktus puslaidininkiuose, apžvalga, suteikianti papildomo supratimo apie toliau pateiktų rezultatų svarbą. Skyriuje 2 aprašomos naudojamos struktūros ir eksperimentiniai metodai naudoti tyrimo metu. Skyriuje 3 pristatomas pirmasis disipatyvios parametrinės generacijos GaAs/AlGaAs supergardenelėse eksperimentinis įrodymas. Tyrimas išplėčiamas Skyriuje 4, įtraukiant didelio signalo stiprinimo modelį, kuris parodo Blocho ir parametrinio stiprinimo sambūvį puslaidininkinėse supergardenelėse. Galiausiai, Skyriuje 5 pateikiamas pirmasis stabilaus beinversinio Blocho stiprinimo eksperimentinis įrodymas elektriškai žadinamoje GaAs/AlGaAs supergardenelėje.

- **Teiginys 1:**

Disipatyvus parametrinis stiprinimas sub-kritiškai legiruotoje GaAs/AlGaAs puslaidininkinėje supergardenėje, kuri yra žadinama stipriu mikrobangų lauku, pasireiškia kaip koherentinė skirtingų žadinančio dažnio sub-harmonikų emisija per daugybę vienu metu vykstančių aukštinančio ir žeminančio dažnio procesų.

- **Teiginys 2:**

Manley-Rowe sąryšiai yra netinkami aprašyti disipatyvaus parametrinio stiprinimo procesus, vykstančius sub-kritiškai legiruotoje GaAs/AlGaAs supergardenėje veikiančioje Esaki-Tsu darbo režime.

- **Teiginys 3:**

Aukšto dažnio stiprinimas sub-kritiškai legiruotoje GaAs/AlGaAs supergardenėje yra Blocho ir parametrinio stiprinimo mechanizmų sambūvis. Stiprinimo mechanizmų sąveika ir jų įnašas yra derinami keičiant žadinančios spinduliuotės elektrinio lauko stiprį bei užtikrinant tinkamą fazės skirtumą tarp žadinančio ir zonduojančio elektrinių laukų.

- **Teiginys 4:**

Sub-kritiškai legiruotose puslaidininkinėse supergardenėse dominuojančio stiprinimo mechanizmo perėjimas iš Blocho į parametrinį yra stebimas tiek išsigimusio, tiek neišsigimusio generacijos proceso metu; stipraus zonduojančio signalo atveju, neišsigimusio proceso metu, energijos perdavimas gali vykti net tik iš nuolatinio žadinančio prieštampio, bet ir tarp dviejų zonduojančių dažnių.

- **Teiginys 5:**

GaAs/AlGaAs prieštampio veikiamoje supergardenėje kambario temperatūros sąlygomis yra stebimas beinversinis Blocho stiprinimas, pasireiškiantis per susietas Bloch-plazmonines (Epshteino) modas; stiprinimas pažymėtas staigiu perėjimu nuo plazmoninės sugerties į Blocho stiprinimo režimą, kuris išsilaiko tiek minijuostos transporto, tiek nerezonansiniame tarpminijuostiniame (Zenerio) tuneliavimo režimuose.

7.2. Metodai

7.2.1. Supergardelės architektūra ir eksperimentinis stendas

Eksperimentų metu buvo naudojama 30 periodų supergardelė, sudaryta iš siličiu legiruotų GaAs kvantinių duobių (5 nm; 10^{16} cm^{-3}) ir $\text{Al}_{0.3}\text{Ga}_{0.7}\text{As}$ kvantinių barjerų (1 nm). Tokia duobių ir barjerų struktūra užtikrina plačią 104 meV minijuostą. Bendras supergardelės ilgis $L = 180 \text{ nm}$. Struktūra (žr. 2.1 paveikslą) yra užauginta naudojant molekulinio pluošto epitaksijos technologiją, auginant ant n -legiruoto ($\sim 500 \mu\text{m}$; 10^{18} cm^{-3}) GaAs padėklo. Pasirinktų parametrų supergardelės kritinis Kroemer koeficientas yra $NL_{\text{cr}} = 2,7 \cdot 10^{11} \text{ cm}^{-2}$ (žr. 1.4.1 skyrių [149]). Kadangi domenų susidarymas eksperimento buvo nepageidautinas, supergardelė buvo legiruojama $N = 10^{16} \text{ cm}^{-3}$, tad gautas NL koeficientas yra $NL = 1,8 \cdot 10^{11} \text{ cm}^{-2}$. Siekiant homogeniško elektrinio lauko, ant supergardelės buvo užgarintas AuTi Schottky kontaktas, kuris papildomai leido prijungti auksinę giją, reikalingą kintamo žadinančio elektrinio lauko sąsajai su supergardelės struktūra. Po supergardele buvo suformuotas injektuojantis kontaktas (gradientinis koncentracijos ir aliuminio ($\text{Al}_{1-x}\text{Ga}_x\text{As}$) kiekio 100 nm storio sluoksnis). Tyrimo metu bus patvirtinta, kad asimetrinių kontaktų naudojimas (Schottky viršuje ir heterostruktūra supergardelės apačioje) užtikrino homogenišką elektrinį lauką supergardelėje. Galiausiai ominis AuGeNi kontaktas buvo užgarintas padėklo apačioje. Naudojant šlapio ėsdinimo technologiją buvo pagamintos $80 \mu\text{m} \times 80 \mu\text{m}$ mezos. Gautos struktūros buvo patikrintos naudojant skenuojantį elektroninį mikroskopą ir Rentgeno spindulių difraktometrą.

Siekiant susieti kintamą žadinantį elektrinį lauką su supergardele buvo panaudota auksinė ($d = 25 \mu\text{m}$) skersmens gija, kuri buvo prijungiama prie viršutinio Schottky kontakto ir kuri leido turėti elektrinio lauko komponentę z -kryptimi reikalingą sąveikai su struktūra. Panaudotas sprendimas nėra naujas ir jau buvo taikomas Guimaraes darbuose [122]. Bet minėtuose tyrimuose buvo atliekamas atviros erdvės eksperimentas, kurio metu žadinančio elektrinio lauko kritimo kampas buvo keičiamas siekiant našiausios sąsajos su supergardelės struktūra. Atlikto eksperimento metu buvo naudojamas bangolaidinis stendas, tad kritimo kampo keitimas buvo neįmanomas. Bangolaidinis eksperimentinio stendo sprendimas buvo pasirinktas dėl geresnės kintamo žadinančio elektrinio lauko sąsajos ir didesnės žadinamos spinduliotės galios.

Supergardelės struktūra buvo talpinama į (17 mm \times 6 mm) bangolaidį, kuris užtikrina padidintą kintamo žadinančio elektrinio lauko stiprį sąsajos su supergardele vietoje. Bandinys yra talpinamas išilgai ilgajai bangolaidžio kraštinei. Auksinė gija, veikianti kaip antena, prijungta prie bangolaidžio, o apatinis ominis kontaktas prijungtas prie koaksialinės linijos per žemo dažnio filtrą

(žr. 2.4 paveikslą).

Ekspertas paremtas praėjusios ir atspindėtos mikrobangų spinduliuotės pokyčio, atsirandančio dėl bandinyje vykstančių procesų, analize [151]. Eksperimentinis stendas yra pavaizduotas 2.5 paveiksle. Eksperimento metu buvo naudojami du skirtingi mikrobangų generatoriai (MWGS). Pirmasis - klistroninis stiprintuvas, užtikrinantis iki 20 mW galios 8,2 GHz–12,4 GHz dažnių ruože. Antrasis - magnetronas, generuojantis iki 10 W galios 9,4 GHz dažnio spinduliuotę. Praėjusi žemo dažnio filtrą (LPF), kuris panaikina antrą ir trečią generatorių harmonikas, žadinančioji spinduliuotė per feritinį cirkuliatorių (FC) yra perduodama į bandinio bangolaidžio liniją, kurioje yra sumontuotas impedanso transformatorius (IT). Impedanso transformatorius yra sudarytas iš dviejų ketvirčio bangos plokštelių, kurias galima stumdyti kartu arba keisti atstumą tarp jų. Toks impedanso transformatoriaus veikimas leidžia minimalizuoti atspindėtą signalą ir valdyti ant bandinio krentančio signalo fazę. Šios galimybės svarba bus plačiai aptarta rezultatų skyriuje. Po tiriamosios struktūros buvo įstatomas bangolaidinis perjungiklis (WS), prie kurio buvo prijungiami bangolaidiniai adapteriai, išplečiantys registruojamo dažnio ruožą. Šio eksperimento metu buvo įstatomi WR-90 (X-juosta: 8 GHz - 12 GHz) į WR-62 (K_u-juosta: 12 GHz - 18 GHz), WR-42 (K-juosta: 18 GHz - 27 GHz) ir WR-28 (K_a-juosta: 27 GHz - 40 GHz). Eksperimento metu taip pat buvo kontroliuojamas atspindėtas signalas. Feritinis cirkuliatorius leidžia nukreipti atspindėtą signalą į atitinkamą liniją išvengiant sąveikos su generuojamomis mikrobangomis. Atspindėtas signalas, kalibruojamas (ATTEN) stiprintuvu, yra registruojamas Schottky diodo detektoriumi (DET). Dažninis atsakas buvo analizuojamas C4-27 spektro analizatoriumi (SpAn). Visi aprašyti eksperimentai vyko kambario temperatūros sąlygomis.

7.2.2. Teoriniai modeliai

Kaip parodoma rezultatų skyriuje, eksperimento metu buvo stebima sveikųjų harmonikų ($\omega_1 = n\omega_0$), pusinių sub-harmonikų ($\omega_1 = n\omega_0/2$) ir trupmeninių sub-harmonikų ($\omega_1 = p\omega_0/q$) generacija (n, p, q - sveiki skaičiai). Modeliavimo metu, taikant realios struktūros parametrus, naudojamas vienos minijuostos modelis, neatsižvelgiant į sąveiką tarp dviejų minijuostų. Elektrinis laukas, nukreiptas išilgai supergardelės auginimo ašiai, yra apibrėžiamas

$$E_{\text{tot}}(t) = E_{\text{pump}} + E_{\text{probe}} \quad (7.1)$$

išraiška. Stebima analogija su žadinimo - zondavimo metodu (angl. *pump-probe*). Šio eksperimento metu zonduojačio elektrinio lauko stipris gali būti nereikšmingai žemas lyginant su žadinančio elektrinio lauko stipriu (galima

taikyti mažo signalo stiprinimo modelį) arba būti palyginamo dydžio (didelio signalo stiprinimo modelio ribos). Didžioji dalis tyrėjų savo darbuose taiko mažo signalo stiprinimo modelį, bet, kaip bus parodyta vėliau, perėjimas prie matematiškai sudėtingesnio didelio signalo stiprinimo modelio yra būtinas, atsižvelgiant į aukštą eksperimento metu registruotą generuoto elektrinio lauko stiprį. Be to, didelio signalo stiprinimo modelis atskleidžia mažo signalo modelio taikymo atveju nepastebimus efektus. Grįžtant prie žadinančio elektrinio lauko, pastarasis gali būti išreikštas

$$E_{\text{pump}}(t) = E_{\text{dc}} + E_{\text{ac}} \cos(\omega_0 t) \quad (7.2)$$

išraiška. Čia E_{dc} yra nuolatinio žadinančio elektrinio lauko stipris, E_{ac} kintamo žadinančio elektrinio lauko stipris ir ω_0 kintamo žadinančio elektrinio lauko dažnis. Kita vertus, zonduojantis elektrinis laukas gali būti analizuojamas išsigimusio ir neišsigimusio proceso ribose. Išsigimusio proceso atveju generacijos procese dalyvauja vieno zonduojančio dažnio spinduliuotė, o neišsigimusio proceso atveju dviejų skirtingų dažnių zonduojantys signalai. Tad

$$\begin{aligned} E_{\text{probe-deg}}(t) &= E_1 \cos(\omega_1 t + \varphi_1) \\ E_{\text{probe-nondeg}}(t) &= E_1 \cos(\omega_1 t + \varphi_1) + E_2 \cos(\omega_2 t + \varphi_2), \end{aligned} \quad (7.3)$$

kur φ_1 ir φ_2 yra santykinės zonduojančių elektrinių laukų fazės, skaičiuojamos kintamo žadinančio signalo atžvilgiu. Siekiant aiškumo taip pat verta modifikuoti dreifo greičio, pateikto 1.5 lygtyje, išraišką, atskiriant eksperimentinius ir struktūros geometrinis parametrus. Pirmiausia išreikškime kritinį elektrinį lauką, ties kuriuo yra pasiekiamas dreifo greičio maksimumas. Kritinio elektrinio lauko išraiška gaunama diferencijuojant 1.5 lygtį,

$$E_{\text{cr}} = \frac{\hbar}{ed\tau}. \quad (7.4)$$

Tada maksimalus dreifo greitis yra

$$v_{\text{p}} = \frac{\Delta d}{4\hbar}. \quad (7.5)$$

Pilna šios lygties išraiška yra pateikta 6.2.1 skyriuje. Atsižvelgiant į gautas lygtis, pertvarkome 1.5 lygtį:

$$v_{\text{d}}(E_{\text{tot}}) = 2v_{\text{p}} \frac{E_{\text{tot}}/E_{\text{cr}}}{1 + (E_{\text{tot}}/E_{\text{cr}})^2} = 2v_{\text{p}} \frac{F_{\text{tot}}}{1 + F_{\text{tot}}^2}. \quad (7.6)$$

Atkreiptinas dėmesys į bedimensinio elektrinio lauko stiprio kintamojo $F_i = E_i/E_{\text{cr}}$ pritaikymą. Šis patogumo dėlei įvestas kintamasis yra plačiai naudojamas šiame darbe. Taip pat svarbu paminėti, kad aprašytos lygtys gali būti

taikomos tik kvazistatinės aproksimacijos ($\omega_i\tau \ll 1$) atveju [152]. Ši sąlyga nustato, kad dreifo greitis supergardenėje, kuri yra žadinama kintamuoju elektriniu lauku, atkartos elektrinio lauko pokytį. Tai įgalina naudoti klasikinės lygtis, išvestas atvejams, kai supergardenė yra veikiamą tik nuolatinio priešįtampio. Iš kitos pusės, dėl šios aproksimacijos taikymo atsiranda naudojamo žadinimo dažnio apribojimas. Atsižvelgiant į eksperimento metu naudotos struktūros parametrus, charakteristinis relaksacijos laikas yra $\tau \approx 200$ fs. Taigi, pristatytos lygtys yra teisingos supergardenę žadinant iki ~ 300 GHz dažniu.

Kaip jau buvo paminėta, priklausomai nuo zonduojančio elektrinio lauko stiprio galima taikyti mažo arba didelio signalo stiprinimo modelį. Mažo signalo stiprinimo modelis gali būti taikomas, kai zonduojančio dažnio signalas yra stipriai mažesnis lyginant su žadinančiuoju ir gali būti taikomas siekiant nustatyti sąlygas generacijos procesams supergardenėje prasidėti. Iš kitos pusės, didelio signalo stiprinimo modelis naudojamas kai zonduojantis signalas yra palyginamas su žadinančiuoju ir yra skirtas aprašyti stiprinimo procesų supergardenėje ribas.

7.3. Rezultatai

7.3.1. Disipatyvaus parametrinio stiprinimo stebėjimas legiruotose GaAs/AlGaAs supergardenėse ir mažo signalo stiprinimo metodas

Parametrinė generacija - procesas, kuris yra stebimas įvairiausiose fizikinėse sistemose, tokiose kaip elektroniniai grandynai, netiesinė optika ir Džozefsono mezoskopiniai prietaisai [153–155]. Šalia šių plačiai tyrinėjamų generacijos mechanizmų egzistuoja mažiau populiarus dispersinis parametrinis stiprinimo mechanizmas, kuris dažniausiai yra stebimas sistemose su netiesiniais osciliatoriais. Šio mechanizmo ypatybė yra galimybė generuoti sub-harmoninius dažnius [64]. Sistemą žadinant išoriniu kintamu elektriniu lauku, neigiamas diferencinės varžos režimas gali būti pasiektas per dalį kintamo žadinančio elektrinio lauko periodo [64, 156]. Šio tyrimo metu buvo nagrinėjami efektai pasireiškintys supergardenėse, veikiančiose stiprios dispersijos sąlygomis ($\omega_0\tau \ll 1$). Parodoma, kad regeneratyvus stiprinimas, atsirandantis dėl periodinio perjungimo į neigiamo diferencinio greičio (NDV) būseną, užtikrina stiprinimą ne tik žeminamojo dažnio keitimo procesais (angl. *down-conversion*), bet ir aukštinamojo dažnio keitimo procesais (angl. *up-conversion*) [140, 157]. Yra parodyta, kad kvantinėse puslaidinikinėse supergardenėse disipatyvaus stiprinimo mechanizmai yra galimi [158, 159], bet, nepaisant 50 metų trunkančių tyrimų, parametrinio stiprinimo galimybė supergardenėse iki šiol nėra eksperimentiškai patvirtinta.

Naudojantis aukščiau aprašytu eksperimentiniu stendu, sėkmingai užfiksuotas daugiadažnis spektras, sugeneruotas dispersinio parametrinio stipri-

mo procesų supergardenelėse metu. Impedanso transformatoriaus panaudojimas leido pilnai kontroliuoti žadinančios spinduliuotės fazę ir atspindį nuo tiriamos struktūros. Žadinančioji elektromagnetinė banga, sėkmingai susieta su supergardenele naudojant auksinę giją, moduliuoja elektronų dreifo greitį ir sužadina koherentinę emisiją, registruojamą spektro analizatoriumi. Naudojant klistroninį stiprintuvą buvo generuojamas žadinantysis 8,45 GHz dažnis. Taip pat supergardenelė buvo veikiamą nuolatine 0,3 V įtampa. Antrasis eksperimentas buvo atliktas supergardenelę žadinant magnetrono šaltinio 9,53 GHz dažnio kintamu elektriniu lauku, supergardenelę papildomai veikiant 0,2 V nuolatine įtampa. Abiem atvejais taikomas priešštampris viršijo įtampą reikalingą Esaki-Tsu kritiniam laukui supergardenelėje susidaryti. Naudotos struktūros atveju tokio priešštamprinio vertė yra $\approx 0,13$ V. Eksperimento metu registruoti spektrai pateikti 3.1 paveiksle.

Galima atkreipti dėmesį, kad buvo stebimi trys harmonikų tipai. Pirmasis (pažymėtas raudonai) atspindi pagrindinio dažnio harmonikas $\omega_1 = n\omega_0$, kur n yra sveikas skaičius. Antrasis tipas yra pusinės sub-harmonikos (pažymėtos žaliai) $\omega_1 = n\omega_0/2$. Galiausiai juodai yra pažymėtos trupmeninės sub-harmonikos $\omega_1 = p\omega_0/q$, kur p ir q yra sveiki skaičiai. Svarbu pabrėžti, kad naudojamu eksperimentiniu stendu neįmanoma registruoti $\omega_0/2$ pusinės harmonikos generacijos dėl bangolaidžio dažninių pralaidumo savybių. Tačiau šio dažnio generacija supergardenelės struktūroje yra numatyta teoriniuose darbuose, tad registruojant kitas pusines harmonikas yra tikėtina. Registruotų dažnių generacija susieta su žadinančiuoju dažniu pasinaudojant

$$\omega_1 \pm \omega_2 = n_{\pm}\omega_0; \quad \omega_1 = n_0\omega_0 \quad (7.7)$$

išraiškėmis, atspindinčiomis atitinkamai neišsigimusį ir išsigimusį procesus. Šiose lygtyse visi n žymi sveikus skaičius. Eksperimentų metu registruotų dažnių priskyrimas atitinkamiems neišsigimusiems procesams pateiktas 3.1 ir 3.2 lentelėse. Dažniai buvo priskirti trupmenoms su 2,5 % nuokrypio riba.

Verta atkreipti dėmesį į reikšmingą $n_- \geq 1$ procesų skaičių. Aukštinančio dažnio keitimo procesų egzistavimas supergardenelės struktūroje yra išskirtinis disipatyvaus mechanizmo bruožas [157, 158]. Kita vertus, žeminančio dažnio keitimo procesai, pasižymintys n_+ , yra universalus parametrinio stiprinimo supergardenelėje požymis [142]. Pastarasis yra papildomai pagrįstas labai stipria priklausomybe nuo žadinančios spinduliuotės fazės, reguliuojamos impedanso transformatoriumi. Iš pateiktų lentelių galima pastebėti, kad beveik visi užregistruoti dažniai dalyvauja keliuose skirtinguose procesuose. Tai suteikia papildomo supratimo apie analizuojamos struktūros sudėtingumą. Eksperimento metu registruojamas atsakas yra ne vieno, bet **daugybės tuo pačiu me-**

tu vykstančių daugiafotonų procesų rezultatas. Visi procesai, pateikti 3.1 ir 3.2 lentelėse, yra parodyti 3.2 paveiksle.

Pavyzdžiui, 8,45 GHz žadinančios kintamos spinduliuotės atveju (3.2 paveiklo kairėje), galima pastebėti raudonas punktyrines linijas, žyminčias penkis tuo pačiu metu vykstančius parametrinio stiprinimo procesus, kuriuose dalyvauja 28,2 GHz dažnio spinduliuotė. Taip pat galima pastebėti, kad skirtinguose procesuose dalyvauja skirtingas žadinančios spinduliuotės fotonų kiekis.

$$\left\{ \begin{array}{l} \mathbf{28,20} + 23,05 = 6 \times 8,45 \text{ GHz (8 fotonai),} \\ \mathbf{28,20} + 13,45 = 5 \times 8,45 \text{ GHz (7 fotonai),} \\ \mathbf{28,20} - 11,20 = 2 \times 8,45 \text{ GHz (4 fotonai),} \\ \mathbf{28,20} - 20,30 = 1 \times 8,45 \text{ GHz (3 fotonai),} \\ 36,25 - \mathbf{28,20} = 1 \times 8,45 \text{ GHz (3 fotonai).} \end{array} \right. \quad (7.8)$$

Lyginant su klasikiniiais parametrinės generacijos procesų atvejais optinėse sistemose, kurie yra aprašomi Manley-Rowe sąryšiais, eksperimento metu buvo stebimi generacijos ir stiprinimo procesai su ryškiai didesniu žadinančios spinduliuotės fotonų skaičiumi. Parodyta, kad stebėti procesai pažeidžia Manley-Rowe sąryšius. Svarbu pažymėti, kad Manley-Rowe sąryšių nepritaikomo supergardenės struktūroje galima tikėtis tik esant stipriam disipatyvumui $\omega_0\tau \ll 1$ ir Esaki-Tsu darbo režimui. Esant mažam disipatyvumui $\omega_0\tau \gg 1$, Manley-Rowe sąryšiai, kaip parodyta [158], yra tenkinami. Daugiau informacijos apie Manley-Rowe sąryšius galima rasti 6.1.3 priede.

Siekiant plačiau suprasti eksperimento metu supergardenėje vykstančius procesus, buvo matuojamos SL struktūros I-V priklausomybės taikant 20 ns trukmės elektros impulsus (žiūrėti pastorintą juodą liniją 3.3 (a) paveiksle). Teigiamas I-V kreivės polinkio kampas yra tipinis sistemoms, pasižyminčiomis neigiama diferencine varža (NDV), veikiančioms stabilaus transporto režime. Gautas kreives galima palyginti su I-V kreivėmis, aprašytomis literatūros apžvalgoje [106,107]. Raudona linija pagrindiniame grafike vaizduoja neutralią I-V charakteristiką, kuri tiesiogiai seka Esaki-Tsu $v(E)$ priklausomybę [63] ir leidžia gauti papildomos informacijos apie struktūroje naudojamus kontaktus. Ankstesniuose darbuose buvo parodyta, kad supergardenių su ominiais kontaktais I-V charakteristikos yra linkusios įsisotinti ties Esaki-Tsu srovės smaile arba virš jos (žiūrėti 3.3 paveiklo intarpą) [105]. Kaip galima pastebėti, eksperimento metu gauta I-V kreivė yra gerokai žemiau smailės srovės. Tai rodo, kad suformuoti neominiai kontaktai. Dėl kontaktų neomiškumo atsirandanti 0,65 V įterptinė įtampa buvo įvertinta ir įskaičiuota į visus toliau pateiktus skaičiavimus.

Taip pat šio tyrimo metu buvo pritaikytas klasikinis netiesinių optinių siste-

mų charakterizavimo metodas matuojant įėjimo-išėjimo galios priklausomybes. Šių priklausomybių nustatymas leidžia palyginti gautas kreives su siūlomais teoriniais modeliais. Paprasčiausias iš modelių numato, kad atitinkama n -toji harmonika turėtų būti apibūdinama n -osios laipsnio funkcijos priklausomybe nuo sužadavimo galios [60, 61]. Tačiau, skirtingai nei aukščiau paminėtuose optiniuose eksperimentuose, šio tyrimo metu struktūroje, pasižymintia kvadratinu netiesiškumu, buvo gautos tiesinės priklausomybės [160, 161]. Skirtingų dažnių tipų priklausomybės (antrosios harmonikos $2\omega_0$, pusinės sub-harmonikos $5\omega_0/2$ ir trupmeninės sub-harmonikos $12\omega_0/5$) pavaizduotos 3.3 (b) paveiksle. Antrosios harmonikos generacijos proceso įėjimo-išėjimo priklausomybė rodo kvadratinę priklausomybę, o sub-harmonikų priklausomybė yra tiesinė, tačiau su skirtingais polinkio kampais. Šis rezultatas dar kartą parodo sistemos sudėtingumą. Neatitikimai su teorinės optikos modeliais yra paaiškinami tuo, kad supergardenės struktūra mikrobangų elektriniame lauke turėtų būti analizuojama ne kaip gryna optinė sistema, o kaip **netiesinė optoelektroninė sistema, veikianti neigiamo diferencinio greičio režime su dominuojančia daugiafotone generacija / stiprinimu**. Sistemos sudėtingumas, atsispindintis daugybėje skirtingų aspektų kurie tik iš dalies buvo aptarti pateiktuose rezultatuose, lemia iki šiol nepilnai išvystytą teorinį modelį.

Mažo signalo stiprinimo modelio pritaikymas

Siekiant apytiksliai įvertinti kintamo žadinančio elektrinio lauko stiprį supergardenėje buvo išmatuotos keletas generuotos spinduliuotės galios priklausomybės nuo prie supergardenės prijungtos nuolatinės įtampos. Charakteristikos gautos keičiant (slopinant) žadinančios kintamos spinduliuotės elektrinį lauko stiprį (viena iš gautų priklausomybių yra pavaizduota 3.5 paveikslo kairėje). Buvo pastebėta, kad tokių priklausomybių išvestinės turi ryškius lokalius (antros išvestinės nuliai) ir globalius (pirmos išvestinės nuliai) ekstremumus (pažymėta su reikšmėmis 3.5 paveikslo dešinėje). Grįžtant prie anksčiau patikrinto mažo signalo stiprinimo modelio ir atsižvelgiant į anksčiau patvirtintą daugybės vienu metu vykstančių procesų išvadą, padaryta prielaida, kad eksperimento metu gautas profilis yra tiesinė kelių procesų superpozicija. Remiantis klasikinių optinių eksperimentų dėsniais buvo nuspręsta, kad procese dalyvaujančių fotonų skaičius yra atvirkščiai proporcingas nagrinėjamo proceso įnašui į bendrą profilį (t.y. daugiau fotonų - mažesnis koeficientas). Šios prielaidos leido apriboti taikomos superpozicijos lygtį iki $n < 4$, tad ieškomam profiliui yra taikoma

$$\frac{\mu}{\mu_{0 \text{ final}}} = C_1 \cdot \frac{\mu}{\mu_0}(n = 1) + C_2 \cdot \frac{\mu}{\mu_0}(n = 2) + C_3 \cdot \frac{\mu}{\mu_0}(n = 3) \quad (7.9)$$

lygtis. Čia μ/μ_0 yra atskiros judrio komponentės, atskirai apskaičiuotos procesams, kuriuose dalyvauja skirtingas žadinančio kintamo elektrinio lauko fotonų kiekis pagal 3 skyriuje pateiktas lygtis. Superpozicijoje atsižvelgiama tik į neigiamą santykinį judrį, nes teigiamo santykinio judrio atveju atitinkamas generacijos / stiprinimo procesas nevyks, tad jis netrukdytų kitiems procesams. Pavyzdinis atvejis yra pateiktas 3.5 paveiksle rodo, kad globali viršūnė yra ties 0,133 V (atsižvelgiant į neominio kontakto įtaką), kas atitinka 5,51 kV/cm elektrinio lauko stiprį arba $1,013E_{cr}$ kritinio Esaki-Tsu elektrinio lauko. Smailės padėtis yra geras atskaitos taškas, kadangi jis leidžia apsiriboti koeficientų ir kintamo žadinančio elektrinio lauko stiprio vertėmis, atitinkančiomis nustatytą smailės poziciją. Be to, nustatyta, kad atstumas tarp lokalių smailių keičiasi priklausomai nuo taikomo kintamo žadinančio elektrinio lauko stiprio (žiūrėti 3.6 paveikslą). Superpozicijos koeficientai C_2 ir C_3 nustatyti parenkant atitinkamus atstumus tarp skirtingų smailių, o C_1 koeficientas gautas vertinant viršūnių santykinį aukštį. Galutinė gauta lygtis

$$\frac{\mu}{\mu_{0 \text{ final}}} = 119 \cdot \frac{\mu}{\mu_0} (n = 1) + 18,85 \cdot \frac{\mu}{\mu_0} (n = 2) + 1 \cdot \frac{\mu}{\mu_0} (n = 3) \quad (7.10)$$

atitinka žadinantį kintamą elektrinį lauką $8,61E_{cr}$. Galima argumentuoti, kad gautas elektrinio lauko stipris yra per didelis, kad jam būtų taikomos mažo signalo stiprinimo modelio prielaidos, ir iš dalies tai būtų teisinga. Šios tyrimo dalies tikslas buvo apytiksliai nustatyti kintamo žadinančio elektrinio lauko stiprį supergardelėje. Kaip minėta anksčiau, mažo signalo modelis buvo žinomas ilgą laiką ir laikomas patikrintu, tad šiame tyrimo etape buvo nuspręsta pasirinkti mažo signalo stiprinimo modelį. Didelio signalo stiprinimo modelio sudėtingumas ir iš jo sekančios išvados, yra plačiau aptariamoms toliau. Atlikto tyrimo metu buvo pasiektas geras eksperimentinių ir teorinių duomenų atitikimas. Taip pat reiktų pažymėti, kad dėl pasiūlyto superpozicijos proceso buvo panaikinta sugerties zona, kurią galima stebėti daugumoje pavienių generacijos / stiprinimo procesų priklausomybių (žr. 3.4 paveikslą). Toks rezultatas dar kartą patvirtina, kad supergardelėje vienu metu vyksta daugybė generacijos / stiprinimo procesų su skirtingu žadinančių fotonų kiekiu.

Generacijos / stiprinimo fizikinis mechanizmas, lemiantis didelį stiprinimo koeficientą supergardelės struktūroje, vertas papildomo komentaro. Iš esmės, pateikta logika seka Hyart darbus [142], kuriuose generuojamos komponentės buvo aiškinamos skersinės elektromagnetinės modos formavimu išoriniame rezonatoriuje. Tačiau šio eksperimento metu naudotoje struktūroje tokio rezonatoriaus nėra. Todėl manoma, kad generacijos / stiprinimo procesai vyksta dėl supergardelės struktūroje besiformuojančių išilginių modų, kurios atsiranda

ir didėja dėl elektronų plazmos svyravimų. Elektromagnetinė banga, sklindanti bangolaidžiu su šviesos greičiu, susisieja su elektronų plazma ir konvertuojasi į lėtą išilginę modą, supergardenės struktūroje sklindančią elektronų dreifo greičiu [113, 164]. Jei sklidimo metu susiformuoja banga, kurios dažnis atitinka vieną iš „leistinų“ procesų, ir santykinis judris yra neigiamas, maža fliktuacija eksponentiškai auga elektronams judant supergardenės struktūroje. Stiprinimas gali būti išreikštas Beero dėsniumi ($I_{\text{out}} = I_{\text{in}} \exp(-\beta_n z)$), kur stiprinimo koeficiento išraiška β_n , priklausanti nuo koncentracijos, judrio ir dreifo greičio [165] yra

$$\beta_n = \frac{2eN\mu_n}{\epsilon v}. \quad (7.11)$$

Svarbu dar kartą pažymėti, kad stiprinimas yra atvirkščiai proporcingas sklindančios bangos greičiui. Priešingai nei elektromagnetinės bangos, kurios sklinda šviesos greičiu, išilginė banga sklinda dreifo greičiu. Atsižvelgiant į teoriškai pasiekiamą $\mu_1/\mu_0 \approx -0,02$ judrio vertę, lėtai sklindančios bangos atveju stiprinimo koeficientas sieks $\beta \gtrsim 10^4 \text{ cm}^{-1}$, kas yra gana įspūdingas skaičius lyginant su šiam momentui paskelbtais kitų generatorių technologijų pasiekimais (žr. 3.7 paveikslą). Galiausiai, generacijos / stiprinimo metu susiformavusios elektrostatinės modos vėl paverčiamos elektromagnetinėmis bangomis, kurios toliau sklinda bangolaidžiu spektro analizatoriaus link.

Apibendrinant, galima pabrėžti šiuos rezultatus:

- Nuolatinis elektrinis laukas žadinama supergardenė patalpinta į mikrobangų elektrinį lauką yra netiesinė optoelektroninė sistema, veikianti neigiamo diferencinio greičio režimu, pasižyminčiu daugiafotoniais generacijos / stiprinimo procesais.
- Eksperimento metu registruotas stabilus koherentinis parametris stiprinimas skirtingose žadinančios spinduliuotės harmonikose ir sub-harmonikose. Stiprinimas registruotas naudojant GaAs/AlGaAs supergardenę, kuri buvo žadinama nuolatinis ir kintamu elektriniais laukais.
- Stebėtas generacijos / stiprinimo efektas aiškinamas lėtų išilginių bangų, sklindančių dreifo greičiu, formavimu, užtikrinančiu stiprinimo koeficientus, viršijančius 10^4 cm^{-1} dėl šviesos greičio ir dreifo greičio skirtumo supergardenėje.
- Parodyta, kad supergardenėje vienu metu vyksta daugybė daugiafotoninių procesų. Registruoti spektrų dažniai buvo susieti per aukštinamuosius ir žeminamuosius dažnio keitimo procesus ($\omega_1 \pm \omega_2 = n_{\pm}\omega_0$). Abiejų tipų procesų egzistavimas buvo pripažintas kaip išskirtinė supergardenių,

veikiančių Esaki-Tsu NDV režimu, disipatyvaus generacijos / stiprinimo mechanizmo savybė.

- Užfiksuoti procesai, kuriuose dalyvauja iki 8 žadinančio elektrinio lauko fotonų.
- Parodyta, kad Manley-Rowe sąryšiai, aprašantys galios perdavimą netiesiniuose elementuose, negalioja disipatyvaus parametrinio stiprinimo sąlygoms ($\omega_0\tau \ll 1$) supergardenelėse, veikiančiose Esaki-Tsu neigiamo diferencinio greičio režime.

7.3.2. Didelio signalo stiprinimas GaAs/AlGaAs supergardenelėje išsigimusių ir neišsigimusių procesų metu

Išsigimę procesai

Gautos įžvalgos apie nuo fazės priklausančio parametrinio stiprinimo procesus supergardenelėse [A1] sudaro pagrindą tolimesniems tyrimams siekiant išplėsti stebėtų fizikinių mechanizmų suvokimą. Eksperimentiniai rezultatai [A1] parodė gerą atitikimą su pusiau klasikinio modelio prognozėmis [142, 147, 158, 159, 166, 167]. Vis dėlto ankstesniuose teoriniuose svarstymuose taikomos prielaidos stipriai riboja jų pritaikymą eksperimentiniu požiūriu. Visų pirma, didžioji dauguma darbų naudojo mažo signalo aproksimaciją skaičiavimams. Antra, minėti tyrimai neįskaito nuo fazės nepriklausančių Blocho stiprinimo efektų bei jų sąveikos su parametrinio stiprinimo procesais [163, 168]. Šis skyrius plečia ankstesnių tyrimų ribas. Pateikiama mažo signalo stiprinimo sąlygų apžvalga, išryškinant pagrindinius skirtumus lyginant su didelio signalo stiprinimo modeliu.

Prieš analizuojant didelio signalo stiprinimo modelį, verta plačiau susipažinti su mažo signalo stiprinimo modelio rezultatais, siekiant vėliau išryškinti skirtumą tarp dviejų modelių. Optimalaus judrio priklausomybės nuo prijungto pastovaus ir kintamo prieštampio skirtingų zonduojančių dažnių tipams yra pateiktos 4.1 paveiklėse. Skaičiavimui buvo taikoma 3.10 lygtis. Pirmas stulpelis atitinka nekoherentinę judrio komponentę, antras – koherentinę, o trečias stulpelis atitinka bendrą judrį, kuris yra lygus dviejų pirmųjų sumai. Atkreiptinas dėmesys, kad nekoherentinė judrio komponentė nepriklauso nuo analizuojamo zonduojančio dažnio. Šis komponentas yra neigiamas (t.y. užtikrina stiprinimą) $F_{dc} > F_{ac}$ prieštampio sąlygomis, kurias toliau vadinsime „I tipo prieštampio sąlygos“. Iš kitos pusės, $F_{dc} < F_{ac}$ sąlygomis („II tipo prieštampio sąlygos“), nekoherentinė komponentė yra teigiama, kas reiškia, kad šiomis prieštampio sąlygomis nekoherentinis stiprinimas yra neįmanomas. Koherentinis stiprinimas, $3\omega_0/2$ ir $\omega_0/2$ zonduojančių dažnių atvejais yra neigiamas

visame nagrinėtame prieštampio ruože. Šiuo atveju svarbu atkreipti dėmesį į skirtingą judrio verčių pasiskirstymą. Pusinėms sub-harmonikoms netipinė judrio priklausomybė $\omega_0/2$ atveju, taikant didelio signalo stiprinimo modelį nulemia daugybę įdomių efektų, kurie šiame darbe bus aprašomi vėliau. Taip pat svarbu atkreipti dėmesį, kad trupmeninės sub-harmonikos atveju koherentinio stiprinimo nesitikima, kadangi judrio komponentė yra teigiama visais prieštampio atvejais. Tokie koherentinio ir nekoherentinio judrio komponentų pasiskirstymai nulemia, kad žadinančio signalo harmonikų ir sub-harmonikų atvejais yra stebimos bent dvi atskirtos neigiamo judrio zonos. Atkreiptina, kad $\omega_0/2$ zonduojančio dažnio atveju stebima viena zona, kuri yra stipriai išplėsta lygiant su kitomis pusinėmis sub-harmonikomis. Trupmeninio zonduojančio dažnio atveju bendras neigiamas judris atitinka nekoherentinio neigiamo judrio prieštampio sąlygas.

Judrio priklausomybės nuo prieštampio sąlygų analizė skirtingiems dažnių tipams yra svarbi ir dėl kitos priežasties. Kaip nagrinėta ankstesniuose darbuose, generacijos procesai supergardenėje gali prasidėti nuo atsitiktinių triukšmo lygio fliktuacijų. Kol generuojamas signalas yra labai mažas, jam galioja mažo signalo stiprinimo modelis, tad galima teigti, kad mažo signalo stiprinimo modelis aprašo sąlygas, **leidžiančias prasidėti generacijos procesams**. Kaip jau buvo pastebėta eksperimento metu, generuojamas signalas gali nesunkiai viršyti mažo signalo stiprinimo modelio pritaikomumo ribas, tad turime taikyti didelio signalo stiprinimo modelį, **apibrėžiantį generacijos proceso ribas**.

Didelio signalo stiprinimo modelis skaičiuojamas pagal 4.2 išraišką. Didelio signalo analizę paprasčiau yra pradėti nuo išsigimusių stiprinimo procesų, kuriuose dalyvauja tik vienas zonduojantis dažnis. Pirmiausia verta atkreipti dėmesį į santykinę fazės skirtumą tarp žadinančio ir zonduojančio elektrinių laukų. Tipinės santykinės galios priklausomybės nuo santykinės fazės ir zonduojančio elektrinio lauko stiprio yra pateiktos 4.2 paveiksle. Grafikuose spalva žymi neigiamą santykinę galią, kurioja vyksta zonduojančio dažnio emisija. 4.2 (a) paveiksle vaizduojamas skirstinys dažniausiai sutinkamas, kai zonduojantis dažnis yra harmonika ir pusinė sub-harmonika. Stebimos akivaizdžios nuo zonduojančio elektrinio lauko stiprio nepriklausančios optimalios santykinės fazės $0, 5\pi$ ir $1, 5\pi$. Svarbu atkreipti dėmesį, kad stiprinimas yra leidžiamas nuo labai mažo zonduojančio elektrinio lauko stiprio, kas reiškia, kad pavaizduoto proceso atveju yra galima generacija iš triukšmo lygio fliktuacijų (tai pavaizduota žalios spalvos rodyklėmis). Taip pat verta atkreipti dėmesį į egzistuojantį santykinės fazės ruožą, kuriame santykinė galia yra teigiama visoms zonduojančio elektrinio lauko vertėms. Pasirinkus tokią santykinę fazę generacijos procesai nevyks iš viso. Tai akivaizdžiai parodo optinės fazės parinkimo svarbą eksperimento metu.

Kita tipinė priklausomybė, dažniausiai sutinkama kai zondojuojantis dažnis yra trupmeninė sub-harmonika, yra pavaizduota 4.2 (b) ir (c) paveiksluose ir atitinka $5\omega_0/3$ ir $7\omega_0/5$ zondojuojančius dažnius. Labai nesunku pamatyti akivaizdžius skirtumus, pasireiškiančius per „stiprinimo salų“ formavimą. Matome, kad net ir optimalios fazės atveju generacija nuo triukšmo lygio yra neįmanoma, nes stiprinimo procesai supergardelėje (neigiama santykinė galia) prasidės zondojuojančiam elektriniam laukui viršijus tam tikrą ribinę vertę išorinio proceso metu (pažymėtas raudonomis rodyklėmis). Tokios priklausomybės parodo, kad išsigimusio proceso metu, trupmeninių sub-harmonikų generacija yra negalima. Atsižvelgiant į santykinės galios priklausomybes nuo santykinės fazės, toliau bus nagrinėjami tik optimalios fazės procesai.

Paveiksle 4.3 yra pavaizduota generacijos metu pasiekiamos maksimalios santykinės galios priklausomybė nuo pastovaus ir kintamo priešįtampio. Grafike 4.3 (A) pavaizduotas $3\omega_0/2$ atvejis. Kaip pastebėta mažo signalo stiprinimo modelio analizės metu, generacija gali vykti dėl nekoherentinio Blocho stiprinimo, koherentinio parametrinio stiprinimo arba jų kombinacijos. Nagrinėjamame 4.3 (A) paveiksle II tipo priešįtampio sąlygomis stebimas grynas parametrinio stiprinimo mechanizmas. Tai galima pamatyti viršutiniame intarpe pavaizduotuose santykinės galios priklausomybėse nuo santykinės fazės ir zondojuojančio elektrinio lauko stiprio esant skirtingoms kintamo žadinančio elektrinio lauko stiprio sąlygoms (atitinka raudonus apskritimus pagrindiniame grafike). Intarpe matomas akivaizdus optimalus dažnis ir visiškos generacijos nebuvimas tam tikrame santykinės fazės ruože nurodo, kad stebimas generacijos procesas yra priskiriamas parametriniam stiprinimui. Priešįtampio sąlygoms $(F_{dc}; F_{ac}) = (0, 5; 4)$ nustatyta 3,2 mW maksimali galia, atitinkanti $E_1 \approx 9,7$ kV/cm.

Situacija pasikeičia nagrinėjant trupmenines sub-harmonikas. Zondojuojančio $3\omega_0/2$ dažnio atvejis yra pavaizduotas 4.3 (B) paveiksle. Matoma, kad II tipo priešįtampio sąlygomis generacija nuo labai silpno zondojuojančio elektrinio lauko stiprio yra negalima, bet joje formuojasi „stiprinimo salos“, ką galima pamatyti dešinėje esančiame intarpe, kuriame yra pavaizduota santykinės galios priklausomybė nuo santykinės fazės ir zondojuojančio elektrinio lauko stiprio. Intarpe esančios priklausomybės pateiktos atitinka pagrindiniame grafike raudonais apskritimais pažymėtas priešįtampio sąlygas. Pastebėtina, kad „stiprinimo salų“ atsiradimas yra išskirtinė didelio signalo stiprinimo modelio savybė.

I tipo priešįtampio sąlygomis ($F_{dc} > F_{ac}$) stipriai padidėja nekoherentinių procesų, priskiriamų Blocho mechanizmui, įtaka. Maksimalios generacijos proceso metu pasiekiamos santykinės galios mechanizmas $\omega_0/2$ zondojuojančio dažnio atveju yra pavaizduotas 4.4 (A) paveikslo kairėje. Maksimalaus pasiekiamo zondojuojančio elektrinio lauko stiprio priklausomybė pavaizduota 4.4 (A) pa-

veikslo dešinėje. Atkreiptinas dėmesys į šių dviejų skirstinių skirtumą. Taip pat svarbu atkreipti dėmesį į skirtingas santykinės galios priklausomybes I priešįtamčio sąlygomis, pavaizduotomis 4.4 ir 4.3 paveiksluose. Pastarasis skirstinys stebimas beveik visais skirtingų zondojuančių dažnių atvejais, tad $\omega_0/2$ yra išskirtinis dėl savo ypatingo mažo signalo stiprinimo modelio analizės metu pavaizduoto skirstinio.

Esant I tipo priešįtamčio sąlygoms, galime stebėti dviejų stiprinimo mechanizmų kombinaciją. 4.4 paveikslo viršuje esančiame intarpe matoma kaip didėjant kintamam žadinačiam elektrinio lauko stipriui plokščia santykinės galios priklausomybė tampa vis labiau priklausanti nuo santykinės fazės, kol galiausiai ties aukštais kintamo žadinančio elektrinio lauko stipriais tampa visiškai koherentinė, kaip jau buvo stebėta II tipo priešįtamčio sąlygų analizės metu. Šis vaizduojamas procesas atitinka perėjimą tarp gryno Blocho stiprinimo ($F_{ac} = 0$) į gryną parametrinį stiprinimo mechanizmą. Tarpinė būseną atitinka parametrinio ir Blocho stiprinimo sambūvis. Taip pat verta atkreipti dėmesį, kad gryno parametrinio stiprinimo mechanizmo būsenos pasiekimas yra unikali $\omega_0/2$ zondojuančio dažnio atvejo pasekmė. Kituose dažniuose, didinant žadinančio kintamo elektrinio lauko stiprį galima stebėti tik hibridinį stiprinimo mechanizmą su didėjančiu parametrinio mechanizmo dominavimu. Priešįtamčio sąlygoms $(F_{dc}, F_{ac}) = (4, 2)$ nustatyta 257 mW maksimali galia, atitinkanti $E_1 \approx 31,5$ kV/cm. Stiprinimo mechanizmo sambūvis taip pat yra stebimas ir trupmeninių sub-harmonikų generacijos atveju (žr. 4.5 paveikslą).

Be to, dėl dviejų procesų sambūvio atsiranda galimybė supergardelę patalpinti į II tipo priešįtamčio „stiprinimo salas” sąlygas nesinaudojant išoriniais zondojuančio dažnio šaltiniais. Tai yra pasiekama keičiant prie supergardelės pridėtos išorinės nuolatinės įtampos dydį.

Neišsigimę procesai

Neišsigimusio proceso metu generacijos / stiprinimo procese dalyvauja du skirtingo dažnio zondojuantys signalai. Šioje santraukos dalyje bus aptariami skirtumai lyginant su aukščiau pristatytais išsigimusio proceso rezultatais. Nagrinėjama vieno iš zondojuančio elektrinio lauko stiprio pokyčio įtaka sistemai, kurioje kiti parametrai (žadinančiųjų ir antro zondojuančio elektrinio lauko) yra pastovūs. Dėl labai didelio kintamųjų skaičiaus šiame skyriuje nagrinėjami tik du eksperimento metu stebėti procesai: $4/3 + 8/3$ atitinkantis trupmeninių sub-harmonikų stiprinimo procesą ir $1/2 + 3/2$ atitinkantis pusinių sub-harmonikos stiprinimo procesą. Siekiant paprastumo mažesnio dažnio zondojuantis elektrinis laukas toliau bus ženklinamas „1”, o didesnio „2”.

4.7 paveiksle pavaizduota pirmo zondojuančio elektrinio lauko santykinės galios priklausomybė nuo fazių skirtumo, pirmo zondojuančio elektrinio lau-

ko stiprio ir antro zonduojančio elektrinio lauko fazių skirtumo (fazių skirtumas yra skaičiuojamas žadinančio elektrinio lauko atžvilgiu). Priklausomybės yra pateiktos $4/3 + 8/3$ procesui, o nekintantys priešįtampio parametrai yra $F_{dc} = 4, F_{ac} = 3, F_2 = 2$. Lyginant su išsigimusio proceso priklausomybėmis, pateiktomis 4.2 paveiksle, galima pamatyti, kad išnyksta neišsigimusio proceso atvejais stebėta simetrija. Taip pat svarbu pastebėti, kad neišsigimusio trupmeninio proceso metu galima stebėti tiek generacijai tinkančią optimalią fazę, tiek „stiprinimo salą“. Šis skirtumas yra labai svarbus, kadangi, kaip žinoma, eksperimento metu trupmeninių dažniu generacija buvo stebima supergardenėje, patalpintoje į II zonos priešįtampio sąlygas. Tokiomis sąlygomis trupmeninių sub-harmonikų generacija negali būti paaiškinama nei žemo signalo stiprinimo modeliu nei didelio signalo stiprinimo modeliu nagrinėjant išsigimusius procesus.

Išsigimusio ir neišsigimusio procesų skirtumai yra atskleidžiami 4.8 paveiksle, vaizduojančiame maksimalaus pasiekiamo 1 zonduojančio elektrinio lauko santykinės galios priklausomybę nuo priešįtampio ir antro zonduojančio elektrinio lauko sąlygų $4/3 + 8/3$ proceso metu. Abu fazių skirtumai šiame grafike yra optimalios. Patvirtinama 4.7 paveikslo analizės metu padaryta išvada, kad neišsigimusio proceso metu galima trupmeninio dažnio generacija esant II tipo priešįtampio sąlygoms. Be to, matoma, kad generacijos mechanizmų skirtumas aptartas išsigimusio proceso analizės metu išlieka: II tipo priešįtampio sąlygose stebimas grynas parametrinis stiprinimas (viršutinis intarpas), o I tipo priešįtampio sąlygose stebimas Blocho ir parametrinės generacijos sambūvis (apatinis intarpas).

Papildomai atlikta galios perdavimo analizė išryškina tris zonas su skirtingų energijos perdavimo krypčių priklausomybe nuo priešįtampio sąlygų.

Apibendrinant buvo suformuluotos tokios išvados:

- Išryškinta zonduojančio elektrinio lauko fazės parinkimo svarba. Atskleidžiant optimalios fazės egzistavimą, užtikrinančios daug didesnę stiprinimą, taip pat parodomas neoptimalios fazės egzistavimas, kurį pasirinkus supergardenėje gali visiškai nevykti generacijos / stiprinimo procesai.
- Parodytos sąlygos „stiprinimo salų“ formavimui, kai stiprinimo procesai supergardenėje pasileidžia zonduojančiam elektriniam laukui viršijus tam tikrą ribinę zonduojančio elektrinio lauko stiprio vertę.
- Parodytas nuo fazės nepriklausančio Blocho ir nuo fazės priklausančio parametrinio stiprinimo mechanizmų sambūvis, atsirandantis nuolatiniame priešįtampio viršijus kritinį Esaki-Tsu elektrinį lauką. Parodytas dominuojančio proceso pasikeitimas keičiant žadinančio kintamo elektrinio lauko stiprį.

- Išsigimusio proceso metu, $\omega_0/2$ zonduojančio elektrinio lauko dažnio atveju grynas parametrinis stiprinimas gali būti pasiektas esant aukštoms (bent kelis kartus viršijančioms kritinės įtampos) kintamo ir nuolatinio priešįtampos vertėms (unikali 1/2 sub-harmonikos savybė).
- Pristatyta supergardenelės patalpinimo į „stiprinimo salos“ režimą metodika, kuri remiasi nuolatinės žadinančios įtampos perjungimu. Metodas leidžia supergardenlei generuoti trupmeninę sub-harmoniką gryno parametrinio stiprinimo mechanizmo metu, nenaudojant išorinio šaltinio, veikiančio zonduojančiame dažnyje.
- Parodyta, kad neišsigimusio proceso metu galima trupmeninės sub-harmonikos generacija (nuo labai mažo zonduojančio signalo) grynu parametriniu mechanizmu.

7.3.3. Stabilus Blocho stiprinimas registruotas per hibridinę Bloch-plazmoninę modą GaAs/AlGaAs supergardenelėje

Yra žinoma, kad koherentinis lazerinis spinduliavimas lazeriuose yra paremtas populiacijos inversija (žr. 5.1 (a) paveikslą) [171, 172]. Šviesos stiprinimas tokiose sistemose yra proporcingas krūvininkų inversijos dviejuose lygiuose skirtumui [173]. Iš kitos pusės, vertą atkreipti dėmesį į kitokį stiprinimo mechanizmą. Realiose sistemose energetiniai lygmenys gali išsiplėsti. Tokiu atveju krūvininkų pasiskirstymas viename lygmenyje tampa nehomogeniškas (žr. 5.1 (b) paveikslą). Tada gali pasireiškti dispersinis stiprinimo mechanizmas, kuris yra stipriai priklausantis nuo dažnio su stiprinimo / sugerties proceso pokyčiu ties dviejų lygmenų rezonansiniu dažniu. Raudonai paslinktas dažnis atitinka stiprinimo sąlygas, o mėlynai paslinktas – sugerties. Kadangi tokio stiprinimo mechanizmo atveju krūvininkų populiacija abiejuose lygmenyse yra apytiksliai vienoda, stebimas procesas yra priskiriamas prie beinversinių stiprinimo procesų.

Pritaikant aprašytus procesus supergardenelėms, yra žinoma, kad nuolatinio priešįtampiu veikiamoje supergardenelėje vienodu atstumu vienas nuo kito susiformuoja Wannier-Starko lygmenys pasižymintys apytiksliai vienodu krūvininkų pasiskirstymu lygmenyse. Tai leidžia tikėtis beinversinio stiprinimo tokiose struktūrose, veikiant žemesniuose už Blocho dažniuose. [174–177]. Vienas iš didžiausių iššūkių, trukdantis sėkmingam tokio stiprinimo registravimui - homogeniško elektrinio lauko supergardenelėje užtvirtinimas. Kadangi, kaip buvo minėta anksčiau, neominių kontaktų panaudojimas užtikrina elektrinio lauko supergardenelėje homogeniškumą, galima tikėtis stabilaus Blocho procesų stiprinimo.

Ankstesniuose darbuose yra parodoma, kad beinversinis stiprinimas gali būti stebimas dviejų lygmenų sistemoje, kuriose žadinimas vyksta lazerine spinduliuote, pavyzdžiui kvantinių kaskadų lazeriuose [15, 16]. Tokiose struktūrose stebimos Blocho osciliacijos yra stipriai priklausančios nuo lazerinio sužadavimo spektrinės formos, užtikrinančios kaimyninių Wannier-Starko lygių saveika (žr. 5.3 (a) paveikslą) [5–7, 65, 127]. Šio eksperimento metu buvo taikomas elektrinis sužadavimo metodas, tad optinė dviejų lygmenų saveika yra negalima. Įrodoma, kad saveika tokio eksperimento metu yra užtvirtinama hibridine Bloch-plazmonine moda (žr. 5.3 (b) paveikslą).

Stebimi stiprinimo efektai yra galimi dėl neigiamo diferencialinio greičio režimo atsiradimo supergardenėje, kuri yra veikiamą tam tikro prieštampio. Tokiomis sąlygomis yra būtina atsižvelgti į skirtingų modų sambūvio galimybę. Ankstesniuose tyrimuose tai yra Blocho osciliacijos, plazmoninė moda ir optiniai fononai [130]. Sambūvio atveju modų elgesys keičiasi lyginant su pavienių modų egzistavimo atveju. Blocho ir plazmoninių modų sambūvio atveju sprendžiama švytuoklės lygtis yra

$$\ddot{\eta} + \omega_P^2 \sin(\eta) = 0, \quad (7.12)$$

Čia η nurodo poslinkį, $\omega_P = \sqrt{4\pi N e^2 / m^*}$ - plazminių osciliacijų dažnį, o N - legiravimą [132, 133]. Puslaidininkinių supergardenių atveju efektinė masė yra aprašoma $m^* = 2\hbar^2 / \Delta d^2$ lygtimi [134]. 7.12 lygties sprendimas aprašo klasikinės dalelės judėjimą $V(\eta) = \omega_P^2 (1 - \cos(\eta))$ periodiniame potenciale su $\omega_B^2 / 2$ energija. Švytuoklės lygtis aprašo perėjimą iš plazminių osciliacijų į Blocho osciliacijas. Kai energija yra mažesnė už potencialo maksimumą, dalelė yra įstrigusi viename potenciale dėl plazmoninio ekranavimo efektų. Jei dalelės energija viršija potencialo barjerą, dalelės svyruos Blocho dažniu. [135]. Šis efektas stebimas ties $\omega_B = 2\omega_P$ dažniu (žr. 1.7 paveikslą). Akivaizdžiai yra stebima plazmoninės ir Blocho modų sambūvio galimybė supergardenėje. [131].

Lyginant eksperimento metu gautas priklausomybes, pateiktas 5.5 paveiksle, su teoriniais skaičiavimais (žr. 1.7 paveikslą) [131], stebima akivaizdi priklausomybių koreliacija. Atkreiptinas dėmesys, kad pranašautas staigus perėjimas nuo plazmoninės į Blocho modą yra išsiplėtęs, kas yra paaiškinama krūvininkų susidūrimais. Akivaizdus teorinių ir eksperimentinių priklausomybių sutapimas leidžia teigti, kad registruotas stiprinimo profilis atitinka **plazmoninį Epshteino efektą** per susietą hibridinę Bloch-plazmoninę modą (žr. 1.7 paveikslą). Kiek yra žinoma, tai yra pirmasis eksperimentinis šio efekto patvirtinimas.

Generuotos spinduliotės galios priklausomybės nuo tiesioginio bei atgalinio prieštampio yra pavaizduotos 5.5 paveiksle. Naudojamas 30 mW galios magnetronas, veikiantis 9,44 GHz dažnyje. Galima matyti, kad abi priklausomybės

yra vienodos formos, bet pastumtos viena kitos atžvilgiu dėl asimetrinių kontaktų struktūroje. Atgalinio priešitampio atveju plazmoninės sugerties erdvė yra labai stipriai išplėsta (iki 3,8 V lyginant su 0,5 V tiesioginio priešitampio atveju) dėl didesnio reikiamo elektrinio lauko stiprio norint injektuoti Bloch stiprinimui pakankamą elektronų kiekį. Minijuostos viduje, kol stiprinimo mechanizmas paremtas minijuostos viduje vykstančia lygmenų saveika, generuojama galia beveik nepriklauso nuo elektrinio lauko stiprio, kol (ties 3,8 V tiesioginio ir 6,7 V atgalinio priešitampio atvejais) Blocho stiprinimas, paremtas tarpminijuostine sąveika, tampa dominuojančiu. Dominuojant Blocho stiprinimui yra stebima tiesinė galios priklausomybė nuo priešitampio. Pabrėžtina, kad aukštadažnis stiprinimas, stebimas tiek minijuostos, tiek tarpminijuostinio krūvininkų transporto modelio rėmuose, yra paaiškinamas neigiamo diferencialinio judrio atsiradimu [186], bet tarpminijuostinio modelio atveju, didėjant elektriniam laukui dreifo greitis mažėja greičiau $v_d \sim E^{-n}$ (n vertė priklauso nuo sklaidos mechanizmo, bet visada yra $n > 1$) [187]. Šis dreifinio greičio elgesio skirtumas paaiškina stebėtų priklausomybių elgesio pokytį, kuris vyksta supergardelėje keičiantis transporto režimui. Tarpminijuostinės generacijos procesai gali būti priskiriami nerezonansiniam Zenerio tuneliavimui, tad stiprinimo didėjimas parodo fazės išsilaikymą tarp minijuostinio ir tarpminijuostinio transporto modeliais aprašomo stiprinimo. Atkreiptinas dėmesys, kad Blocho stiprinimo įsisotinimas minijuostos stiprinimo režime gali būti siejamas su sklaida ir bedispersine fononinės modos sąsaja su Blocho osciliacijomis.

Siekiant patvirtinti, kad eksperimento metu stebėtas efektas gali būti priskiriamas prie plazmoninio Epshteino efekto, tiriamai struktūrai buvo nustatytas perėjimo dažnis tarp plazmoninės-fononinės ir Bloch-fononės modos. Yra žinoma, kad plazminis dažnis supergardelėje yra išreikštas

$$f_P = \sqrt{\frac{e^2 N}{m_0 \epsilon_0 \epsilon_r}} \quad (7.13)$$

lygtimi. Čia $m_0 = 2\hbar^2/\Delta d^2$ yra efektinė masė [131, 188]. Tad gaunamas plazminis dažnis yra $f_P \approx 1,24$ THz. Eksperimento metu perėjimas buvo stebimas ties 0,5 V priešitampį. Šios priešitampio sąlygos atitinka 21,6 kV/cm elektrinio lauko stiprį. Atsižvelgiant į Blocho dažnio lygtį

$$f_B = \frac{edE}{2\pi\hbar}$$

gauname $f_B = 3,14$ THz Blocho dažnį. Taip pat reikia atsižvelgti į struktūros įtaką. Įsivaizduojama, kad supergardelė yra kondensatorius, įterptas tarp dviejų laidžių sluoksnių. Tada tiek plazmos, tiek Blocho dažnis turi būti modifikuoti (žr. [15] komentarą [131]). Modifikatoriai yra išreikšti

$$f_B = f_B \varepsilon_\infty / \varepsilon_r; \quad f_P = f_P \sqrt{\varepsilon_\infty / \varepsilon_r} \quad (7.14)$$

lygtimis. Čia ε_∞ ir ε_r yra atitinkamai aukšto ir žemo dažnio dielektrinės konstantos. GaAs atveju šios vertės yra lygios 10,9 ir 12,9. Pritaikius modifikatorių galutiniai dažniai yra $f_P = 1,14$ THz ir $f_B = 2,65$ THz. Gautas dažnių santykis ($f_B/f_P \approx 2,33$) yra pakankamai arti teoriškai numatyto 2. Stebimas neatitinkimas gali būti paaiškinamas nenuline srove, kuri atsiranda dėl priešitampio ir nėra įskaityta teoriniame modelyje.

Gauti rezultatai leidžia sudaryti bendrą vaizdą bei pastebėti ypatybes esant skirtingam krūvininkų transporto mechanizmui, atsirandančiam dėl skirtingo taikomo priešitampio. Šių mechanizmų iliustracija yra pateikta 5.6 paveiksle [182]. Didėjant priešitampiui, krūvininkų transporto mechanizmas keičiasi iš omino režimo į Blocho stiprinimo režimą, kuris pereina į tarpminijuostinį transporto režimą, kuris yra sąlygotas nerezonansinio Zenerio tuneliavimo proceso.

Apibendrinant:

- Pirmą kartą puslaidininkinėse supergardenelėse pademonstruotos eksperimentiškai susieta hibridinė Bloch-plazmoninė (Epshteino) moda.
- Didinant nuolatinį priešitampį stebimas staigus stiprinimo mechanizmo perėjimas nuo susietos plazmoninės modos link stabilaus Blocho stiprinimo režimo.
- Kambario temperatūros sąlygomis GaAs/AlGaAs supergardenelėje buvo registruojamas stabilus beinversinis Blocho stiprinimas mikrobangų intervale. Stiprinimas išlieka supergardelei esant miniujuostiniame ir tarpminiujuostiniame krūvininkų transporto režimuose.
- Keičiant priešitampio sąlygas krūvininkų transporto režimas supergardenelėje gali būti derinamas nuo omino, Blocho stiprinimo arba tarpminijuostinio tuneliavimo režimo.

7.4. Paveikslų ir lentelių sąrašas

1.7 paveikslas: Trijų modų sambūvio priklausomybė nuo dažnio: plazmonfononinės modos sąsaja $f < 2f_p$ ir Bloch-fononinės modos sąsaja $f > 2f_p$ atvejais. Brūkšniuota linija žymi švytuoklės 7.12 lygties sprendinį, o simboliai parodo modifikuotos lygties sprendimą [131]. Nesant krūvininkų susidūrimų galima tikėtis staigaus perėjimo tarp dviejų modų. Aperiodinio elektrono judėjimo sritis yra pažymėta vertikaliomis juodomis linijomis.

2.1 paveikslas: Padidintas analizuojamos GaAs/AlGaAs supergardenės vaizdas. AuTi Schottky kontaktas yra patalpintas virš supergardenės, o supergardenės apačioje yra MBE būdu užauginta heterostruktūra. Prie viršutinio kontakto pritvirtinta 25 μm auksinė gija skirta kintamo elektrinio lauko sąsajai su tiriamąja struktūra ir nuolatinio prieštampio prijungimui. Ominis kontaktas užgarintas struktūros apačioje. Šlapio išdininimo būdu buvo suformuotos 80 $\mu\text{m} \times 80 \mu\text{m}$ mezos.

2.4 paveikslas: Tiriamojo stendo dalis, vaizduojanti bandinio patalpimą į bangolaidį. Bandinys pozicionuojamas išilgai ilgajai bangolaidžio (17 mm \times 8 mm) kraštinei. 25 μm gija, skirta kintamo elektrinio lauko sąsajai su tiriamąja struktūra ir nuolatiniam prieštampiui prijungti, yra pritvirtinama prie bangolaidžio, o apatinis ominis kontaktas yra prijungiamas prie koaksialinės linijos per žemo dažnio filtrą. Galutinis struktūros storis $\approx 1,3 \mu\text{m}$.

2.5 paveikslas: Eksperimentinis stendas. Žadinančių mikrobangų generacija buvo atliekama klistroninių stiprintuvu (8,2–12,4 GHz dažnių ruože) arba 9,53 GHz dažnio magnetronu (MWGS). Žadinanti spinduliuotė, praėjusi pro žemo dažnio filtrą (LPF), naikinančiu aukštesnes žadinančio dažnio harmonikas, feritiniu cirkulatoriumi (FC) yra nukreipiama į bandinio bangolaidžio liniją. Bangolaidžio linijoje sumontuotas impedanso transformatorius (IT) suteikia galimybę slopinti žadinančio signalo atspindžius ir valdyti žadinančios spinduliuotės fazę. Impedanso transformatoriaus derinimas atliekamas ieškant didžiausio išeinančio signalo. Bangolaidinis jungiklis (WS), leidžiantis prijungti tris WR-90/WR-XX adapterius (WR-XX: WR-62, WR-42, WR-28), leidžia išplėsti vienu metu detektuojamą dažnio ruožą. Praėjęs signalas buvo analizuojamas C4-27 spektro analizatoriumi (SpAn). Atspindėto signalo analizė buvo atliekama Schottky dioddo detektoriumi (DET), prijungtu prie LeCroy Waverunner skaitmeninio osciloskopo, per stiprintuvą (ATTEN) ir izoliatorių (FI).

3.1 paveikslas: Eksperimento metu stebėti daugiadažniai spektrai. Grafikas kairėje vaizduoja spektrą supergardenę žadinant 8,45 GHz klistroniniu stiprintuvu, grafikas dešinėje gautas supergardenę žadinant 9,53 GHz magnetronu. Atkreiptinas dėmesys į skirtingomis spalvomis pažymėtus dažnius, atitinkančius skirtingus generuotų dažnių tipus. Stora raudona linija atitinka žadinančią dažnį, plonos raudonos linijos atitinka žadinančio dažnio harmonikas. Žalios linijos atitinka pusines sub-harmonikas. Pusinis $\omega_0/2$ dažnis nėra registruojamas. Juodos linijos atitinka trupmenines sub-harmonikas.

3.1 lentelė: Galimos stiprinimo procesų išraiškos atitinkančios $\omega_1 + \omega_2 = n_+\omega_0$ (viršuje) ir $\omega_1 - \omega_2 = n_-\omega_0$ (apačioje) lygtis. Išraiškos pateiktos atsižvelgiant į eksperimento metu registruotą daugiadažnį spektrą supergardenelę žadinant 8,45 GHz klitroniniu stiprintuvu. Priskiriant dažnius sub-harmonikoms buvo taikoma 2,5 % paklaida.

3.2 lentelė: Galimos stiprinimo procesų išraiškos, atitinkančios $\omega_1 + \omega_2 = n_+\omega_0$ (viršuje) ir $\omega_1 - \omega_2 = n_-\omega_0$ (apačioje) lygtis. Išraiškos pateiktos atsižvelgiant į eksperimento metu registruotą daugiadažnį spektrą, kuris buvo gautas supergardenelę žadinant 9,53 GHz magnetronu. Priskiriant dažnius sub-harmonikoms buvo taikoma 2,5 % paklaida.

3.2 paveikslas: Leistini eksperimento metu stebėti generacijos / stiprinimo procesai ir juose dalyvaujantys dažniai bei žadinančios spinduliuotės fotonų kiekis. Grafikas kairėje atitinka žadinimą 8,45 GHz dažnio klitroniniu stiprintuvu, o dešinėje pavaizduotas 9,53 GHz dažnio žadinimo magnetronu atvejis. Dažniai yra normuoti į žadinančio kintamo elektrinio lauko dažnį. Spektro linijos grafikų gale atitinka registruotas harmonikas (raudoni), pusines sub-harmonikas (žali) ir trupmenines sub-harmonikas (juodi). Ryšiai horizontalioje plokštumoje atitinka 3.1 išraišką, o ryšio spalva atitinka procese dalyvaujantį žadinančio kintamo elektrinio lauko fotonų kiekį. Stora raudona linija horizontalioje plokštumoje paryškina kelis procesus, kuriuose dalyvauja 28,20 GHz dažnis. Tai parodo, kad supergardenelėje vienu metu gali vykti keli daugiafotoniai procesai (žr. 3.2 išraišką).

3.3 paveikslas: (a) Nagrinėjamos supergardenelės eksperimentinės I-V charakteristikos (stora juoda linija). Vertikali punktyrinė žalia linija atitinka Esaki-Tsu maksimalios srovės (raudona linija) įtampą $E_{cr}L \approx 0,1$ V. Maksimali srovė siekia $I_p \approx 2,4$ A. Intarpas vaizduoja Esaki-Tsu kreivės (raudona linija (2)) ir struktūros su ominių kontaktu (oranžinė linija (1)) I-V charakteristikų palyginimą. Stebimas ryškus I-V charakteristikų skirtumas dar kartą pabrėžia neominių kontaktų naudojimo svarbą parametrinės generacijos procesams stebėti. (b) Įvesties-išvesties galių priklausomybė skirtingų dažnių tipams. Šio eksperimento metu supergardenelė nebuvo veikiamą nuolatinio priešitampio. Supergardenelė buvo žadinama 8,45 GHz dažnio elektriniu lauku. Atkreiptinas dėmesys į registruotų priklausomybių skirtumą: harmonikų atveju stebima kvadratinė priklausomybė, o pusinių ir trupmeninių sub-harmonikų atveju stebimos skirtingo polinkio tiesinės priklausomybės [A1].

3.4 paveikslas: Neigiamo judrio μ^{opt}/μ_0 erdvės keičiant priešitampio sąlygas

skirtingiems $\omega_1 = n\omega_0$ dažniams (n aprašo generacijos procese dalyvaujantį kintamo žadinančio elektrinio lauko fotonų skaičių). Priešįtampis yra normuotas į Esaki-Tsu kritinį elektrinį lauką. Baltos erdvės apibrėžia priešįtampio sąlygas kai judris yra teigiamas ir stiprinimas / generacija yra neįmanomi. Spalva nurodo santykinio judrio dydį. Atkreiptinas dėmesys į vientisą generacijos stiprinimo zoną $n = 1$ atveju ir akivaizdžiai išskirtas generacijos / stiprinimo erdves $n > 1$ atveju.

3.5 paveikslas: (a) $5\omega/2_{\text{exc}}$ pusinės sub-harmonikos pavyzdinė išvado galios priklausomybė nuo prijungto nuolatinio priešįtampio, žadinant 8,45 GHz klistroniniu stiprintuvu. (b) Išvado galios priklausomybės nuo prijungto nuolatinio priešįtampio išvestinė. Atkreiptinas dėmesys į keturis taškus (pažymėti rodyklėmis), kurie yra tipiniai šioms priklausomybėms. Santykinis atstumas tarp šių taškų buvo vienas iš parametrų, naudojamų kintamo žadinančio elektrinio lauko stipriui supergardenėje surasti.

3.7 paveikslas: Parametrinės generacijos procesas supergardenės struktūroje. Aukšto dažnio kintamas žadinantis elektrinis laukas, susietas su supergardenėle per aukšinę giją, yra nukreipiamas išilgai z -ašiai. Banga, sąveikaudama su elektronais minijuostoje, sužadina augančias plazmonines bangas registruotuose dažniuose. Generuota išilginė elektrostatinė banga slenka išilgai supergardenės struktūrai elektronų dreifo greičiu. Paveikslas schematiškai atvaizduoja elektronų tankio erdvinę moduliaciją, atsirandančią dėl lėtų bangų slinkimo struktūroje.

4.1 paveikslas: Nekoherentinė (kairysis stulpelis), koherentinė (vidurinis stulpelis) ir bendra (dešinysis stulpelis; dviejų pirmųjų suma) neigiamo judrio komponentės μ^{opt}/μ_0 , apskaičiuotos naudojant mažo signalo stiprinimo modelį. Vaizduojamos priklausomybės nuo nuolatinio ir kintamo žadinančių elektrinių laukų stiprio (elektrinių laukų stipris normuotas į Esaki-Tsu kritinį elektrinį lauką, o judris yra normuotas į Drude judrį). Spalva atitinka neigiamo judrio sąlygas, o balta spalva žymi teigiamo judrio sąlygas, kuriose nesitikima stiprinimo / generacijos procesų. Pateiktos priklausomybės trimis skirtingiems dažnių tipams: pirma eilutė atitinka $3\omega_0/2$ pusinę sub-harmoniką; antra eilutė atitinka $\omega_0/2$ dažnį (šios sub-harmonikos unikalumas yra paaiškinamas vėliau); trečia eilutė atitinka $5\omega_0/3$ dažnį ir vaizduoja tipinį trupmeninės sub-harmonikos atvejį. Išties raudonos linijos vaizduoja nekoherentinio stiprinimo zonos ribas. Atkreiptinas dėmesys, kad nekoherentinė komponentė nepriklauso nuo dažnio tipo. Be to, bendras judris $3\omega_0/2$ dažnio atveju, būdamas tipiniu pusinėms sub-harmonikoms, pasižymi dvejomis atskirtomis neigiamo judrio erdvėmis, pa-

žymėtomis I (dešinėje apačioje; $F_{dc} > F_{ac}$) ir II (kairėje viršuje; $F_{ac} > F_{dc}$). Ši atskirtis yra labai svarbi tolimesnei generacijos, stiprinimo procesų analizei. Taip pat verta atkreipti dėmesį į vientisą neigiamo judrio zoną $\omega_0/2$ dažnio atveju. Galiausiai, atkreiptinas dėmesys, kad trupmeninės sub-harmonikos atveju koherentinė judrio komponentė yra visada teigiama. Pavaizduotos priklausomybės suteikia pradinį stiprinimo procesų supergardenėje supratimą, kuris yra būtinas tolimesnei analizei naudojant didelio signalo stiprinimo modelį, kadangi mažo signalo stiprinimo modelis tiksliai aprašo priešįtamčio sąlygas, užtikrinančias generacijos procesų supergardenėje pradžią [A3].

4.2 paveikslas: Pavyzdinės santykinės zondojuojančio dažnio galios priklausomybė nuo zondojuojančio dažnio elektrinio lauko stiprio ir fazių skirtumo, apskaičiuota fiksuoto priešįtamčio ir zondojuojančio dažnio sąlygomis naudojant didelio signalo stiprinimo modelį. (a) $\omega_1/\omega_0 = 2$, $F_{dc} = 0$, $F_{ac} = 5$. Galima akivaizdžiai stebėti dvi atskiras generacijos / stiprinimo erdves, atitinkančias $\varphi_{opt} = \pi/2$ ir $3\pi/2$. Nustatytomis sąlygomis galima pasiekti iki $3E_{cr}$ elektrinio lauko stiprį (žr. žalius apskritimus, rodančius, kad generacijos procesas, prasideda nuo triukšmo lygio signalo). (b) $\omega_1/\omega_0 = 5/3$, $F_{dc} = 0$, $F_{ac} = 5$. Naudojant didelio signalo stiprinimo modelį stebimos neigiamos santykinės galios vertės (stiprinimas), esant tam tikrai optimaliai fazei bei prasidedančios zondojuojančio elektrinio lauko stipriui viršijus tam tikrą ribinę vertę. Toks stiprinimo procesas pažymėtas raudonu apskritimu (stiprinimas, leidžiamas nuo didelio signalo vertės, stipriai viršijančios triukšmo lygį). Siekiant stebėti stiprinimą tokiais sąlygomis, turi egzistuoti išorinis mechanizmas, užtikrinantis zondojuojančio elektrinio lauko sužadimą virš ribinės vertės (raudona rodyklė), po kurios supergardenėje prasidės stiprinimo procesai (žalia rodyklė). Tokių stiprinimą užtikrinančių sąlygų atvejis yra vadinamas „stiprinimo salomis“. (c) $\omega_1/\omega_0 = 7/5$, $F_{dc} = 1$, $F_{ac} = 10$. Atkreiptinas dėmesys į reikšmingą ribinio elektrinio lauko stiprio vertės padidėjimą, didėjant trupmeninio dažnio vardikliui. Spalva parodo santykinės galios $\bar{P} = P/P_0$ vertę, o baltai pažymėtu erdvių atveju santykinė galia yra teigiama (nesitikima stiprinimo ar generacijos procesų) [A3].

4.3 paveikslas: (A) Generacijos metu maksimalios pasiekiamos santykinės galios priklausomybė nuo priešįtamčio sąlygų, apskaičiuota esant optimaliai fazei naudojant didelio signalo stiprinimo metodą. Skaičiuojamas $3\omega_0/2$ zondojuojančio dažnio atvejis (tipinė pusinė sub-harmonika). Spalvotos erdvės atitinka generuojamą santykinę galią \bar{P} , o baltos erdvės atitinka priešįtamčio sąlygas kuriose generacijos procesai yra negalimi. Juoda punktyrinė linija ir raudoni apskritimai, atitinkantys II tipo priešįtamčio sąlygas, vaizduoja priešįtamčio

vertes ($F_{dc} = 0, 5$ ir $F_{ac} = 2 : 1 : 4$) kurios buvo panaudotos viršutiniame intarpe (a) - (c), vaizduojant santykinės galios priklausomybes nuo zonduojančio dažnio elektrinio lauko stiprio ir fazių skirtumo. Stebimi fazių skirtumo intervalai, kuriuose generacijos procesai yra neleistini, parodo parametrinę analizuojamo proceso prigimtį. Atkreiptinas dėmesys į reikšmingą kintamo elektrinio lauko priešįtamčio ribinę vertę ($F_{ac} > 2$), kuri turi būti viršyta norint stebėti gryną parametrinį stiprinimą. (B) Generacijos metu maksimalios pasiekiamos santykinės galios priklausomybė nuo priešįtamčio sąlygų, apskaičiuota esant optimaliai fazei, naudojant didelio signalo stiprinimo metodą. Skaičiuojamas $5\omega_0/3$ zonduojančio dažnio atvejis (tipinė trupmeninė sub-harmonika). Juoda punktyrinė linija ir raudoni apskritimai, atitinkantys II tipo priešįtamčio sąlygas, vaizduoja priešįtamčio vertes ($F_{dc} = 0, 5$ ir $F_{ac} = 4 : 0, 5 : 5$) kurios buvo panaudotos kairiajame intarpe (d) - (f), vaizduojant santykinės galios priklausomybes nuo zonduojančio dažnio elektrinio lauko stiprio ir fazių skirtumo. Stebimas „stiprinimo salų“ formavimas, nurodantis, kad generacijos procesai iš triukšmo lygio signalo yra neleistini [A3].

4.4 paveikslas: (A) Generacijos metu maksimalios pasiekiamos santykinės galios (kairėje) ir maksimalaus pasiekiamo elektrinio lauko (dešinėje) priklausomybės nuo priešįtamčio sąlygų, apskaičiuoti esant optimaliai fazei, naudojant didelio signalo stiprinimo metodą. Skaičiuojamas $\omega_0/2$ zonduojančio dažnio atvejis. Spalvotos erdvės atitinka generuojamą santykinę galią \bar{P} arba elektrinio lauko stiprį, kuris yra normuotas į Esaki-Tsu kritinį elektrinį lauką $F_1^{(s)}$. Baltos erdvės atitinka priešįtamčio sąlygas kuriuose generacijos procesai yra negalimi. Juoda punktyrinė linija ir raudoni apskritimai, atitinkantys I tipo priešįtamčio sąlygas vaizduoja priešįtamčio vertes ($F_{dc} = 4$ ir $F_{ac} = 0 : 1 : 4$) kurios buvo panaudotos viršutiniame intarpe (a) - (f), vaizduojant santykinės galios priklausomybes nuo zonduojančio dažnio elektrinio lauko stiprio ir fazių skirtumo. Raudonos linijos atitinka neigiamo nekoherentinio judrio komponentę, apskaičiuotą naudojantis mažo signalo stiprinimo modeliu. Intarpas akivaizdžiai atskleidžia nuo fazės nepriklausančio Blocho ir nuo fazės priklausančio parametrinio stiprinimo mechanizmų sambūvį. Dominuojantis stiprinimo mechanizmas keičiasi didėjant kintamo žadinančio elektrinio lauko stipriui: žemo kintamo žadinančio elektrinio lauko stiprio atveju dominuojantis Blocho stiprinimo mechanizmas (a) perteikia dominavimą parametrinio stiprinimo procesui, kol nėra pasiekiamas grynas parametrinis stiprinimo mechanizmas (f). Atkreiptinas dėmesys, kad gryną parametrinį procesą galima stebėti tik tais atvejais, kai yra leistina generacija už neigiamos nekoherentinio judrio komponentės ribų. Be to, grynas parametrinis procesas, kaip yra rodoma vėliau, yra išskirtinė $\omega_0/2$ sub-harmonikos ypatybė, atsirandanti dėl specifinio mažo signalo stip-

rinimo modelio analizės metu nagrinėto judrio skirstinio (žr. 4.1 paveikslą). (B) Viršutinėje dalyje pavaizduotas išdidintas 4.4 (A) paveikslas, atitinkantis mažą kintamo žadinančio elektrinio lauko stiprį ir nuolatinį žadinantį elektrinio lauko stiprį $F_{dc} \approx 1$. Trys raudoni apskritimai atitinka $F_{ac} = 10^{-3}$ ir F_{dc} vertes, kurios yra šiek tiek mažesnės ir didesnės už kritinį elektrinio lauko stiprį. Apačioje pavaizduotos priklausomybės rodo stiprinimo procesų evoliuciją dėl nedidelio nuolatinio priešįtampio pokyčio. Atkreiptinas dėmesys į skirtingus stiprinimo procesus: didėjant nuolatiniam žadinančiam elektriniam laukui parametrinis stiprinimo procesas pereina į Blocho stiprinimo procesą. Toks perėjimas yra unikali $\omega_0/2$ sub-harmonikos savybė [A3].

4.5 paveikslas: Perėjimas iš nuo fazės nepriklausančio Blocho stiprinimo į hibridinį Blocho ir parametrinio stiprinimo mechanizmą didinant kintamo žadinančio elektrinio lauko stiprį ($F_{dc} = 4, F_{ac} = 0 : 1 : 4$). Pateikti grafikai vaizduoja santykinės galios priklausomybę nuo zonduojančio elektrinio lauko stiprio ir fazių skirtumo $5\omega_0/3$ ir $5\omega_0/4$ dažnių atveju. Spalva pažymėtos neigiamos santykinės galios, atitinkančios generacijos procesus supergardelėje, o balta spalva žymimos teigiamos santykinės galios (sugertis). Matoma, kad grynas parametrinis stiprinimas taip ir nėra pasiekiamas, nes išsigimusio proceso atveju tai yra unikali $\omega_0/2$ sub-harmonikos ypatybė. Dviejų mechanizmų sambūvio egzistavimas šiuo atveju leidžia teigti apie „stiprinimo salų“ formavimąsi esant I tipo priešįtampio sąlygoms. „Stiprinimo salų“ formavimąsi taip pat parodo generacijos nebuvimas esant aukštam kintamam žadinančiam elektriniam laukui ($F_{ac} > 4$) [A3].

4.7 paveikslas: Pirmo zonduojančio dažnio santykinės galios priklausomybė nuo pirmo zonduojančio elektrinio lauko fazės ir elektrinio lauko stiprio skirtingu antro zonduojančio dažnio fazių atveju. Analizuojamas neišsigimęs $8/3 + 4/3$ generacijos procesas. Modeliavimo metu naudotos pastovios priešįtampio sąlygos: $F_{dc} = 4; F_{ac} = 3; F_2 = 2$. Spalva nurodo sąlygas, kuriose santykinė galia yra neigiama ir pirmo zonduojančio dažnio generacijos procesai yra leistini. Baltos erdvės atitinka sąlygas, kai santykinė galia yra teigiama ir generacijos procesai nevyksta (sugertis). Atkreiptinas dėmesys į simteriškumo praradimą priklausomybėse. Taip pat vienoje priklausomybėje yra stebimi du skirtingi procesai - generacija nuo triukšmo lygio signalo ir „stiprinimo salos“ formavimasis.

4.8 paveikslas: Pagrindinis paveikslas (centre): maksimalios galimos pirmo zonduojančio dažnio santykinės galios priklausomybė nuo priešįtampio sąlygų ir antro zonduojančio dažnio elektrinio lauko stiprio $4/3 + 8/3$ neišsige-

musio generacijos proceso atveju. Kiekvienas sąlygų rinkinys atitinka maksimaliai pasiekiamą pirmo zonduojančio elektrinio lauko santykinę galią esant optimalioms pirmo ir antro zonduojančių elektrinių laukų fazėms. Spalvotos zonos nurodo sąlygas, kai generacija yra leistina, o baltos – kai draudžiama. Viršutinis intarpas ((a) - (e)): pirmo zonduojančio elektrinio lauko fazės priklausomybė nuo pirmo zonduojančio elektrinio lauko fazės ir elektrinio lauko stiprio, esant skirtingam antro zonduojančio elektrinio lauko elektrinio lauko stipriui. Prieštampio sąlygos atitinka raudonų pussferių padėtis pagrindiniame paveiksle ($F_{dc} = 0,5; F_{ac} = 4; F_2 = 0 : 0,5 : 2$ - II tipo prieštampio sąlygos). Atkreiptinas dėmesys, kad, skirtingai nei išsigimusio proceso atveju, yra leidžiami trupmeninių sub-harmonikų generacijos procesai nuo triukšmo lygio signalo. Šis pastebėjimas patvirtina 3 skyriaus eksperimentinius rezultatus. Apatinis intarpas ((f) - (j)): pirmo zonduojančio elektrinio lauko stiprio priklausomybė nuo pirmo zonduojančio elektrinio lauko fazės ir elektrinio lauko stiprio, esant skirtingam antro zonduojančio elektrinio lauko stipriui. Prieštampio sąlygos atitinka geltonų pussferių padėtis pagrindiniame paveiksle ($F_{dc} = 4; F_{ac} = 3; F_2 = 0 : 0,5 : 2$ - I tipo prieštampio sąlygos). Atkreiptinas dėmesys į išliekantį išsigimusio proceso metu stebėtą dviejų stiprinimo mechanizmų sambūvį. Didėjant antro zonduojančio elektrinio lauko stipriui stebimas parametrinio stiprinimo proceso įtakos didėjimas. Žalia pussferė pagrindiniame grafike atitinka prieštampio sąlygas, pavaizduotas 4.7 paveiksle.

5.1 paveikslas: (a) Klasikinis lazerio veikimo principas, paremtas krūvininkų inversija - trijų lygmenų veikimo schema (kairėje) ir dėl sklaidos išplitę energijos lygmenys (dešinėje). (b) Beinversinis stiprinimas, atsirandantis dėl nehomogeniško krūvininkų pasiskirstymo kiekviename energijos lygmenyje.

5.3 paveikslas: Skirtingi sąsajos mechanizmai, užtikrinantys Blocho stiprinimą. (a) Beinversinis Blocho stiprinimas, atsirandantis dėl lygmenų sąsajos išplitusiu žadinančio lazerio spektru (pažymėtas žalia linija). (b) Beinversinė Blocho stiprinimo schema, kurioje sąsaja yra realizuota per hibridinę Bloch-plazmoninę (Epshteino) modą. Toks sąsajos mechanizmas atitinka tolimesniuose grafikuose šviesiai žalia spalva pažymėtas prieštampio sąlygas.

5.5 paveikslas: Perduotos galios priklausomybė nuo nuolatinio prieštampio (taikomo tiesiogine ir atgaline kryptimis), išmatuota supergardele papildomai žadinant magnetronu. Atkreiptinas dėmesys į tris skirtingas erdves. Mažesnės nei 0,6 V įtampos atveju stebima plazmoninė sugertis; 0,6 V–3,8 V atveju - stabilus Blocho stiprinimas minijuostoje; didesnės nei 4 V įtampos atveju - ne-rezonansinis tarpminijuostinis (Zenerio) tuneliavimas. Atgalinio prieštampio

atveju plazmoninės sugerties erdvė yra stipriai išplėsta, o Blocho stiprinimo erdvė stipriai suspausta dėl struktūroje naudojamų kontaktų asimetriškumo.

5.6 paveikslas: Skirtingų dominuojančių krūvininkų transporto priklausomybė nuo prieštamčio. Žemiau kritinio Esaki-Tsu elektrinio lauko stebimas ominis režimas. Įtampai didėjant stebimos Blocho osciliacijos ir ominio režimo metu stebėta plazmoninė moda pereina į stabilų Blocho stiprinimą. Aukšto prieštamčio sąlygomis dominuoja tarpminijuostinis krūvininkų pernašos mechanizmas, pasireiškiantis per nerezonansinius Zenerio tuneliavimo procesus.

CURRICULUM VITAE

Name: Vladislovas
Surname: Čižas
Date of birth: 1995-01-29
Place of birth: Vilnius, Lithuania
E-mail: vladislovas.cizas@ftmc.lt

Education:

2019 – 2023 Center for Physical Sciences and Technology
Ph.D. studies.

2017 – 2019 Vilnius University, Faculty of Physics
Master's degree in Technological Sciences.

2014 – 2017 Vilnius University, Faculty of Physics
Bachelor's degree in Applied Physics.

2002 – 2014 Vilnius Lukiškių high school.

Work experience:

2022-06 – now Center for Physical Sciences and Technology, Department of Optoelectronics,
Junior research fellow.

2019-07 – 2022-06 Center for Physical Sciences and Technology, Department of Optoelectronics,
Engineer.

2015-09 – 2019-01 Vilnius University, Institute of Photonics and Nanotechnology,
Student intern.

2014-07 – 2014-08 Center for Physical Sciences and Technology, Department of Laser Technologies,
Student intern.

Vardas: Vladislovas
Pavardė: Čižas
Gimimo data: 1995-01-29
Gimimo vieta: Vilnius, Lithuania
El. paštas: vladislovas.cizas@ftmc.lt

Išsilavinimas:

2019 – 2023 Fizinių ir Technologijos mokslų centras
Doktorantūros studijos.

2017 – 2019 Vilniaus Universitetas, Fizikos Fakultetas
Magistro studijos. Optoelektronikos medžiagos ir technologijos.

2014 – 2017 Vilniaus Universitetas, Fizikos Fakulteta
Bakalauro studijos. Taikomoji fizika.

2002 – 2014 Vilniaus Lukiškių vidurinė mokykla.

Darbo patirtis:

2022-06 – dabar Fizinių ir Technologijos mokslų centras, Optoelektronikos skyrius,
Jaunesnysis mokslo darbuotojas.

2019-07 – 2022-06 Fizinių ir Technologijos mokslų centras, Optoelektronikos skyrius,
Inžinierius.

2015-09 – 2019-01 Vilniaus Universitetas, Fotonikos ir Nanotechnologijų institutas,
Studentas, praktika.

2014-07 – 2014-08 Fizinių ir Technologijos mokslų centras, Lazerinių technologijų skyrius,
Studentas, praktika.

NOTES

NOTES

Vilnius University Press
Saulėtekio al. 9, LT-10222 Vilnius
e-mail: info@leidykla.vu.lt,
www.leidykla.vu.lt
Print run copies 20